

WRDC-TR-90-2094  
Volume 1



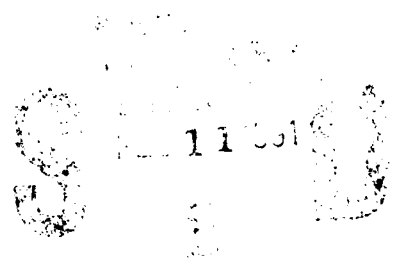
COMBUSTION DIAGNOSTIC DEVELOPMENT AND APPLICATION

L. P. GOSS  
G. L. SWITZER

Systems Research Laboratories, Inc.  
*A Division of Arvin/Calspan*  
2800 Indian Ripple Road  
Dayton, OH 45440-3696

November 1990

Final Report for Period 16 September 1985 - 16 June 1990



Approved for public release; distribution unlimited.

AERO PROPULSION AND POWER LABORATORY  
WRIGHT RESEARCH AND DEVELOPMENT CENTER  
AIR FORCE SYSTEMS COMMAND  
WRIGHT-PATTERSON AIR FORCE BASE, OH 45433-6563

AD-A231 667

91 2 06 032

## NOTICE

WHEN GOVERNMENT DRAWINGS, SPECIFICATIONS, OR OTHER DATA ARE USED FOR ANY PURPOSE OTHER THAN IN CONNECTION WITH A DEFINITELY GOVERNMENT-RELATED PROCUREMENT, THE UNITED STATES GOVERNMENT INCURS NO RESPONSIBILITY OR ANY OBLIGATION WHATSOEVER. THE FACT THAT THE GOVERNMENT MAY HAVE FORMULATED OR IN ANY WAY SUPPLIED THE SAID DRAWINGS, SPECIFICATIONS, OR OTHER DATA, IS NOT TO BE REGARDED BY IMPLICATION, OR OTHERWISE IN ANY MANNER CONSTRUED, AS LICENSING THE HOLDER, OR ANY OTHER PERSON OR CORPORATION; OR AS CONVEYING ANY RIGHTS OR PERMISSION TO MANUFACTURE, USE, OR SELL ANY PATENTED INVENTION THAT MAY IN ANY WAY BE RELATED THERETO.

THIS REPORT HAS BEEN REVIEWED BY THE OFFICE OF PUBLIC AFFAIRS (ASD/PA) AND IS RELEASABLE TO THE NATIONAL TECHNICAL INFORMATION SERVICE (NTIS). AT NTIS IT WILL BE AVAILABLE TO THE GENERAL PUBLIC INCLUDING FOREIGN NATIONS.

THIS TECHNICAL REPORT HAS BEEN REVIEWED AND IS APPROVED FOR PUBLICATION.

*W. M. Roguemoire*

W. MELVYN ROQUEMORE  
Fuel Combustion Group  
Fuels Branch

*Charles L. Delaney*

CHARLES L. DELANEY  
Chief, Fuels Branch  
Fuels and Lubrication Division

FOR THE COMMANDER

*L. S. Harootyan, Jr.*

LEO S. HAROOTYAN, JR., Acting Chief  
Fuels and Lubrication Division  
Aero Propulsion and Power Directorate

IF YOUR ADDRESS HAS CHANGED, IF YOU WISH TO BE REMOVED FROM OUR MAILING LIST, OR IF THE ADDRESSEE IS NO LONGER EMPLOYED BY YOUR ORGANIZATION PLEASE NOTIFY WL/POSF, WRIGHT-PATTERSON AFB, OH 45433-6563 TO HELP MAINTAIN A CURRENT MAILING LIST.

COPIES OF THIS REPORT SHOULD NOT BE RETURNED UNLESS RETURN IS REQUIRED BY SECURITY CONSIDERATIONS, CONTRACTUAL OBLIGATIONS, OR NOTICE ON A SPECIFIC DOCUMENT.

UNCLASSIFIED

SECURITY CLASSIFICATION OF THIS PAGE

## REPORT DOCUMENTATION PAGE

Form Approved  
OMB No. 0704-0188

1a. REPORT SECURITY CLASSIFICATION <b>Unclassified</b>			1b. RESTRICTIVE MARKINGS			
2a. SECURITY CLASSIFICATION AUTHORITY			3. DISTRIBUTION / AVAILABILITY OF REPORT Approved for public release; distribution unlimited.			
2b. DECLASSIFICATION / DOWNGRADING SCHEDULE						
4. PERFORMING ORGANIZATION REPORT NUMBER(S) 6890 Final, Volume 1			5. MONITORING ORGANIZATION REPORT NUMBER(S) WRDC-TR-90-2094, Volume 1			
6a. NAME OF PERFORMING ORGANIZATION Systems Research Laboratories, Inc., Division of Arvin/Calspan		6b. OFFICE SYMBOL (if applicable)	7a. NAME OF MONITORING ORGANIZATION Aero Propulsion and Power Lab. (WRDC/POSF) Wright Research and Development Center			
6c. ADDRESS (City, State, and ZIP Code) 2800 Indian Ripple Road Dayton, OH 45440-3696			7b. ADDRESS (City, State, and ZIP Code) WRDC/POSF Wright-Patterson AFB, OH 45433-6563			
8a. NAME OF FUNDING / SPONSORING ORGANIZATION		8b. OFFICE SYMBOL (if applicable)	9. PROCUREMENT INSTRUMENT IDENTIFICATION NUMBER F33615-85-C-2562			
8c. ADDRESS (City, State, and ZIP Code)			10. SOURCE OF FUNDING NUMBERS			
			PROGRAM ELEMENT NO. 62203F	PROJECT NO. 3048, 2301	TASK NO. 05, S1	WORK UNIT ACCESSION NO. 53, 27
11. TITLE (Include Security Classification) Combustion Diagnostic Development and Application						
12. PERSONAL AUTHOR(S) Goss, L. P., and Switzer, G. L.						
13a. TYPE OF REPORT Final		13b. TIME COVERED FROM 85Sep16 TO 90Jun16		14. DATE OF REPORT (Year, Month, Day) Nov 90		15. PAGE COUNT 221
16. SUPPLEMENTARY NOTATION						
17. COSATI CODES			18. SUBJECT TERMS (Continue on reverse if necessary and identify by block number)			
FIELD	GROUP	SUB-GROUP	Coherent Anti-Stokes Raman Spectroscopy (CARS), Combustion Diagnostics, Laser Doppler Velocimetry (LDV), Thin-Filament Pyrometry (TFP), Planar Laser-Induced (continued)			
21	02					
20	06					
19. ABSTRACT (Continue on reverse if necessary and identify by block number) Numerous advanced combustion-diagnostic techniques have been developed and evaluated for flame studies. These techniques include a combined coherent anti-Stokes Raman spectroscopy (CARS)/laser-Doppler velocimetry (LDV) system for simultaneous temperature and velocity measurements; thin-filament-pyrometry (TFP) for high-speed, multi-dimensional thermometry; flame-visualization techniques [reactive Mie scattering (RMS), two-dimensional Rayleigh, and planar laser-induced fluorescence (PLIF) of the OH Radical] for obtaining two-dimensional flame-structure information; two-color particle-imaging velocimetry (PIV) for two-dimensional velocity measurements in low- and high-speed flowfields; hardened CARS system for thermometry in large-scale combustion systems; and a combined CARS/phase Doppler particle analyzer (PDPA) system for temperature, velocity, and particle-size measurements in spray-combustion systems. In addition, the LDV technique was utilized extensively for pointwise velocity measurements. These techniques were developed, evaluated, and applied to the study of turbulent combustion flames. (continued)						
20. DISTRIBUTION / AVAILABILITY OF ABSTRACT <input type="checkbox"/> UNCLASSIFIED/UNLIMITED <input type="checkbox"/> SAME AS RPT. <input checked="" type="checkbox"/> DTIC USERS			21. ABSTRACT SECURITY CLASSIFICATION Unclassified			
22a. NAME OF RESPONSIBLE INDIVIDUAL W. M. Roquemore, Ph.D.			22b. TELEPHONE (Include Area Code) (513) 255-6813		22c. OFFICE SYMBOL WRDC/POSF	

DD Form 1473, JUN 86

Previous editions are obsolete.

SECURITY CLASSIFICATION OF THIS PAGE

UNCLASSIFIED

UNCLASSIFIED

Block 18. SUBJECT TERMS (Continued)

Fluorescence (PLIF), Reactive Mie Scattering (RMS), Phase Doppler Particle Analyzer (PDPA), Two-Color Particle Imaging Velocimetry (PIV), Spray Diagnostics, Droplet-on-Demand Generator, Jet Diffusion Flames, Axially Symmetric Swirl Combustor, Fractal Analysis.

Block 19. ABSTRACT (Continued)

Experimental results obtained with the advanced diagnostic instrumentation were used in the evaluation of several numerical flame models. Both small (Bunsen and jet diffusion flames) and large (6- and 10-in.-diam. combustors) systems were studied utilizing the advanced diagnostic techniques.

UNCLASSIFIED

# PREFACE

This report was prepared by L. P. Goss, Ph.D., and G. L. Switzer and covers work performed during the period 16 September 1985 through 16 June 1990 under Air Force Contract F33615-85-C-2562. The contract was administered under the direction of the Wright Research and Development Center, Aero Propulsion and Power Laboratory, Wright-Patterson Air Force Base, Ohio, with W. M. Roquemore, Ph.D., and S. W. Kizirnis as Government Project Monitors.

<b>Accession For</b>	
NTIS GRA&I	<input checked="" type="checkbox"/>
DTIC TAB	<input checked="" type="checkbox"/>
Unannounced	<input type="checkbox"/>
Justification	
By _____	
Distribution/	
Availability Codes	
Dist	Avail and/or Special
A-1	



## TABLE OF CONTENTS

<u>Section</u>		<u>Page</u>
1	INTRODUCTION .....	1
2	ADVANCED COMBUSTION DIAGNOSTIC DEVELOPMENT AND EVALUATION .....	3
2.1	General Overview .....	3
2.2	Combined CARS/LDV System .....	3
2.3	Thin-Filament Pyrometry .....	71
2.4	Flame Visualization .....	107
2.5	Two-Color Particle-Imaging Velocimetry .....	152
2.6	Spray-Diagnostic Development .....	174

## Section 1

### INTRODUCTION

This report describes the results of experimental and theoretical investigations on advanced combustion-diagnostic techniques and the application of these techniques to turbulent flames studies. The goals of this effort were to develop and evaluate advanced laser-based combustion diagnostic techniques and to apply the most promising techniques to the study of flame systems of interest in combustion-model evaluation and validation.

In addressing the technical goals of combustor designers (especially for advanced engine designs), models must be developed which not only provide design and testing aids but also produce new insights into the basic behavior of high-temperature chemically reacting flows. Major strides in the development of computational-fluid-dynamic (CFD) models have been made over the past decade; however, the ability to calculate accurately the fields of velocity, species concentration, temperature, and pollutants in practical systems (i.e., gas turbines, internal-combustion engines, and industrial furnaces) remains limited.

Validation of CFD models requires the measurement of velocity in conjunction with several scalars which allows evaluation of cross correlations. The techniques developed and evaluated during the course of this program were directed toward the measurement of quantities which are important for model development and evaluation. The techniques investigated and/or developed include a combined coherent anti-Stokes Raman spectroscopy (CARS)/laser Doppler velocimetry (LDV) system for simultaneous temperature/velocity measurements and correlations; thin-filament pyrometry (TFP) for high-speed and multi-dimensional thermometry; flame visualization techniques [reactive Mie scattering (RMS), two-dimensional Rayleigh, and planar laser-induced fluorescence (PLIF) of the OH radical] for obtaining two-dimensional flame-structure information; two-color particle-imaging velocimetry (PIV) for two-dimensional velocity measurements in low- and high-speed flowfields; hardened CARS system for thermometry in large-scale combustion systems; and a combined CARS/phase Doppler particle analyzer (PDPA) system for temperature, velocity, and particle-size measurements in spray-combustion systems. In addition, the LDV technique was extensively utilized for pointwise velocity measurements.

These techniques were developed, evaluated, and applied to the study of turbulent-combustion flames. Experimental results obtained with the advanced diagnostic instrumentation were utilized in the evaluation of several numerical flame models. Both small (Bunsen and jet diffusion flames) and large (6- and 10-in.-diam. combustors) systems were studied with the advanced diagnostic techniques.

The research conducted during this program resulted in 96 publications, presentations, and patents; a list of these is included in the Appendix to Volume 2. The summary of research efforts in this report is divided into two parts. The first (summarized in Sect. 2 of this volume) deals with the development and evaluation of advanced diagnostic techniques, while the second (summarized in Volume 2) treats the applications of the advanced techniques to combustion studies.

## Section 2

### ADVANCED COMBUSTION DIAGNOSTIC DEVELOPMENT AND EVALUATION

#### 2.1 GENERAL REVIEW

A general review of the diagnostic development and evaluation conducted in this program was given in a paper entitled, "Development of Laser Diagnostics for Combustion Research," which was presented at the 1986 Spring Technical Meeting of the Central States Section of the Combustion Institute (see p. 5). This paper described efforts during the early stages of this program. A second paper, "Optical Diagnostics for Reacting and Non-Reacting Flows: Recent Developments and Results," presented at the 28th Aerospace Sciences Meeting discussed later developments in the program (see p. 37).

#### 2.2 COMBINED CARS/LDV SYSTEM

The experimental study of turbulent transport processes is very difficult because of the need for simultaneous measurement of velocity and scalar variables. The development of the LDV technique has led to the routine measurement of velocities in reacting flows. The measurement of scalar quantities, however, has lagged in development. The CARS technique which has been extensively investigated in this laboratory is capable of temperature and major-flame-species measurements in hostile, reacting flow environments. Because of the unique features of the CARS technique and familiarity with both the CARS and LDV methods, a combined CARS/LDV system was developed and evaluated. This instrument is capable of making simultaneous two-component velocity and temperature measurements in hostile combusting flowfields. A detailed discussion of the initial combined instrument can be found in the article entitled, "Combined CARS/LDA Instrument for Simultaneous Temperature and Velocity Measurements," which appeared in *Experiments in Fluids* (see p. 47). A second-generation instrument which incorporated several improvements was discussed in two papers; the first entitled, "Combined CARS-LDV System for Turbulent Flame Studies," was presented at the 1988 Spring Technical Meeting of the Central States Section of the Combustion Institute (see p. 57). The second, a full-length article entitled, "Second-Generation CARS-LDV Instrument for Simultaneous Temperature

and Velocity Measurements in Combusting Flows," appeared in *Review of Scientific Instruments* (see p. 63).

.

.

.

.

# DEVELOPMENT OF LASER DIAGNOSTICS FOR COMBUSTION RESEARCH

W. M. ROQUEMORE, R. P. BRADLEY, T. A. JACKSON AND S. W. KIZIRNIS  
AFWAL AERO PROPULSION LABORATORY  
WRIGHT-PATTERSON AFB, OH 45433-6563

L. P. GOSS, G. L. SWITZER, D. D. TRUMP and B. SARKA  
SYSTEMS RESEARCH LABORATORIES, INC.  
DAYTON, OH 45440-3696

D. R. BALLAL, A. J. LIGHTMAN, P. P. YANEY AND T. H. CHEN  
UNIVERSITY OF DAYTON  
DAYTON, OH 45469-0001

## 1986 SPRING TECHNICAL MEETING



**CENTRAL STATES SECTION  
The Combustion Institute**

**MAY 5 - 6, 1986**

NASA Lewis Research Center  
21000 Brookpark Road  
Cleveland, OH 44135

# DEVELOPMENT OF LASER DIAGNOSTICS FOR COMBUSTION RESEARCH

W. M. Roquemore, R. P. Bradley, T. A. Jackson and S. W. Kizirnis  
AFWAL Aero Propulsion Laboratory  
Wright-Patterson AFB, OH 45433-6563

L. P. Goss, G. L. Switzer, D. D. Trump and B. Sarka  
Systems Research Laboratories, Inc.  
Dayton, OH 45440-3696

D. R. Ballal, A. J. Lightman, P. P. Yaney and T. H. Chen  
University of Dayton  
Dayton, OH 45469-0001

## Abstract

In 1977, the AFWAL Aero Propulsion Laboratory initiated the Combustor Model Evaluation research program with two primary objectives: to develop and evaluate the performance of probes and laser measurement techniques and to use the proven techniques in well conceived experiments to aid in the evaluation and development of combustion models. This paper provides an overview of the Combustion Model Evaluation program with special emphasis on the laser diagnostic techniques that have been developed and applied in combustion research and the techniques that are being considered for future development.

## Background and Introduction

The environment was right in the early 1970's for the awakening of a new technical field often referred to as combustion diagnostics. A Project SQUID Workshop entitled Laser Raman Gas Diagnostics [1] clearly demonstrated that Laser Raman Spectroscopy (LRS) and Coherent Anti-Stokes Raman Spectroscopy (CARS) could be used to study flames. A second Project SQUID workshop entitled Combustion Measurements [2] and a study sponsored by The American Physical Society entitled "The Role of Physics in Combustion" [3] provided excellent overviews of the potentials and the limitations of laser spectroscopic techniques in combustion research.

The initial driving force for the development of laser diagnostics was the study of pollutants and their formation processes in combusting flows. However, this was not sufficient in itself to sustain the area. Fortunately, the Organization of Petroleum Exporting Countries added impetus to the area with the oil

embargo of the mid 70's. The realization that new sources of energy would be needed in the future provided the stimulus required to place new importance on combustion research. Several workshops formulated the direction this research should take [4,5]. That is, long-term research programs should be established at centers where computer-based combustion models and laser-based combustion diagnostics could be developed and evaluated in mutually supporting roles.

The combustion research needs of the Air Force [6] are similar to those addressed by the workshops. The design of gas turbine combustors are based upon empirical correlations, experience and the cut-and-try approach. Computer models have the potential of greatly enhancing the design methodology. They are being developed and utilized in some combustor development programs in an attempt to reduce the development cycle time and the associated development cost [7,8,9]. The combustor design models presently provide information about performance trends, and give insights into the combustion processes, but are unable to provide accurate quantitative design information [10]. Studies performed for the NASA HOST program have shown that considerable work is needed to thoroughly assess the performance of existing and future design models and to improve their predictive capabilities in both fundamental and practical combusting environments [11,12,13].

The Combustion Model Evaluation (CME) program established at the Air Force Aero Propulsion Laboratory (APL) was conceived in 1973. However, it was 1977 before the necessary resources became available to effectively start the program. The CME program is viewed as a long-term program with two primary objectives: to develop and evaluate the performance of probes and advanced laser measurement techniques in combustion environments and to use the proven techniques in well conceived experiments to add to the existing data base for the evaluation and development of combustion models.

Numerous resources are required to successfully conduct such a broad scope program. First, and most importantly, an imaginative and energetic research team is required which has expertise in spectroscopy and instrumentation development, combustion and combustion models, facility development and operation, and computer hardware and software. Second, facilities in which fundamental combustion experiments can be performed with conventional and laser instrumentation are required along with a laboratory for evaluating and developing the laser techniques. Third, the optical equipment that can be used in developing the laser techniques are required. Such a program also requires substantial support over a long period of time and a good technical and management approach which can bring all the resources together. It is also very important that one's management be understanding and patient because it takes a long time from conception of such a program until the first results are obtained. The Aero Propulsion Laboratory has attempted to bring these

resources together in the CME program.

This paper provides an overview of the CME program with special emphasis on the laser diagnostic techniques that have been developed and applied in combustion research and the techniques that are being considered for future development. The paper is arranged into four sections: Research Team and Program Organization, Facilities, Optical Instrumentation and Applications, and Concluding Remarks.

### Research Team and Program Organization

The CME program is organized into three research teams. Responsibilities and resources of each team, are depicted in Figure 1. The primary objective of the Systems Research Laboratory team is to evaluate and develop laser-based combustion diagnostic techniques. This program includes fundamental investigations of new combustion diagnostic techniques. It also involves developing a proven technique into a system that is hardened for use in a test cell environment. The instrumentation development and evaluation research is performed in the Diagnostics Development Laboratory which is well equipped with a vertical combustion tunnel, lasers and other optical equipment. Their recent accomplishments include: coupling CARS and Laser Doppler Anemometer (LDA) systems so that temperature and velocity measurements can be made simultaneously, the application of CARS in a recirculating combustor flow, and the development of an optoacoustic beam-deflection technique for making high sampling rate temperature measurements in flames.

The responsibilities of the University of Dayton team is to utilize the laser techniques in performing baseline experiments which can be used in evaluating and developing combustion models and exploring the fundamental physics of turbulent combustor flows. Their recent accomplishments have been the application of a high data rate Raman system to a turbulent mixing layer, the coupling of a two-component Laser Doppler Anemometer (LDA) and a Laser Raman/Rayleigh Scattering system for making high sampling rate velocity and species concentration measurements simultaneously, and the development of a Fundamental Combustion Laboratory.

The responsibilities of the Air Force team are to conduct fundamental combustion and spray research as it pertains to the burning of fuels in gas turbine combustors. The development of a laser sheet-lighting technique for flow visualization and the modification of the Combustion Tunnel Facility to accommodate a swirl combustor are recent accomplishments. Further, a Spray Research Laboratory is under development. These facilities will be discussed in the next section.

## Facilities

The Combustion Tunnel Facility has been the primary test rig in which computer model evaluation experiments have been performed. It also serves as a test device for evaluating combustion diagnostic techniques in complex combusting flows. Considerable effort went into selecting a research combustor configuration for this facility. It was desirable that the combustor simulate some of the features of an actual gas turbine combustor and have a geometry simple enough to be modeled. It should also provide easy optical access to the combustor inlet plane and the reaction zone. The configuration should also be capable of being modified through logical steps so that the flow field becomes progressively closer to that in an actual gas turbine combustor.

A centerbody combustor was chosen for the initial test configuration because it seemed to have the above mentioned characteristics [14]. Figure 2 depicts the centerbody combustor and its derivatives. Research with the Phase I centerbody combustor is complete. The facility, as modified for the Phase II combustor, is shown in Figures 3 and 4. The Phase II combustor is installed and currently undergoing checkout tests. This facility is the center of much of the activities of the CME program because it is one of the few facilities that bridges the gap between the more fundamental burner configurations and the very complex combustors developed by industry. Much of the research performed in this facility is described in Ref. 15.

The Fundamental Combustion Laboratory has been developed for the purpose of conducting fundamental combustion experiments in well controlled environments [16]. Figure 5 is a schematic diagram of a small combustion tunnel that was developed for this facility. The tunnel is referred to as the vertical combustion tunnel because it is mounted vertically on an x,y,z platform. This has the advantage of allowing detail profiling of combusting flows with fixed optical systems. An identical vertical tunnel is used for diagnostic development in the Diagnostic Laboratory.

Computers are considered essential to the development and application of laser diagnostic techniques. A computer is needed to handle the large quantity of data collected with the laser techniques and to allow different optical systems to be coupled for simultaneous measurements. Indeed, the manhours devoted to computer software development is as large as that devoted to actually developing the diagnostic systems. Each of the CME laboratories has a similar dedicated computer and all of the laser and conventional instrumentation are required to interface with them. This provides the flexibility of developing a diagnostic system in one laboratory and applying it in any of the others without major software changes.

Hardened CARS System

The hardened CARS system has evolved over a period of about 10 years. The first system used a ruby laser (1 Hz pulse rate) and had a colinear-beam optical configuration. This system was used to demonstrate the feasibility of making single shot CARS temperature measurements in the Combustion Tunnel Facility [17]. The low data rate and poor spatial resolution seriously limited the value of this system as a combustion research tool. To solve these two problems, a second system was developed based upon a frequency-doubled Nd-YAG laser operating at a 10 Hz repetition rate and in a folded BOXCARS optical geometry. This combination allowed high temporal (10 ns) and spatial (1 mm<sup>3</sup>) measurement resolution within the combusting medium. The optical and electronic configurations are shown in Figures 6 and 7, respectively. This system with some minor modifications is referred to as the hardened CARS system. Detail descriptions, design features and experimental results obtained with this system can be found in Refs. [18-20]. Other CARS research performed on the CME program are contained in [21-23].

The hardened CARS system is designed to make instantaneous and simultaneous measurements of gas temperature and concentrations of N<sub>2</sub> and O<sub>2</sub> at a common point and at a rate of 10 Hz. These capabilities have been demonstrated in extensive calibration and checkout testing on a laboratory flame [18]. However, checkout tests in the Combustion Tunnel Facility revealed that large thermally induced index-of-refraction gradients cause a decrease in CARS scattering intensity. While this intensity loss does not detract from the spectral content (i.e., temperature-dependent information), it does prohibit determination of N<sub>2</sub> concentration by relative intensities. Because of this, reliable concentration measurements could not be made with the CARS system in the near-wake region of the centerbody combustor. Future research will include the investigation of methods for compensating the CARS signals for turbulent beam steering.

Figure 8 is a demonstration of the detailed average temperature mapping that has been accomplished with the hardened CARS system in the highly sooting, recirculating, near-wake region of the centerbody combustor [20]. Such time averaged CARS measurements are important because they can be used to evaluate combustion models as illustrated in Figure 8 by the comparison with model predictions. However, the CARS temperature pdf's give a better insight into the physics of the combustion process as illustrated in Figure 9. The bimodal shape of the temperature pdf's at radial locations near the edge of the centerbody indicate that vortices are being shed from the combustor face as depicted in Figure 8. As the vortices rotate, they transport annulus air into the recirculation zone. This air is initially unmixed with combustion products and can be tracked by it's 300 K temperature. By denoting the radial locations of the temperature pdf's in Figure 9 where there

are significant populations in the 300 K bin, one can tell how far the large vortex structures actually transport unmixed air from the annulus region into recirculation zone at different axial locations [20]. The probability of the 300 K bin also gives the fraction of time that unmixed annulus air is actually transported to a given location. The CARS technique is probably the most reliable method currently available of measuring temperatures in such a complex combusting environment and, as illustrated, it can give considerable insight into the physics of the flow.

### Hardened LDA System

The hardened LDA system design is based on experience obtained in the Combustion Tunnel Facility with a single component system. A schematic diagram of the LDA system is shown in Figure 10. It can simultaneously measure two velocity components at a rate in excess of 30,000 velocity realizations per second. Polarization is used to separate the two velocity components and a Bragg cell is used to remove directional ambiguity. The direction of polarization and relative position of the beams forming the measurement volume are shown in Figure 11. Note that this system also includes a technique for measuring flame luminosity. Detail descriptions of the hardened LDA system and research performed with it are given in Refs. [24-28].

Figures 12 and 13 illustrate results obtained with the hardened LDA/Luminosity system in the Combustion Tunnel Facility. These data illustrate how a velocity bias error was detected using luminosity measurements to conditionally sample the velocity data. The measurements were made on centerline and downstream of the recirculation zone established behind the centerbody combustor. The flame luminosity measurements were made along a line-of-sight that passed through the LDA measurement volume. Figure 12 illustrates a time record of axial velocities (top) and flame luminosity (bottom) obtained simultaneously. Note that the flame is intermittent. Figure 13 shows the number of realizations of the axial velocities using: all the LDA data (total), only those where there is no luminous signal (no flame), and only where there is luminosity. Figure 13 clearly shows that the distribution and mean values of the velocity measurements are different when conditioned with the presence of flame. The important feature of the distributions is that the velocity measurements in the flame are much less frequent than they should be. The fraction of time that the flame was present, as measured from a large sampling of the luminosity time traces, was considerably larger than when it was not present. The number of velocity realizations indicates the opposite is true. This discrepancy illustrates that the mean velocity measurement are weighted towards the colder fluid elements.

Two causes can be given for the observed velocity bias error. Unknown to us at the time, other researchers had shown that  $\text{TiO}_2$  seed particles, which were used in the experiment, do not scatter effectively at high temperatures [29]. This could cause a bias in the mean velocities towards the colder temperatures.

Also, there could be a density weighting effect which would cause more velocity realizations in the cold, high density fluid elements than in the hot regions. As will be discussed in the next section, conditional sampling measurements, made with the combined CARS/LDA system, indicate that both the  $\text{TiO}_2$  scattering and the density weighting effects are occurring.

### CARS/LDA System

Studies of turbulent transport characteristics in flames require simultaneous measurements of velocity and a scalar. The feasibility of making nearly simultaneous temperature and two velocity component measurements using a laboratory CARS system and the hardened LDA system have been demonstrated in a propane/air premixed Bunsen burner flame [30]. The optical layout of the combined CARS/LDA system, shown in Figure 14, provides a common measurement volume while effectively keeping the two optical systems intact. The integration of the systems occurs in the electronics and the computer software that governs the timing sequence (See Figure 15). The approach involves creating a 100  $\mu\text{s}$  window during every 100 ms firing interval of the CARS laser. If a velocity realization is recorded during the window, the CARS laser is fired 4  $\mu\text{s}$  later. This guarantees nearly simultaneous temperature and velocity measurements, and hence, the ability to measure velocity temperature correlations (See Figure 16). If no realization occurs, then there is a 100 ms waiting period before the CARS laser can be fired. This sequence was established by the operating characteristics of the Nd:YAG laser used in the CARS system and the desire to obtain nearly simultaneous velocity and temperature measurements. The CARS/LDA system is described in Ref. 30. Other investigations for combining these two systems are given in [31,32].

The main advantage of the CARS/LDA over other techniques that provide temperature/velocity correlations is that it can operate in adverse environments involving highly sooting flames that are stabilized by complex, swirling recirculation zones and fueled by spray nozzles. The main disadvantage of the approach used to ensure simultaneous CARS/LDA measurements is that very low data rates are observed ( $<0.5/\text{s}$ ). A new approach to be implemented in the CARS/LDA system developed for the Fundamental Combustion Laboratory is to fire the CARS laser at a constant rate of 10 Hz while free running the LDA system. Coincidence will be achieved by interpolation of the LDA data to obtain the two velocity components at the same time as the CARS laser firing.

The abilities of the CARS/LDA system to examine bias errors due to the presence of seed particles are illustrated in Figures 17 and 18. The low temperature biasing of  $\text{TiO}_2$  seed particles is noted by comparing the free running (unconditioned) CARS temperature measurements ( $T_U$ ) with those conditioned by the simultaneous velocity measurements ( $T_C$ ) in Figure 17. This bias was shown to be primarily due to the

reduction in effective scattering from the  $\text{TiO}_2$  particles at high temperatures [30].  $\text{Al}_2\text{O}_3$  seed particles seemed to hold up in the flame environment but exhibited a density weighted (Favre) bias. This is shown in Figure 18 by comparing the calculated density weighted pdf's ( $T_F$ ) and the conditioned pdf's  $T_C$ . It appears that the inherent seeding of flows to make LDA measurements results in Favre averaged velocities if the data are not taken at equal time intervals.

### CARS-Phase Doppler

An understanding of the dynamics of liquid sprays in a combusting environment is essential to the understanding of the processes occurring in gas turbine combustors. To study these dynamics, a system is being developed which will combine the temperature and concentration measurement capabilities of the previously described hardened CARS system with a system capable of performing droplet size and two-component velocity measurements.

The Phase Doppler technique developed by Bachalo and Houser [33] is being employed to provide simultaneous measurements of drop size and velocity. This instrument is configured as a two-beam LDA device except for the position and internal configuration of the detector. The detector is positioned  $30^\circ$  off the forward axis and consists of a single compound lens and three photomultiplier tubes, positioned to observe three spatially distinct positions of the lens. Drop size information is encoded in the spacing of fringes projected to the receiver lens by droplets interacting with the interferometric probe volume. The spatial variation of fringe spacing in the receiver plane results from the relative phase shift in the rays of light reaching the receiver after traveling paths of different lengths through the droplet. Any two of the detectors can measure this phase shift. The third detector serves to identify a phase shift larger than  $2\pi$  radians. The phase shift is linearly related to drop diameter.

Droplet velocities are encoded in the period of the Doppler burst measured at all three detectors. This frequency information is analyzed as in a standard LDA instrument. Both size and velocity measurements have been shown to be unaffected by incident beam attenuation provided the signal-to-noise ratio is sufficiently large. Preliminary work on dense sprays has been quite encouraging [33-35]. The results indicate that accurate droplet velocity and size measurements can be made in extremely dense spray media.

Since both the CARS and Phase Doppler instruments are stand alone systems, integration of their optical systems can be as straight forward as that diagrammed in Figure 19. Here the CARS and Phase Doppler systems are arranged with counter propagating beams through the sample volume. The 30 degree forward scattering geometry of the Phase Doppler configuration allows convenient separation of the two signal paths.

Once the optical signals from the CARS and Phase Doppler systems have been detected, the electrical information is processed as diagramed in Figure 20. The CARS and Phase Doppler information can be collected independently of the operation of the two systems. With the insertion of an event marker/time word capability, events occurring in the two data streams can be uniquely identified and correlations obtained.

Several problems which must be addressed with the combined CARS-Phase Doppler instrument occur primarily with the ability of the CARS technique to work in dense spray environments. As observed in the combined CARS-LDA system operation, high-density solid seed particles can cause problems with the high-peak-power lasers due to optical breakdown. This may constitute an acute problem in dense sprays where the droplet size can become quite large. Another problem might be the added nonresonant background contribution due to the presence of the spray. If the droplets do not induce catastrophic absorption of the CARS beams they may still increase the nonresonant-to-resonant signal ratio which can complicate the analysis of the CARS spectra. One approach to avoiding these problems is to delay the CARS measurement until the sample volume is clear of droplets. The amount of this delay will thus determine the degree of simultaneity of the two measurements.

#### (Raman) LRS/LDA System

The LRS/LDA system is designed to provide nearly simultaneous measurements of two velocity components and two scalar quantities. The LDA system in the combined instrument is almost identical to the previously described hardened LDA system. The optical layout of the LRS (Raman) system is shown in Figure 21. The optical integration of the two systems is illustrated in Figure 22. Details of the integrated system are given in Ref. 14. The LRS/LDA system is currently being used in cold flow mixing and premixed flame experiments in the Fundamental Combustion Laboratory. Results from these studies will be published in the near future.

The LRS system has several noteworthy characteristics. It uses photon counting and is capable of measuring either the concentration of two gases in cold flow or temperature and concentration fluctuations of a single gas species, such as  $N_2$ , in a flame. The use of this system in flame studies is limited by the low signal strength that results from the small Raman scattering cross-sections of gas molecules. The Raman signal is enhanced by using the pure Stokes rotational Raman lines of the probe gas, a 9 W cw Argon-ion laser, and a multipass cell. This provides sufficient signal to permit sampling rates up to 2 kHz in flames and up to 5 kHz in cold flows. A unique feature of the LRS system is the use of high spectral resolution which permits Raman measurements in the presence of LDA seed. The design details and results obtained with this system are given in Refs. 37-41.

The LRS system was recently used in a study of a cold flowing mixing layer which won the 1985 AIAA National Award for outstanding research paper [39]. The experiments and some of the results are shown in Figure 23. The mixing layer development downstream of a splitter plate can be described by three regions. The first is a laminar-like flow region in which an instability develops and grows to orderly coherent eddies that dominate the second region. In the third region, fully developed turbulent motion prevails. The energy of the low frequency eddies could be reduced substantially by putting a coarse grid just upstream of the splitter plate tip. This is shown by the LRS-determined power spectral density function of the concentration fluctuations in Figure 23. The LRS system provided pdf's of the concentration fluctuations which supported the three-region description of the shear layer development. The impact of these measurement on turbulence model development is also discussed in Ref. 39.

#### Optoacoustic Laser Deflection (OLD)

The ability to measure temperature at very high data rates is important in the study of turbulent combustion processes. High-frequency thermometry has, to date, been carried out using fine-wire thermocouples or Rayleigh scattering. Both methods are extremely difficult to apply in complex sooting flames. An Optoacoustic Laser Deflection technique (OLD) that has the capability of measuring temperatures at 1.4 kHz rates has recently been demonstrated [42,43]. The technique involves measurement of the propagation velocity of an acoustic impulse between two measurement points defined by monochromatic beams. The method is nonintrusive at the point of measurement, does not require focus coincidence of multiple beams, and can be used with a number of commercially available high-repetition-rate lasers.

The OLD technique is illustrated in Figure 24. The output from the XeCl laser is focused to a line on a titanium or titanium-alloy wire, which--due to high and rapid heating from the absorption of optical radiation--generates a megahertz-frequency sound pulse. A cylindrical wave is generated by this approach which helps to minimize the spatial spreading of the sound pulse. This scheme provides a maximum spatial resolution of 2.1 mm. The speed of the sound pulse is then monitored as it traverses a section of the flame. This is accomplished by monitoring the deflection of two HeNe probe beams separated by 1 mm. As the sound pulse travels through the flame, the local index of refraction is changed by two events--first, the adiabatic compression of the sound wave which induces a small (<0.1 K) temperature rise and, secondly, the pressure dependence of the index of refraction. The HeNe probe lasers respond to the index change by being deflected. The deflection is detected by an aperture-limited silicon diode. A wire target is used for sound production to minimize the energy requirements of the laser source [44], allowing low power, high repetition rate laser to be employed. The wire is typically located downstream of the measurement location to assure a nonperturbing measurement. A block diagram of the electronics used to measure the transit time of the sound pulse is shown in Figure 25. The details of this system are found in Reference 42.

Figure 26 illustrates time traces of the temperature at different radial locations in a premixed propane-air flat flame. The OLD measured average temperature at the center of the flame of  $2010 \pm 75$  K showed excellent agreement with the CARS measured value of  $2030 \pm 100$  K. At the edge of the flame, the well documented (11 Hz) flame instability was measured. The data presented in Figure 26 were taken at 200 Hz. Data taken at 1.4 kHz showed the same behavior, indicating no high-frequency components in this region of the flame.

Figure 27 displays the results from studies on a Bunsen burner flame in which higher-frequency-component temperature fluctuations were observed. Note the large temperature fluctuations observed in the vicinity of the reaction zone. These measurements were made at 100 Hz, except for the upper location in the reaction zone where they were made at 1 kHz (Figure 27b). This figure indicates that 1 kHz is not a sufficiently fast rate for following the temperature fluctuations completely in this area of the flame. Experiments are in progress to investigate the potential of using the OLD technique to measure temperatures at a 5 kHz rate in a turbulent flame using a Cu-vapor laser.

### Flow Visualization

Flow Visualization is an essential part of the CME program. It is used: (1) to identify the scales of processes taking place in different regions of combusting flows, (2) as an aid in interpreting single point measurements such as CARS and LDA, and (3) to provide insights into the dynamics of the mixing and transport processes. Visual observations and high speed movies of flames are simple and valuable diagnostic techniques. They have been extensively used in studying the centerbody flow field in the Combustion Tunnel Facility [16].

A new laser sheet lighting technique, which can provide very detailed information about the mixing and transport processes occurring inside of flames, has recently been demonstrated [45]. Figure 28 illustrates the experimental set-up of the laser sheet-lighting technique for observing the near-wake region of a centerbody with a 56% blockage ratio in the vertical combustion tunnel. The technique involves seeding the central fuel jet with  $\text{TiCl}_4$  vapor. As the fuel is mixed with the annulus air, the  $\text{TiCl}_4$  reacts spontaneously and nearly instantaneously with the water in the air to form micron size  $\text{TiO}_2$  particles and HCl. The Mie scattering from the  $\text{TiO}_2$  particles, observed at right angles to the plane of the laser-sheet, provides a view of the flow field inside the flame. The technique is simple and easy to implement. The only major equipment items required are a laser and camera. Although a 4 watt Argon Ion laser was used in these experiments, a lower powered laser would work if the beam is scanned or swept through the flame at a high rate.

Very little heat is released from the  $\text{TiCl}_4/\text{H}_2\text{O}$  reaction so that it can be used to study reacting flows with and without heat release. This is demonstrated in Figure 29 where a flame stabilized by a centerbody with a 33% blockage (which is smaller than that used in the Ref. 45 study) is shown: as it looks to the eye (left), using the laser sheet-lighting technique (center), and under the same flow conditions without combustion (right). In the combustive case, some of the scattered light is due to the soot particles formed in the flame. High speed movies using laser sheet-lighting provide a remarkable view of the dynamics of the mixing processes occurring in the centerbody flow.

The laser sheet-lighting technique provides a better visualization of jet diffusion flames than conventional techniques and has revealed several new processes occurring in these flames [46]. The jet diffusion flame set-up used to compare different visualization techniques is shown in Figure 30. In this experiment, both the dry annulus air and the central fuel jet were seeded with  $\text{TiCl}_4$  vapor. The only water present to react with the  $\text{TiCl}_4$  is that formed in the combustion process. Figure 31 illustrates the visualization of a propane diffusion flame using smoke with laser sheet-lighting (left), a shadowgraph (center) and the  $\text{TiCl}_4$  laser sheet-lighting technique (right). The structures formed in this flame are much clearer when viewed with the  $\text{TiCl}_4$  laser sheet-lighting technique than those obtained with the conventional techniques. The structures identified by the  $\text{TiCl}_4/\text{H}_2\text{O}$  reaction also have a physical interpretation. They represent the interface between the fuel and the water product. The technique has revealed the presence of a stationary vortex in the potential core of a low velocity propane jet diffusion flame and the shedding of these inner vortices as the fuel flow is increased. It has also been shown that there are typically three instability zones radially distributed across jet flames instead of the two previously revealed by the schlieren technique [47].

Since HCl is formed in the  $\text{TiCl}_4$  reaction with the water vapor, some precautions must be taken when applying the technique. Very little  $\text{TiCl}_4$  is used to seed the flow and the concentration of the HCl formed is very small. However, care must be taken to vent the exhaust products from the laboratory and to flush the burner with  $\text{N}_2$  or other dry gas after use. The only adverse effect that has been noted in using the  $\text{TiCl}_4/\text{H}_2\text{O}$  reaction is that a sticky condensate can collect in the hood and drip on the floor or burner. This problem is eliminated by letting the hood run continually and putting a lip on the inside rim of the hood to collect any condensate.

### Concluding Remarks

Most of the diagnostics research conducted in the CME program has involved the development of single-point temperature, species concentration and velocity measurement capabilities using CARS, LRS and LDA. The CARS and LRS systems have been successfully combined with the LDA systems so that correlations between scalar and vector quantities can be measured. The LRS/LDA system is currently being used in cold flow and premixed flame experiments in the Fundamental Combustion Laboratory. When these experiments are completed, the LRS/LDA system will be replaced with a CARS/LDA system which will be used to study diffusion flames. The integration of the hardened CARS system with a Phase Doppler spray analyzer is in progress. This CARS-Phase Doppler system should have the capabilities of making simultaneous measurements of temperature,  $N_2$  and  $O_2$  concentrations, drop size, and two velocity components. This system will be used to study a spray flame established in the Phase II swirl combustor and in more basic cold flow turbulent drop interaction experiments in the Spray Laboratory.

Future diagnostic research will concentrate on obtaining quantitative multipoint measurements of temperature, species concentration and velocity. A method for making two-dimensional measurements of flame temperature, that relies on fluorescence from a seed material, is under development. This method involves the use of rare-earth ions embedded into various crystal lattices. The approach is to grind the solid into small seed particles that can track the flow. The fluorescence from the particles stimulated by a laser beam or a laser sheet will be used to measure temperatures at multiple points in the flow. Streak photography or a variation of it will be used in conjunction with the fluorescence measurements to obtain the velocities of the particles at the same time the temperatures are measured. Simultaneous temperature and two velocity components will be measured at multiple points in a combusting flow field if this approach succeeds. Other approaches for obtaining multipoint measurements of velocity and temperature are being considered but are not as far along as the fluorescence particle approach.

### Acknowledgements

The authors would like to thank Mr Ron Britton for assisting with the figures and Ms Roma Bush for helping with the typing of the manuscript and Ms Marion Whitaker for reproductions. This research is sponsored by the AFWAL Aero Propulsion Laboratory and the Air Force Office of Scientific Research on in-house Work Units 30480536, 2301S127 and 2308S705 and on Air Force contracts F33615-85-C-2562 with Systems Research Laboratories, Inc. and F33615-82-2255 with the University of Dayton Research Institute.

## References

1. Marshall Lapp and C. M. Penney eds., Laser Raman Gas Diagnostics, Plenum Publishing Corp., New York, 1974.
2. R. Goulard ed., Combustion Measurements, Academic Press, 1976.
3. D. L. Hartley, D. R. Hardesty, M. Lapp, J. Dooher and F. Dryer eds. "The Role of Physics in Combustion", APS Report PB-242-688, NTIS, Springfield, VA, 1975.
4. Irvin Glassman, and William A. Sirignano, "Summary Report of the Workshop on Energy-Related Basic Combustion Research," Report No. 1177, Department of Aerospace and Mechanical Sciences, Princeton University, 1974.
5. "Workshop on the Numerical Simulation of Combustion for Application to Spark and Compression Ignition Engines," Sponsored by NSF Rann, Held in La Jolla, California, 23-25 April 1975.
6. W. S. Blazowski, T. J. Rosfjord, and W. M. Roquemore, "Combustion Research Needs in Turbopropulsion Combustion," Presented at the Eastern States Section of the Combustion Institute Fall Meeting, Nov. 1976.
7. I. T. Osgerby, "Literature Review of Turbine Combustor Modeling," AIAA Jour., 12, 743-754 (1974).
8. T. W. Bruce, H. C. Mongia and R. S. Reynolds, "Combustor Design Criteria Validation Vol. 1, Element Tests and Model Validation," USAR TL-TR-78-55A (March 1979).
9. G. J. Sturgess, and S. A. Syed, "Application of Numerical Modeling to Gas Turbine Combustor Development Problems," Symposium on Fluid Mechanics of Combustion Systems, Joint ASME/ASCE Mechanics Conference, Boulder, Colorado, pp. 241-250 (June 1981)
10. Melvin Gerstein, ed., "Fundamentals of Gas Turbine Combustion," NASA Conference Publication 2087 (Feb. 1979).
11. Geoffrey J. Sturgess, "Aerothermal Modeling," Phase I Final Report, NASA Contract NAS3-23524, May 1983.

12. M. J. Kenworthy, S. S. Correa, and D. L. Burrus, "Aerothermal Modeling," Phase I Final Report, Volumes I and II, NASA Contract NAS3-23525, Nov. 1983.
13. R. Srinivasan, R. Reynolds, I. Ball, R. Berry, K. Johnson, and H. Mongia, "Aerothermal Modeling," Phase I Final Report, Volumes I and II, NASA Contract NAS3-23523, Nov. 1983.
14. W. M. Roquemore, R. P. Bradley, J. S. Stutrud, C. M. Reeves, and L. Krishnamurthy, "Preliminary Evaluation of a Combustor for Use in Modeling and Diagnostic Development," ASME Publication 80-GT-43 (March 1980).
15. W. M. Roquemore, R. P. Bradley, J. S. Stutrud, C. M. Reeves, C. A. Obringer, and R. L. Britton, "Utilization of Laser Diagnostics to Evaluate Combustion Models." AGARD-CP-353, pp. 36-1to 36-2, (1983).
16. D. R. Ballal, A. J. Lightman, and P. P. Yaney, "Development of Test Facility and Optical Instrumentation for Turbulent Combustion Research," AIAA-86-0045.
17. G. L. Switzer, L. P. Goss, W. M. Roquemore, R. P. Bradley, P. W. Schreiber, and W. B. Roh, "Application of CARS to Simulated Practical Combustion Systems," J. Energy 4, 209 (1980).
18. G. L. Switzer, and L. P. Goss, "A Hardened CARS System for Temperature and Species Concentration Measurements in Turbulent Diffusion Flames by the CARS Technique," Temperature Its Measurement and Control in Science and Industry, Vol. 5 (1982) pp. 583-587 (Ed., James F. Schooley).
19. G. L. Switzer, D. D. Trump, L. P. Goss, W. M. Roquemore, R. P. Bradley, J. S. Stutrud, and C. M. Reeves, "Simultaneous CARS and Luminosity Measurements in a Bluff-Body Combustor." AIAA Paper 83-1481, June 1983.
20. G. L. Switzer, et al. "CARS Measurements in the Near-Wake Region of an Axisymmetric Bluff- Body Combustor," AIAA-85-1106. Also, to be published in the June Issue of AIAA Journal 1986.
21. L. P. Goss, D. D. Trump, B. G. MacDonald and G. L. Switzer, "10-Hz Coherent Anti-Stokes Raman Spectroscopy Apparatus for Turbulent Combustion Studies," Rev. Sci. Instr., 54, 5, 563 (May 1983).
22. L. P. Goss, G. L. Switzer, and D. D. Trump, "Temperature and Species Concentration Measurements in Turbulent Diffusion Flames by the CARS Technique," AIAA Paper 82-0240.

23. Won B. Roh, Paul W. Schreiber, and J. P. E. Taran, "Single-Pulse Coherent Anti-Stokes Raman Scattering," *App. Phy Lett.* Vol. 29, No. 3, (August 1976).
24. P. D. Magill, et al., "Simultaneous Velocity and Emission Measurements in a Bluff-Body Combustor," AIAA-82-0883 (June 1982).
25. A. J. Lightman, R. D. Richmond L. Krishnamurthy, P. D. Magill, W. M. Roquemore, R. P. Bradley, R. S. Stutrud, and C. M. Reeves, "Velocity Measurements in a Bluff-Body Diffusion Flame," AIAA-80-1544 (July 1980).
26. A. Lightman, P. D. Magill and R. J. Andrews, "Laser Diagnostic Development and Modeling of Turbulent Flowfields of Jets and Wakes, Part I Two-Dimensional Laser Doppler Anemometer Measurements of Isothermal Flowfields in a Ducted Centerbody Combustor," AFWAL-TR-83-2044, Part I (June 1983).
27. T. -H. Chen and A. J. Lightman, "Effects of Particle Arrival Statistics on Laser Anemometer Measurements," International Symposium on Laser Anemometry, A. Dybbs, and P. A. Pfund, eds., pp. 231-234. The American Society of Mechanical Engineers, New York.
28. Allan J. Lightman and Robert J. Andrews, "A Robust High-Speed Laser Doppler Anemometer System Used to Measure Ducted Coaxial Flows with a Centerbody," Symposium on Laser Anemometry, 1985 ASME Winter Annual Meeting, Miami, FL. (1985).
29. I. Ebrahimi and R. Kline, "The Nozzle Flow Concentration Fluctuation Field in Round Turbulent Free Jets and Jet Diffusion Flames," Sixteenth (International Symposium on Combustion, p1711, (1977).
30. L. P. Goss, D. D. Trump, and W. M. Roquemore, "A Combined CARS/LDA Instrument for Simultaneous Temperature and Velocity Measurements," Submitted to *Exps. in Fluids*.
31. L. P. Goss, D. D. Trump, W. M. Roquemore, "Simultaneous CARS and LDA Measurements in a Turbulent Flame," AIAA 84-1458.
32. L. P. Goss, D. D. Trump, and W. M. Roquemore, "An Investigation of Temperature and Velocity Correlations in Turbulent Flames," in Experimental Measurements and Techniques in Turbulent Reactive and Non-Reactive Flows, p 215 (Eds. R. M. So, J. H. Whitelaw and M. Lapp), New York: The American Society of Mechanical Engineers.

33. W. D. Bachalo and M. J. Houser, "Phase/Doppler Spray Analyzer for Simultaneous Measurements of Drop Size and Velocity Distributions," *Optical Engineering*, Vol. 23, No. 5, pp. 583-590, Sept./Oct. 1984.
34. W. D. Bachalo and M. J. Houser, "Spray Drop Size and Velocity Measurements Using the Phase/Doppler Particle Analyzer," presented at the International Conference on Liquid Atomization and Spray Systems, Imperial College, London, July, 1985.
35. T. A. Jackson and G. S. Samuelsen, "Performance Comparison of Two Interferometric Droplet Sizing Techniques," presented at SPIE's 29th Annual International Technical Symposium on Optical and Electro-Optical Engineering, San Diego, Aug. 1985.
36. W. D. Bachalo and M. J. Houser "Evolutionary Behavior of Sprays Produced by Pressure Atomizers," AIAA-86-0296.
37. P. P. Yaney, R. J. Becker, P. T. Danset, and M. R. Gallis, "Laser Diagnostic Development and Modeling of Turbulent Flowfields of Jets and Wakes, Part III The Development of a Two-Channel CW Time-Resolved Laser Raman Spectroscopy (TiLaRS) System for Measurements in Gas Flowfields," AFWAL-TR-83-2044 Part III (June 1983).
38. P. P. Yaney, R. J. Becker, P. T. Danset, M. R. Gallis and J. I. Perez, "The Application of Rotational Raman Spectroscopy to Dynamic Measurements in Gas Flowfields," *Progress in Aero. and Astronautics*, AIAA, 95, pp. 627-69, New York (1985).
39. D. R. Ballal, T. H. Chen, and P. P. Yaney, "An Experimental Investigation of Turbulent Mixing Using Rotational Raman Spectroscopy," AIAA-85-1105.
40. P. P. Yaney, R. J. Becker, P. D. Magill, and P. Danset, "Dynamic Temperature Measurements of Flames Using Spontaneous Raman Scattering," Temperature, Its Measurement and Control in Science and Industry, J. F. Schooley, ed., pp. 639-645. American Institute of Physics, New York.
41. D. R. Ballal, T-H. Chen, and P. P. Yaney, "Scalar Fluctuations in Turbulent Combustion - An Experimental Study," AIAA-86-0367.
42. L. P. Goss, D. F. Grosjean, B. Sarka, and S. W. Kizirnis, "Time-Resolved Temperature Measurements in a Premixed Flame Using the Optoacoustic Beam Deflection Technique," AIAA-85-1445.

43. D. F. Grosjean, B. Sarka, and L. P. Goss, " Time-Resolved Temperature Measurements in a Laboratory Flame Using the Optoacoustic Beam-Deflection Method," *Opt. Lett.*, 10, 324-327 (1985).
44. S. W. Kizirnis, R. J. Brecha, B. N. Ganguly, L. P. Goss, and R. Gupta, *Appl. Opt.* 23, 3873 (1984).
45. W. M. Roquemore, R. S. Tankin, H. H. Chiu and S. A. Lottes, "A Study of a Bluff-Body Combustor Using Laser Sheet Lighting," in Experimental Measurements and Techniques in Turbulent Reactive and Non-Reactive Flows, pp.159-174, (Eds. R. M. So, J. H. Whitelaw and M. Lapp), New York: The American Society of Mechanical Engineers. To appear in *Exps. in Fluids*.
46. L. D. Chen and W. M. Roquemore, "Visualization of Jet Flames," To appear in *Combustion and Flame*.
47. A. J. Yule, N. A. Chigier, S. Ralph, R. Boulderstone, and J. Ventura, "Combustion-Transition Interaction in a Jet Flame," *AIAA J.*, Vol. 19, pp. 752-760 (1981).

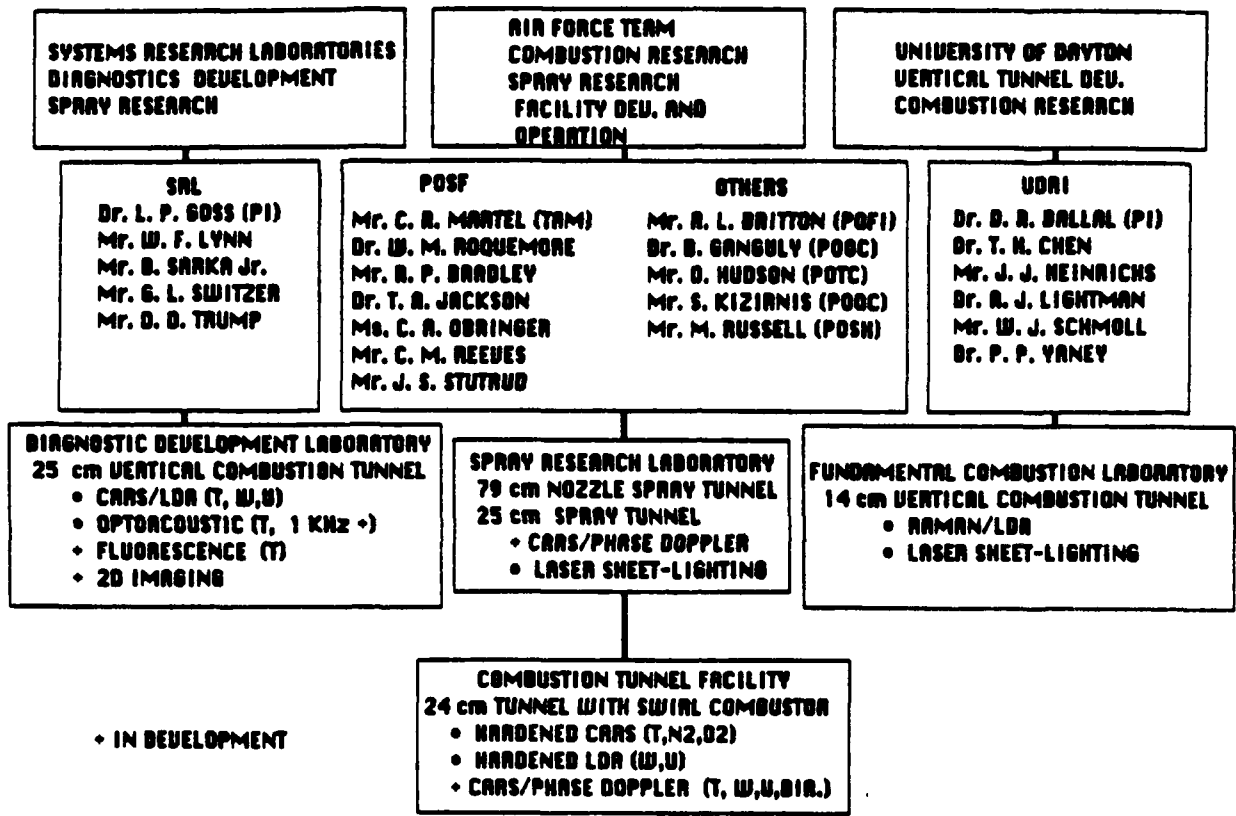


Figure 1. Block Diagram of Program Organization

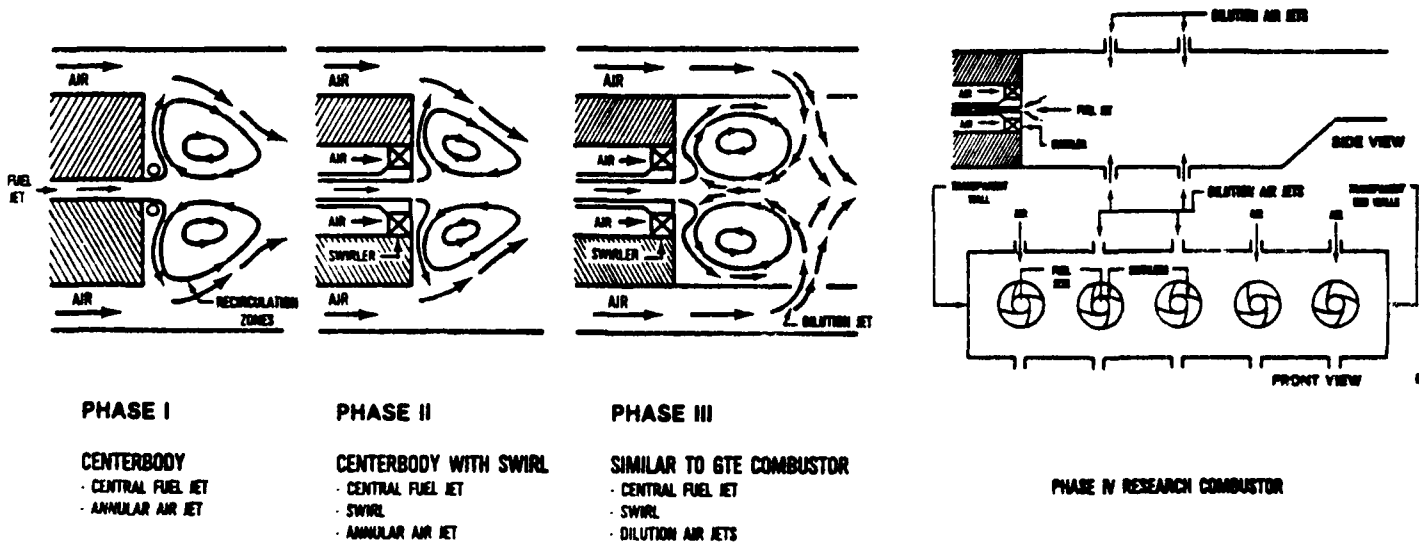


Figure 2. Research Combustor Configurations for the Combustion Tunnel Facility.

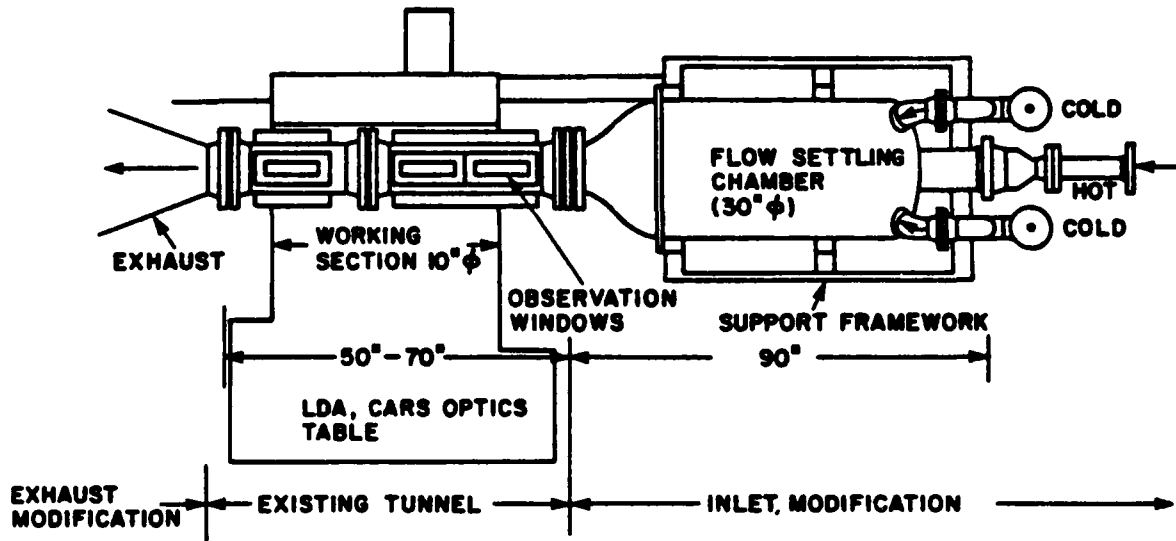


Figure 3. Combustion Tunnel Illustrating the Optical Table for the Hardened Systems and the Recently Completed Intake and Exhaust Modifications.

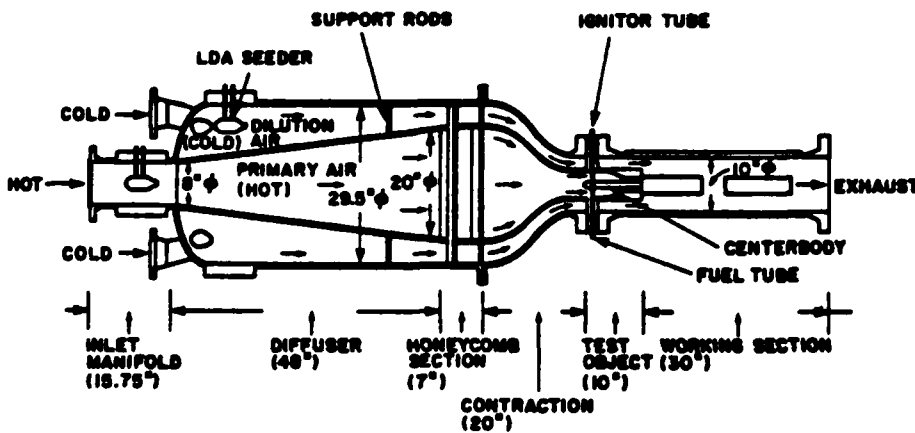


Figure 4. Combustion Tunnel Inlet Settling Chamber Shown with the Phase II Swirl Combustor.

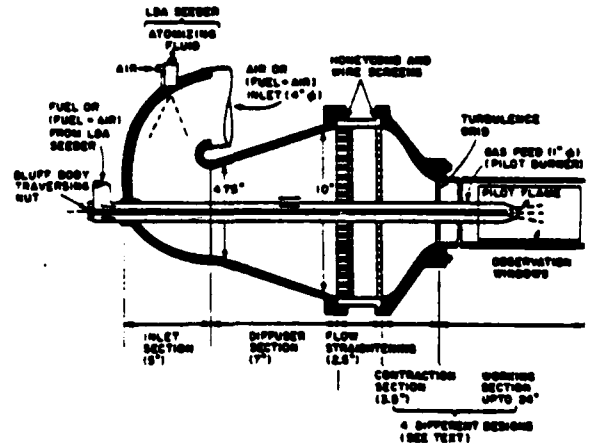


Figure 5. Schematic Diagram of the Vertical Combustion Tunnel.

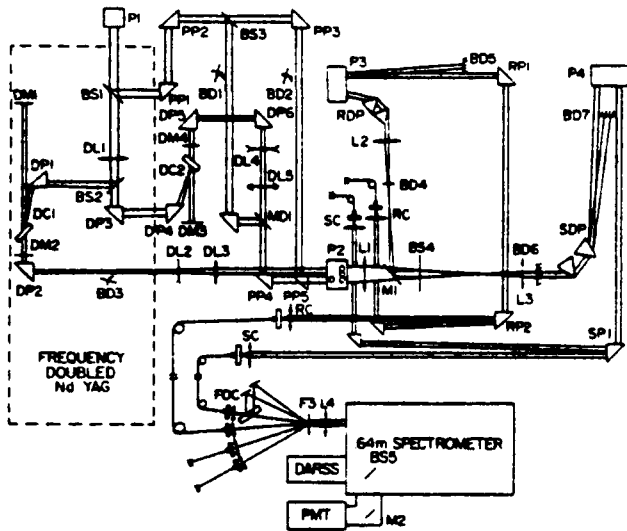


Figure 6. CARS Optical-System Schematic.

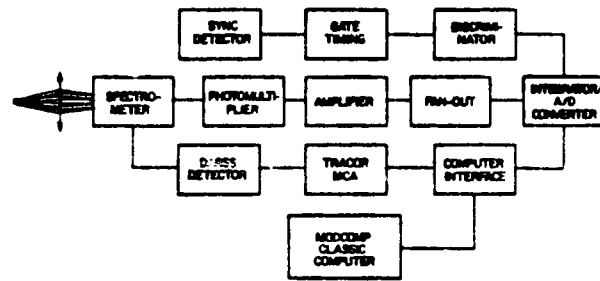


Figure 7. CARS Signal-Detection and Data-Collection Electronics Configuration.



Figure 8. A Comparison of Time Averaged CARS Temperature Measurements (Top) and TEACH Predictions of Temperature and Velocity with an Illustration of Shed Vortices (Bottom).

BLUFF—BODY FACE

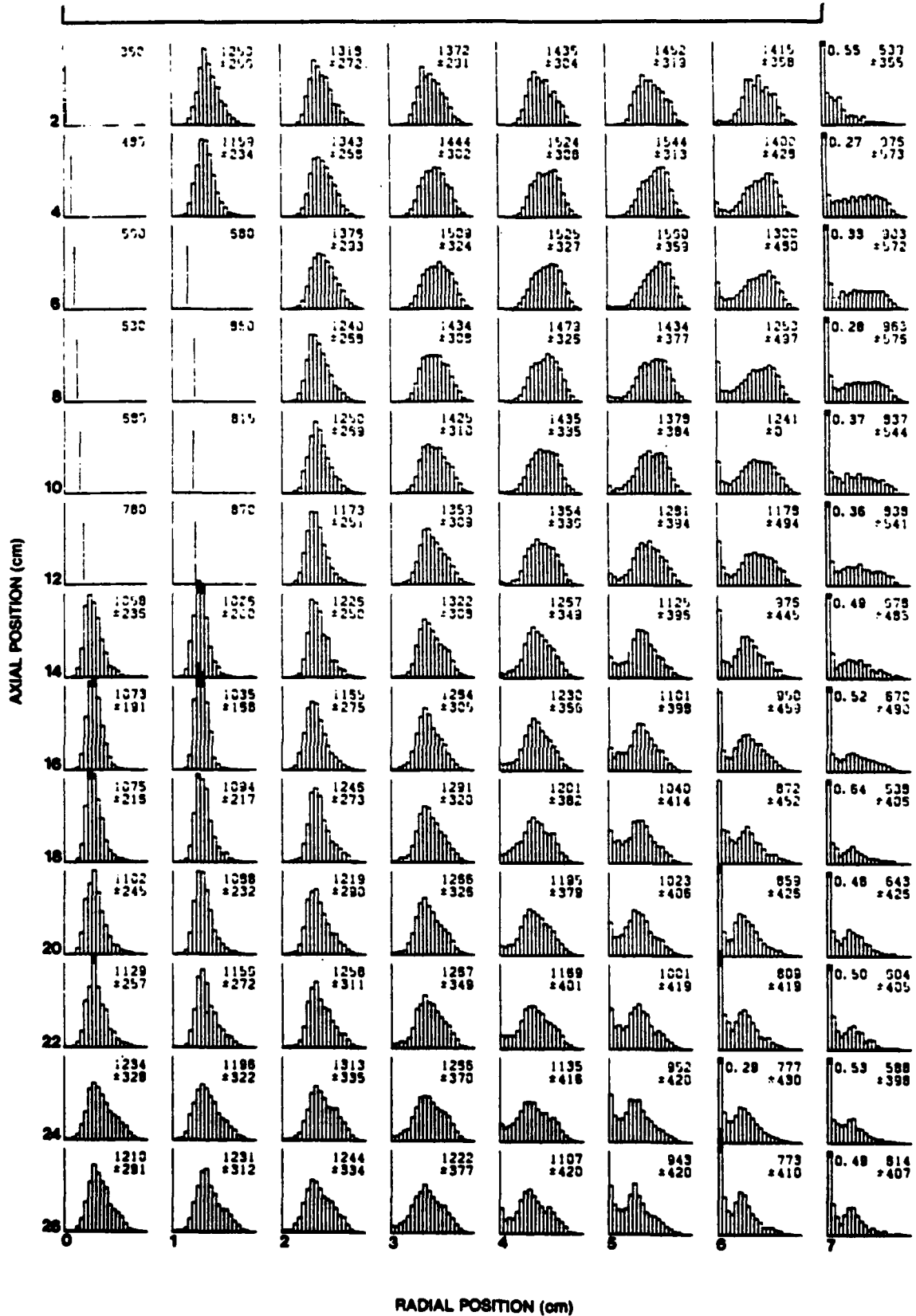


Figure 9. CARS Temperature pdf's in the Near-Wake Region of the Phase I Centerbody Combustor.

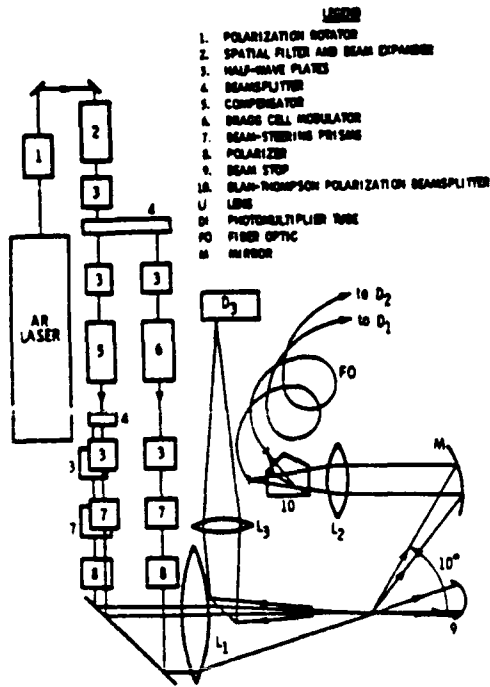


Figure 10. Schematic Diagram of the LDA/Luminosity Optical System.

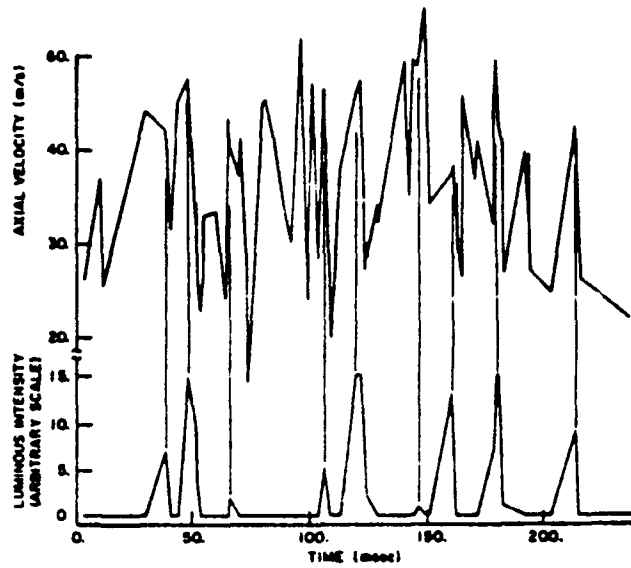


Figure 12. Time History of the Simultaneous Axial Velocity and Luminosity Measurements.

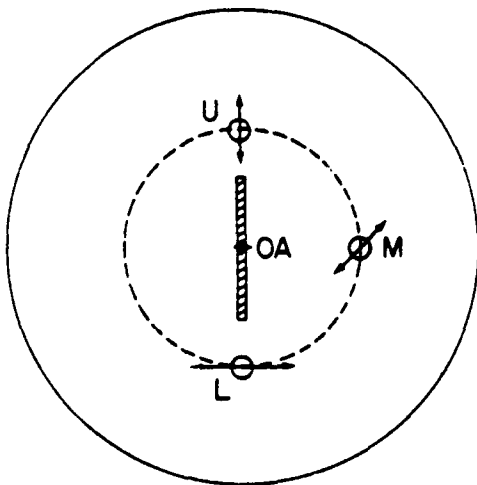


Figure 11. The Relative Positions and Sizes of the LDA Beams and the Luminosity Observation Slit.

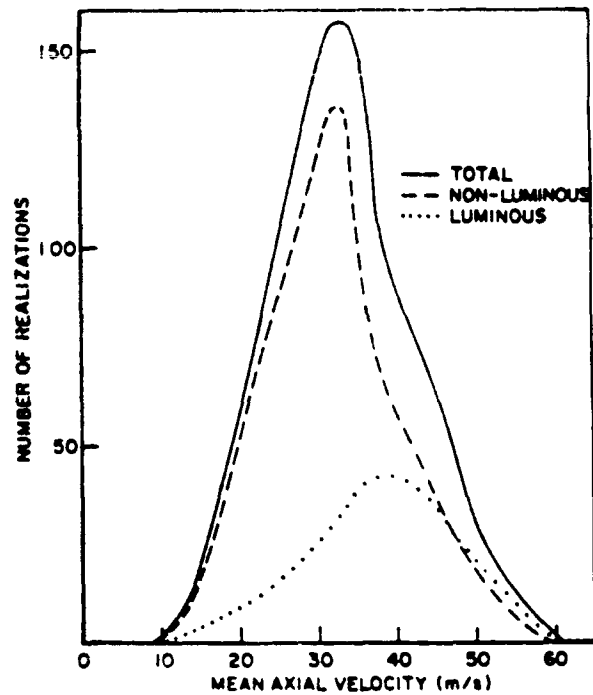


Figure 13. Distribution of the Axial Velocity Measurements. The Two Distributions Obtained by Conditional Sampling are Shown with the Total (Unconditioned) Sampling Distribution.

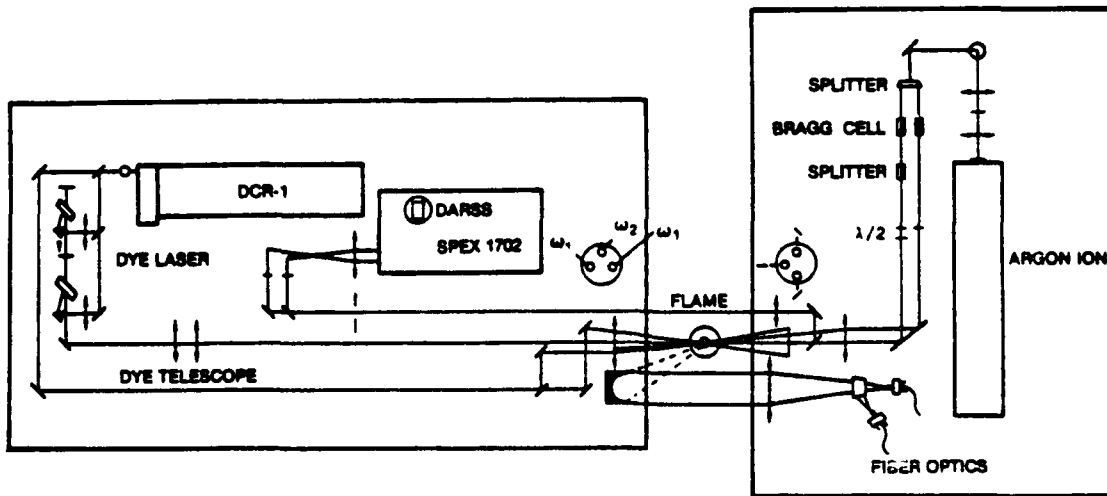


Figure 14. Optical Layout of the Combined CARS/LDA Instrument.

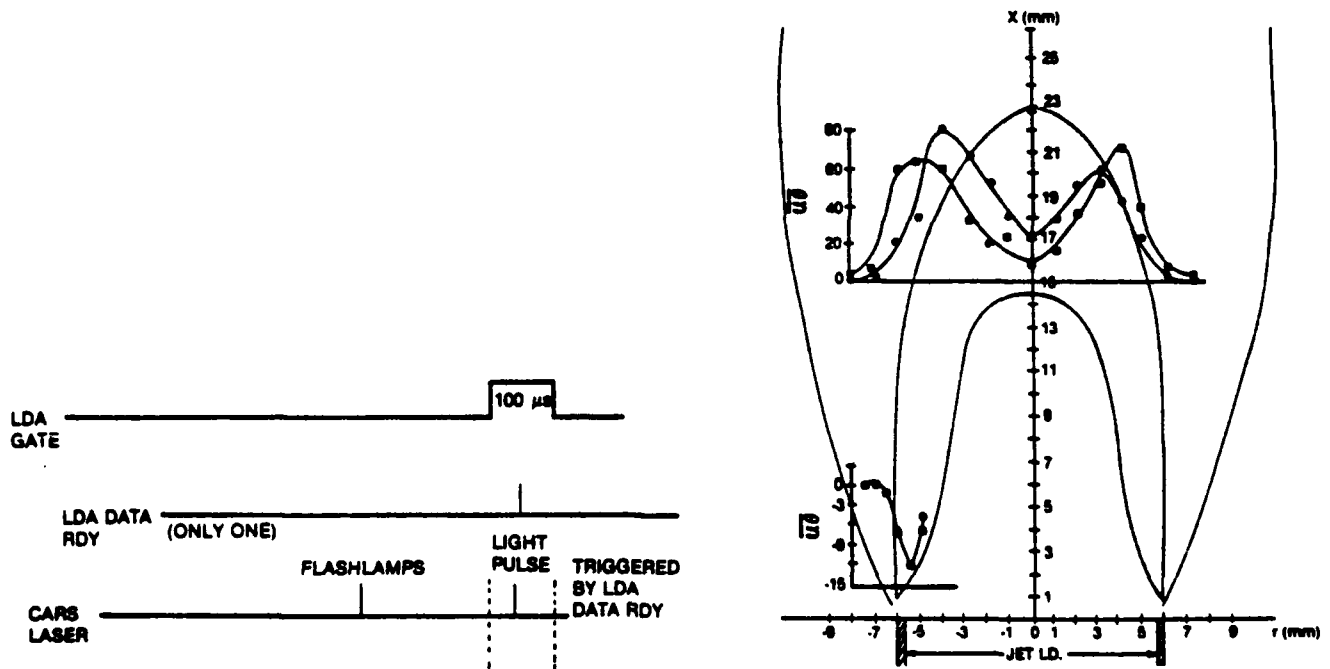


Figure 15. Timing Sequence for the Data Acquisition for the Combined CARS/LDA Instrument.

Figure 16. Favre (●) and Reynolds (●) Averaged Axial Velocity/Temperature Correlations about the Mean in a Bunsen Burner Propane/Air Premixed Flame.

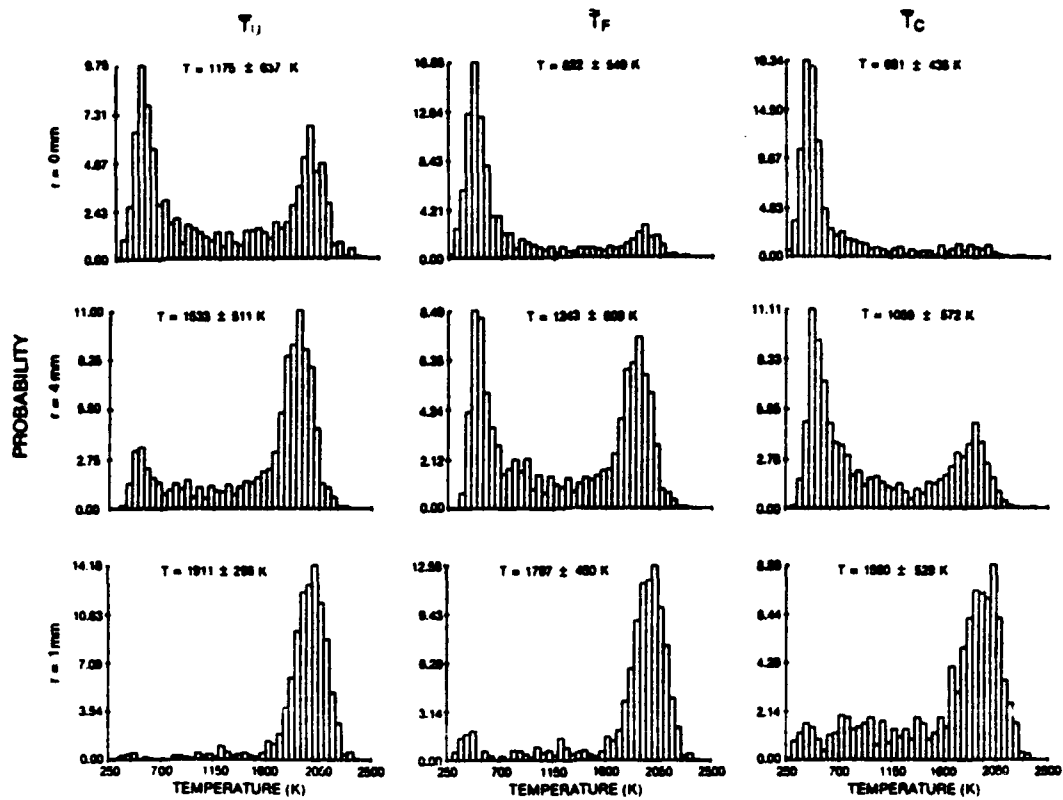


Figure 17. CARS Temperature pdf's in a Premixed Bunsen Burner Propane/Air Flame Using  $TiO_2$  Seed Particles.  $T_U$  Represents Temperatures Measured Independently of LDA Velocities,  $T_F$  are Favre Averages of  $T_U$ , and  $T_C$  are Temperatures Measured Simultaneously (Conditioned) with LDA Velocities.

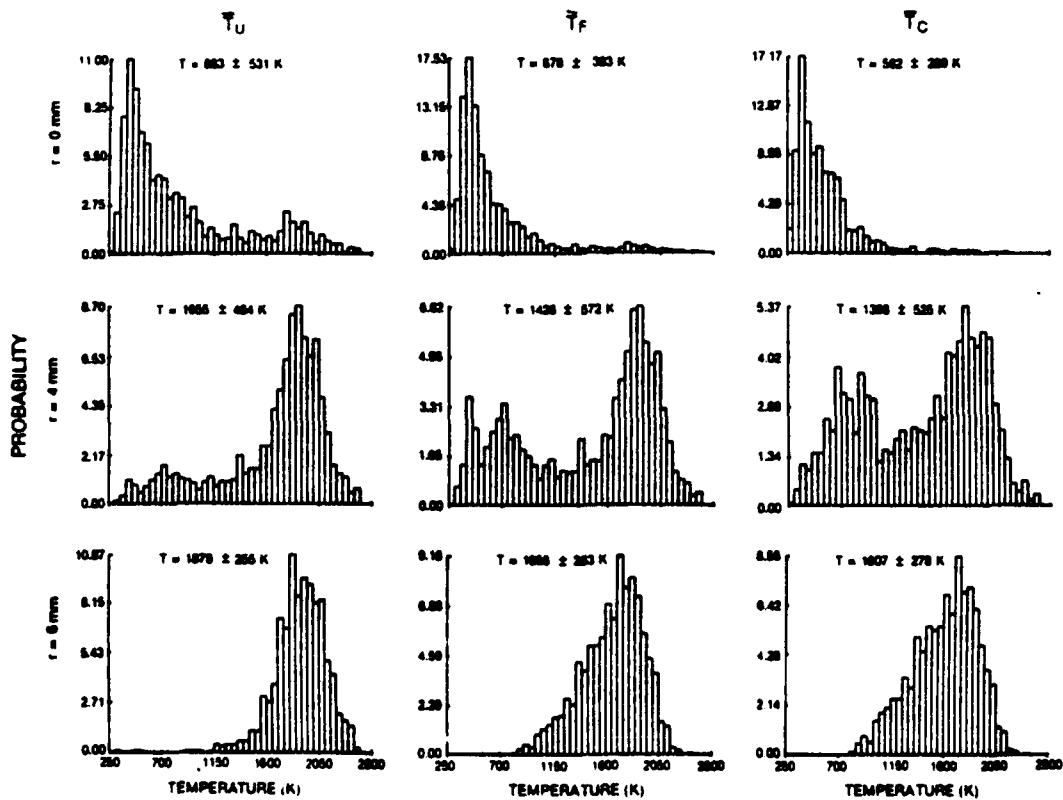


Figure 18. CARS Temperature pdf's in a Premixed Bunsen Burner Propane/Air Flame Using  $Al_2O_3$  Seed Particles.  $T_U$  Represents Temperatures Measured Independently of LDA Velocities,  $T_F$  are Favre Averages of  $T_U$ , and  $T_C$  are Temperatures Measured Simultaneously (Conditioned) with LDA Velocities.

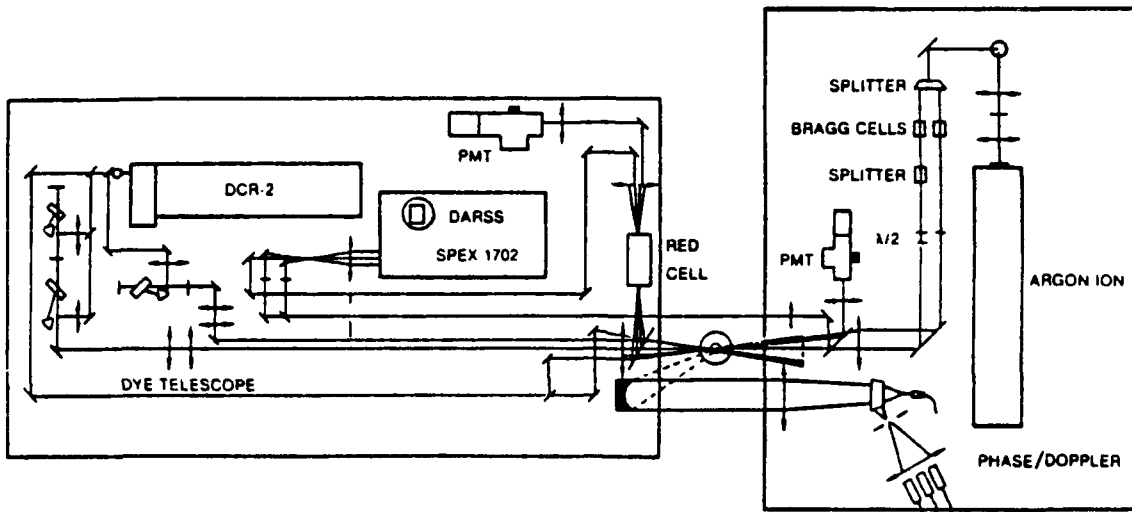


Figure 19. Optical Layout of Phase Doppler System.

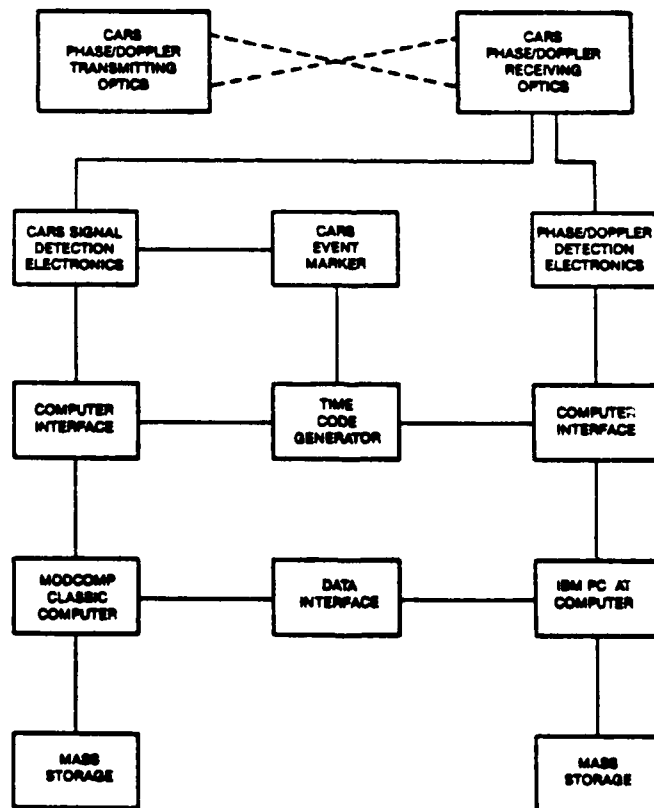


Figure 20. Block Diagram of CARS/Phase Doppler Integration.

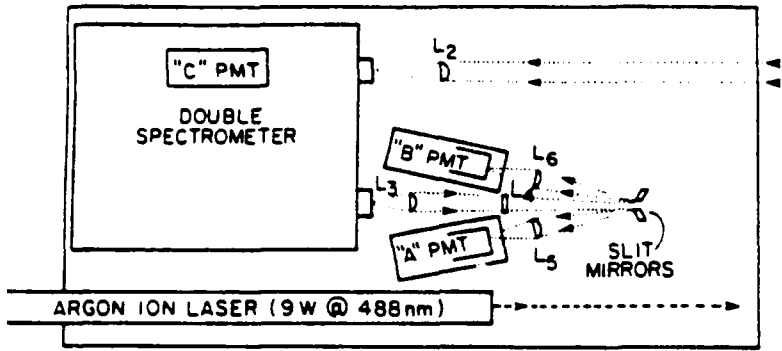


Figure 21. Optical Layout of the 2-Channel Laser Raman/Rayleigh System.

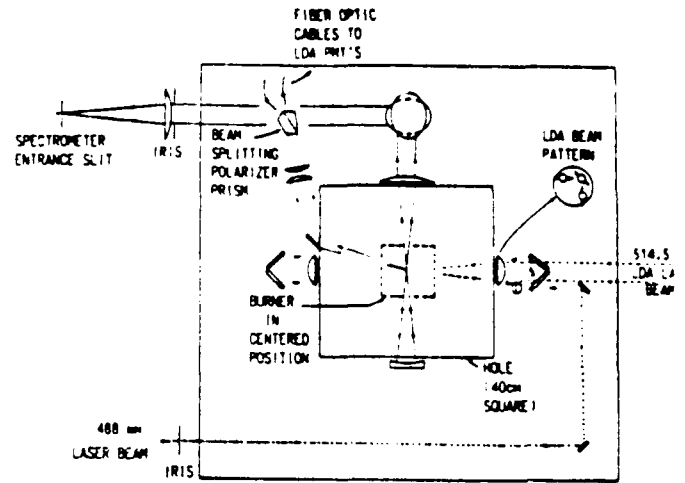


Figure 22. Diagram II Illustrating the Integration of the Raman/LDA.

MIXING LAYER DEVELOPMENT

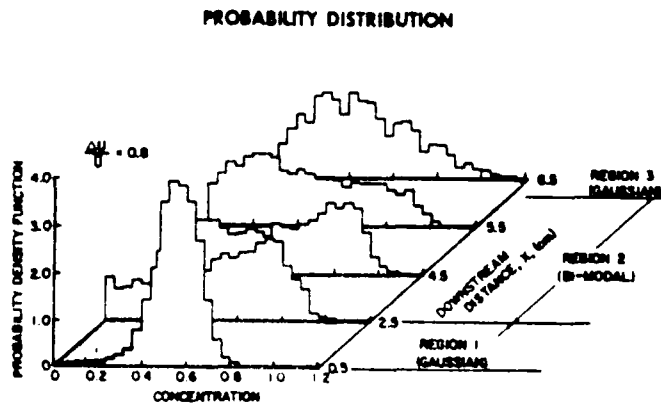
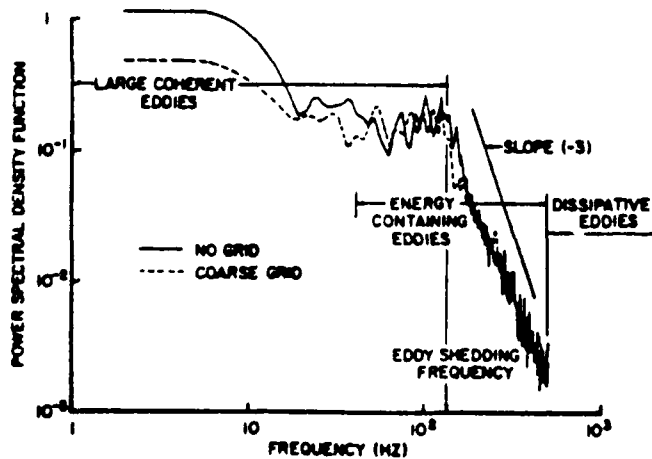
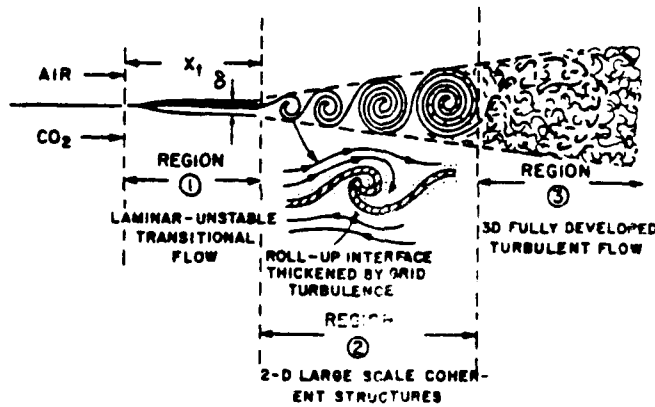


Figure 23. Illustration of Mixing Layer Experiment with Concentration Power Spectral and Probability Density Functions Obtained with the LRS System.

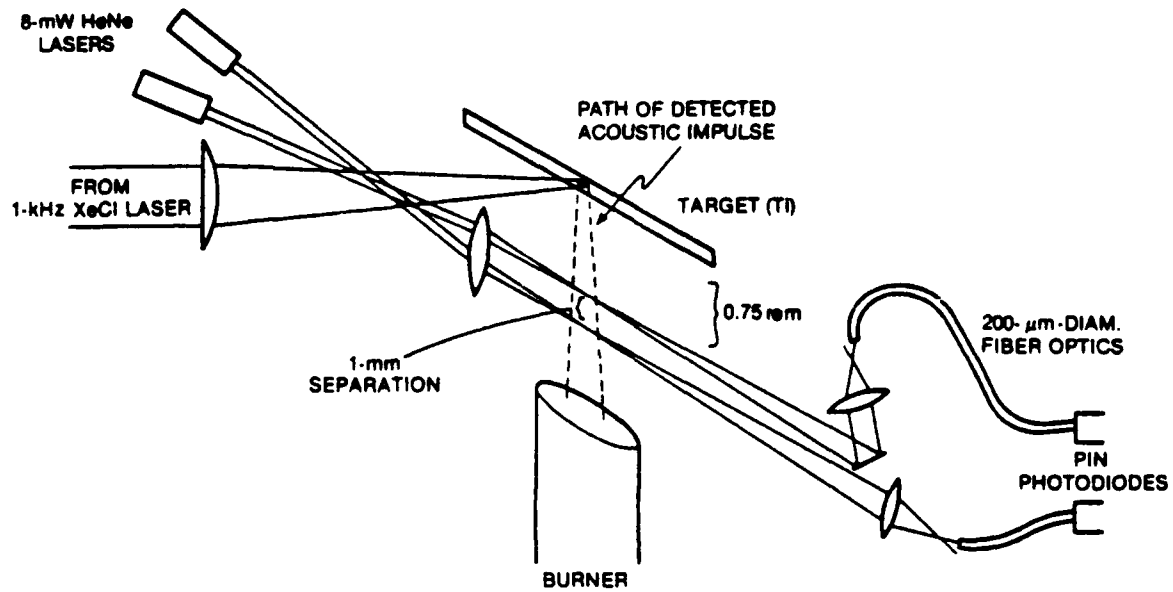


Figure 24. Schematic Illustration of the Optoacoustic Thermometric Experimental Arrangement.

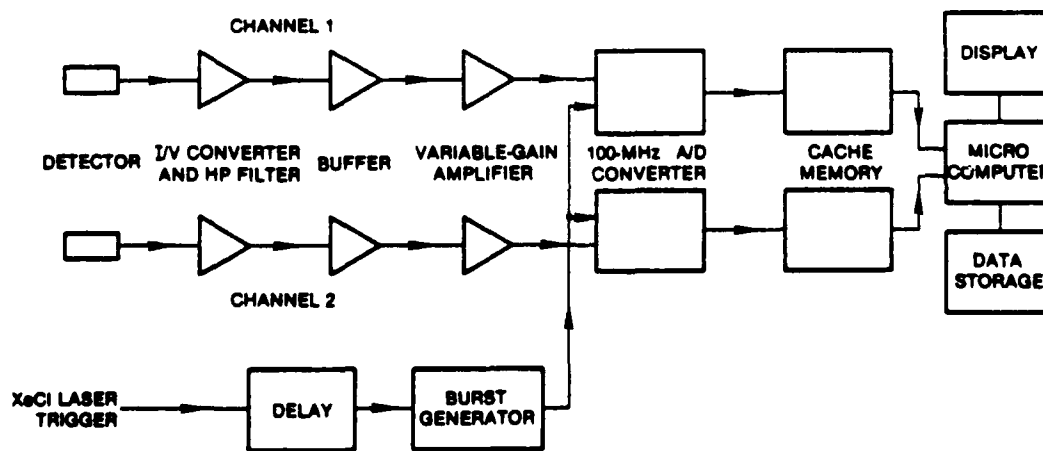


Figure 25. Block Diagram of Detection and Processing Electronics for the Optoacoustic Thermometric Technique.

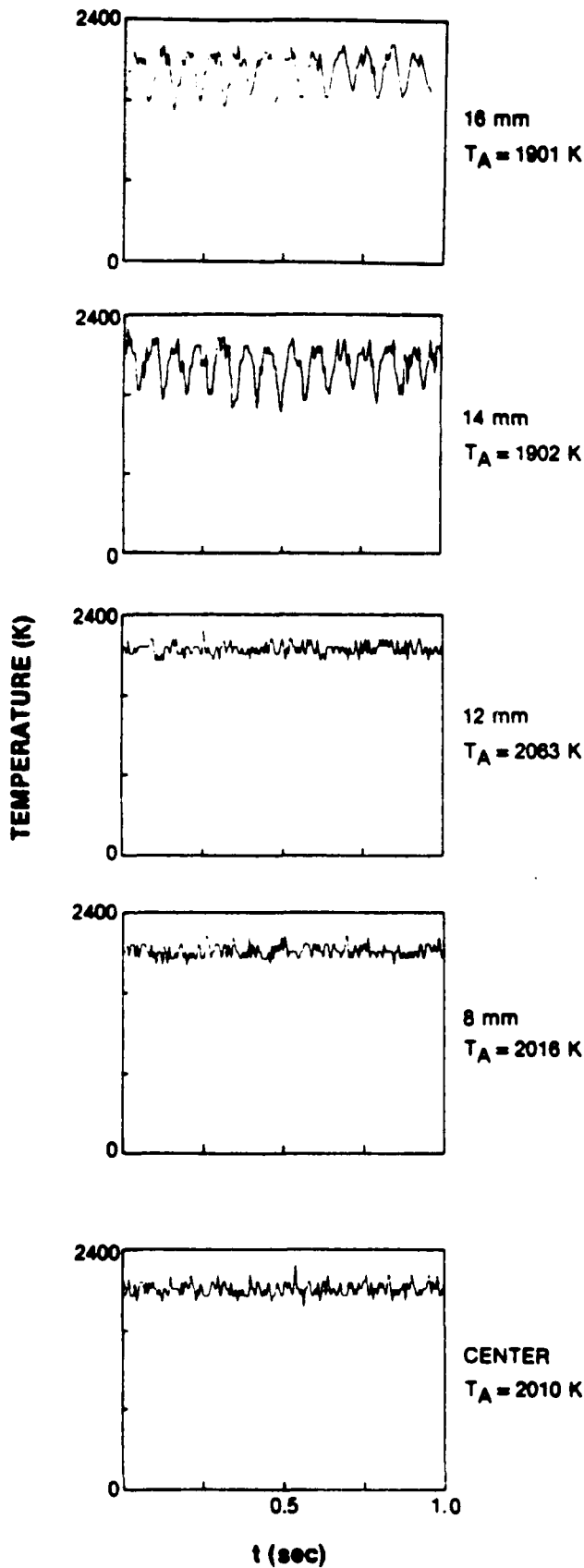


Figure 26. Plots of Optoacoustic Measured Temperature vs. Time in a Premixed Propane/Air Bunsen Burner Flame.

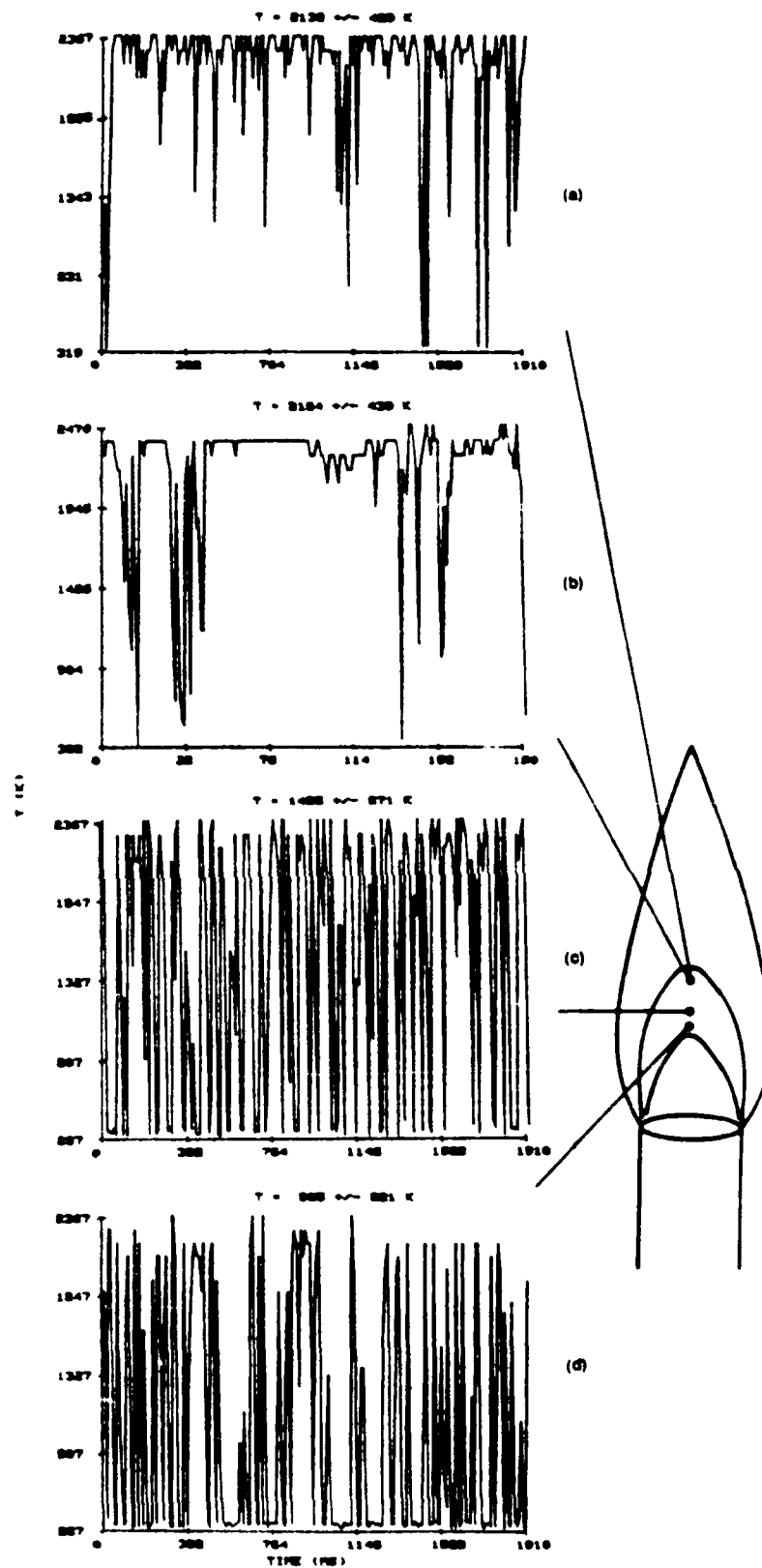


Figure 27. Temporal-Spatial Profile of Bunsen Burner Flame at 100 Hz except for (b) which is at the same Location as (a) but at 1000 Hz.

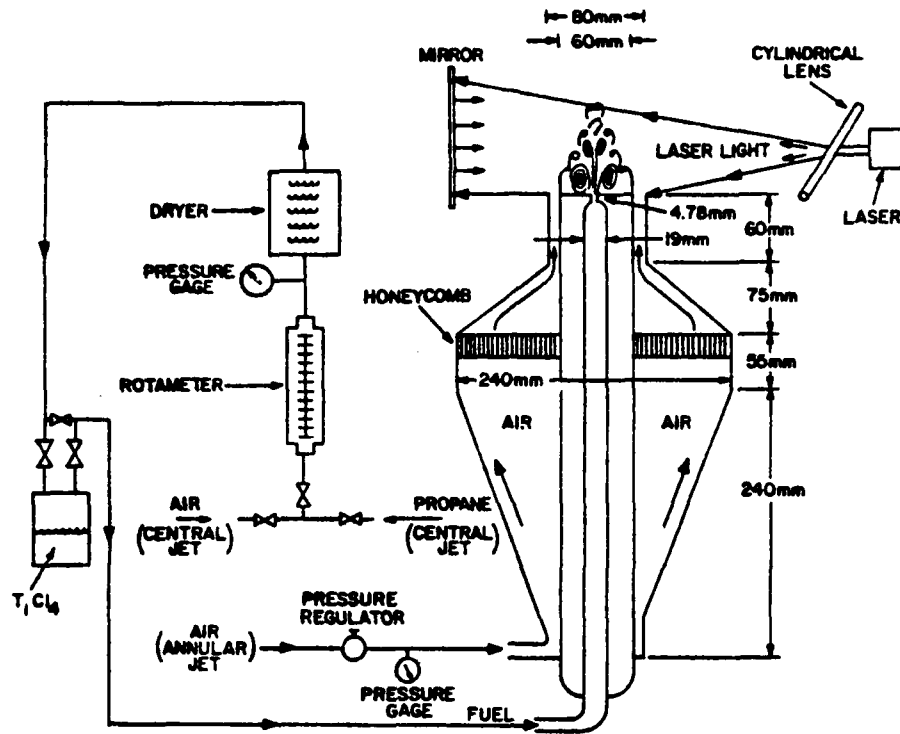


Figure 28. Illustration of the Laser Sheet-Lighting Experimental Set-Up for the Centerbody Combustor Installed in the Vertical Combustion Tunnel with the Central Propane Fuel Jet Seeded with  $TiCl_4$  Vapor.



Figure 29. Photographs of the Near-Wake Region of the Centerbody Combustor with the Central Propane Fueled Jet Seeded with  $TiCl_4$  Vapor. From Left to Right: the Flame, Sheet-Lit Flame. Non-Combusting Flow.

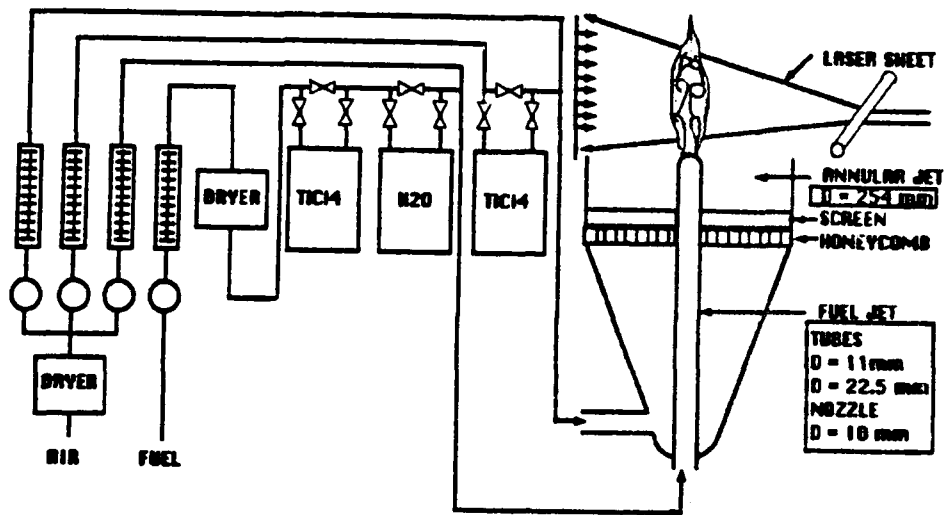
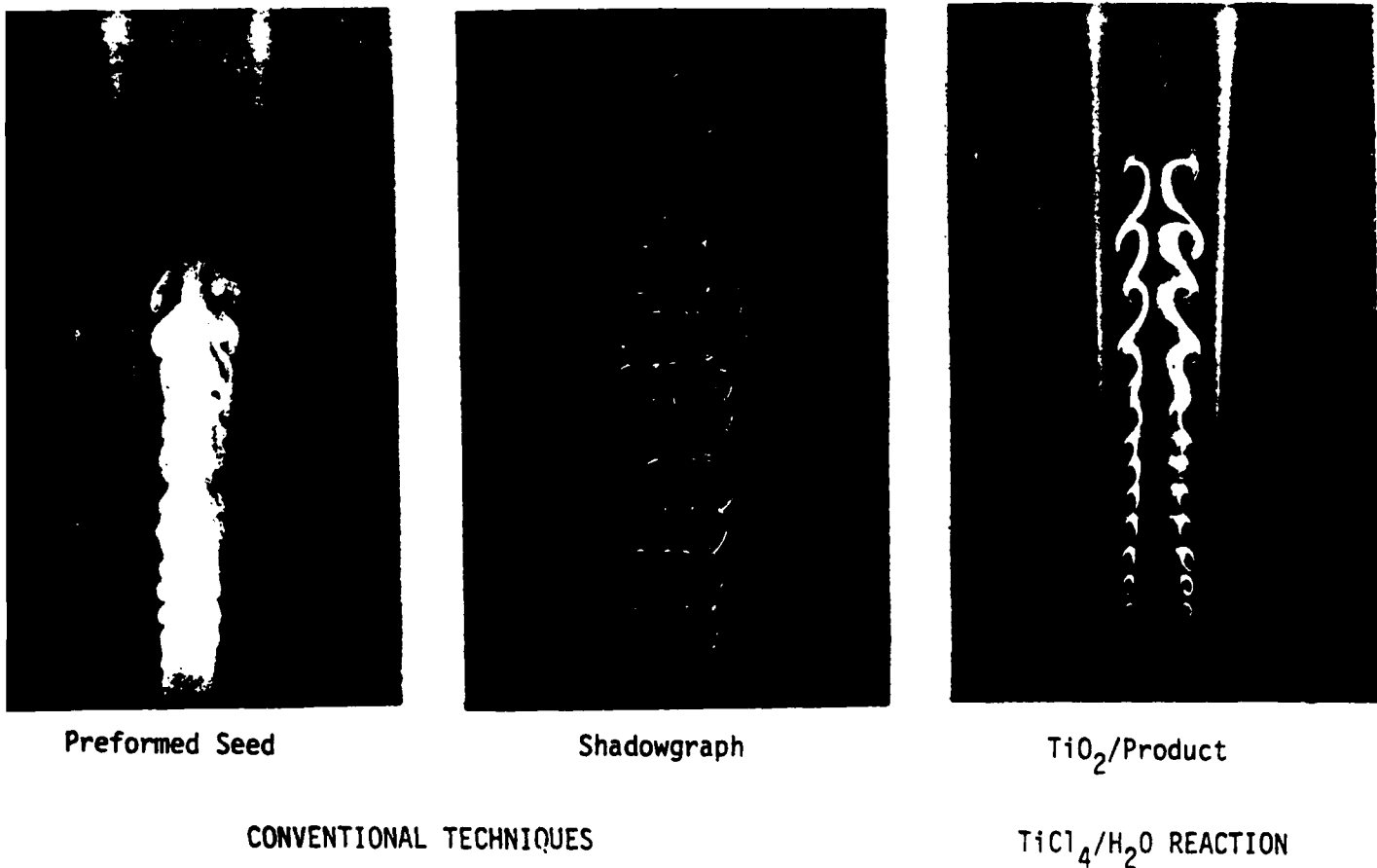


Figure 30. Experimental Set-Up of Jet Diffusion Flame Visualization Experiments.



Preformed Seed

Shadowgraph

TiO<sub>2</sub>/Product

CONVENTIONAL TECHNIQUES

TiCl<sub>4</sub>/H<sub>2</sub>O REACTION

Figure 31. Comparison of a Preformed Seed, Shadowgraph, and TiCl<sub>4</sub>/H<sub>2</sub>O Reaction Visualization Techniques of a Jet Diffusion Flame.



**AIAA-90-0156**

**Optical Diagnostics for Reacting  
and Non-Reacting Flows: Recent  
Developments and Results**

**L. P. Goss, T. H. Chen, V. Vilimpoc,  
M. E. Post, D. D. Trump, and B. Sarka**

**Systems Research Laboratories, Inc.  
*A Division of Arvin/Calspan*  
2800 Indian Ripple Road  
Dayton, OH 45440-3696**

**28th Aerospace Sciences Meeting**

**January 8-11, 1990/Reno, Nevada**

# OPTICAL DIAGNOSTICS FOR REACTING AND NON-REACTING FLOWS: RECENT DEVELOPMENTS AND RESULTS

L. P. Goss,\* T. H. Chen,\*\* V. Vilimcic,† M. E. Post,††  
D. D. Trump,‡ and B. Sarka‡‡  
Systems Research Laboratories, Inc.  
A Division of Arvin/Calspan  
2800 Indian Ripple Road  
Dayton, Ohio 45440-3696

## ABSTRACT

Two novel, multipoint combustion-diagnostic techniques have been developed for the study of jet diffusion flames--thin-filament pyrometry (TFP) for the measurement of flame temperature and two-color particle-imaging velocimetry (PIV) for two-dimensional velocity measurements. In the TFP technique the thermal characteristics and their influence upon the spatial and temporal response of the SiC filament have been assessed by a numerical heat-transfer model. The flame-tracking capability of the filament at different frequencies has been evaluated and found to exhibit negligible errors in the 50 - 100 Hz range and relatively small errors up to 500 Hz. The addition of a CCD camera in the TFP method has allowed extension of the technique to multifilaments and sooty flames. The two-color PIV technique is similar to existing PIV techniques except that two different-color laser sources are used to form the light sheets required for exposing the position of the particles in a seeded flowfield. Analysis of the two-color images consists of digitizing the exposed film with color filters to separate the green- and red-particle image fields and processing the digitized images with velocity-displacement software. The two-color PIV technique has the advantage that direction as well as particle displacement is uniquely determined since the green-particle image occurs before the red one by a known time increment. Velocity measurements utilizing this technique on a propane jet diffusion flame have been made, and the results are discussed.

## INTRODUCTION

Developments in combustion-diagnostic techniques have experienced tremendous growth

\*Chief Scientist, Optical Diagnos., Member AIAA

\*\*Sr. Research Scientist, Sr. Member AIAA

†Chemical Engineer

††Research Physicist

‡Project Engineer

‡‡Electrical Engineer

over the past decade, with applications ranging from simple laboratory burners to commercial jet engines. Point-measurement techniques such as laser-induced fluorescence (LIF), Raman scattering and coherent anti-Stokes Raman spectroscopy (CARS) have been developed to the point where they can be applied to real-world combustor systems. Multipoint techniques are not so well developed but offer the possibility for two-dimensional scalar and velocity measurements in complex flow systems. In this paper two multipoint techniques are discussed which have been under development at the Wright Research and Development Center at Wright-Patterson Air Force Base for the study of complex combustion flow systems--1) thin-filament pyrometry (TFP) for high-sampling-rate measurement of single- and multiple-line thermometry and 2) two-color particle-imaging velocimetry (PIV) for two-dimensional velocity measurements. The TFP technique relies upon the blackbody emission from a thin ceramic filament to determine the local flame temperature. The two-color technique utilizes two different colored laser light sheets to mark particles in a flowfield as a function of time and remove direction ambiguities which arise with single-color velocimetry techniques. Both techniques require a CCD camera to capture multipoint spatial information. The TFP and two-color PIV techniques along with their flame applications are discussed below.

## THIN-FILAMENT PYROMETRY

### Background

The TFP technique relies upon the blackbody emission from a thin ceramic filament (SiC) for measurement of the temperature distribution in a combusting flowfield. The emission is recorded spatially along the length of the filament, allowing the radial temperature distribution to be evaluated. The filament is made of commercially available ultrafine  $\beta$ -SiC.<sup>1</sup> The filament diameter is 15  $\mu\text{m}$ , and its thermal conductivity is relatively low, being  $\sim 10 \text{ kcal/m hr } ^\circ\text{C}$  along the filament axis at room temperature. This is  $\sim 40$

times lower than the thermal conductivity of Pt-PtRh wire, which drastically reduces the spread in the temperature profile along the filament. Because of its small size, the filament can respond quickly to temperature changes in its surroundings; its high emissivity (0.88), which is constant over the temperature range of interest, allows quantitative conversion of filament intensity to temperature. The technique has been applied to several flame studies involving non-sooting laminar,<sup>2</sup> turbulent,<sup>3-4</sup> and--more recently--sooting flames.<sup>5</sup> The thermal properties of the filament were modeled (steady-state) in two earlier studies,<sup>6-7</sup> and a full non-steady time-dependent heat-transfer model has been developed recently.<sup>8</sup> Because of the strong dependence of the response of the filament upon the Reynolds number and the thermal properties of the flowfield, the time-dependent heat transfer model will be discussed in detail.

### Theoretical and Numerical Model

From the consideration of the energy balance, the temperature change for a thin-filament element with length  $dx$  is found to be governed by<sup>9</sup>

$$\rho C_p V \frac{dT_f}{dt} = -hA_p(T_f - T_a) - \epsilon A_p(T_f^4 - T_a^4) + kA_i \left( \frac{dT_f}{dx} \Big|_R - \frac{dT_f}{dx} \Big|_L \right) \quad (1)$$

(a)                      (b)                      (c)

convection            radiation            conduction

where  $\rho$  is the density of the filament,  $C_p$  its heat capacity,  $V$  volume,  $T_f$  filament temperature,  $t$  time,  $h$  convective heat-transfer coefficient,  $A_p$  surface area,  $T_a$  gas temperature,  $\epsilon$  emissivity of the filament,  $\sigma$  Stefan-Boltzmann constant,  $T_a$  room temperature,  $k$  thermal conductivity,  $A_i$  cross-sectional area,  $|_R$  marker of the right-hand side of the control volume,  $|_L$  marker of the left-hand side of the control volume,  $r$  radius of the filament, and  $dx$  length of the filament element. In Eq. (1), (a) represents the convective heat-transfer term, (b) the radiation term, and (c) the conduction term. By utilizing the thermal properties of the filament and the surrounding air in Eq. (1), the relative contributions from the various heat-transfer terms can be evaluated and the response of the filament determined.

The response curve of the filament, calculated by means of experimentally determined heat-transfer coefficients,<sup>8</sup> is presented in Fig. 1. The input function for this plot was sinusoidal, having a temperature of 2300 K and a minimum temperature of 900 K--a difference of 1400 K. The input frequency,  $F_0$ , varied from 20 to 1000

Hz. The phase delay of the filament response (dashed line) and the difference between the maximum and minimum filament temperature (solid line) are plotted as functions of frequency in Fig. 1. Under low-frequency modulation the filament responds with only a small-amplitude attenuation and phase delay. As the thermal-input frequency increases, however, the magnitude of the attenuation and the phase delay increases significantly. Recently the response data shown in Fig. 1 were verified experimentally by Chen, *et al.*<sup>8</sup>

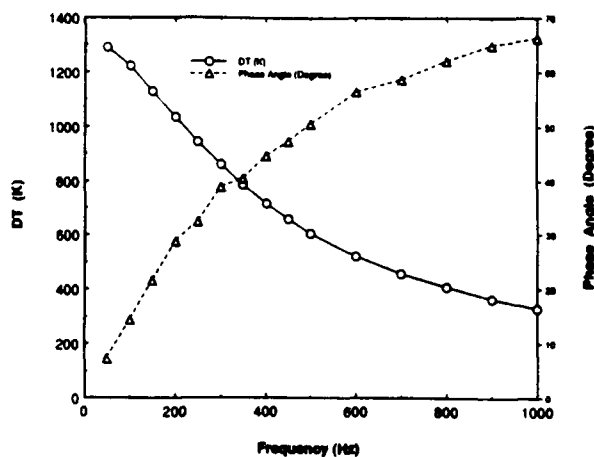


Fig. 1. Plot of filament response and phase-angle delay as function of thermal input frequency.

To verify the utilization of the filament to track the time variation of the flame, the thermal code was used to simulate the response of the thin filament under an oscillating flame condition. The input function used for this purpose was

$$T_a(x,t) = T_d \exp\left[-\left(\frac{x - x_f}{W_h}\right)^2\right] + T_a \quad (2)$$

$$x_f = x_{f0} + L_f \sin\left(\frac{2\pi t}{F_0}\right)$$

where  $x_f$  is the instantaneous flame-surface position,  $x_{f0}$  reference flame position,  $L_f$  magnitude of the flame-surface oscillation,  $F_0$  oscillation frequency for the simulation,  $T_a = 300$  K, and  $T_d = 1700$  K. The temperature difference between ambient air and the flame surface was set to 1700 K, corresponding to the adiabatic flame condition for a methane or propane flame. A portion of the input thermal function for a 500-Hz oscillation is shown in Fig. 2(a). The filament response,  $T_f$ , to the input thermal wave

as a function of axial position and time is plotted in Fig. 2(b). At this high modulation frequency, the temperature response of the filament is slightly attenuated and displays a phase delay, as shown in Fig. 2(c). From this type of trace function, statistical quantities such as mean flame position, fluctuation magnitude, and instantaneous flame-fluctuation velocity can be calculated. It was determined that these statistical quantities for the input and output functions agree within 15% for a 500-Hz modulation. For a 50-Hz oscillation which is typical of the jet diffusion flames studied by the TFP technique to date, the input and output functions are indistinguishable.

The development of an accurate thermal model of the filament response allows compensation for the amplitude attenuation and phase delay at high frequencies. This procedure requires knowledge of the constituent gases and their thermal properties as well as the velocity field. Chen, *et al.*,<sup>8</sup> recently demonstrated that the response time of the filament under different flow conditions can be measured directly. In this work the filament is placed in the flowfield to be studied and heated by a chopped cw-CO<sub>2</sub> laser. Because the response of the filament under these conditions is dominated by convective heat transfer [(term a in Eq. (1)), the experimentally measured decay time of the heat pulse on the filament allows the convection term to be measured directly. This simplifies the need for a complete knowledge of the constituents and the flowfield and allows evaluation of the frequency response of the filament.

### Multipoint Measurements and Soot Compensation

Early studies conducted with the TFP technique were directed toward taking advantage of its high-speed thermometric capabilities which involved capturing the emission along the length of the filament with a rotating-mirror arrangement. Temperature and flame-position information along the filament as a function of time was obtained in this manner and utilized in the study of laminar and turbulent jet diffusion flames.<sup>2-4</sup> The temperature of the filament is determined by ratioing the observed emission intensity to that from a flame of known temperature. The ratioed intensity is then converted to temperature using a calibration curve. Once the temperature has been determined in this manner, it must be corrected for radiative heat losses. The extent of this correction is dependent upon the magnitude of the convective heat transfer.

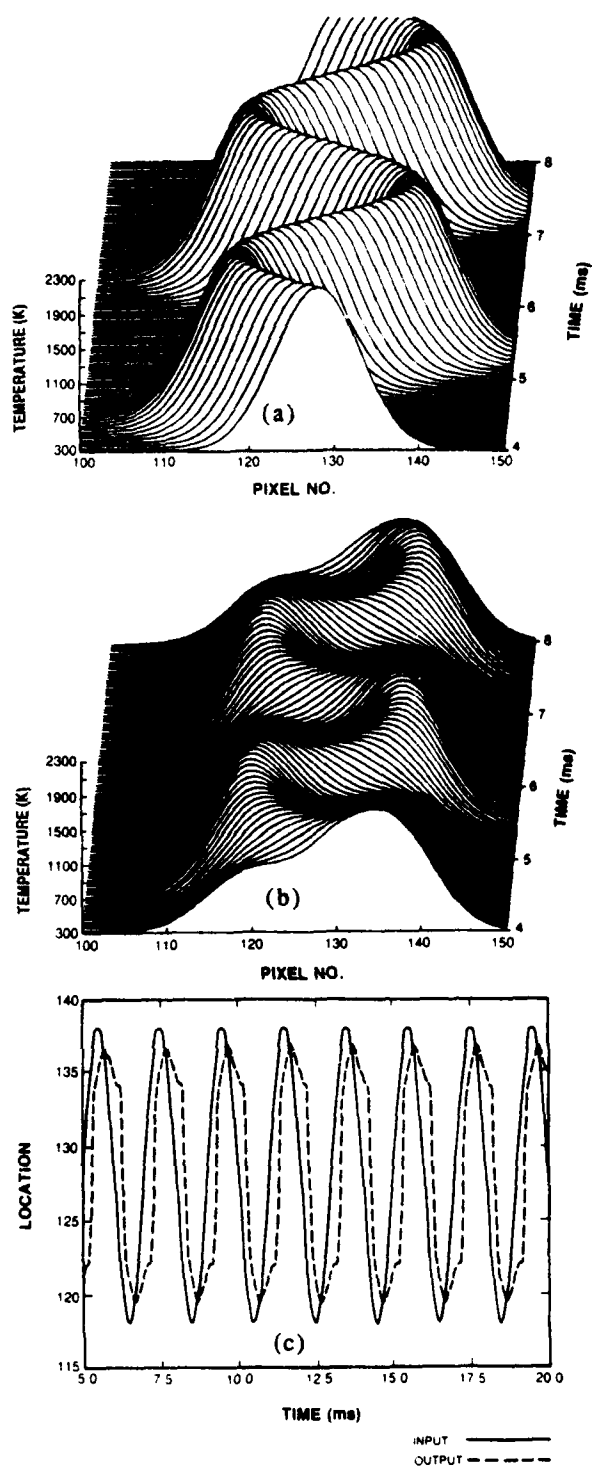


Fig. 2. Plots of (a) Input thermal wave (500 Hz) for modeling reactance of filament; (b) Output response of thin filament to input thermal wave; and (c) Trace of peak filament temperature for 500-Hz thermal excitation wave (solid line - input wave; dashed line - filament response).

To extend the capability of the technique to multifilament measurements, a ten-filament rake system was devised for suspending multiple filaments in a flame; the emission from each filament was captured by a 1024 x 1024 pixel CCD camera, isolated, normalized (to the emission from a flame of known temperature), and converted to a temperature. The use of a CCD camera allows imaging not only of multiple filaments but also of the surrounding emission of the flame. In the case of a sooting flame, the blackbody emission from the soot must be separated from the filament emission to allow temperature measurements. Separation of the soot from the filament emission is a multistep process involving determination of the filament locations, fitting of the soot background, subtraction of the fitted background from the filament emission, and final conversion to temperature. For isolation of the filaments and determination of their exact location, a one-dimensional Laplacian operator was employed. This operator acts as a high-spatial-frequency bandpass filter in the direction perpendicular to the filaments and allows the filaments to be isolated from the slowly varying soot background. The filament locations are then extracted and used in determining the background subtraction. Next, the surrounding soot emission on both sides of the filament (in the perpendicular direction) is fit with a fourth-order polynomial and used to estimate the soot contribution at the filament location. The background is then subtracted from the filament in the original image and the resulting background-free image converted to a temperature in the normal manner.

This technique has been recently applied to the study of a low-velocity propane jet diffusion flame dominated by buoyancy and displaying low-frequency (14-Hz) structures which can be used for synchronization. This flame has been the subject of an intensive experimental and numerical study, the results of which were reported by Chen, *et al.*<sup>5</sup> Figure 3 displays this sooty flame and the resulting temperatures determined by the multifilament TFP technique.

## TWO-COLOR PARTICLE-IMAGING VELOCIMETRY

### Background

In complex flowfields, i.e., recirculating flows, it is important to obtain an instantaneous two-dimensional picture of the entire flowfield rather than be restricted to a pointwise time-averaged

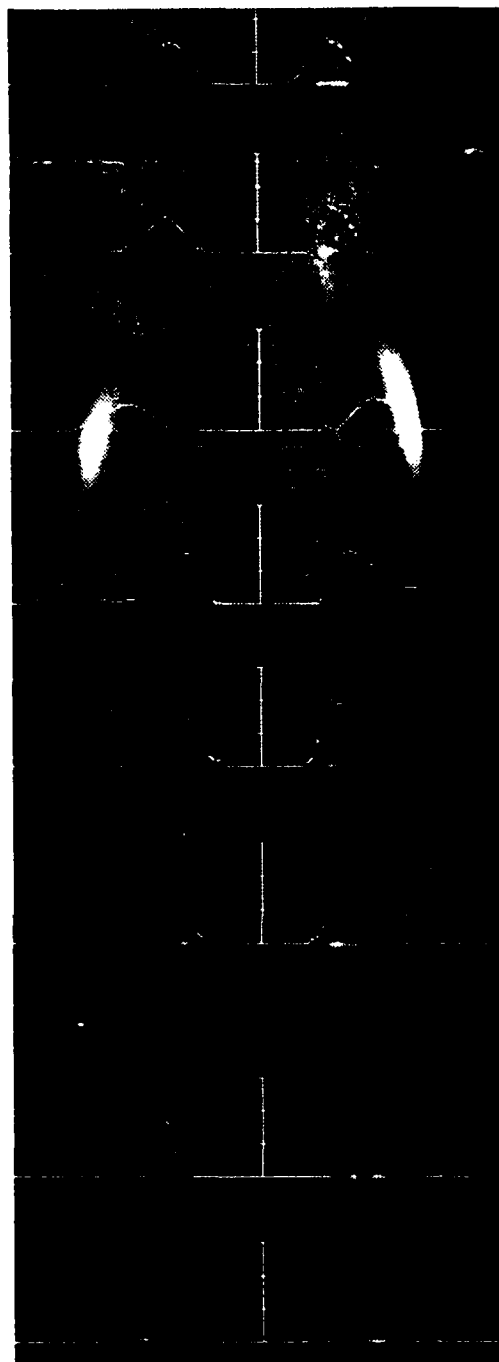


Fig. 3. Multiple-filament emission recorded in sooty jet diffusion flame with derived temperatures superimposed.

map. Several techniques have been reported in the literature which have the capability to determine the velocity of a two-dimensional flowfield. These techniques can be divided into three categories: particle-tracking schemes,<sup>10-17</sup> time-of-flight techniques,<sup>18-20</sup> and laser Doppler

methods.<sup>21-24</sup> For low-to-moderate velocity flowfields, particle-tracking techniques are efficient, offering a wide velocity range and allowing two-dimensional measurement of the velocity flowfield. Particle tracking, or particle-image velocimetry (PIV), is basically an extension of speckle photography which has been employed extensively in solid mechanics. The PIV technique consists of 1) double pulsing a particle-laden flowfield, 2) recording the scattered light either by conventional photography or holography, and 3) processing the photographs to obtain velocity information. While the first two steps are relatively simple to implement, the data analysis is typically complex and requires computerized image processing.

### Image Analysis

The two-color PIV technique utilizes color to remove directional ambiguities and reduce tracking errors. However, because the standard Young's-fringe<sup>1</sup> analysis approach cannot distinguish the different-color particle fields, an alternative correlation-tracker analysis approach was developed. The analysis procedure consists of 1) digitizing the color negative with a CCD array, 2) determining the spatial locations of the digitized particle images, 3) constructing a correlation map from which the most probable displacement vector can be determined, and 4) using this information in a tracker which identifies green/red-particle vector pairs from the digitized image.

### Determination of Particle Coordinates

In the present study in order to take full advantage of the resolution available with the color film on which images were recorded (~100 line pairs per mm), an enlarger was used to subdivide the image for analysis. An automated x,y,z traversing mechanism was used to set the position of the enlarger to within 20 mm in any direction. Each section of the enlarged image was digitized twice using a CCD camera system. The first digitized image was taken with a green filter for identifying the green-particle images and the second with a red filter for identifying the red-particle images. These digitized images were processed in an identical manner to determine the coordinates of the green and red particles.

A typical digitized image displays peaks associated with the particles superimposed on a slowly varying background. In order to simplify procedures for finding the coordinates of each

particle, components of the background, which are constant or slowly varying over the scale of the particle size, are removed by application of a two-dimensional Laplacian operator to the digitized image. This Laplacian operator basically acts as a spatial-frequency filter, passing high-frequency (small-size) components of the image but suppressing low-frequency (background) components. The particle images can be further enhanced above the background and film noise if the step size of the Laplacian operator is approximately the particle size. Next, the processed image is scanned in two dimensions for local maxima, and a series of tests is performed to identify those local maxima which correspond to particles.

### Determination of Most Probable Vector Displacement

Several methods have been used to determine the most probable displacement (correlation) for vector pairs in a section of the image. The histogram (correlation-map) approach which was found to be computationally efficient was utilized for this study. In the histogram approach, a correlation-histogram map is constructed from the green- and red-particle images; the maximum of these images contains the most probable displacement vector. The software for this analysis functions by first finding an initial particle image in the green digitized image. The exact location of the green particle is determined and used for mapping. A 120 x 120 pixel area of the red-particle image centered about the green-particle coordinates is then copied into a histogram map (correlation space). This procedure is then repeated for all the green-particle images and their associated surrounding fields in the red-particle images. This process is represented mathematically by

$$H(\xi, \psi) = \sum_n g(x_c, y_c) r(x_c - \xi, y_c - \psi) \quad (3)$$

where  $H(\xi, \psi)$  is the correlation histogram,  $g(x_c, y_c)$  center coordinates of the green-particle images,  $r(x - \xi_c, y - \psi_c)$  red-particle images surrounding the green particle being mapped, and the summation is over all green-particle images.

As green/red-particle pairs having the same velocity--and, thus, displacement--are mapped onto correlation space, peaks are built up. The maximum of this map corresponds to the most probable displacement from the center coordinate, illustrated in Fig. 4. If only a single-color image had been used instead of a two-color

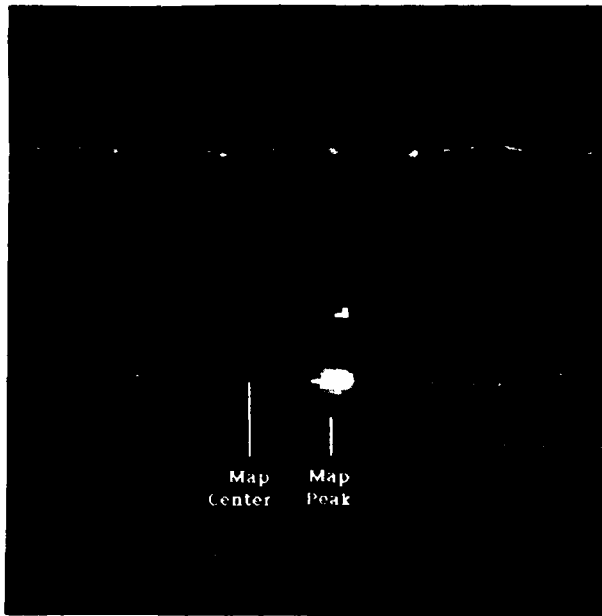


Fig. 4. Correlation map of two-color PIV double-pulsed image. Notice absence of self-correlation center peak.

image, the resulting correlation map would have been symmetric and centered about a large self-correlation peak at the center of the map. The result would have been a 180-deg. directional ambiguity which would have had to be resolved by phase shifting or by having *a priori* knowledge of the flowfield. Because only the red-particle images were mapped into the histogram with respect to the green, neither the self-correlation peak nor the symmetry and associated 180-deg. directional ambiguity is observed in this figure. Thus, both displacement and directional information are determined from the histogram map. The analysis software determines the direction and displacement by searching for the maximum; the displacement is then determined from the maximum to the center, which corresponds to the most likely velocity and direction averaged over the x,y array examined. For determining the individual velocity vectors, a tracker must be employed.

#### Determination of Vector Pairs (Tracker)

A tracker routine was developed to permit use of the average velocity and directional information obtained from the correlation map to find green/red-particle pairs which fit this value within a preset uncertainty. The tracker, starting from each green-particle image, adds the most probable vector displacement and

searches for the corresponding red-particle pair. If a red particle is present at the projected coordinates, then a velocity match is made and a vector drawn. If no red particle is found at these coordinates, a small *window* is opened around the target coordinates; this *window* is expanded incrementally to a selected percentage of the vector length. Figure 5 is a graphical representation of this process. If the number and size of the window increments become too large, the number of erroneous matches may become large. Generally, good results are obtained with three window increments, with the maximum increment being 20% of the vector length. The tracker portion of the analysis is very efficient, with normally < 30 sec being required to process a full 384 x 576 digitized image. The combination of correlator and tracker was found to be the most efficient and effective approach in determining velocity vectors in the two-color images recorded in this study.

#### Application to Jet Diffusion Flame

The experimental arrangement for two-color PIV measurements is shown in Fig. 6. Two separate Nd:YAG lasers are used in forming the different-color light sheets for exposing the

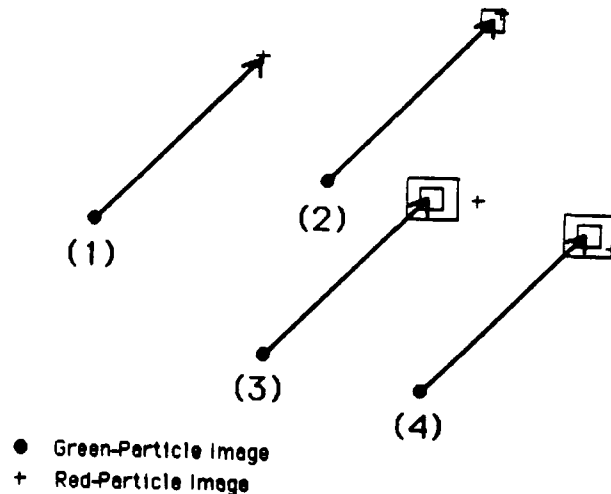


Fig. 5. Schematic illustration of two-color PIV tracker. Most probable velocity vector is drawn from each green-particle image (●) to locate corresponding red-particle image (+). Case (1) depicts exact match; Case (2), match obtained with first uncertainty box; Case (3), no match; Case (4), match obtained with second uncertainty box.

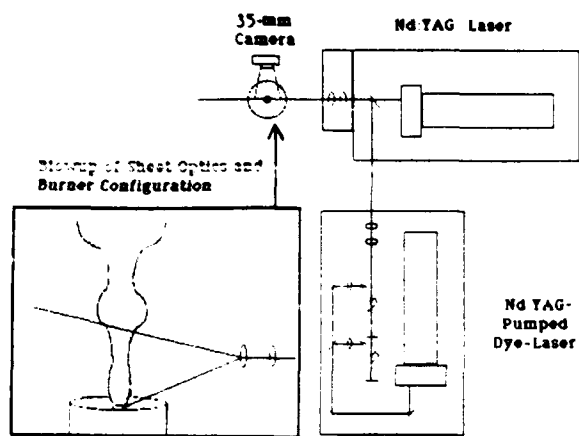


Fig. 6. Schematic diagram of experimental arrangement utilized for study of two-color PIV technique on propane jet diffusion flame. Both a Nd:YAG and a Nd:YAG-pumped dye laser are employed for sheet lighting of flame.

position of the particles in the seeded flowfield. The green-laser light sheet is formed from the doubled output of a Nd:YAG laser (Quanta-Ray DCR 1A) at 532 nm. The second laser employed for the red-laser light sheet is a broadband dye laser operating at 607 nm. The outputs from both the dye and Nd:YAG lasers are combined by a dichroic mirror and directed into sheet-forming optics. These optics consist of a cylindrical lens which spreads the laser beams two dimensionally and a plano-convex lens which controls the beam waist of the laser sheets. The laser sheet was  $\sim 10$  cm in height and 1 mm in thickness in the test area.

A Nikon 35-mm format camera was used to record the Mie scattering from the seeded flowfield. A macro zoom lens operating with an f/8.4 aperture was employed for obtaining the images reported in this study. This lens-aperture combination resulted in a magnification factor of 0.39. To reduce the contribution of the soot emission of the flame, a Uniblitz high-speed camera shutter operating at a 1/500-sec. exposure was employed. Synchronization of the camera shutter with the laser firing was controlled by custom-built timing electronics. The 100 ASA color film used to record the two-color PIV images was developed commercially. After processing, the film was digitized by a 384 x 576 Thompson CCD array camera (Photometrics, Ltd.) using a film projector to enlarge a section of the film onto the camera. Each section of the film was digitized twice--once with a green-color filter and then with a red-color filter. The digitized film sections typically covered a  $1.5 \text{ cm}^2$

area of the recorded image (which was  $\sim 54 \text{ cm}^2$ ). This corresponded to a pixel resolution of  $\sim 20 \mu\text{m}$  which was considered to be adequate for capturing the particle images. The 35-mm film was typically divided into 36 segments which were digitized and stored on magnetic tape for analysis.

The experimental arrangement for the jet diffusion flame consisted of a round central jet of 22.5-mm diam. surrounded by an annular coflowing air jet of 254-mm diam. The velocities of the central fuel jet and annular air were  $\sim 10$  and  $\sim 15 \text{ cm/sec.}$ , respectively. The fuel used in this study was propane diluted with 50%-by-mass of nitrogen. This flame has been studied experimentally using the reactive Mie scattering (RMS) and thin-filament pyrometry (TFP) techniques in which visualization and temperature profiles were obtained and compared with numerical predictions of Davis, *et al.*<sup>25-26</sup> Both experimental and numerical evidence indicates that the low-velocity propane jet is unusual in that a stagnation (weak-recirculation) zone is established approximately two diameters downstream of the nozzle. The presence of this stagnation zone is due to the high density of propane which tends to overcome the weak momentum of the fuel jet, eventually halting the upward fuel flow. It is thought that the flame develops downstream from the stagnation zone due to the acceleration effects of buoyancy. This flowfield is, thus, relatively complex and a good test for two-dimensional velocity methods which can distinguish direction.

A 500-msec time separation between the green- and red-laser sheets was used for this study. Assuming a maximum velocity in the flowfield of 3 m/sec, the minimum spatial resolution is  $\sim 1.5 \mu\text{m}$ . The lowest velocity is determined from the minimum particle separation divided by the time separation between laser pulses. For the collection optics and film used in this study, this corresponded to a particle separation of  $\sim 15 \mu\text{m}$ , and the lowest detectable velocity was thus  $\sim 0.03 \text{ m/sec.}$  The seed employed in this study was alumina of  $\sim 1 \mu\text{m}$  nominal size. The seed was injected both into the fuel jet and coannular air jet prior to exiting the tubes.

The processed two-color PIV image for the 2.54-cm propane jet is shown in Fig. 7. The initial velocity of the fuel jet was  $\sim 0.15 \text{ m/sec}$  at the nozzle exit. As the fuel jet progressed downstream, the velocity of the jet decayed, approaching zero at  $\sim 1.5$  diameters downstream. The development of the stagnation zone was due to the high density of the propane fuel which

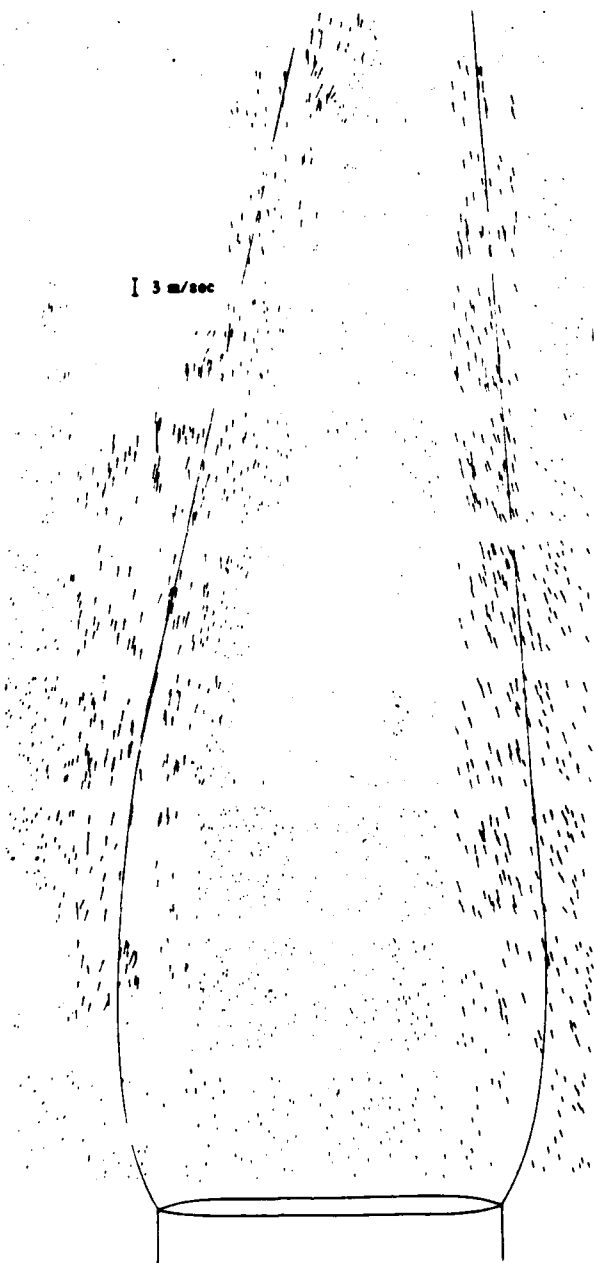


Fig. 7. Processed velocity-vector map of propane jet diffusion flame. Solid line in flow represents visible flame surface.

overcame the initial momentum of the fuel jet. Just above this stagnation zone the fuel jet accelerated due to the proximity of the fast hot burning gases. Notice that these hot regions display a velocity much higher than that of the cold central fuel jet. This high velocity is thought to be due to the buoyancy effect which accelerates the hot (low-density) combusting gases. The gases in the combusting areas reach a velocity of  $\sim 3$  m/sec. Notice the cooler outer air

being entrained into the flame at downstream locations. This process acted to mix burning fuel with air and, thus, sustain combustion at downstream locations. The existence of the stagnation zone and the flowfield acceleration due to buoyancy have been qualitatively demonstrated by the RMS flow-visualization technique on this jet diffusion flame.<sup>25</sup> Numerical results of Davis, *et al.*,<sup>25,5</sup> have confirmed the importance of the role of buoyancy in establishing the unique character of this flame.

## CONCLUSIONS

The influence of the thermal characteristics upon the spatial and temporal response of the thin SiC filament utilized in the TFP technique has been evaluated by a numerical model. The numerical simulation showed that the convection term is dominant over the conduction and dissipation terms; thus, the filament possesses high temporal response and spatial response suitable for tracking the motion of the flame. Also, for a typical lifted flame-base motion with measured flow velocities of  $\sim 2.0$  m/s and fluctuation frequencies of  $\sim 50 - 125$  Hz, the filament can accurately track the flame motion. For a modulation frequency  $> 500$  Hz, the tracking error was determined to be  $< 15\%$ . The addition of a CCD camera in the TFP technique allows imaging of multiple filaments as well as the flame background emission. This allows the emission from a sooty flame to be captured and compensated.

The two-color PIV technique has the advantage that direction as well as particle displacement is uniquely determined since the green particle image occurs before the red one by a known time increment. The technique is, thus, applicable to complex flowfields (i.e., recirculating), where the normal 180-deg. directional ambiguity of single-color techniques can be troublesome. Velocity measurements employing the two-color PIV technique on a propane jet diffusion flame indicated that the large change in flow speed and direction associated with this flowfield can be studied by this technique.

## ACKNOWLEDGEMENT

This work was supported by and performed at the Wright Research and Development Center/Aero Propulsion Laboratory under Contract No. F33615-85-C-2562. The authors are indebted to Drs. W. M. Roquemore and C. D. MacArthur for support and discussions concerning this work

and to M. Whitaker for editorial assistance and preparation of the manuscript.

#### REFERENCES

1. Dow Corning Corp. (Nippon Carbon Company Ltd.), Midland, MI 48686-0994.
2. Vilimpoc, V., Goss, L. P., and Sarka, B.: *Optics Letters* 13, 93 (1988).
3. Chen, T. H., and Goss, L. P.: "Flame Lifting and Flame/Flow Interactions of Jet Diffusion Flames," AIAA-89-0156.
4. Chen, T. H., Goss, L. P., Vilimpoc, V., Sarka, B., Trump, D. D., Post, M. E., and Roquemore, W. M.: "Flame Visualization Using Thin-Filament Pyrometry at High Sampling Rates," Presented at the ASME Winter Annual Meeting, San Francisco, CA, December 10-15, 1989.
5. Davis, R. W., Moore, E. F., Roquemore, W. M., Chen, L.-D., Vilimpoc, V., and Goss, L. P.: "Numerical/Experimental Study of the Structure of a Buoyant Jet Diffusion Flame," *Combustion and Flame* (in review).
6. Vilimpoc, V., and Goss, L. P.: *Twenty-Second Symposium (International) on Combustion* (The Combustion Institute, Pittsburgh, PA, 1988), p. 1907.
7. Goss, L. P., Vilimpoc, V., Sarka, B., and Lynn, W. F.: *Journal of Engineering for Gas Turbines and Power*, Transactions of the ASME 111, 46 (1989).
8. Chen, T. H., Post, M. E., and Goss, L. P.: "Numerical and Experimental Assessments of the Thermal Response of a Thin Filament," Submitted for presentation at the Twenty-Third Symposium (International) on Combustion, Orleans, France, July 22-27, 1990.
9. Eckert, E. R. G., and Drake, R. M., Jr.: *Analysis of Heat and Mass Transfer* (McGraw-Hill, NY, 1972).
10. Meynart, R.: *Applied Optics* 19: 1385 (1980).
11. Meynart, R.: *Applied Optics* 22:, 535 (1983).
12. Yao, C. S., and R. J. Adrian: *Applied Optics* 23, 1687 (1984).
13. Adrian, R. J., and C. S. Yao: *Applied Optics* 24, 44 (1985).
14. Adrian, R. J.: *Applied Optics* 25, 3855 (1986).
15. Landreth, C. C., Adrian, R. J., and Yao, C. S.: "Double-Pulsed Particle Image Velocimetry with Directional Resolution for Complex Flows," Presented at the Tenth Biennial Symposium on Turbulence, 1986.
16. Coupland, J. M., Pickering, C. J. D., and Halliwell, N. A.: *Applied Optics* 23, 11 (1987).
17. Ruess, D. L., Adrian, R. J., Landreth, C. C. D., French T., and Fansler, T. D.: "Instantaneous Planar Measurements of Velocity and Large-Scale Vorticity and Strain Rate in an Engine Using Particle-Image Velocimetry," SAE Technical Paper 890616.
18. Hiller, B., Booman, R. A., Hassa, C., and Hanson, R. K., *Review of Scientific Instruments* 55, 1964 (1984).
19. Miles, R. B., Connors, J. Markovitz, E. Howard, P., and Roth, G.: *Physics of Fluids A*, 1, 389 (1989).
20. Boedeker, L. R.: *Optics Letters* 14, 473 (1989).
21. Hiller, B. J., McDaniel, J. C., Read, J. E. C., and Hanson, R. K.: *Optics Letters* 8, 474 (1983).
22. McDaniel, J. C., Hiller, B., and Hanson, R. K.: *Optics Letters* 8, 51 (1983).
23. Hiller, B., and Hanson, R. J.: *Optics Letters* 10, 206 (1985).
24. Hiller, B., and Hanson, R. K.: *Applied Optics* 27, 33 (1988).
25. Davis, R. W., Moore, E. F., Chen, L. D., Vilimpoc, V., Goss, L. P., and Roquemore, W. M.: "Numerical/Experimental Study of the Dynamic Structure of a Buoyant Jet Diffusion Flame," Presented at the 1989 Spring Technical Meeting of the Central States Section of The Combustion Institute, Dearborn, MI, April 30 - May 3, 1989.

## Combined CARS/LDA instrument for simultaneous temperature and velocity measurements

L. P. Goss and D. D. Trump

Systems Research Laboratories Inc., Dayton, OH 45440, USA

W. M. Roquemore

Air Force Wright Aeronautical Laboratories, Wright-Patterson Air Force Base, OH 45433, USA

**Abstract.** The performance of a combined CARS/LDA instrument capable of measuring temperature and two velocity components with a time coincidence of about  $4\ \mu\text{s}$  is evaluated in a turbulent premixed propane-air Bunsen-burner flame. Measurements near the base of the flame exhibit negative axial correlations, indicative of normal gradient transport; those near the flame tip show strong positive axial correlations, indicative of transport counter to the temperature gradient. The radial correlations are positive both in the reaction zone and in the plume. An analysis of temperature data from measurements made (1) independent of and (2) coincidental with LDA measurements indicates that the CARS/LDA instrument provides a density-weighted velocity, temperature, and velocity temperature correlation due to the density variations in the flame.

### 1 Introduction

Experimental studies of turbulent transport processes are very difficult because simultaneous measurements of velocity and a scalar variable are required. The development of laser Doppler anemometry (LDA) has provided the means for measuring velocities in combusting flows; however, reliable scalar measurements have proven to be much more difficult. Shepherd and Moss (1983), Shepherd et al. (1982), Tanaka and Yanagi (1983), Yanagi and Mimura (1981), and Heitor et al. (1984) combined LDA with a thermocouple to make simultaneous temperature and velocity measurements in premixed flames. Brum et al. (1983) used LDA and a thermocouple to study a complex diffusion flame. Pulsed Raman and LDA were combined in studies conducted by Warshaw et al. (1981), Lederman and Posillico (1981), and Dibble et al. (1984). Simultaneous density and velocity measurements were made by Dibble et al. (1981) using Rayleigh scattering and LDA. Mie scattering and LDA were used by Starner and Bilger (1980) to obtain mixture fraction and velocity correlations. Coherent anti-Stokes Raman spectroscopy (CARS) and LDA have been used by Fujii et al. (1983), Fujii et al. (1984), and Goss et al. (1984a, b) to obtain velocity-temperature correlations.

A combined CARS/LDA instrument designed for simultaneous measurements of velocity and temperature in reacting flows is described herein. This instrument was developed to minimize the time difference between velocity and temperature measurements. The advantages of combining the LDA and CARS instrument are: (1) the demonstrated ability of CARS to obtain temperatures in diverse flame environments, (2) the nonintrusive nature of the measurements, and (3) the ability to examine the effects of seed biasing. The last advantage is quite significant in demonstrating the density-weighted bias error which occurs with the LDA measurement. The density bias affects not only the average temperature and velocity measurements obtained simultaneously but also the correlations between the velocity and temperature, as will be discussed in detail in this paper.

### 2 CARS instrument

The design and the data-reduction routines of the CARS instrument (Fig. 1) have been discussed in detail by Goss et al. (1983b), and only the salient features will be mentioned here. The frequency-doubled output from a Quanta-Ray DCR-2 Nd:YAG laser was used to pump a broadband dye laser (oscillator-amplifier combination). It was also used as the pump beam in the CARS process. A folded BOXCARS configuration was used to achieve a spatial resolution of 2 mm along the major beam axis. This system was designed to acquire CARS data at a 10-Hz rate which required interfacing to a minicomputer for control of the data acquisition. Data reduction consisted of fitting the observed  $\text{N}_2$  CARS spectral band-shape by means of a nonlinear least-squares iterative routine.

The primary differences between the CARS system described by Goss et al. (1983a) and the system used in this study are associated with a change in the photodiode-array detector. The previously used TN1223 detector was replaced with a TN6132 1024-element detector. The latter detector, when directly compared with the former, displayed less cross-talk, a larger dynamic range, and little, if

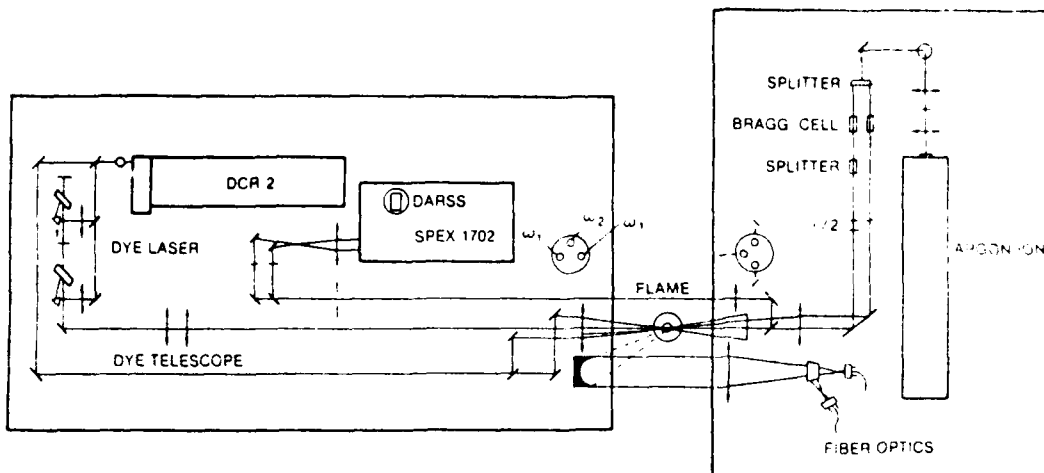


Fig. 1. Optical layout of the combined CARS/LDA instrument

any, memory retention. As a result, the splitter arrangement as well as the data-acquisition software of the previous system could be simplified. Calibration of the new detector has been described by Goss et al. (1983b). This CARS system displayed 80-K precision for repeated single-shot temperature measurements and 10-K accuracy in time-averaged measurements, as compared to a chromel-alumel thermocouple.

### 3 LDA instrument

The LDA system shown in Fig. 1 was built by Lightman et al. (1983) and is a two-velocity-component, real-fringe system based on polarization separation of the velocity components. The spatial resolution was 3 mm. The processor electronics consisted of two 1990 TSI burst-counter processors which were modified to permit coincident velocities as well as CARS data to be obtained. A computer interface allows data rates in excess of 30,000 velocities/s to be transferred and stored on a mini-computer. A 40-MHz Bragg shifter was used to remove direction ambiguities in the experiments reported by Goss et al. (1984b). This, however, resulted in a relatively coarse velocity resolution (0.5 m/s) due to the bit resolution of the 1990 processors. To circumvent this problem, the 40-MHz signal was mixed with a 35-MHz signal, resulting in a 5-MHz Doppler signal with a velocity resolution of 0.06 m/s which is better suited for the low-velocity flames under study.

In the earlier studies conducted by Goss et al. (1984a) with the combined CARS/LDA instrument,  $\text{TiO}_2$  particles were used exclusively as the seed. It was observed in the present work that  $\text{TiO}_2$  displays a higher-than-expected dropout rate at high temperatures. The velocity realization rate is expected to decrease at higher temperatures due to

the density weighting of the LDA measurement (high temperatures, low seed density). However, the LDA data rate for  $\text{TiO}_2$  was two to three times lower than could be explained by a density-weighting mechanism. Several suggestions have been made by Moss (1980), Ebrahimi and Kleine (1977), and Kennedy (1982) to explain this phenomenon. For example, it was suggested that  $\text{TiO}_2$  may undergo a phase transition at high temperatures which results in a smaller scattering cross section and reduced signal strengths. It has also been suggested that the  $\text{TiO}_2$  particle may break up to form smaller particles at high temperatures, thus reducing the scattering cross section. Alumina particles, when tested under flame conditions similar to those used with the  $\text{TiO}_2$ , displayed close agreement with the expected density-weighted LDA data rates. Thus, alumina seed particles were used for the experiments reported in this paper, unless otherwise stated. The density-weighted biasing will be discussed in more detail in a later section.

### 4 Combined CARS/LDA system

The Nd:YAG laser used in the CARS experiment operates most efficiently at a 10-Hz rate, whereas the LDA instrument processes velocities at a rate which is related to the passage of the seed particles through the fringe pattern. Since particle arrival is random in nature, the coupling of the two instruments requires that random events be coupled to a 10-Hz repetitive event.

The approach followed in combining these two instruments involved creating a 100- $\mu\text{s}$  window during every 100-ms firing interval of the Nd:YAG laser. If an LDA realization should occur during this window, the CARS laser would be allowed to Q-switch. The firing sequence of the Nd:YAG laser consists of first discharging the

flashlamps to obtain a population inversion and then pulsing the Q-switch to depopulate the upper laser levels and, thereby, obtain a giant laser pulse. The time separation between the flashlamp discharge and the Q-switch pulsing is 250  $\mu\text{s}$ . The 100- $\mu\text{s}$  LDA window is centered about the optimum 250- $\mu\text{s}$  delay after the flashlamp firing. The width of the 100- $\mu\text{s}$  window was determined experimentally by varying the time delay between the lamp firing and the Q-switching. When the window is centered on the optimum delay, firing the Nd:YAG laser 50  $\mu\text{s}$  on either side of center corresponds to a 25% drop in laser power. The net result of such an approach is that the coincidence time is determined by (a) the time required by the burst-counter processor to determine the velocity from Doppler burst (4  $\mu\text{s}$ ) and (b) the time required for the laser to fire after the Q-switch pulse has occurred (50 ns). With this method a 50-m/s fluid element would move only 200  $\mu\text{m}$  in the 4- $\mu\text{s}$  interval between velocity and temperature measurements.

The drawback of such an approach is that a substantially reduced data-acquisition rate is obtained due to the narrow window over which the LDA event is accepted. With the LDA in the free-run mode, 500 velocity realizations per second are observed in the flame. With a 100- $\mu\text{s}$  window opening every 100 ms, the total sampling time per second is 1 ms. This allows, on the average, only one simultaneous velocity-temperature measurement every two seconds.

The experimental arrangement of the combined CARS/LDA instrument is displayed in Fig. 1. To minimize the changes in optical configuration of the separate systems, a counter-propagating arrangement was used in which the instruments were on separate optical tables. The collimating lens and turning mirrors of the CARS system were rearranged on the LDA optics table, while the parabolic forward-scattering collection mirror of the LDA system was placed on the CARS table. This caused no major problem for either system and also minimized the number of optical changes necessary. To ensure overlapping of the measurement volumes for the two systems, a 100- $\mu\text{m}$  circular aperture was used to locate and align the foci at a common point. An 80-cm-focal-length lens was used with the CARS beams to minimize the optical break-down caused by the presence of a seed particle in the measurement volume at room temperature. The CARS/LDA combined measurement volume was 3 mm along the major beam axis.

The timing sequence for data acquisition is shown in Fig. 2. The CARS shot gate is initiated by a machine-code software program from the TN 1710 controller (LSI 11/02 microprocessor). If a velocity realization occurs during the gate, data are transferred under direct-memory-access (DMA) control to the 7810 Modcomp computer for storage on a 20-Mbyte disc system. The data-ready signal from the TSI 1990 burst-counter processor is sent to the TN1710 unit which, in turn, sends the fire Q-switch

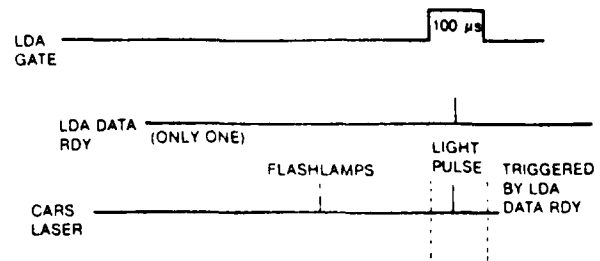


Fig. 2. Timing sequence for data-acquisition for the combined CARS/LDA instrument

command signal to the Nd:YAG laser. The TN6132 multichannel detector transfers the CARS data to the spectral-data memory (SMD) of the TN 1710 from which the data are transferred under DMA control to the 7840 computer. Before the data are transferred to the 7840 computer, the least ten channels of the 1024-channel CARS data are overwritten with the shot count for that particular laser firing. The shot count is used for book-keeping by analysis programs.

For low-velocity flows the seed particle does not have sufficient time to clear the sample volume before the CARS laser fires; thus, potential problems related to the presence of the seed during the CARS measurement must be addressed. Possible problems include: (1) optical breakdown, which has been discussed, (2) a contribution to the overall non-resonant susceptibility produced by the particles, which would effectively increase the measured CARS temperature, and (3) a reduction in the temperature of the flame due to heat loss in the form of blackbody emission by the seed. To determine whether the presence of the seed particle affects the CARS measurement, an experiment was conducted in which the plume region of the premixed flame was measured with and without seed particles. The result was that the two measured mean temperatures always agreed to within 10 K. The 10-K difference is well within the reproducibility of the burner experiments; thus, no major effects were observed due to the presence of the seed particle in the measurement volume.

## 5 Results and discussion

### 5.1 Flame characteristics

A turbulent Bunsen-burner flame was chosen for this study because experiments have demonstrated that large velocity-temperature correlations exist in and around the reaction zone. The detection of similar correlations with the combined CARS/LDA system would indicate that the system was functioning properly. Yanagi and Mimura (1981) and Tanaka and Yanagi (1983) observed both positive and negative correlations in different regions of a premixed propane-air flame. Extensive mapping of the

velocity-temperature correlations was carried out in the Tanaka and Yanagi (1983) study using a two-component LDA system and a fine-wire thermocouple. Although significant differences exist between that experiment and the present one, in general, the qualitative trends of the time-averaged flame characteristics and the velocity-temperature correlations are very similar. These similarities and differences will be discussed in this section.

The Bunsen burner employed by Tanaka and Yanagi (1983) made use of screens to generate turbulence, and the flame was stabilized by a pilot flame surrounding the burner port. The present investigation revealed that the seed particles clogged the screen when such a burner was operated for long periods of time. With the low data rates being employed, it was essential that the burner operate stably for long time periods; therefore, the screen approach was abandoned.

The burner employed in the present study was a standard Bunsen burner, except that the air-inlet holes were covered and the needle valve replaced to permit use of a controlled, premixed propane-air mixture. Turbulence and flame stabilization were achieved in the burner by use of three intrusions separated by  $120^\circ$  and located on the inside surface of the burner about 1 cm from the exit. The intrusions extended about 2 mm into the mixture flow. Tanaka and Yanagi (1983) used a natural gas-air mixture with an equivalence ratio of 0.6; in the present study, it was found that a propane-air mixture with an equivalence ratio of 1.3 provided a highly turbulent, but stable, flame.

The tip of the visible flame here was 23 mm (2.1 D); whereas, the flame used by Tanaka and Yanagi (1983) had a visible length of 6.2 D. In a comparison of the results of these two studies, it is assumed that the processes occurring in the respective reaction zones should be similar if scaled by the respective lengths of the visible reaction zone.

The average and rms temperature, axial velocity, and radial velocity at two axial positions are plotted in Figs. 3-5. These data were collected with the CARS and LDA systems operating independently. Superimposed on these plots is a time-averaged display of the premixed flame obtained from a long-exposure flame photograph. At an axial position of 15 mm, just inside the visible flame region, the temperature profile in Fig. 3 shows a large dip in the central region of the reaction zone and a peak in the surrounding plume; whereas, the rms fluctuations peak at the center and decrease sharply in the plume region. As noted in Fig. 4, at this axial location, the axial velocity and corresponding fluctuation are nearly constant through much of the flame. The radial velocity profile at 15 mm shown in Fig. 5 is similar to the temperature profile, with a peak value occurring just outside the flame zone very near the edge of the burner and the fluctuations being nearly flat. One of the intrusions used to stabilize the flame was inadvertently located in the measurement plane to the right of the centerline, no intrusion occurred to the

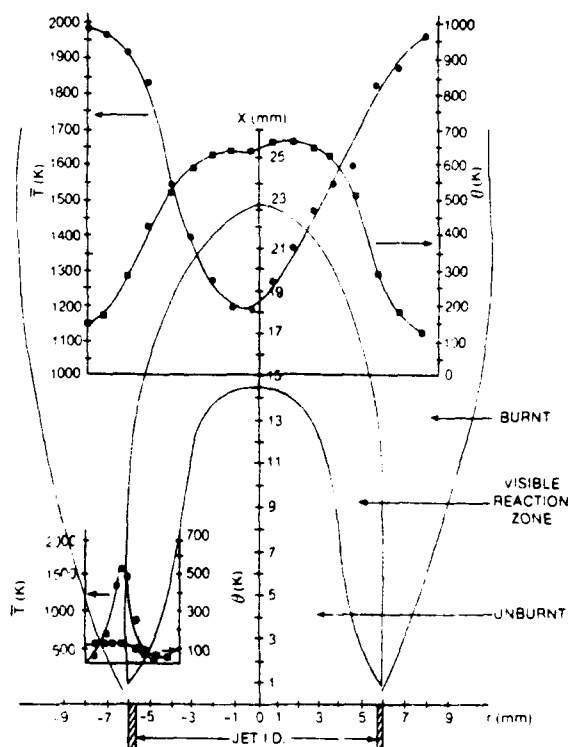


Fig. 3. The time-averaged ( $\bar{T}$ ) and rms ( $\theta$ ) temperature profiles at axial locations of 1.5 and 15 mm; CARS temperature measurements were made independently of the LDA measurements at a rate of 10 Hz

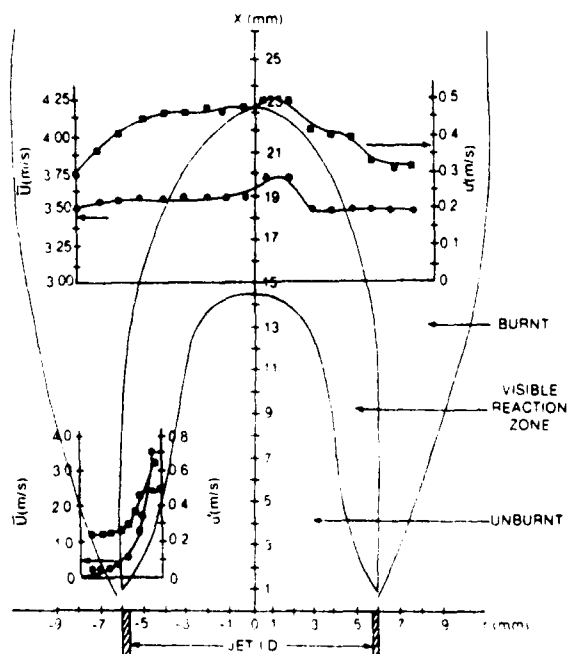


Fig. 4. Time-averaged ( $\bar{U}$ ) and rms ( $u'$ ) axial velocity profiles at axial locations of 1.5 and 15 mm; LDA measurements were made independently of CARS measurements at an average rate of 500 realizations/s

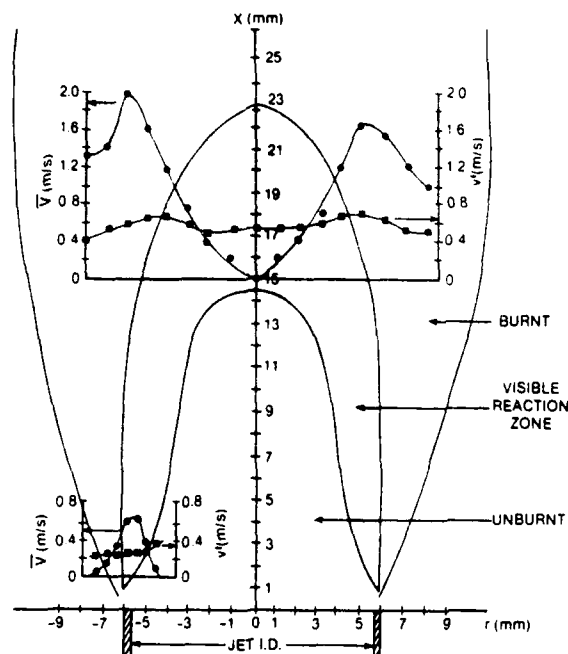


Fig. 5. Time-averaged ( $\bar{V}$ ) and rms ( $v'$ ) radial velocity profiles at axial locations of 1.5 and 15 mm; LDA measurements were made independently of the CARS measurements at an average rate of 500 realizations/s

left of the centerline. This is believed to be the cause of the asymmetry noted in Figs. 3–5. Disregarding the asymmetry, the observed trends for the mean and fluctuations at the 15-mm position are similar to those observed by Tanaka and Yanagi (1983) near the bottom of the visible flame.

At the 1.5-mm axial position, the flame is quite stable and displays little temperature fluctuation, as noted in Fig. 3. The mean temperature (Fig. 3) and radial velocity (Fig. 5) have peaks near the plume-reaction zone interface and decrease on either side due to the narrow width of the flame in this area. This observation is different from that of Tanaka and Yanagi (1983); the peak temperature occurred at the edge of their pilot burner. Nevertheless, the time-averaged characteristics of their flame and ours are quite similar if scaled by the visible flame length.

## 5.2 Bias errors

The individual CARS and LDA measurements can be used, with conditional sampling techniques, to determine whether bias errors are present in the combined CARS/LDA system. A CARS/LDA measurement is initiated by the presence of a seed particle in the measurement volume during the time interval (window) when the CARS laser is ready to fire. Since the distribution of seed particles in the flow determines the measurement sampling statistics, bias errors due to seeding may occur. The presence and magnitude of seed biasing errors are very difficult to

assess because an accurate unbiased measurement is also required. CARS measurements made at constant rate, independent of LDA measurements, do not have a seed-related bias error and, thus, are considered to be unconditionally sampled measurements. These “unconditioned” measurements provide a truly random sample and are thus free from a bias error, provided that the measurement frequency is not locked to an instability frequency in the flame. These unconditioned measurements are referred to as unbiased. By comparing the mean and probability distribution functions (pdf’s) for conditional and unconditional temperature measurements, bias errors can be examined for different test conditions.

Three different seed bias errors are known to occur in LDA measurements in cold flows. First, velocity measurements will be biased toward the low velocities if the seed particles are too large to follow the flow field. It is generally accepted that such errors do not exist in turbulent flows when the particles are  $\sim 1 \mu\text{m}$  or less in diameter. The second type of error is due to a variation of seed density which results from nonuniform seeding (Durst 1974; Yule et al. 1980). The third type of error was first considered by McLaughlin and Tiederman (1973) and more recently by Edwards and Baratuci (1984) and Chen and Lightman (1985); here a bias error in a uniformly seeded flow may result because there is a higher probability that a seed particle is present in the faster-moving fluid elements.

Additional errors can occur as a result of combustion. High flame temperatures can cause a reduction in the effective scattering cross sections of certain seed materials. This can result in a higher probability of sampling low-temperature fluid elements. As mentioned earlier, Ebrahimi and Kleine (1977) observed such an effect for  $\text{TiO}_2$ . Figure 6 demonstrates that the CARS/LDA system, through the use of conditional sampling, can detect this effect. Each pdf contains about 1500 individual measurements. The conditionally sampled pdf’s in Column C are strongly weighted toward the lower temperatures, as compared to the unconditionally sampled pdf’s in Column A. This is especially notable for the pdf’s at  $r = 0$ .

Another bias error which may occur in flames is due to a variation in gas density. Assuming that the ideal gas law applies, the seed density will be proportional to the gas density. This will result in a higher probability of measuring low-temperature, high-density fluid elements if the samples are not collected at a constant rate. This bias error might be somewhat offset by the McLaughlin-Tiederman high-velocity bias if the lower-density fluid elements are moving faster than the high-density elements. However, the two bias errors need not cancel out. A gas-density bias error was suggested by Magill et al. (1982) to explain a bias toward low-velocity, low-temperature fluid elements in an experiment where high-velocity, high-temperature fluid elements were known to be present more than 60% of the time. Recently, Heitor et al. (1984) computed a

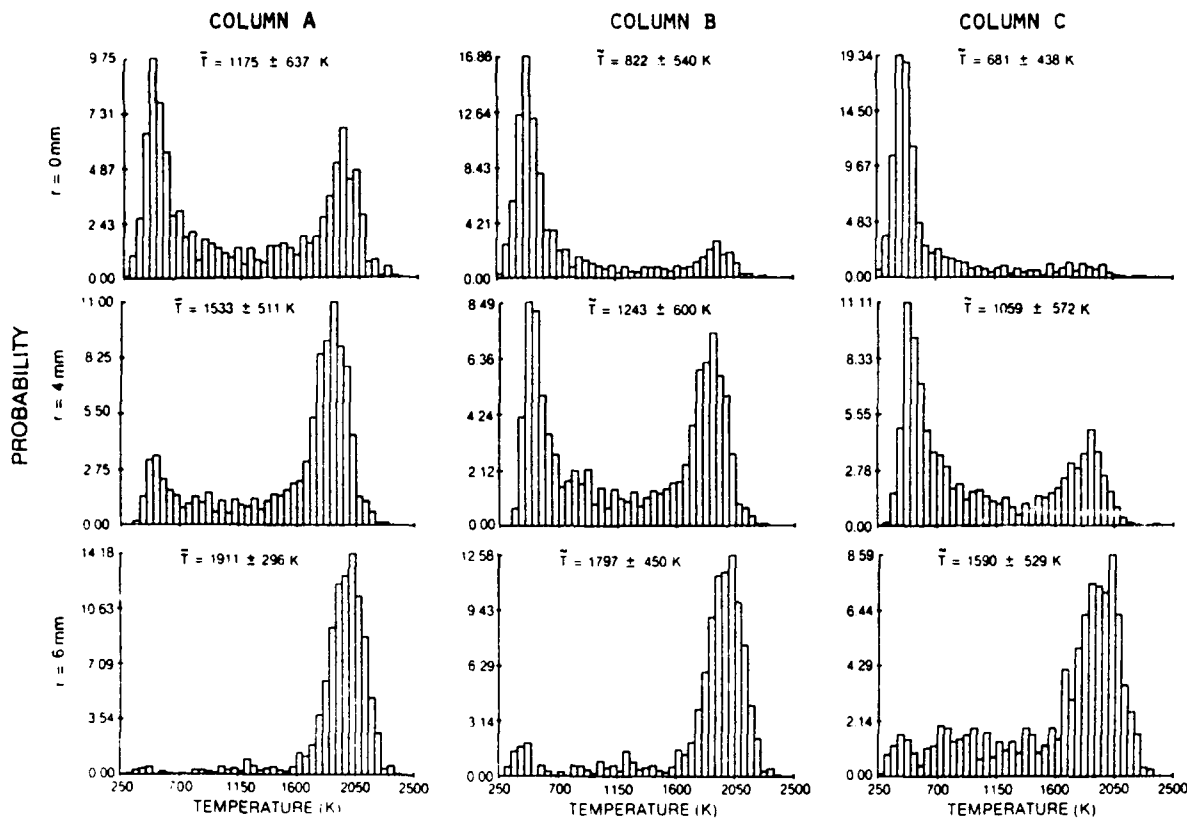


Fig. 6. CARS temperature pdf's obtained at an axial location 21.5 mm and radial locations of 0, 4, and 6 mm; column A represents the CARS temperatures measured independently of LDA velocities (unconditional), column B represents the calculated Favre average of the temperature pdf's in column A, and column C represents the CARS temperatures measured simultaneously with LDA velocities using  $TiO_2$  seed particles (conditional)

density-weighted pdf from unconditional (constant-sampling-rate) thermocouple measurements and compared the results with a pdf obtained from conditionally sampled simultaneous LDA and thermocouple measurements. Although their data samples were not sufficiently large to rule out statistical sampling errors, the density-weighted and conditional pdf's had similar shapes.

The low-temperature bias error noted in Fig. 6 may be due, in part, to gas-density variations. To determine whether this is the case, the unconditional pdf's ( $B_i$ ) can be density weighted using Eqs. (1) and (2) where the density was assumed to obey the ideal gas law at constant pressure,

$$\bar{B}_i = \frac{M_i B_i}{T_i \left( \frac{M}{T} \right)}, \quad \bar{T} = \frac{1}{\left( \frac{1}{T} \right)} \quad (1), (2)$$

$\bar{B}_i$  is the density-weighted probability of measuring a temperature  $T_i$ ,  $\bar{T}$  the Favre-averaged or density-weighted temperature,  $T$  the unconditioned temperature,  $M_i$  the molecular weight of gas for the  $i$ -th measurement, and  $B_i$  the probability of measuring temperature  $T_i$ . It is estimat-

ed that the molecular weights of the mixture and products for our premixed flame are only about 1.5% more than that of air. For our calculations, using Eq. (1), the molecular weight is assumed to be constant, which causes no appreciable error in the pdf's. A comparison of the pdf's in Columns C and B in Fig. 6 reveals that the low temperatures are more pronounced than would be expected as a result of density weighting. Indeed, the data rate of the LDA measurements taken with  $TiO_2$  was lower by about a factor of three than expected from assuming that the number density of the seed particle varied as the gas density. The data in Fig. 6 indicate that  $TiO_2$  is not a good seed particle for combusting flows, as noted by other investigators (Kennedy 1982).

Figure 7 illustrates the density bias error which may result from the use of  $Al_2O_3$  seed particles. This figure contains pdf's obtained from unconditionally and conditionally sampled temperature measurements made at three radial locations and an axial location of 15 mm. The average temperatures of the conditionally sampled data are more than 270 K lower than those collected unconditionally, and the pdf's are weighted toward the low-temperature, high-density values. A comparison of the

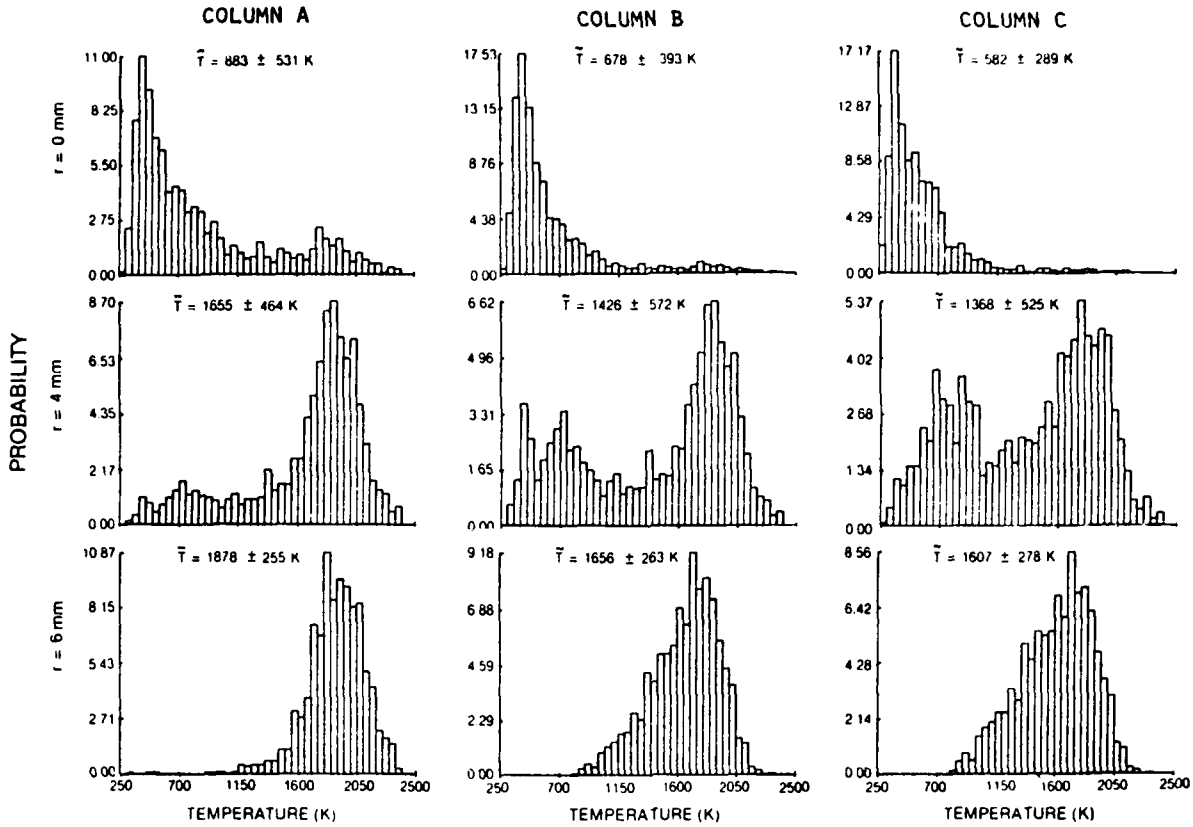


Fig. 7. CARS temperature pdf's obtained at an axial location of 15 mm and radial locations of 0, 4, and 6 mm; column A represents the CARS temperature measurements made independently of the LDA measurements (unconditional); Column B represents the calculated Favre average of the temperature pdf's in column A, and column C represents the CARS temperature measurements made simultaneously with LDA measurements using Al<sub>2</sub>O<sub>3</sub> seed particles (conditional)

shapes of the conditionally sampled pdf's in column C with the density-weighted values in column B [calculated using the unconditional data in column A and Eq. (1), assuming a constant molecular weight] gives strong support to the proposition that the measurements conditioned by the presence of seed particles are density weighted. This view is also supported by the good agreement between the Favre-averaged temperatures listed in columns B and C of Table 1. The large deviations of the rms values in Table 1 suggest that the 1,500 samples per radial location were insufficient to obtain a statistically valid sample. Typically about 17,000 samples would be required to reduce the deviation of the rms values to a value which is comparable to the deviation of the mean in Table 1, assuming a sampling error which varies as  $1/\sqrt{n}$ .

The possibility exists that the combined CARS/LDA measurements may be biased to a greater extent than expected from density weighting alone. The simultaneous measurements depend not only on the presence of seed particles but also on the window (time interval) during which the CARS laser fires. It is conceivable that an additional bias error could result due to the window width. For example, Nejad and Davis (1986) observed

bias errors in 2D LDA measurements in cold flows due to the window width when data were obtained at a uniform rate. The possibility of a window bias for the CARS/LDA measurement was examined in the present investigation by comparing axial velocity pdf's obtained simultaneously with and independently of the CARS measurements. The results indicate that such a bias would be less than 1% of the mean velocity value.

### 5.3 Temperature-velocity correlations

As discussed in Sect. 5.2, the velocity measurements appear to be density weighted when alumina seed particles are used. Since the temperature is determined simultaneously with the velocity, the Reynolds-averaged correlations can be determined by correcting the individual measurement using

$$\overline{u \theta} = \frac{\sum_{i=1}^N \left( \frac{\bar{T}_i}{M_i} \right) u_i'' \bar{\theta}_i}{\sum_{i=1}^N \left( \frac{\bar{T}_i}{M_i} \right)} \quad (3)$$

**Table 1.** Comparison of time-averaged and rms temperatures at an axial location of 15 mm and various radial locations: unconditioned (A), calculated Favre average using data in column A (B), and seed conditioned (C)

$r$ (mm)	Average temperature (K)				rms (K)			
	A	B	C	$\frac{B-C}{B}$	A	B	C	$\frac{B-C}{C}$
0.0	883	678	582	0.140	531	393	289	0.265
1.0	1,002	742	722	0.027	547	439	378	0.138
2.0	1,040	782	774	0.010	541	449	391	0.129
3.0	1,342	1,029	994	0.034	568	566	472	0.166
4.0	1,655	1,426	1,368	0.041	464	572	525	0.082
5.0	1,885	1,816	1,744	0.040	285	356	384	0.079
6.0	1,878	1,656	1,607	0.030	263	255	278	0.083
7.0	1,806	1,783	1,741	0.024	190	199	263	0.322
8.0	1,759	1,733	1,611	0.070	203	211	273	0.294

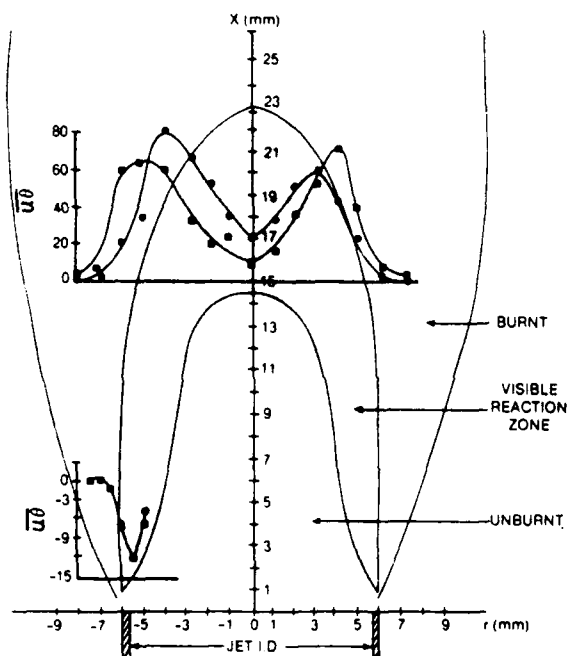


**Fig. 8.** Favre- (■) and Reynolds- (●) averaged axial velocity/temperature correlations about the mean at axial locations of 1.5 and 15 mm;  $\text{Al}_2\text{O}_3$  particles were used to seed the flow

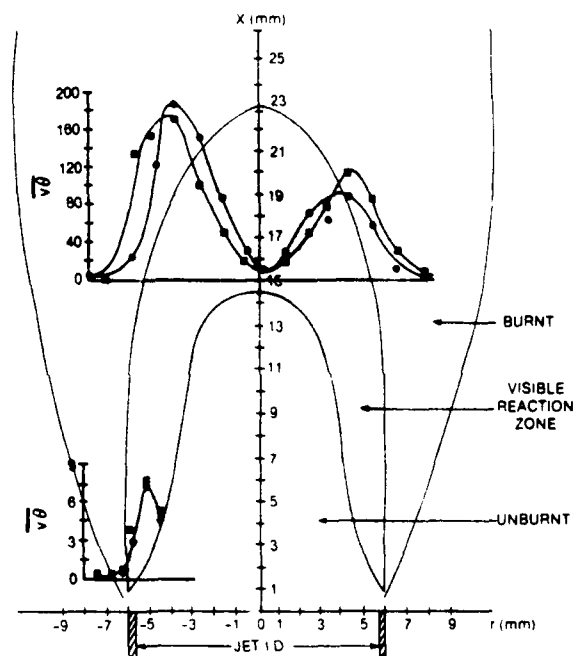


**Fig. 9.** Favre- (■) and Reynolds- (●) averaged radial velocity/temperature correlations about the mean at axial locations of 1.5 and 15 mm; the LDA measurements were made using  $\text{Al}_2\text{O}_3$  particles

where  $u_i'$  is the axial velocity fluctuation about the Favre average of the  $i$ -th measurement,  $\bar{T}_i$  the  $i$ -th temperature measured by an instrument which gives a density-weighted mean,  $\bar{\theta}_i$  the  $i$ -th measured temperature fluctuation about the Favre average,  $M_i$  the molecular weight for the  $i$ -th density-weighted measurement, and  $N$  the total number of measurements. This allows a direct comparison between the Reynolds- and Favre-averaged correlations.

The axial and radial velocity correlations with temperature (near the base of the burner in Figs. 8 and 9) show the same trends as those observed by Tanaka and Yanagi (1983). They found a negative correlation between

axial velocity and temperature at the interface of the reaction zone and the burnt mixture and a positive correlation between radial velocity and temperature very near the same radial location. The same trends can be observed in the 1.5-mm profiles shown in Figs. 8 and 9. Figures 8 and 9 also show velocity-temperature correlation profiles at the 15-mm position near the tip of the reaction zone. The axial velocity-temperature correlation has a minimum at the centerline where the average temperature is a minimum and has a peak of 81 near the reaction zone, indicating strong positive correlation (high temperature, high velocity) in this region. Since the mean temperature gradient is also positive at this location (Fig. 3), transport

is occurring in a direction counter to the temperature gradient.

The large fluctuations in the reaction-zone area are due to the penetration of the unburnt gases into this region, as demonstrated by the pdf's shown in Fig. 7. Disregarding the conditionally sampled pdf's in this figure, the unconditionally sampled pdf (sampled without the LDA) displayed bimodal peaks in the central region of the flame ( $r = 0$ ). Notice the strong low-temperature peak indicative of the penetration of unburnt gases. In the plume region ( $r = 6$ ), the pdf has a single mode, indicating primarily burnt gases.

The effect of density weighting upon the axial and radial correlations shown in Figs. 8 and 9 is very similar. Both an amplitude and a spatial difference are observed between the density-weighted and density-corrected axial and radial correlations. The amplitude difference in the radial-correlation case is somewhat smaller,  $\cong 1.4$ , than in the axial,  $\sim 2$ ; but the spatial shift of the maxima is approximately the same, 1 mm. Thus, while the general features of the density-weighted correlations are the same as those of the density-corrected correlations, the amplitudes as well as the spatial locations of the maxima are different and must be taken into account if accurate determinations of the correlations are to be made.

## 6 Summary and conclusions

The ability of a combined CARS/LDA instrument to make temperature and two-velocity-component measurements nearly simultaneously (within  $4 \mu\text{s}$ ) at a common point in a flame has been demonstrated. A turbulent premixed propane-air Bunsen-burner flame was examined during this study because of the following characteristics: (1) positive radial velocity and temperature correlations in the turbulent reaction zone where the temperature gradient is positive, (2) negative axial velocity and temperature correlations near the burner base, and (3) positive correlations near the tip of the reaction zone. The CARS/LDA measurements confirmed these characteristics for the Bunsen-burner flame. These results are viewed as a necessary condition for demonstrating the performance of the CARS/LDA system.

The ability of the CARS/LDA system to examine bias errors due to the presence of seed particles has been demonstrated. Comparisons of CARS temperature pdf's obtained independently (unconditionally) and simultaneously (conditionally) with LDA measurements, using  $\text{Al}_2\text{O}_3$  seed particles, show a strong weighting toward low temperatures (high densities). Density-weighted temperature pdf's, which were calculated using the unconditionally sampled pdf data, compared favourably with the measured conditionally sampled pdf's. This suggests that the CARS/LDA system provides density-weighted and, thus, Favre-averaged data.

The low data-sampling rate of  $< 0.5/\text{s}$  was a drawback with the CARS/LDA system which led to undersampling of some of the data. Low sampling rates were caused by the narrow  $100\text{-}\mu\text{s}$  window used in obtaining the  $4\text{-}\mu\text{s}$  coincidence between the velocity and temperature and the low seeding rates which normally occur in flames.

In order for the CARS/LDA system to become a practical tool for studying turbulent flames, increased data-acquisition rates which approach the speed of the CARS laser firing are essential. Increased rates can be achieved by improving seeding techniques. The development of a high-constant-output seeder is important for future transport studies in turbulent flames. Another improvement to the CARS/LDA system which should result in increasing data rates is to eliminate the  $100\text{-}\mu\text{s}$  window and fire the CARS laser at a constant rate of 10 Hz while free running the LDA. Coincidence would be achieved by interpolation of the LDA data to obtain the two velocity components at the time of the CARS laser firing. This approach will be investigated in future studies.

## Acknowledgements

The authors would like to express their appreciation to Ms. M. M. Whitaker for editing and typing this paper and to T. H. Chen for the many helpful discussions on bias errors.

## References

- Brum, R. D.; Seiler, E. T.; LaRue, J. C.; Samuelson, G. S. 1983: Instantaneous two-component laser anemometry and temperature measurements in a complex flow model combustor. AIAA-83-0334
- Chen, T.-H.; Lightman, A. J. 1985: Effects of particle arrival statistics on laser anemometer measurements. Proceedings of ASME, Winter Annual Meeting, Miami/FL November 17–21, 1985
- Dibble, R. M.; Kollmann, W.; Schefer, R. W. 1984: Conserved scalar fluxes measured in a turbulent nonpremixed flame by combined laser Doppler velocimetry and laser Raman scattering. *Combust. Flame* 55, 307–321
- Dibble, R. M.; Rambach, G. D.; Hollenbach, R. E.; Ringland, J. T. 1981: Simultaneous measurements of velocity and temperature in flames using LDV and CW laser Rayleigh thermometry. Presented at Fall Meeting of the Western State Section of the Combustion Institute, WSS/C I 81–84, October
- Durst, F. 1974: Informal presentation. In: Proc. of the Second International Workshop on Laser Velocimetry, vol. 2, pp. 471–476. (eds. Thompson, H. D.; Stevenson, W. H.) Purdue University
- Ebrahimi, I.; Kleine, R. 1977: The nozzle flow concentration fluctuation field in round turbulent free jets and jet diffusion flames. In: Sixteenth (International) Symposium on Combustion, pp. 1711–1723. Pittsburgh: The Combustion Institute
- Edwards, R. V.; Baratuci, W. 1984: Simulation of particle measurement statistics for laser anemometers. Presented at the Ninth Turbulence Symposium, Rolla/MS
- Fujii, S.; Gomi, M.; Eguchi, K. 1983: A remote laser-probe system for velocity and temperature measurements. *J. Fluids Eng.* 105, 128–133
- Fujii, S.; Gomi, M.; Eguchi, K.; Yamayuchi, S.; Jin, L. 1984: Time resolved LDV and CARS measurements in a premixed reacting flow. *Combust. Sci. Technol.* 36, 211

- Goss, L. P.; Trump, D. D.; MacDonald, B. G.; Switzer, G. L. 1983a: 10-Hz coherent anti-Stokes Raman spectroscopy apparatus for turbulent combustion studies. *Rev. Sci. Instrum.* 54, 563-571
- Goss, L. P.; Trump, D. D.; Switzer, G. L. 1983b: Laser optics/combustion diagnostics. Quarterly Status Report 6603-13 under USAF Contract F33615-80-C-2054, covering the period September-December, Dayton: Systems Research Laboratories, Inc.
- Goss, L. P.; Trump, D. D.; Roquemore, W. M. June 1984a: Simultaneous CARS and LDA measurements in a turbulent flame. *AIAA* 84-1458
- Goss, L. P.; Trump, D. D.; Roquemore, W. M. 1984b: An investigation of temperature and velocity correlations in turbulent flames. In: *Experimental measurements and techniques in turbulent reactive and non-reactive flows*, pp. 215-221 (eds. So, R. M.; Whitelaw, J. H.; Lapp, M.), New York: ASME
- Heitor, M. V.; Taylor, A. M. K. P.; Whitelaw, J. H. 1984: Simultaneous velocity and temperature measurements in a premixed flame. In: *Experimental measurements and techniques in turbulent reactive and non-reactive flows*, pp. 243-274 (eds. So, R. M.; Whitelaw, J. H.; Lapp, M.), New York: ASME
- Kennedy, I. M. 1982: Some aspects of seeding flames with refractory oxide particles. *Combust. Sci. Technol.* 27, 247-252
- Lederman, S.; Posillico, C. 1981: Unified spontaneous Raman and CARS system. *AIAA J.* 19, 824-825
- Lightman, A.; Magill, R. D.; Anderson, R. J. 1983: Laser diagnostic development and measurement and modeling of turbulent flowfields of jets and wakes, part I. *AFWAL-TR-83-2044*
- Magill, P. D.; Lightman, A.; Orr, C. E.; Bradley, R. P.; Roquemore, W. M. 1982: Simultaneous velocity and emission measurements in a bluff-body combustor. *AIAA* 82-0883
- McLaughlin, D. K.; Tiederman, W. G. 1973: Biasing correction for individual realization of laser anemometer measurements in turbulent flows. *Phys. Fluids* 16, 2082-2088
- Moss, J. B. 1980: Simultaneous measurements of concentration and velocity in an open premixed turbulent flame. *Combust. Sci. Technol.* 22, 119-129
- Nejad, A. S.; Davis, D. L. 1986: Velocity biasing in 2d individual realization LDV systems. In: *ICALEO 86 Proceedings*, 58, pp. 78-88. Toledo: Laser Institute of America
- Shepherd, I. G.; Moss, J. B. 1983: Characteristic scales for density fluctuations in a turbulent premixed flame. *Combust. Sci. Technol.* 33, 231-243
- Shepherd, I. G.; Moss, J. B.; Bray, K. N. C. 1982: Turbulent transport in a confined premixed flame. In: *19th Symposium (International) on Combustion*, pp. 423-431. Pittsburgh: The Combustion Institute
- Stamer, S. H.; Bilger, R. W. 1980: Measurements of scalar-velocity correlations in a turbulent diffusion flame. In: *18th Symposium (International) on Combustion*, pp. 921-930. Pittsburgh: The Combustion Institute
- Tanaka, H.; Yanagi, T. 1983: Cross-correlation of velocity and temperature in a premixed turbulent flame. *Combust. Flame* 51, 183-191
- Warshaw, S.; Lapp, M.; Penny, C. M.; Drake, M. C. 1981: Temperature-velocity correlation measurements for turbulent diffusion flames from vibrational Raman scattering data. In: *Laser Probes for Combustion Chemistry* (ed. Crosely, D. R.), Washington DC: The American Chemical Society
- Yanagi, T.; Mimura, Y. 1981: Velocity temperature correlation in premixed flame. In: *18th Symposium (International) on Combustion*, pp. 1031-1040. Pittsburgh: The Combustion Institute
- Yule, A. J.; Chigier, N. A.; Boulderston, R.; Ventura, J. 1980: Combustion-transition interaction in a jet flame. *AIAA J.* 19, 752-760

Received May 5, 1987

## Combined CARS-LDV System for Turbulent Flame Studies

D. D. Trump, L. P. Goss, and T. H. Chen  
Systems Research Laboratories  
A Division of Arvin/Calspan  
2800 Indian Ripple Road  
Dayton, OH 45440-3696

W. J. Schmoll  
The University of Dayton  
300 College Park Avenue  
Dayton, OH 45469

### INTRODUCTION

The development of computer models for predicting combust-ing-flowfield behavior requires simultaneous measurement of velocity and temperature. For velocity measurement, Laser Doppler Velocimetry (LDV) has been the technique of choice. For temperature measurement, the Coherent Anti-Stokes Raman Scattering (CARS) technique possesses the advantages of demonstrated ability to perform in diverse flame environments, nonintrusive nature of the technique, and ability to examine seed biasing effects. This paper describes a second-generation combined CARS-LDV instrument and demonstrates some of its capabilities. A more-detailed description of this instrument is available elsewhere.<sup>1</sup>

### CARS INSTRUMENT

Since the basic CARS instrument (shown in Fig. 1) has been discussed previously, only the salient features will be mentioned here. The frequency-doubled output of a Quanta-Ray Nd:YAG laser was used to pump a broadband dye laser and was also utilized as the pump frequency in the CARS process. A folded BOXCARS arrangement was used to obtain a spatial resolution of  $\sim 1$  mm along the major beam axis. The CARS signal was fed through an intensity splitter, a Spex 3/4-m monochromator, and onto a Tracor-Northern IDARSS detector system. The splitter arrangement was used for extending the effective dynamic range of the detector to allow study of the temperature range from 300 to 2300 K. The CARS system displays an 80-K precision for single-shot measurements and a 10-K accuracy in time-averaged measurements as compared to a chromel-alumel thermo-couple in oven studies.<sup>2</sup>

### LDV INSTRUMENT

The LDV system shown in Fig. 1 was built by Lightman, *et al.*,<sup>3</sup> and is a two-component real-fringe system based on polarization separation of the velocity components. The 514.5-nm line from a Spectra-Physics argon-ion laser was used as the light source, with  $\sim 1$ - $\mu$ m-diam. alumina ( $Al_2O_3$ ) particles serving as the scattering medium. The Doppler burst was collected in the forward direction slightly off-axis ( $\sim 10$  deg.). The two velocity components were separated by a Glan-Thompson polarization beam splitter and sent to two 1990 TSI burst-counter processors through fiber

optics. Dual Bragg cells having a 5-MHz frequency difference were employed to remove directional ambiguities and maintain the Doppler-burst frequencies in an optimum range for the velocities under study.

### COMBINED CARS-LDV INSTRUMENT

As with the first-generation combined instrument,<sup>2</sup> this second-generation instrument was arranged in such a way as to minimize changes in the optical systems. The two instruments are aligned head-on, maximizing overlap of their measurement volumes. They share no common optics which allows them to be operated separately or jointly without interference. The major improvements with this second-generation instrument involve the electronics and acquisition software. For purposes of establishing time coincidence, a common clock tags each measurement as it is made. Analysis software is later employed to sort the data according to time, based on the tagword. To reduce the amount of noncoincident data recorded, the LDV data acquisition is gated, limiting acquisition to a 10-ms window centered on the CARS measurement time.

Within this framework three variations of the acquisition scheme are possible (see Fig. 2). Method 1 involves only the constraints described thus far--the two systems essentially are operating independently. CARS data are taken at the nominal 10-Hz rate of the YAG laser, and any LDV realizations within  $\pm 5$  ms of the CARS measurement time are recorded. Time coincidence between the two measurements occurs purely by chance. In contrast, Methods 2 and 3 trigger coincident measurements and record only coincident data. Method 2 is similar to Method 1, except that the occurrence of the LDV realization triggers the CARS-laser flashlamps, with the Q-switch (light pulse and measurement time) following 250  $\mu$ s later. The guaranteed coincidence of 250  $\mu$ s between measurements provided by Method 2 is adequate for low-to-medium velocity studies. For studies involving higher velocities, Method 3 offers measurements with coincidence as close as 4  $\mu$ s. To achieve this coincidence, Method 3 triggers the CARS measurement directly by pulsing the CARS laser Q-switch in response to an LDV realization. The disadvantage of Method 3 is that the Q-switch time can be varied only  $\sim \pm 50$   $\mu$ s from optimum before the loss of power in the CARS laser renders flame-temperature measurement impractical. This 100- $\mu$ s window during which the LDV data can be recorded reduces coincident data rates by a factor of 100 as compared to those of Method 2. Therefore, Method 3 is used only for studies requiring such small coincidence times.

### ACQUISITION AND ANALYSIS SOFTWARE

The heart of the acquisition software is a machine-language program which runs on the Tracor-Northern control unit; the function of this program is to control (1) gating of the LDV data acquisition, (2) firing of the CARS laser, and (3) transfer of CARS spectral data to a ModComp mini-computer system. Each method of simultaneous acquisition has a separate program. Each program is a loop of 100-ms duration, corresponding to the 10-Hz nominal repetition rate of the CARS laser. The loop is composed of the commands required to implement (1), (2), and (3) above in the proper sequence, with waiting loops between each event, ensuring that the events occur at the proper time, as shown in Fig. 2.

The acquisition software on the ModComp computer for CARS and LDV is similar and controls the positioning of the burner system, the number of spatial locations at which data are to be taken, and the number of data points to be acquired at each location. The interface control is mainly carried out by the Tracor-Northern program, but analysis of the raw spectral and period data is conducted exclusively on the ModComp computer.

The first steps in processing the raw data consist of fitting the CARS spectral data to obtain temperatures and converting the period data from the TSI 1990 burst counters to velocities. The time tagword associated with each data point is then extracted and the data sorted according to time. Once this has been accomplished, the means, rms, and correlations between temperature and velocity components can be determined. By recording the time associated with each measurement, the correlations can be examined as a function of the simultaneity of the CARS-LDV measurements. This allows investigation of the autocorrelations between the temperature and velocity components. The reduced data can then be displayed as needed for study or presentation.

## RESULTS AND DISCUSSION

Figure 3 is an example of the measured joint velocity and temperature correlation coefficients, these coefficients being the normalized turbulent axial heat flux,  $u'T'$  and the radial heat flux,  $v'T'$ . In this experiment, a vee-gutter stabilized turbulent premixed flame was studied. The maximum values of the correlation coefficients for velocity and temperature are  $\sim 0.35$ . This strong correlation is due to the flame brushing, which is highly intermittent. From Fig. 3 the width of the flame brushing can be estimated to be  $\sim 6$  mm.

Bias sampling errors are not normally associated with CARS measurements; however, when joint measurements are made using Method 2 or Method 3, the sampling becomes dependent on the seed-particle arrival and biasing effects can be observed. The largest bias effect which has been observed with the combined instrument is the density bias or Favre-averaging<sup>4</sup> which occurs because of density weighting of the LDV measurement. The seed density, in general, follows the density of the gases in which the seed has been introduced; thus, as the gas temperature increases, the probability of catching a seed particle in the sample volume decreases. This effect can be observed by comparing CARS temperature PDFs obtained at the same point in a flame using independent CARS measurements and joint CARS-LDV measurements. The temperatures obtained in the joint measurements are lower than those measured by the independent CARS instrument.

## CONCLUSIONS

Successful integration of CARS and LDV systems into a second-generation combined instrument capable of simultaneous temperature and velocity measurement has been demonstrated. Improvements over previous versions include reduced measurement volume and more-efficient acquisition and analysis software and interface hardware which allows a higher volume of data to be taken in a shorter period of time. The capability to detect seed-bias effects has been demonstrated.

## ACKNOWLEDGEMENT

This effort was supported by USAF Contract Nos. F33615-85-C-2562 and F33615-87-C-2767.

## REFERENCES

1. L. P. Goss, D. D. Trump, W. F. Lynn, T. H. Chen, and W. J. Schmoll, "Second-Generation Combined CARS-LDV Instrument for Simultaneous Temperature and Velocity Measurements in Combusting Flows," Submitted for presentation at the Twenty-Second International Symposium on Combustion to be held in Seattle, Washington, August 14-19, 1988.
2. L. P. Goss, D. D. Trump, and W. M. Roquemore, "Simultaneous CARS and LDV Measurements in a Turbulent Flame," AIAA 84-1458.
3. A. Lightman, R. D. Magill, and R. J. Anderson, "Laser Diagnostic Development and Measurement and Modeling of Turbulent Flowfields of Jets and Wakes. Part 1," AFWAL-TR-83-2044 (Air Force Wright Aeronautical Laboratories, Wright-Patterson Air Force Base, OH, 1983).
4. L. P. Goss, D. D. Trump, and W. M. Roquemore, "Combined CARS/LDA Instrument for Simultaneous Temperature and Velocity Measurements," *Exp. Fluids* 6, 189 (1988).

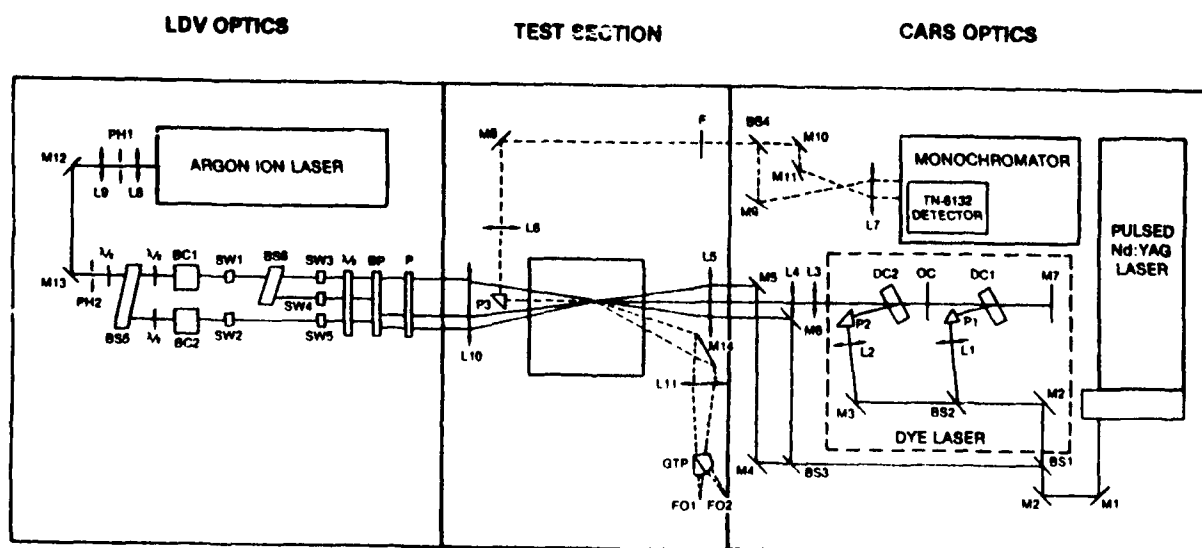


Figure 1. Optical Arrangement of Combined CARS-LDV Instrument.

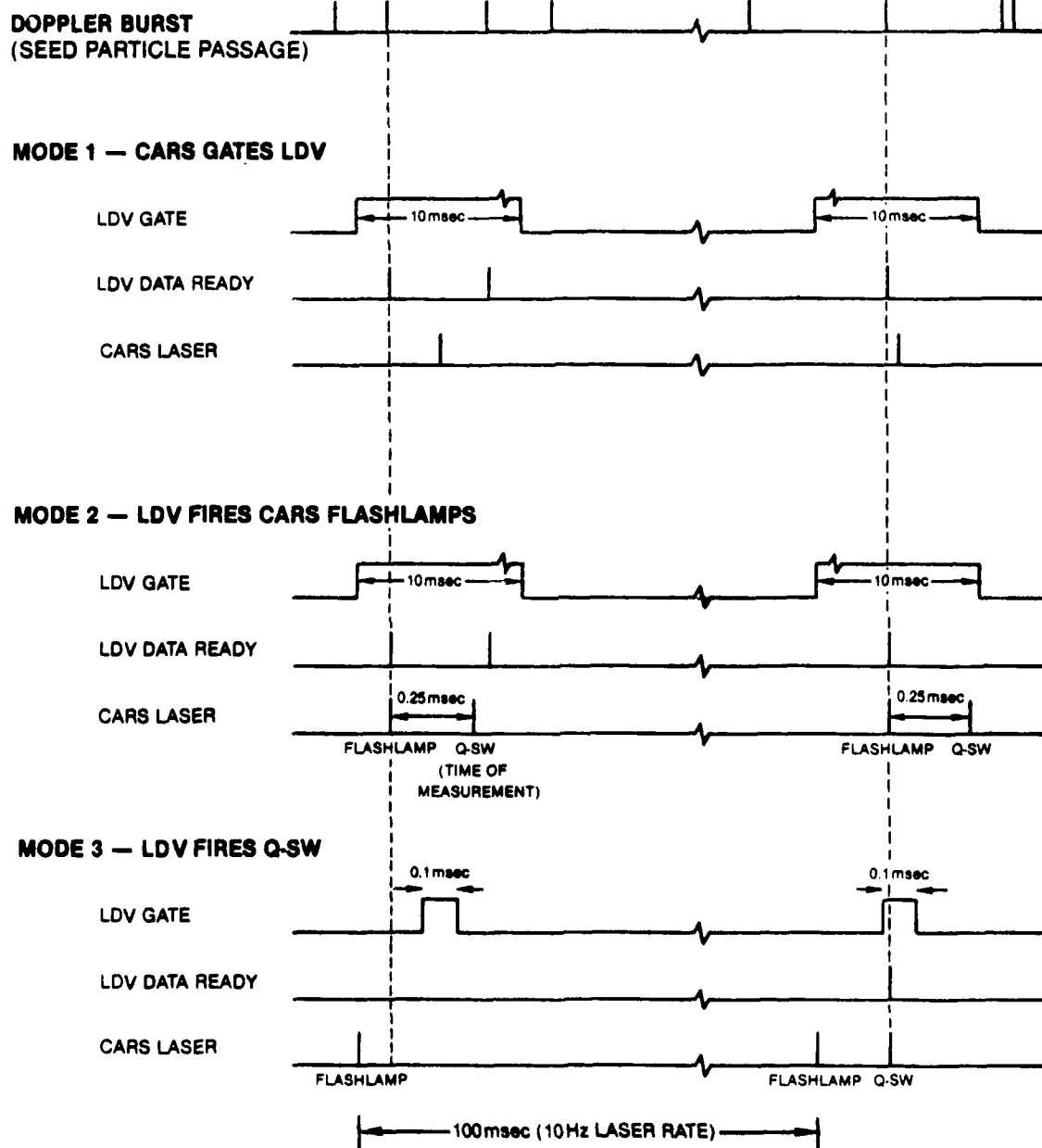


Figure 2. Timing Diagram for Three Acquisition Modes of Combined CARS-LDV Instrument.

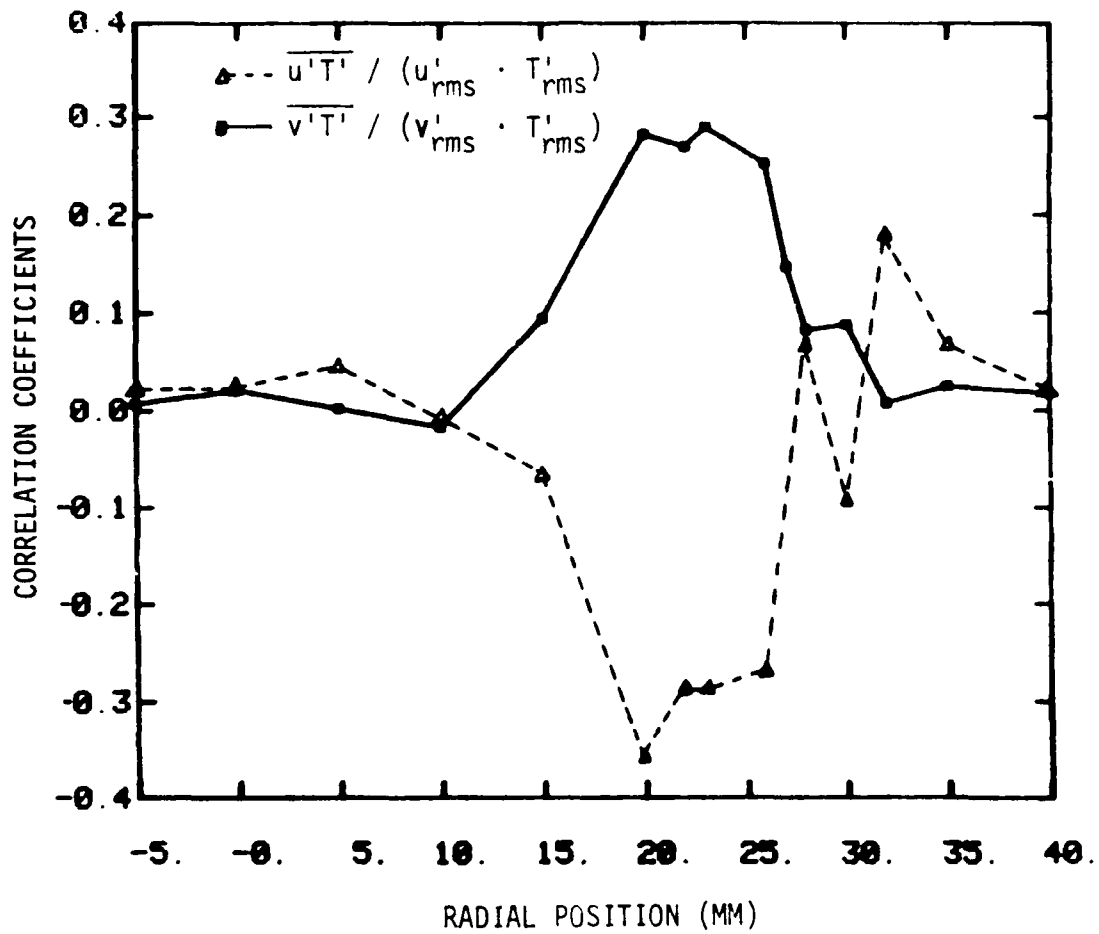


Figure 3. Measured Correlation Coefficients for Temperature and Velocities. Radial scans at Z = 40 mm.

# Second-generation combined CARS-LDV instrument for simultaneous temperature and velocity measurements in combusting flows

L. P. Goss, D. D. Trump, W. F. Lynn, and T. H. Chen

*Systems Research Laboratories, A Division of Arvin/Calspan, Dayton, Ohio 45440-3696*

W. J. Schmoll

*The University of Dayton, Dayton, Ohio 45469*

W. M. Roquemore

*Air Force Wright Aeronautical Laboratories, Aero Propulsion Laboratory (AFWAL/POSF), Wright-Patterson Air Force Base, Ohio 45433-6563*

(Received 26 September 1988; accepted for publication 7 November 1988)

This article describes the design and operation of a second-generation combined CARS-LDV instrument capable of measuring temperature and two velocity components in a turbulent combusting flowfield. Improvements to the instrument over the first-generation system include multiple acquisition modes ranging from independent to 4- $\mu$ s time coincidence, more extensive automation of the data acquisition and burner controls, and improved procedures for analysis and display of raw data. Measurements made on a propane-air diffusion flame are discussed.

## INTRODUCTION

Computer models, which are being used to predict flowfield behavior in practical combustor systems, require simultaneous measurement of temperature and velocity. Numerical solution of the conservation equations of mass, momentum, species, and energy requires a detailed knowledge of velocity-temperature correlation terms such as  $\overline{uT}$ ,  $\overline{vT}$ ,  $\overline{uc}$ . Practices such as the use of gradient transport closure to describe transport terms can promote gross inaccuracies in prediction of flows, especially those dominated by large-scale turbulence and where counter-gradient diffusion is known to occur. In such cases, the magnitude of these terms must be measured experimentally.

The simultaneous measurement of velocity and scalar quantities is a difficult task, and only a limited number of these experiments have been reported in the literature.<sup>1-16</sup> In combusting-flowfield studies, the technique of choice for velocity measurements has been laser Doppler velocimetry (LDV). The choice of instrument for the associated scalar measurement, however, has not been so clear-cut. Techniques which have been employed include thermocouples,<sup>1-6</sup> Mie scattering,<sup>7</sup> Rayleigh scattering,<sup>8</sup> Raman scattering,<sup>9-11</sup> and coherent anti-Stokes Raman scattering (CARS).<sup>12-16</sup> The advantages of using the CARS technique for joint scalar measurements are the demonstrated ability of the technique to obtain temperatures in diverse flame environments, the nonintrusive nature of the technique, and the ability to examine the effects of seed biasing. The last advantage is quite significant in demonstrating the density-weighted bias error which occurs with LDV measurements. The disadvantages associated with this technique involve its cost and complexity and the expertise required to operate a CARS instrument.

The second-generation combined CARS-LDV instrument described in this article was built especially for making

simultaneous measurements in diverse combusting flowfields; it is an extension of an earlier combined instrument which was described in detail in Refs. 14-16. Improvements to the acquisition software and electronics will be discussed along with measurements on a propane jet diffusion flame.

## I. CARS INSTRUMENT

Since the basic CARS instrument as shown in Figs. 1 and 2 has been discussed previously, only the salient features will be mentioned here. The frequency-doubled output from a Quanta-Ray DCR-2 Nd:YAG laser was used to pump a broadband dye laser and was also utilized as the pump frequency in the CARS process. Maximum spatial resolution with a 50-cm-focal-length lens was achieved through use of a folded BOXCARS arrangement. The spatial resolution was measured by traversing a small 200- $\mu$ m CO<sub>2</sub> jet across the sample volume and found to be  $\sim 1$  mm along the major beam axis. The CARS signal from the sample volume was fed through a splitter arrangement which divided it in a 33 to 1 ratio and sent it through a Spex  $\frac{3}{4}$ -m monochromator, where it was detected by a Tracor-Northern IDARSS detector system. The splitter arrangement is used to extend the dynamic range of the detector, which allows the temperature range of 300-2300 K to be studied. The CARS system typically displays an 80-K precision for repeated single-shot temperature measurements and a 10-K accuracy in time-averaged measurements as compared to chromel-alumel thermocouples in oven studies.<sup>14</sup>

## II. LDV INSTRUMENT

The LDV system shown in Figs. 1 and 2 was built by Lightman, *et al.*,<sup>17,18</sup> and is a two-component real-fringe system based on polarization separation of the velocity compo-

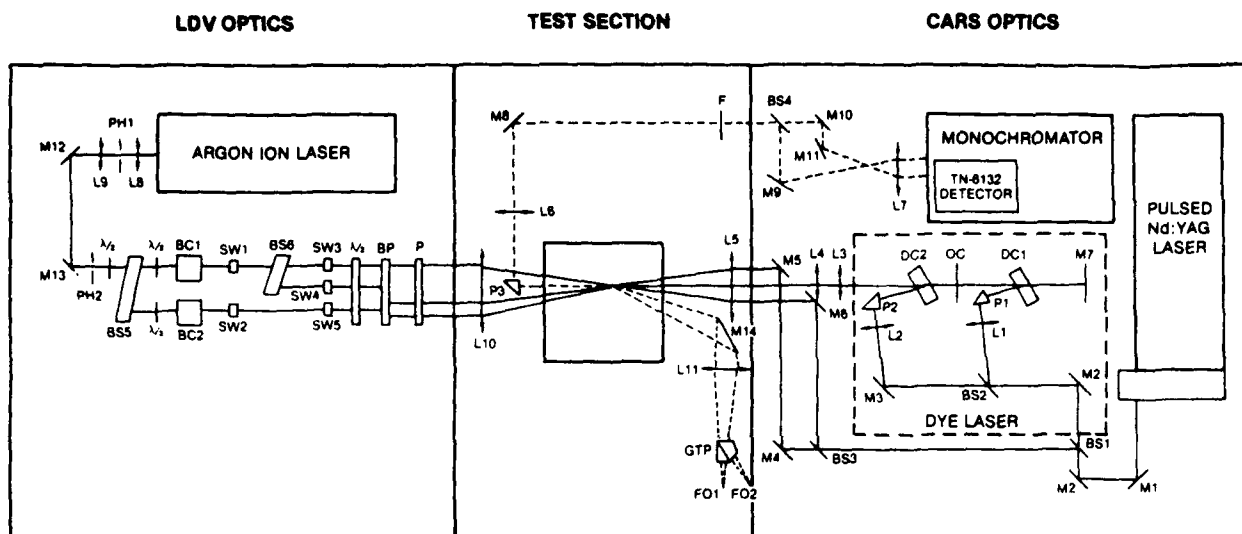


FIG. 1. Optical arrangement of combined CARS-LDV instruments. Optics include: CARS: M1, M2, M3, M4, M5, M6:  $R_{max}$  532-nm mirrors; BS1, BS3: 50% 532-nm beam splitters; BS2: 30% 532-nm beam splitter; M7:  $R_{max}$  607-nm mirror; OC: output coupler 20% 607-nm mirror; L1, L2: 30-cm lens; L3, L4: 10-cm, 20-cm lens (Dye Telescope); P1, P2, P3: right-angle prisms; L5, L6: 50-cm lens; M8, M9, M10, M11: broadband mirrors; F: 532-nm blocking filter; BS4: 3% beam splitter; L7: 10-cm cylindrical lens. LDV: L8, L9: 5-cm lens; PH1, PH2: 100- $\mu$  pinholes; M12, M13:  $R_{max}$  514.5 nm; BS5, BS6: 50% beam splitters;  $\lambda/2$ : half-wave plates; BC1, BC2: 35, 40-MHz Bragg cells; SW1, SW2, SW3, SW4, SW5: stirring wedges; BP: beam positioning prisms; P: periscope; L10: 50-cm focusing lens; M14: collection mirror; L11: 20-cm collection lens; GTP: Glan-Thompson prism; FO1, FO2: fiber-optic cables.

nents. The 514.5-nm line from a Spectra-Physics argon-ion laser was used as the light source, with  $\sim 1\text{-}\mu\text{m}$ -diam alumina ( $\text{Al}_2\text{O}_3$ ) particles serving as the scattering medium. The Doppler burst was collected in the forward direction

slightly off-axis ( $\sim 10^\circ$ ). The two velocity components were separated by a Glan-Thompson polarization beam splitter and sent to two 1990 TSI Burst-Counter Processors through fiber optics. Dual Bragg cells having a 5-MHz frequency

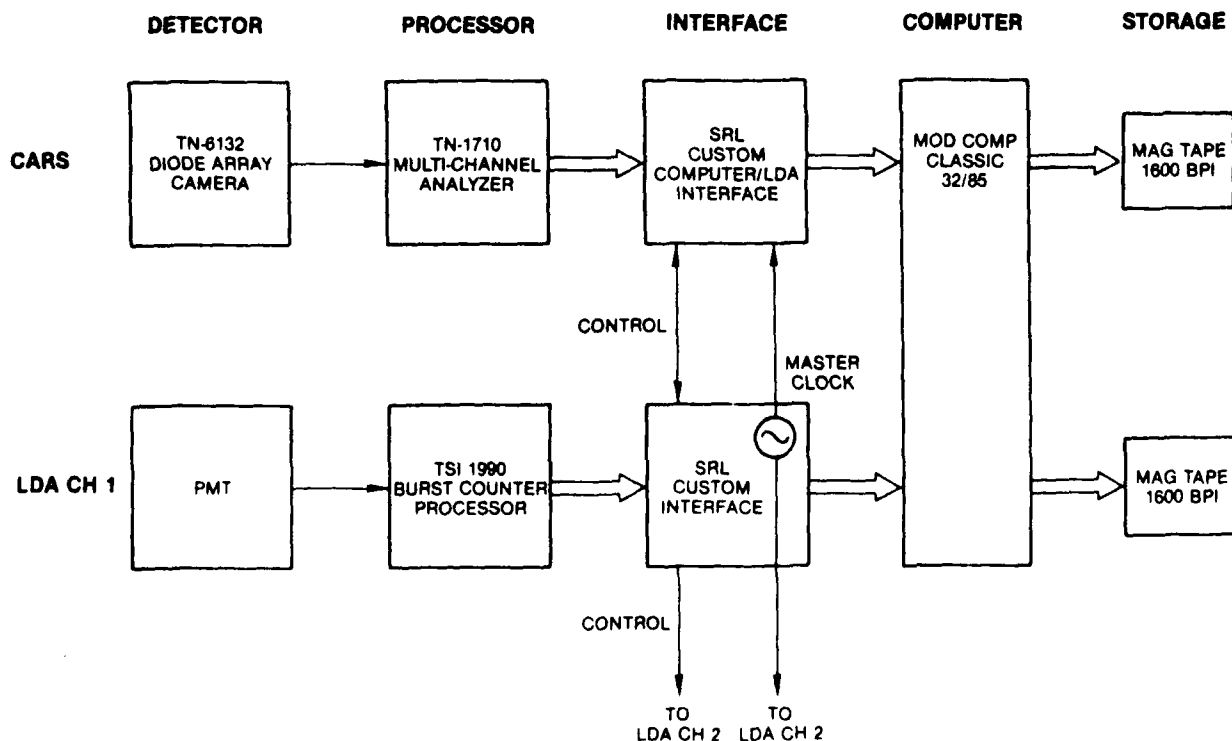


FIG. 2. Schematic diagram of data-acquisition components of CARS and LDV instruments. Electronics include: CARS: TN 6132 camera; Tracor-Northern TN1710 multichannel analyzer; Custom-built Computer/LDV interface; ModComp 32/85 classic computer. LDV: Photomultiplier; TSI 1990 burst counter processors; Custom-built LDV interface; ModComp computer.

difference were employed to remove directional ambiguities and maintain the Doppler burst frequencies in an optimum range for the velocities under study.

### III. COMBINED CARS-LDV INSTRUMENT

As with the first-generation combined instrument reported previously,<sup>14-16</sup> this second-generation combined instrument was arranged in such a way as to minimize changes to the optical systems. The two instruments are aligned head-on and have no common optics, which allows them to be operated separately or jointly without interference. The major changes with this second-generation instrument have involved the electronics and acquisition software. To understand these differences a discussion of the basic philosophy of the instruments is in order.

Basic operation of the CARS instrument involves repetitive firing of the Nd:YAG laser at a 10-Hz rate; spectral-temperature information is obtained during each laser shot. The basic operation of the LDV instrument involves measuring the Doppler burst from a seed particle as it traverses the sample volume. The passage of the seed particle is a near-random event and depends on the seeding as well as the flow conditions of the study. The CARS measurements take place at 100-ms intervals. The problem lies in synchronizing a random and a repetitive event. To understand the magnitude of this problem, one must examine the firing sequence of the Nd:YAG laser, as shown in Fig. 3. The firing sequence consists of discharging the flashlamps to obtain a population inversion and then pulsing the Q-switch to depopulate the upper laser levels, which provides a giant laser pulse. The time separation between the flashlamp discharge and the Q-switch firing is  $\sim 250 \mu\text{s}$ . The Q-switch firing can be varied by  $\sim \pm 50 \mu\text{s}$  about the 250- $\mu\text{s}$  value, with a loss of  $\sim 25\%$  power. However, because of thermal loading, the Nd:YAG laser must be fired at a repetition rate of 8–14 Hz to prevent power loss. The Nd:YAG laser is, thus, not a pulse-on-demand laser. Therefore, three different schemes were incorporated into the second-generation combined CARS-LDV instrument to allow simultaneous measurements.

The simplest approach (Method 1) consists of letting the two instruments free-run. In order to establish time coincidence, a common clock is used for the instruments; when a measurement is made, the data are tagged with the time. Analysis software is then employed to sort the independent data according to time based on the tagword. This approach allows the two instruments to acquire data independently, each at its maximum rate. The disadvantage of this method is that the LDV instrument acquires data at a much higher rate than the 10-Hz CARS system and, therefore, much of the LDV data are not sufficiently close in time to a CARS

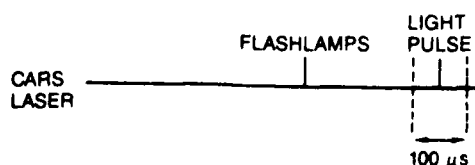


FIG. 3. Firing sequence of Nd:YAG laser used in CARS system.

event to be considered as coincident data. To circumvent this drawback, a 10-ms gate was incorporated to window the LDV data acquisition about the CARS laser firing. This gate opens  $\sim 5$  ms before the flashlamps are discharged and remains open  $\sim 5$  ms after the laser fires. The Nd:YAG laser is fired even if no LDV realization has occurred in the gate. The sole purpose of the gate is to limit the LDV acquisition to a certain time period about the CARS event.

The second approach (Method 2) involves a deeper level of interaction between the two instruments and, thus, is more complicated than Method 1. In Method 2 the LDV data acquisition is inhibited until the CARS flashlamp is ready to fire, as in Method 1. A 10-ms gate is opened about the flashlamp firing, and LDV realizations can be transferred only during this gate. If a velocity realization occurs, the flashlamps are discharged; 250  $\mu\text{s}$  later, the Q-switch fires. This guarantees at least one simultaneous measurement with a time coincidence of 250  $\mu\text{s}$ . If no LDV realization occurs, the flashlamps are discharged at the end of the window but—unlike in Method 1—the Q-switch is not fired. Discharging the flashlamps guarantees that the thermal loading of the laser cavity (and, thus, power level) will be maintained. All LDV realizations are collected during this 10-ms window to permit examination of all time coincidences. This method allows for a moderate time coincidence with the maximum data rates for both instruments and is best suited for low- to moderate-velocity flow studies.

Method 3 is the most stringent method, both in terms of time coincidence and simultaneous data rates. In this approach the LDV is gated as in Method 2, with the exception that the gate is only 100  $\mu\text{s}$  wide and centered on the optimum 250- $\mu\text{s}$  delay between the flashlamp and the Q-switch firing. The flashlamps are discharged repeatedly and the narrow 100- $\mu\text{s}$  gate opened after each discharge. Any LDV realization occurring within this gate will fire the Q switch and allow the CARS measurement to be made. The coincidence time in this case is the time required by the TSI processors to process the Doppler burst and transmit a data-ready signal to the Tracor interface electronics, which fires the Q switch. This entire process occurs in  $\sim 4 \mu\text{s}$ . Thus, Method 3 provides the best possible simultaneous measurement times and is well suited for moderate- to high-velocity flow studies. These advantages are not gained without sacrifice, however. The price paid for the improved time coincidence is a decrease in the repetition rate. The CARS laser fires with a 10-Hz rate; during each pulse a 100- $\mu\text{s}$  gate is opened for LDV realizations. Thus, the LDV system is allowed to store data only over a 1-ms period per second. Data-acquisition rates are, thus, reduced by a factor of 100 as compared to those of Methods 1 and 2. Method 3 is, therefore, recommended only for those studies where the flow rates preclude use of Methods 1 and 2.

In the previous CARS-LDV instrument, the electronics were constructed such that Method 3 was used primarily for data acquisition. This meant very long acquisition times, especially in low-velocity flow experiments. The second-generation system allows the operator to choose any one of the three methods at the CARS control console by loading an appropriate program from disk. In all three methods, the

time tagword is stored along with the data during acquisition. After conversion of the raw LDV period data to velocities and the CARS spectral data to temperatures, the processed data are sorted according to the time tagword. The analysis software sorts the data about a time window that is selected by the operator and allows correlation of velocity and temperature to be studied as a function of this coincidence window. Correlations such as  $\overline{uT}$ ,  $\overline{vT}$ , and  $\overline{uv}$  can then be determined for the flowfield under study.

Experimentally, the measurements must be not only temporally coincident but also spatially coincident. To align the six beams at a common focus, a 100- $\mu\text{m}$  circular aperture was used. The focus of each set of beams was determined first by examining the extinction of the beam by the edge of the aperture, which acted as a knife edge. The power in the CARS laser was reduced over the normal operational power by detuning the Q-switch from the optimum delay, thus maintaining the thermal loading and divergence of the Nd:YAG beams while lowering the laser power. The main focusing lens of both the CARS and the LDV system was adjusted to ensure that the focus occurred at a common

point. All six beams were then crossed and aligned through the 100- $\mu\text{m}$  aperture. Once this alignment is complete, the system must not be adjusted because of the possibility of uncrossing the two sample volumes.

One of the major disadvantages of combining the CARS and LDV instruments lies in the use of seed particles for the velocity measurement. Seeds such as alumina can affect the CARS data in many ways, including attenuation of the laser beams (and, thus, lowering of the CARS signal), production of a nonresonant signal whose contribution would increase the fitted temperature, or—in the worst case—catastrophic breakdown at the surface of the particle. Catastrophic breakdown occurs when a particle of sufficient size passes through the sample volume during Nd:YAG laser firing. The surface temperature of the particle is heated to an extreme temperature, and a plasma is formed. The plasma then acts to absorb the pump laser light, thus robbing the CARS process of needed power. The probability of breakdown occurring is dependent upon the particle size and the power in the laser beams. To minimize this effect, the smallest possible seed particles and the lowest laser power should be used. The

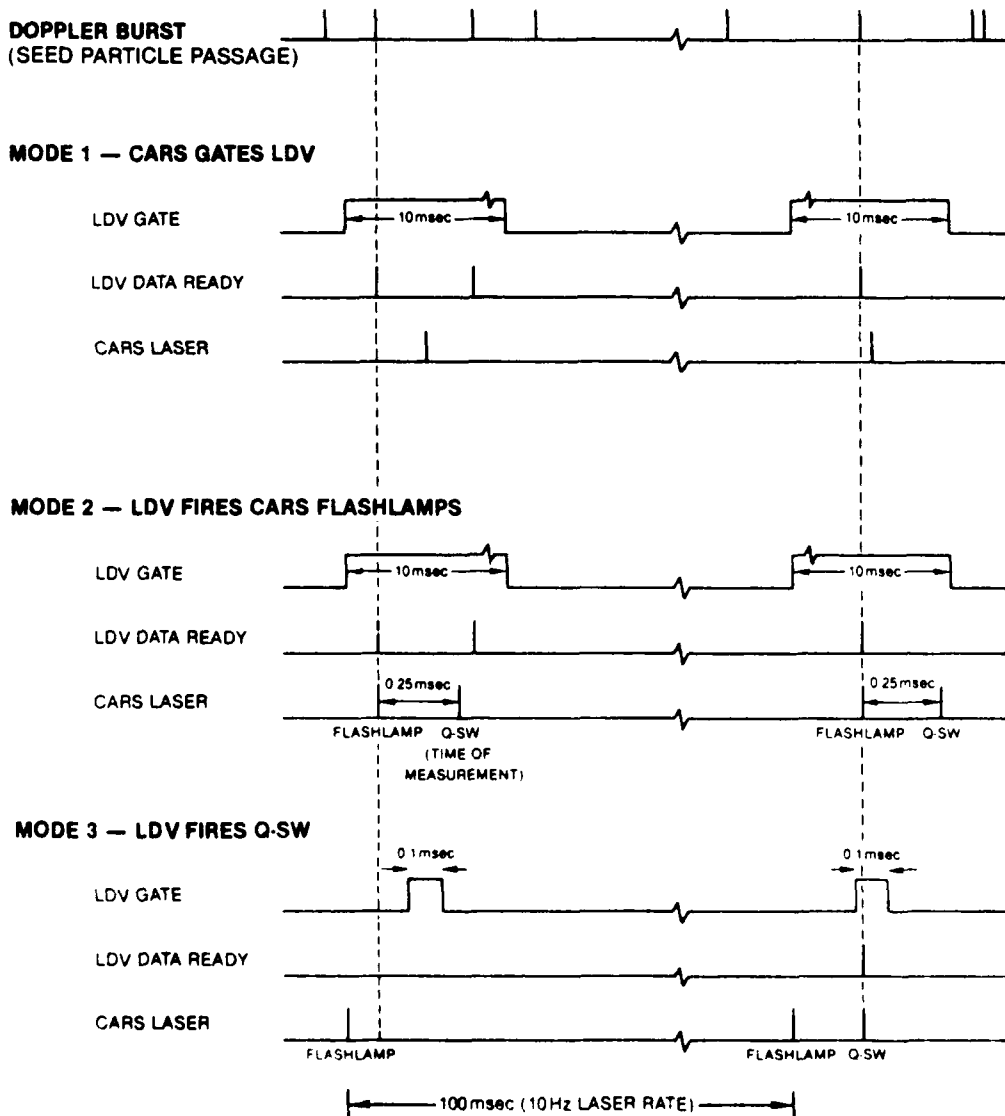


FIG. 4. Timing diagram for three acquisition modes of combined CARS-LDV instrument. Mode 1 LDV—data is windowed about CARS event with large 10-ms window. Both systems are essentially independent. Mode 2—LDV is windowed with 10-ms window, and CARS flashlamp fires if LDV realization occurs within window. Maximum time coincidence is 250  $\mu\text{s}$ . Mode 3—CARS flashlamp is fired independent of LDV. 100- $\mu\text{s}$  window is open about optimum delay for Q-switch. If LDV realization occurs, then fire Q-switch. Maximum time coincidence is 4  $\mu\text{s}$ .

effect is most notable inside a cold fuel jet where the seed and gas densities are relatively large. When breakdown occurs, the CARS data are rejected and excluded from the analysis. This is accomplished by monitoring the amount of scattered laser light around the sample volume. If the scattered-light level reaches a preset threshold, then a breakdown is known to have occurred and the data are rejected.

#### IV. ACQUISITION AND ANALYSIS SOFTWARE

The past and present approaches to mating the CARS and LDV instruments involved combining the instruments both optically and electronically, such that a minimum number of changes would be required. The optical arrangement of the second-generation CARS-LDV system shown in Fig. 1 confirms this. However, extensive changes were required in the interface electronics and acquisition software in order to incorporate the various acquisition methods outlined above (see Fig. 2). The heart of the acquisition software is a machine-language program which runs on the Tracor-Northern control unit; the function of this program is to control the transfer of CARS spectral data to a ModComp Classic minicomputer system, the firing sequence for the Nd:YAG laser, and the necessary gating pulses to the LDV interfaces based upon the particular acquisition mode selected.

The timing schemes for the three acquisition modes are shown in Fig. 4. When the program is initiated, the system is in the independent acquisition mode, which allows the operator to observe the CARS signal strength and determine whether optical adjustments must be made. By loading a different program, the operator can select the acquisition

mode to be employed. The acquisition software is similar for the three modes. The program begins by opening a 10-ms gate to allow LDV data acquisition, waiting 5 ms to discharge the flashlamps, waiting another 250  $\mu$ s to fire the Q-switch, and then interrogating the ModComp interface to determine whether a data-transfer request has been issued. The gate to the LDV is open for 10 ms. If the data-transfer request from the ModComp has been issued, the CARS spectral data are transferred in  $\sim$ 45 ms. The program must then wait another 55 ms before repeating the sequence. If no data-transfer request has been sent, the Tracor waits the full 100 ms by counting to itself. The last word in the CARS data is overwritten with the contents of the common clock (time tagword) before transfer. This basically describes the independent operation of the system.

In Method 2 the machine-language program opens the 10-ms window and waits for a velocity data-ready signal from the LDV burst-counter processors. If the signal is detected, the flashlamps are discharged and 250  $\mu$ s later the Q-switch fires. The CARS spectral information is then transferred to the ModComp computer. If a velocity data-ready signal has not been detected at the end of the 10-ms window, the flashlamps are discharged but the Q-switch does not fire and CARS data are not transferred. In either case, the program waits another 90 ms, and the cycle is repeated.

In Method 3 the machine-language program discharges the flashlamps, waits 200  $\mu$ s, and then opens a 100- $\mu$ s gate. If a velocity data-ready signal is detected during this gate, the Q-switch is fired and the data subsequently transferred to the ModComp computer. If no data-ready signal is detected, the program counts to itself for  $\sim$ 99 ms and the process is repeated.

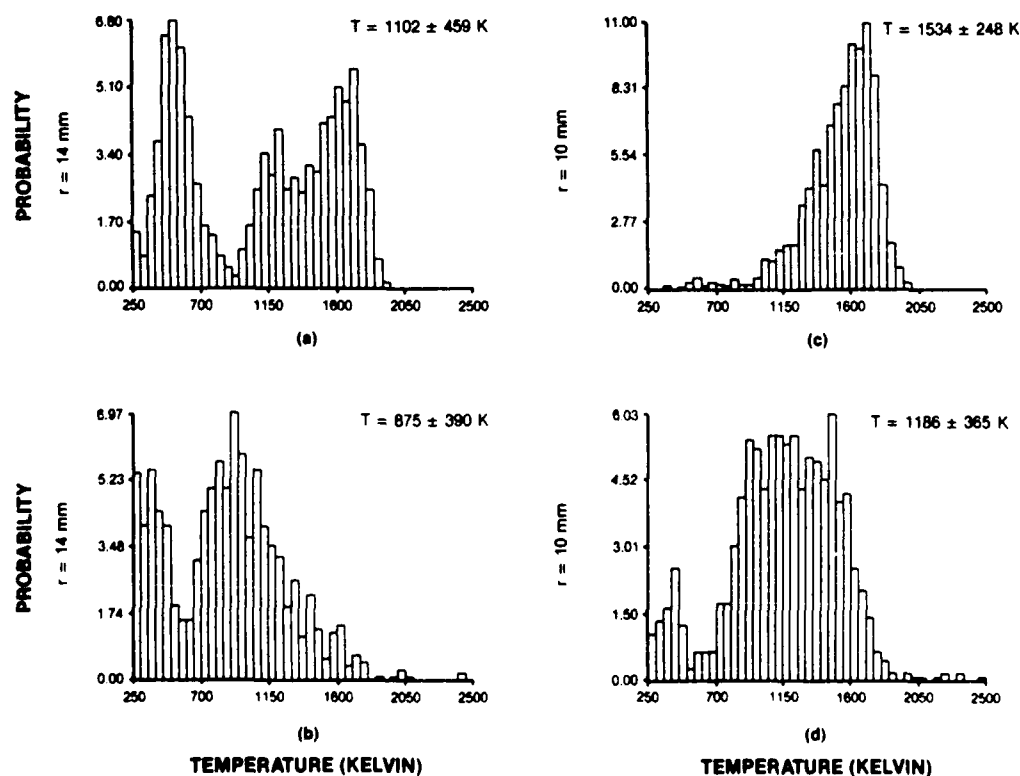


FIG. 5. Temperature pdfs obtained in propane jet diffusion flame at 200-mm axial location, independent of LDV (a, c) and simultaneous with LDV (b, d). Density-weighted biasing of temperature is observed when CARS and LDV measurements are made simultaneously, as witnessed by lower average temperatures at same flame positions.

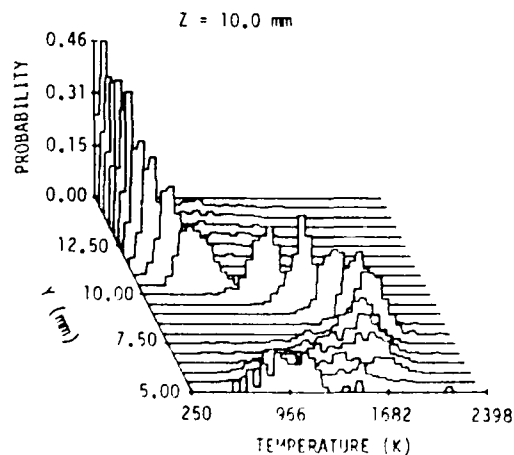
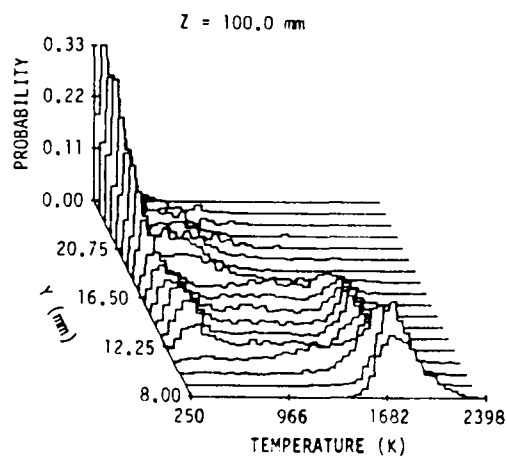
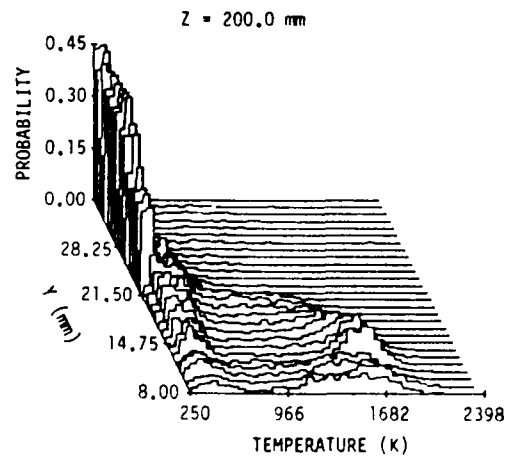
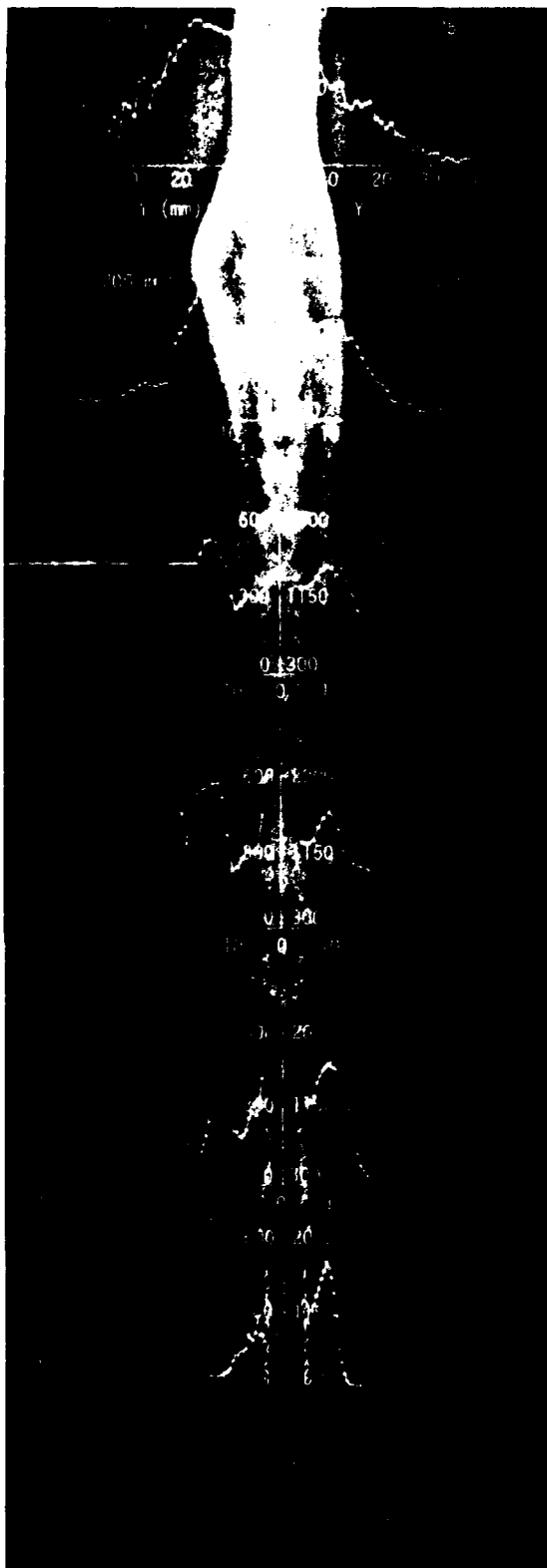


FIG. 6. Mean, rms, and pdf temperatures in propane jet diffusion flame ( $Re = 4000$ ) obtained by CARS instrument

The acquisition software on the ModComp computer for the CARS and LDV is similar and controls the positioning of the burner system, the number of spatial locations at which data are to be taken, and the number of data points to

be acquired at each location. The interface control is mainly carried out by the Tracor-Northern program, but analysis of the raw spectral and period data is conducted exclusively on the ModComp computer.

The first steps in processing the raw data consist of fitting the CARS spectral data to obtain temperatures and converting the period data from the TSI 1990 burst counters into velocities. The time tagword associated with each data point is then extracted and the data sorted according to time. Once these tasks have been accomplished, the means, rms, and correlations between temperature and velocity components can be determined. By recording the time associated with each measurement, the simultaneous data can be examined as a function of the coincidence time of the CARS-LDV measurements. This allows investigation of the autocorrelations between the temperature and the velocity components. The reduced data can then be displayed as needed for study and presentation.

## V. BIAS ERRORS

Bias sampling errors are not normally associated with the CARS technique because the measurements are made in a low-frequency repetitive manner. Such an ensemble measurement should not be biased except in the case where the frequency matches a natural frequency of the flame. When the CARS technique is combined with the LDV technique, however, the sampling becomes dependent upon the seed-particle arrival, and biasing effects can be observed. The largest bias effect which has been observed with the combined instrument is the density bias or Favre-averaging, which occurs because of density weighting of the LDV measurement. The seed density, in general, follows the density of the gases in which the seed has been introduced; thus, as the gas temperature increases, the probability of catching a seed particle in the sample volume decreases. This result (shown in Fig. 5) indicates that the simultaneous measurements are Favre-averaged—a factor which must be taken into account when interpreting the data. Bias errors due to seed effects other than density biasing may also be present in the simultaneous data; therefore, care must be taken in the use and interpretation of these data. One of the unique features of the combined CARS-LDV instrument is its ability to determine the extent of biasing; this is possible because the independent CARS measurements are unbiased. This feature allows Favre-weighted data to be converted to Reynolds-averaged data.<sup>16</sup>

## VI. BURNER DESCRIPTION

The burner setup used for these studies is discussed in detail in Ref. 19. The system consisted of a contoured 1-cm fuel jet surrounded by a 24-cm coannular air jet. The fuel employed was propane at a flow rate of 8.5 standard liters per minute. The velocity of the coannular air jet was 15 cm/s, which was sufficient to reduce room-air disturbances but have little effect upon the visible flame structure.

## VII. PROPANE-DIFFUSION-FLAME MEASUREMENTS

To demonstrate the capabilities of the combined instrument and to complement earlier CARS studies, a propane jet diffusion flame was chosen for examination. Flow-visualization studies on this flame have indicated the presence of large

toroidal vortices which form outside the visible flame zone.<sup>19</sup> These vortices interact with the flame and are responsible for low-frequency oscillations or flame flicker. The vortices are believed to be the result of a Kelvin-Helmholtz-type instability which is formed by a buoyancy-driven shear layer. A sheet-lighting visualization photograph of the jet diffusion flame is shown in Fig. 6. Superimposed on this figure are the results of independent CARS measurements. The interaction between the outside vortices and the flame surface is evident. Figure 6 displays bimodal temperature probability distribution function (pdf) in the areas associated with the flame bulge. The temperature pdf's can be interpreted as that fraction of time during which the flame zone is located in the sample volume. The bimodal behavior is typical of a flame surface which is oscillating as a function of time. The oscillations are evident in the temperature rms data as well.

Simultaneous CARS and LDV measurements were taken at the 200-mm axial location because of the presence of the flame bulge in this area. The  $\overline{uT}$ ,  $\overline{vT}$ , and  $\overline{uv}$  correlations are depicted in Fig. 7. The  $\overline{uT}$  data show a strong correlation between axial velocity and temperature in the flame-bulge area associated with the acceleration of the flame front due to buoyancy. This large positive  $\overline{uT}$  correlation is expected in a flowfield dominated by buoyancy. The Reynolds shear stress  $\overline{uv}$  displays similar behavior, indicating the strong interaction between the outer vortices and the flame. The  $\overline{vT}$  correlation is lower in magnitude but peaks in the bulge-vortices region. Thus, the dominance of the buoyancy effect in relatively low Reynolds-number jet diffusion flames can be clearly seen from the visualization, independent temperature pdf, and simultaneous data.

The combined CARS-LDV instrument has been utilized in the study of not only the propane jet diffusion flame<sup>20</sup> but also a rod-stabilized jet diffusion flame<sup>21</sup> and a premixed vee-gutter flame.<sup>22</sup>

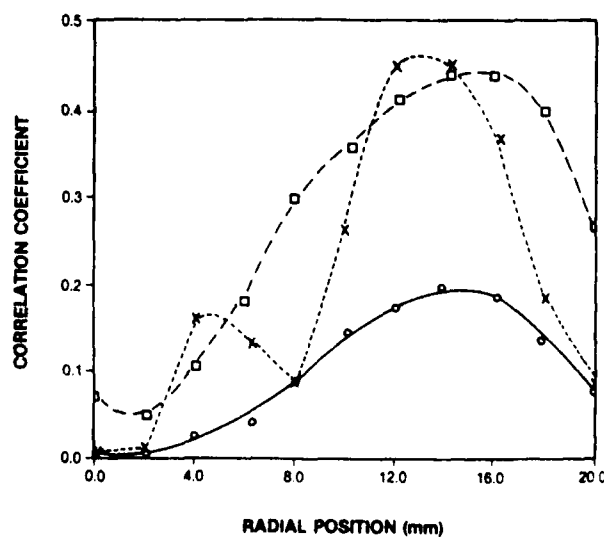


FIG. 7. Correlation coefficients obtained at 200-mm axial location in propane jet diffusion flame.  $\square$ :  $\overline{uT}$ ,  $\circ$ :  $\overline{vT}$ , and  $\times$ :  $\overline{uv}$ .

## VIII. DISCUSSION

In conclusion, a second-generation CARS-LDV instrument has been built and operated which allows simultaneous temperature and velocity measurements to be made. The instrument is capable of independent or combined measurements with a time coincidence of  $\sim 4 \mu\text{s}$ . The acquisition and analysis software for this instrument has been improved over that of previous versions, allowing a single operator to control both instruments. A unique feature of the combined instrument is that bias errors due to the use of seeds can be evaluated. The combined measurements were determined to be Favre-averaged due to the heavy density weighting of the LDV measurements.

- <sup>1</sup>I. G. Shepherd, and J. M. Moss, *Comb. Sci. Technol.* **25**, 127 (1981).
- <sup>2</sup>I. G. Shepherd, J. M. Moss, and K. N. C. Bray, *Nineteenth Symposium (International) on Combustion* (The Combustion Institute, Pittsburgh, PA, 1982), p. 423.
- <sup>3</sup>H. Tanaka and T. Yanagi, *Comb. Flame* **51**, 183 (1983).
- <sup>4</sup>T. Yanagi and Y. Mimura, *Eighteenth Symposium (International) on Combustion* (The Combustion Institute, Pittsburgh, PA, 1981), p. 1031.
- <sup>5</sup>M. V. Heitor, A. M. K. P. Taylor, and J. H. Whitelaw, *Experimental Measurements and Techniques in Turbulent Reactive and Non-Reactive Flows*, edited by R. M. C. So, J. H. Whitelaw, and M. Lapp (The American Society of Mechanical Engineers, New York, 1984), p. 243.
- <sup>6</sup>R. D. Brum, E. T. Seiler, J. C. LaRue, and G. S. Samuelsen, *Instantaneous Two-Component Laser Anemometry and Temperature Measurements in a Complex Flow Model Combustor*, AIAA-83-0334.
- <sup>7</sup>S. H. Starmer and R. W. Bilger, *Eighteenth Symposium (International) on Combustion* (The Combustion Institute, Pittsburgh, PA, 1980), p. 921.
- <sup>8</sup>R. M. Dibble, G. D. Rambach, R. E. Hollenbach, and J. T. Ringland, "Simultaneous Measurements of Velocity and Temperature in Flames Using LDV and CW Laser Rayleigh Thermometry," Paper presented at the Fall Meeting of the Western States Section of the Combustion Institute, Tempe, AZ, October 1981.
- <sup>9</sup>S. Warshaw, M. Lapp, C. M. Penny, and M. C. Drake, *Laser Probes for Combustion Chemistry*, edited by D. R. Crosley (The American Chemical Society, Washington, DC, 1981), p. 239.
- <sup>10</sup>S. Lederman and C. Posillico, *AIAA J.* **19**, 824 (1981).
- <sup>11</sup>R. M. Dibble, W. Kollmann, and R. W. Schefer, *Comb. Flame* **55**, 307 (1984).
- <sup>12</sup>S. Fujii, M. Gomi, and K. Eguchi, *J. Fluids Eng.* **105**, 129 (1983).
- <sup>13</sup>S. Fujii, M. Gomi, K. Eguchi, S. Yamayuchi, and L. Jin, *Comb. Sci. Technol.* **36**, 211 (1984).
- <sup>14</sup>L. P. Goss, D. D. Trump, and W. M. Roquemore, "Simultaneous CARS and LDA Measurements in a Turbulent Flame," AIAA 84-1458.
- <sup>15</sup>L. P. Goss, D. D. Trump, and W. M. Roquemore, *Experimental Measurements and Techniques in Turbulent Reactive and Non-Reactive Flows*, edited by R. M. So, J. H. Whitelaw, and M. Lapp (The American Society of Mechanical Engineers, New York, 1984), p. 215.
- <sup>16</sup>L. P. Goss, D. D. Trump, and W. M. Roquemore, *Exp. Fluids* **6**, 89 (1988).
- <sup>17</sup>A. Lightman, R. D. Magill, and R. J. Anderson, *Laser Diagnostic Development and Measurement and Modeling of Turbulent Flowfields of Jets and Wakes, Part 1*, Air Force Wright Aeronautical Laboratories. AFWAL-TR-83-2044, 1983.
- <sup>18</sup>P. D. Magill, A. Lightman, C. E. Orr, R. P. Bradley, and W. M. Roquemore, "Simultaneous Velocity and Emission Measurements in a Bluff-Body Combustor," AIAA 82-0883.
- <sup>19</sup>W. M. Roquemore, L. D. Chen, L. P. Goss, and W. F. Lynn, "The Structure of Jet Diffusion Flames," Paper presented at the United States-France Joint Workshop on Turbulent Reactive Flows, Rouen, France, July 1987.
- <sup>20</sup>D. R. Ballal, T. H. Chen, W. J. Schmoll, L. P. Goss, and D. D. Trump, "Measurements of Joint PDFs and Scalar Fluxes in a Turbulent Flame Using an Integrated CARS-LDA System," Paper presented at the 1987 Spring Technical Meeting of the Central States Section of The Combustion Institute, Argonne, IL, May 1987.
- <sup>21</sup>D. R. Ballal, T. H. Chen, W. J. Schmoll, and D. D. Trump, "Experiments on a Rod-Stabilized Turbulent Jet Diffusion Flame," Paper presented at the Fall Meeting of the Eastern States Section of the Combustion Institute, Gaithersburg, MD, November 1987.
- <sup>22</sup>T. H. Chen, W. J. Schmoll, L. P. Goss, and D. D. Trump, "Studies of Turbulent, Premixed Conical Flame Using CARS-LDA Techniques," AIAA-88-3194. Accepted for publication in *J. Propul. Power*.

## 2.3 THIN-FILAMENT PYROMETRY

A complete study of turbulent flames requires the use of diagnostic techniques which are capable of measurement rates in excess of the change in the scalar properties being measured. Nonintrusive techniques, in general, are not capable of such high measurement rates (in excess of 5 kHz). However, one method which has been developed and applied successfully for this purpose is thin-filament pyrometry (TFP). This technique relies upon the blackbody emission of a thin ceramic filament for measurement of the temperature distribution in a flame. High-repetition thermometry is possible because of the small size, low thermal conductivity, and high emissivity of the filaments.

The groundwork for the TFP technique evolved from studies with a blackbody fiber-optic probe which was developed and evaluated by SRL's Optical Diagnostics Group. U. S. Patent No. 4,679,934 was awarded for the design of this probe, and a copy of the patent is included in this section (see p. 73). One of the major drawbacks of the fiber-optic probe for high-speed thermometry is the large thermal mass of the probe. This mass reduces the frequency response of the probe and requires that some form of compensation be used to achieve moderate-speed thermometry. If the mass of the probe could be reduced, an attendant reduction in the natural response time of the probe would result. Finally, it was realized that if small ceramic filaments (~ 15  $\mu\text{m}$ ) were utilized as the probe, natural response times in excess of 700 Hz would result.

The development and evaluation of the TFP technique as a thermometric probe for combustion studies was discussed in several articles. The first entitled, "Evaluation of Optical Diagnostic Techniques for High-Frequency Temperature Measurements," was presented at the 1987 Spring Technical Meeting of the Central States Section of the Combustion Institute (see p. 84). A second article entitled, "Spatial Temperature-Profile Measurements by the Thin-Filament-Pyrometry Technique," appeared in *Optics Letters* (see p. 89). A third which discussed a steady-state thermal model of the filament entitled, "SiC-Based Thin-Filament Pyrometry: Theory and Thermal Properties," was presented at the 22nd Symposium (International) on Combustion (see p. 92). A fourth paper entitled, "Thin-Filament Pyrometry: A Novel Thermometric Technique for Combusting Flows," appeared in the *Journal of Engineering for Gas Turbines and Power* (see p. 100). A fifth entitled, "Turbulent Flame Visualization Using Thin-Filament Pyrometry at High Sampling Rates," was presented at the 1989 Winter

Annual Meeting of the ASME (see p. 109). Finally, a time-dependent thermal model of the filament was developed and discussed in the paper, "Optical Diagnostics for Reacting and Non-Reacting Flows: Recent Developments and Results," which was presented at the 28th Aerospace Sciences Meeting (see p. 37).

[54] **FIBER OPTIC PYROMETRY WITH LARGE DYNAMIC RANGE**

[75] **Inventors:** Blawa Ganguly, Beavercreek; Larry P. Goas, Dayton; William M. Roquemore, Dayton; Darryl D. Trump, Dayton, all of Ohio

[73] **Assignee:** The United States of America as represented by the Secretary of the Air Force, Washington, D.C.

[21] **Appl. No.:** 763,575

[22] **Filed:** Aug. 8, 1985

[51] **Int. Cl.:** G01J 5/48

[52] **U.S. Cl.:** 356/43; 356/45

[58] **Field of Search:** 356/43, 44, 45; 374/130, 131, 161

[56] **References Cited**

**U.S. PATENT DOCUMENTS**

3,222,930	12/1965	Smith	356/45
3,486,378	12/1969	Carlson	73/343
3,635,088	1/1972	Poncet	356/45
4,326,798	4/1982	Kahn	356/45
4,362,057	12/1982	Gottlieb et al.	356/44
4,367,040	1/1983	Goto	356/44
4,376,890	4/1983	Engström et al.	374/130
4,409,476	10/1983	Lofgren et al.	250/277
4,420,265	12/1983	Everest et al.	374/133
4,558,217	12/1985	Alves	374/161

**OTHER PUBLICATIONS**

R. R. Dils and D. A. Tichenor, "A Fiberoptic Probe for Measuring High Frequency Temperature Fluctuations in Combustion Gases", Sandia Report No. SAND-33-8871, Feb. 1984.

"High Temperature Optical Fiber Thermometry", ac-cufiber informational brochure.

*Primary Examiner*—R. A. Rosenberger

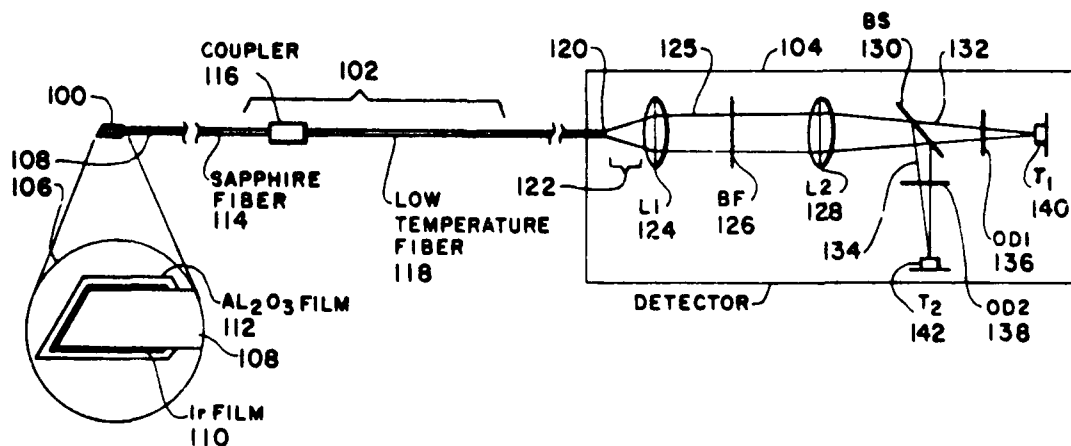
*Assistant Examiner*—Crystal D. Cooper

*Attorney, Agent, or Firm*—Gerald B. Hollins; Donald J. Singer

[57] **ABSTRACT**

Fiber optic probe apparatus usable for measuring temperatures with increased dynamic range and frequency domain response and desirable measurement accuracy. A black body signal source, fiber optic signal coupling, and extension of the transducer dynamic range with optical multiplexing are employed; the instrument operates in the range of 1.6 micrometers of optical energy wavelength and preferably employs recently improved indium gallium arsenide photodiode transducer devices and transducer frequency domain compensation. Use of the instrument in measuring combustion flame transient temperatures is disclosed.

**23 Claims, 5 Drawing Figures**



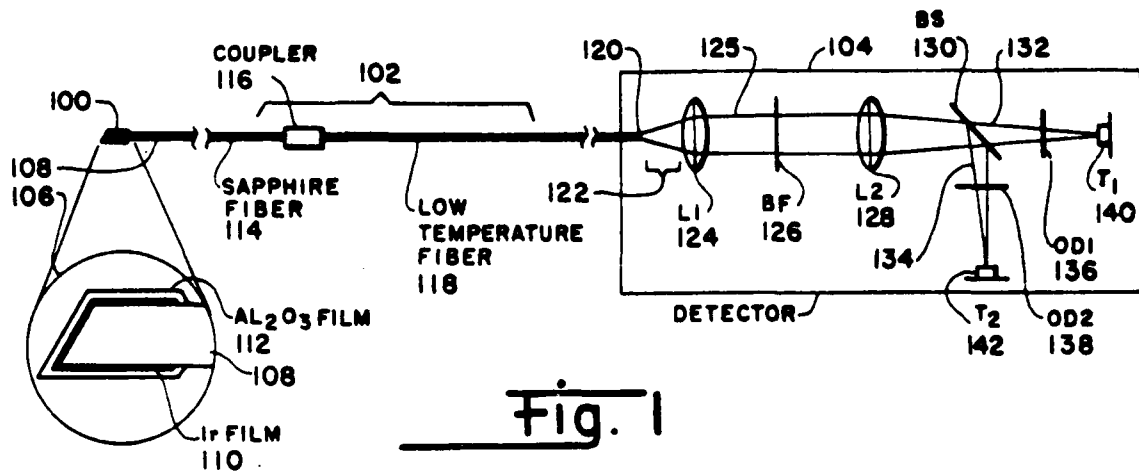


Fig. 1

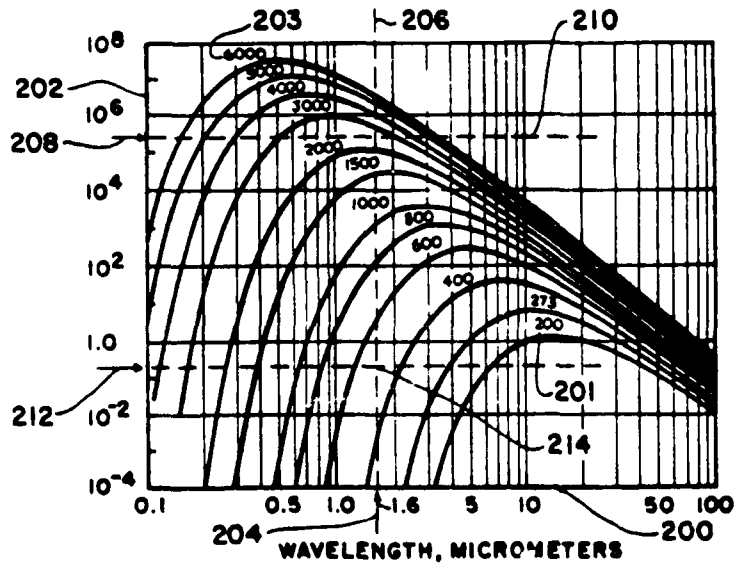


Fig. 2

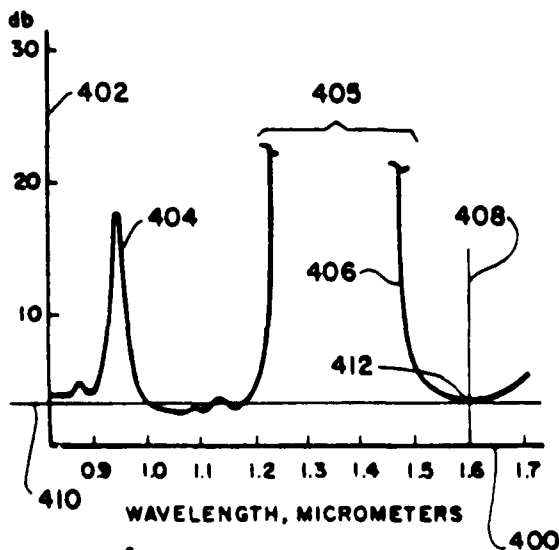


Fig. 4

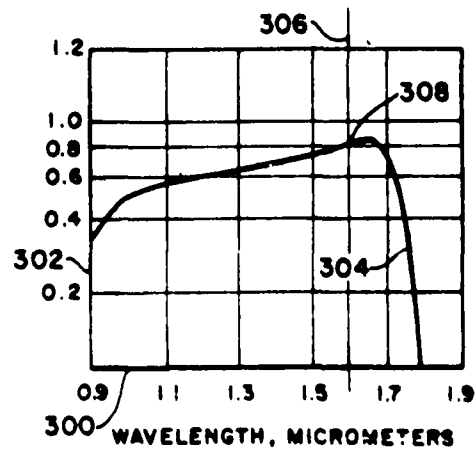


Fig. 3

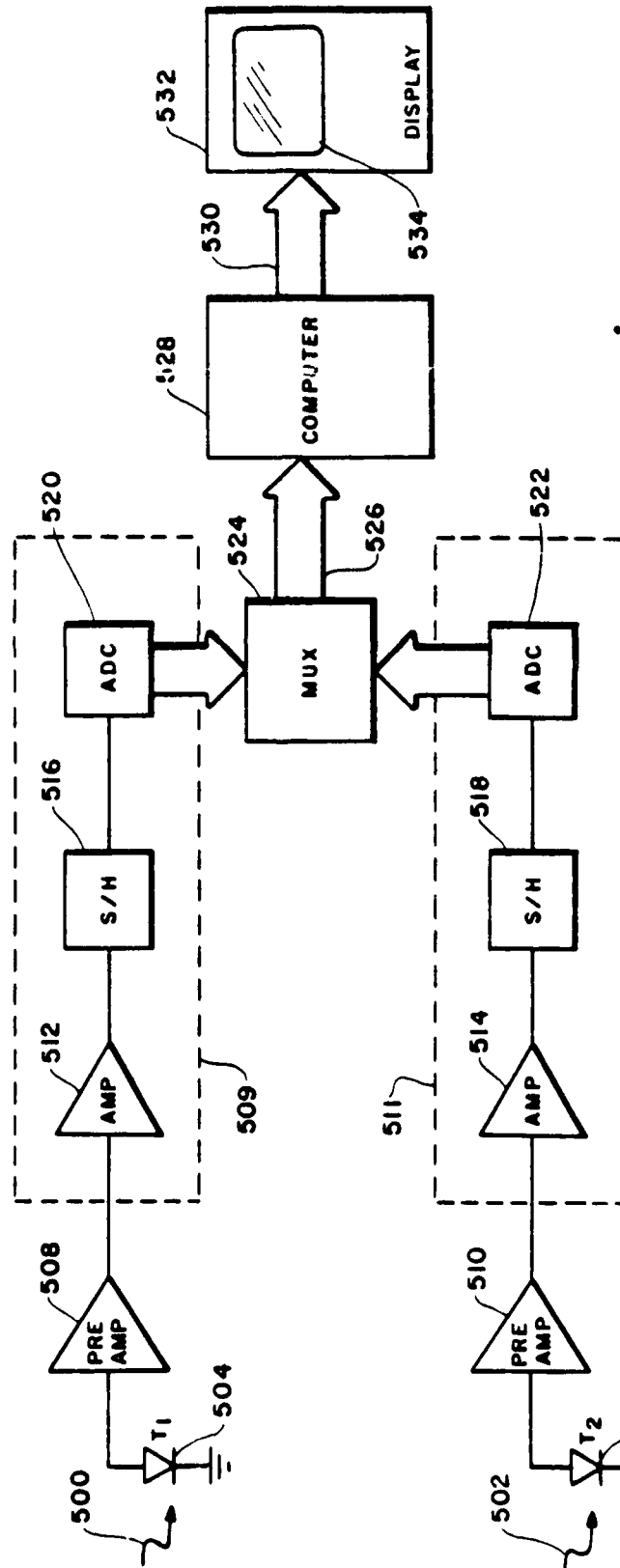


Fig. 5

## FIBER OPTIC PYROMETRY WITH LARGE DYNAMIC RANGE

### RIGHTS OF THE GOVERNMENT

The invention described herein may be manufactured and used by or for the Government of the United States for all governmental purposes without the payment of any royalty.

### BACKGROUND OF THE INVENTION

This invention relates to the field of multi-channelled fiber optic temperature measuring instruments and to the use of fiber optic coupled black body transducers in the wide range, rapidly changing measurement of temperatures.

High temperature fiber optic thermometry offers a plausible solution for several complex problems in the temperature measurement art. Among these problems is the measurement of rapidly fluctuating temperatures, as found in a flame; temperature measurement in the presence of strong electromagnetic fields, as in electric furnaces or induction furnaces; temperature measurement in a nuclear radiation environment, and temperature measurement with greater accuracy than afforded by the present-day thermocouple measurement. Fiber optic thermometry also provides new answers for the problems of temperature probe or thermocouple lead heat conduction, temperature probe gas flow disruption, and new approaches to laboratory standard temperature measurements. Fiber optic thermometry is perhaps most importantly, however, one of the most promising approaches for measuring the temperature transients encountered in a turbulent combustion or sooty combustion atmosphere.

The recent advent of improved solid state phototransducer devices having useful properties in the infrared spectral range and intended principally for use in the fiber optic communications field has added new dimensions to the capability of fiber optic temperature measurement systems. An example of such phototransducer devices is found in the indium gallium arsenide photodiode device currently manufactured by RCA Corporation, and known as the C30980E Photodiode. The C30980E photodiode, which is preferred in the described embodiment of the present invention, is described technically in a data sheet titled "C30979E, C30979EQC, C30980E, C30980EL InGaAs Photodiodes" which was printed in September 1982 and July 1984 by RCA Corporation and in RCA advertisements such as appear at page 178 of the journal *Laser Focus and Fiberoptic Technology*, April 1982. Such photodiodes are sold by RCA Corporation from a New Products Division Office on New Holland Avenue in Lancaster, PA 17604-3140 and from a Photodetector Marketing Office located at Ste. Anne de Beillevue, Quebec, Canada H9X 3L3. The RCA and similar solid state photoelectric transducer devices which may be or become available from other commercial suppliers have favorable response characteristics in a portion of the infrared spectrum that is desirable for performing temperature measurements.

Improvements in optical temperature measurement have also been recently achieved at the National Bureau of Standards, by R. R. Dils and others, as exemplified by the Dils articles "High-temperature Optical Thermometer" published in the *Journal of Applied Physics*, Vol. 54, 1983, p. 1198 and "A Fiberoptic Probe for

Measuring High Frequency Temperature Fluctuations in Combustion Gases", Sandia Report 83-8871 published during the first half of 1984 by R. R. Dils and D. A. Tichenor. Both of these Dils publications are hereby incorporated herein by reference.

The patent art includes several examples of high temperature measuring systems which precede the present invention. Included in this patent art is the patent of D. A. Kahn, U.S. Pat. No. 4,326,798, which concerns an optical pyrometer system employing spectral segregation of signal components received from a workpiece being measured, i.e., from a temperature elevated engine turbine blade. The Kahn patent is especially concerned with the avoidance of measurement errors resulting from transient spurious sources of heat in the measurement field, sources such as might be provided by heated particles of carbon in the workpiece atmosphere. Although the Kahn patent teaches the use of such herein employed elements as a beamsplitter, dual optical-to-electrical transducers, dual amplifier channels and the use of a workpiece-inherent black body member, the thrust of the Kahn patent is in the direction of performing accurate measurements in the presence of transient spurious sources of heat and in the elimination of effects from these transient spurious heat sources.

The patent of Folke Lofgren et al, U.S. Pat. No. 4,409,476, concerns a fiber optic temperature measurement arrangement which also includes an optical beamsplitter and a pair of optical-to-electrical transducer elements and additionally includes a photoluminescent black body solid material subjected to the temperature being measured. The photoluminescent material used in the Lofgren patent is in the nature of a semiconductor compound and exhibits the characteristic of responding to excitation by a light source, such as a light emitting diode, by emitting light of a different wavelength—the emitted light wavelength being dependent on the temperature of the semiconductor material. The Lofgren patent contemplates use of optical signals of different spectral content at two photodetector devices. An optical filter is inserted in the path of one or both photodetector devices. The Lofgren patent also contemplates the use of time multiplexing in exciting the light emitting diodes—in order to segregate signals resulting from the different photoluminescent detector devices. The Lofgren patent therefore involves a time multiplexed sensing of photoluminescent materials excited by pulses of light emitting diode light using a beamsplitting arrangement for achieving different spectral responses in the detector unit.

The patent of Kenya Goto, U.S. Pat. No. 4,367,040, concerns a multichannel multiplexed optical temperature measuring system wherein light supplied from an external source such as a laser diode, is transmitted bi-directionally along optical fiber transmission paths to and from a reflection or transmission type of optical sensor. The optical sensors of the Goto apparatus modulate the intensity of the supplied light beam in response to temperature or other physical quantities being measured.

The patent of C. E. Everest, U.S. Pat. No. 4,420,265, concerns an infrared responsive temperature measuring system intended primarily for agricultural applications and having the ability to compensate for sky radiation variations included in the measured signal. The patent of G. J. Carlson, U.S. Pat. No. 3,486,378, also concerns a temperature measuring apparatus wherein two detec-

tor cells are multiplexed—with the multiplexing of infrared energy in this case being achieved with a rotating disk modulator and with one of the detectors being excited by an incandescent lamp or other reference light source.

While each of these patents help identify the state of the fiber optic, multiplexed signal, temperature measurement art preceding the present invention, none of the measurement devices taught by these patents achieve the advantages of dynamic range multiplexing and the other techniques of the present invention.

### SUMMARY OF THE INVENTION

An object of the present invention is to provide a fiber optic temperature measuring apparatus of unusual temperature range capability.

Another object of the invention is to provide a fiber optic temperature measuring arrangement wherein plural phototransducers are employed in order to cover a large dynamic range.

Another object of the invention is to provide a fiber optic temperature measurement arrangement wherein the solid state phototransducer devices are reasonably protected from excess optical signal physical damage.

Another object of the invention is to provide a fiber optic temperature measurement arrangement which combines the advantages of a black body thermal transducer with operation in a desirable portion of the infrared spectrum.

Another object of the invention is to provide a fiber optic temperature measurement arrangement which employs the characteristics of newly available photodiode transducer devices to achieve a desirable spectral operating region, a wide dynamic operating range and other advantages.

Another object of the invention is to provide a fiber optic temperature measuring system which minimizes the disadvantages of materials such as sapphire, which have high cost and relatively poor temperature signal conductivity, but are nevertheless needed for desirable high-temperature thermal properties.

Another object of the invention is to provide a fiber optic temperature measuring system using the inherent filtering properties of optical coupling members in combination with optical bandpass filtering elements to achieve operation in an unusual and desirable portion of the infrared spectrum.

Another object of the invention is to provide a temperature measuring apparatus of unusual frequency domain response capability.

Another object of the invention is to provide a fiber optic temperature measuring arrangement suitable for use in combustion analysis of turbulent combustion and sooty combustion work environs—environs affording less than ideal temperature measuring conditions.

Additional objects and features of the invention will be understood from the following description and the accompanying drawings.

These and other objects of the invention are achieved by an apparatus providing means for transducing a work environment atmospheric temperature into an intensity modulated black body radiant optical signal, means for selecting a predetermined spectral band of the black body radiant signal as an intensity analog signal representation of the work environment temperature band, means for splitting the intensity analog signal into a plurality of intensity range segregated optical components, means for converting each of the component optical signals

into an electrical signal, a plurality of electrical signals each corresponding to a component optical signal resulting, and means for generating a temperature indication signal from selected of the plural electrical signals.

### BRIEF DESCRIPTION OF THE DRAWINGS

FIG. 1 is a diagram of a fiber optic temperature measuring apparatus made in accordance with the invention.

FIG. 2 is a graphic representation of a wavelength versus signal strength tradeoff field controlling operation of the FIG. 1 apparatus.

FIG. 3 shows the spectral response of a phototransducer device preferred in the FIG. 1 apparatus.

FIG. 4 shows the optical signal attenuation versus optical wavelength characteristics for signal transmitting media usable in the FIG. 1 apparatus.

FIG. 5 is a block diagram of an electronic system usable for converting signals from the FIG. 1 apparatus into temperature indications.

### DETAILED DESCRIPTION

FIG. 1 of the drawings shows a fiber optic temperature measuring apparatus capable of temperature measurements over an unusually large dynamic range of  $1E7$  or greater. The principals exhibited in FIG. 1 can be extended to achieve dynamic ranges of even larger value. The notation form  $1E7$  used herein will be understood to mean 1 times  $10^7$  raised to the seventh power, or  $1 \times 10^7$ . The notation  $1E7$  is therefore an abbreviation for one times ten raised to the exponent (E) seven and is a notation frequently used in computer programming and similar arts.

The term "dynamic range" in instruments of the FIG. 1 type is understood to mean the ratio of maximum usable signal power to power of the minimum signal discernible in the inherent noise of the instrument; in other words, the ratio of maximum usable signal power to inherent noise signal power. Limited dynamic range has been a characteristic of instruments preceding the FIG. 1 system.

The FIG. 1 apparatus includes three major components, a work environment black body signal source 100, a signal transmitting optical fiber array 102, and a detector assembly 104. Preferred arrangement details of the black body signal source 100 are shown in the expanded view 106 and include black body cavity-shaped radiating member 110 which is surrounded by a protective film layer 112 and received on the end of a high temperature optical fiber member 108.

As indicated in the view 106 in FIG. 1, the black body radiating member 110 is preferably fabricated as an irridium metal film, while the protective film layer 112 is preferably fabricated as an aluminum oxide film, and the optical fiber member 108 is preferably made from a bundle of sapphire (aluminum oxide) fiber elements. Alternates for these preferred materials are of course, possible, and include the use of a platinum metal film for the black body radiating member 110, other oxide materials for the protective film layer 112, and quartz fibers in limited temperature range applications for the sapphire fiber bundle 108. The black body cavity radiating member 110 is preferably formed over the end of the optical fiber bundle 108 by sputtering metal deposition techniques. Other fabrication arrangements including an irridium or tungsten wire disposed in front of the fiber bundle terminal or a mechanically deformed metallic sheet stock member; or alternately, a direct

image of flame radiation emission can be used in some applications of the FIG. 1 apparatus.

Optical signals from the black body radiating member 110 are conducted along the sapphire fiber bundle 114 to a low temperature fiber bundle 118. The low temperature fiber bundle 118 is used to conduct signal over the majority of the distance between the black body signal source 100 and the detector assembly 104. Optical signal coupling between the sapphire fiber bundle 114 and the low temperature fiber bundle 118 is accomplished by an optical coupler 116 of a type known in the fiber optic art. The sapphire fiber bundle 114 is of course, employed at the work environ end of the path between the black body signal source 100 and the detector assembly 104 in order to withstand the elevated temperatures existing in the work environ, i.e., the temperatures being measured by the FIG. 1 apparatus. The sapphire fibers in the bundle 114 are capable of withstanding such work environ temperatures, but are undesirably inefficient as conductors of the optical signal generated by the black body source 100; in view of this conduction limitation and the cost of sapphire conductors, the bundle 114 is preferably arranged to be as short as possible.

The optical signal transmitted along the fiber array 102 in FIG. 1 emerges from the end terminus 120 located within the detector assembly 104 as the divergent optical signal indicated at 122. This divergent signal is captured and collimated by the lens L1, 124, which may have a focal length in the range of 2.5 cm. The collimated signal 125 emerging from the lens L1, 124, is captured by a second lens L2, 128, which is preferably of a focal length in the range of 25 cm. The lens L2, 128 serves to focus the collimated light signal 125 on the active surface of a pair of photodiode transducer elements T1, 140, and T2, 142. A bandpass filter BF, 126 is located in the path of the collimated light signal 125 in order to select a specific spectral band of optical signal frequencies for use in the transducer elements T1, 140 and T2, 142. As indicated subsequently herein, the filter 126 together with optical wavelength selective signal attenuation characteristics inherent in the optical fibers 102, can be used to elect a desirable range of the optical spectrum for operating the FIG. 1 apparatus.

In the FIG. 1 apparatus, optical signal from the lens L2, 128 is received on the surface of a pellicle or optical beamsplitting member BS, 130 which preferably has the capability of dividing the optical signal into ten percent and ninety percent intensity ratio components. These components are subsequently converted into electrical signals having different intensity weighting factors. The beam splitter reflected optical signal component 134 preferably represents ten percent of the optical energy incident on the beamsplitting member 130, while the transmitted component 132 represents ninety percent of the beamsplitter received optical energy.

Each of the beamsplitter output components 132 and 134 is further attenuated by a pair of optical density attenuators OD1, 136, and OD2, 138, located intermediate the beamsplitting member 130 and the photodiode transducer elements 140 and 142. The optical path of the reflected ten percent component signal 134 preferably includes an optical density attenuator, 138 of attenuation factor between 3 and 3.5, while the optical path of the transmitted component 132 includes an optical density filter of a lesser attenuation factor—between 0.4 and 0.6. (An optical attenuator of attenuation factor or neutral density 3 provides attenuation of  $1E3$ , or  $10^3$ , while an attenuator of neutral density 4 provides an

attenuation of  $1E4$ , or  $10^4$ .) As a result of the reflected component 134 being only ten percent of the beamsplitting member received optical energy and the attenuation of the density attenuator 138 falling between 1,000 and 10,000, the photodiode transducer element T2, 142 is effectively energized only upon receipt of high intensity optical signals.

The photodiode transducer element T1, 140 by way of receiving the beamsplitter ninety percent component and having relatively small optical attenuation in the optical density attenuator OD1, 136 is responsive to low-level optical signals. During receipt of optical signals of sufficient intensity to activate the transducer element T2, 142, the low level photodiode transducer element T1, 140 is however, protected from physical damage by the presence of the attenuator 136 and its characteristic of attenuating the transmitted optical signal component 132 by a factor of  $1E4$  to  $1E6$ .

Transducer elements of the preferred solid state type are found generally to have a physical damage threshold in the range of 500 milliwatts of incident optical energy; the optical density filter OD1, 136 is therefore provided with the capability of attenuating the largest expected transmitted signal component 132 to this or a lower level and is principally incorporated in the FIG. 1 apparatus to achieve such protection. Optical-to-electrical transducers of the solid state photodiode type are preferred for use in the FIG. 1 apparatus for inter alia reasons relating to transducer physical damage since the most plausible alternative transducer device, the photomultiplier vacuum tube is found to readily incur photocathode physical damage from incident optical energy in a FIG. 1 type apparatus.

Each of the transducers T1, 140 and T2, 142 in the FIG. 1 apparatus is preferably a type C30980E photodiode supplied by RCA Corporation, or alternately, is a device of similar characteristics from another source. Devices of this type are sold by RCA Corporation in a variety of sizes and configurations, including some arrangements which incorporate light pipes, optical fibers, or preamplifiers. Such devices inherently have good speed of response and quantum efficiencies, however tradeoff among these and other characteristics are indicated in the RCA published device characteristics. Such devices are capable of providing the spectral response indicated in FIG. 3 of the drawings. Transducers or detectors of this type are preferably fabricated from alloys of indium, gallium, and arsenic or indium gallium arsenic/indium phosphide and are described in the above-referenced RCA Corporation data sheet. A series of published articles also describes transducers of this type. Several articles of this nature are to be found in the Institute of Electrical and Electronic Engineers (IEEE) Transactions on Electron Devices and notably in special issues on optoelectronic devices and light emitting diodes and long wavelength photodetectors found at Volume ED-29, Number 9, September 1982 and Volume ED-30, Number 4, April 1983. The paper "Long-Wavelength (1.3 to 1.6  $\mu\text{m}$ ) Detectors for Fiber Optical Communications" by G. E. Stillman, L. W. Cook, G. E. Bulman, N. Tabatabaie, R. Chin, and P. D. Dapkus in the September 1982 transactions publication and the papers "InGaAsP Photodiodes" by E. E. Stillman, L. W. Cook, N. Tabatabaie, G. E. Bulman, and V. M. Robbins found at page 364, and "Large-Area and Visible Response VPI InGaAs Photodiodes" by P. P. Webb and G. H. Olsen found at page 395 of the April 1983 transactions publication are of special interest with

respect to such devices. The text of these IEEE special issues is hereby incorporated by reference herein. Detectors of this type can be operated either as a photovoltaic device—an EMF generator, or as a photoconductive device—a variable impedance element. Since the noise related leakage current (and also the transducer output signal response) is lower in the photoconductive mode of operation, this mode of transducer operation is preferred in FIG. 1.

Transducers of this type have principally evolved in response to a need in the fiber optics communications field where signals in the infrared spectral region are coupled between a light emitting diode and a receptor by way of long lengths of fiber optic media. Photodiode transducer elements of this type are capable of operating over a linear dynamic range in the order of  $1E4$ . By way of the 10/90 beamsplitting member 130 and the optical density attenuators 136 and 138 in FIG. 1, two individual linear ranges of  $1E4$  are stacked or added to provide an overall detector assembly dynamic range in the order of  $1E8$  in the FIG. 1 apparatus. The beamsplitting member, neutral density attenuator, and multiple transducer element arrangement of the detector 104 in FIG. 1 can be extended to include additional transducer elements and additional operating dynamic range with the inclusion of adequate protection for the most sensitive of the transducer elements. T1, 140 in FIG. 1, for example requires protection from physical damage during receipt of optical signals of the highest contemplated intensity. Generally, however, some difficulty is to be expected in extending the dynamic range of a FIG. 1 type apparatus significantly beyond the  $1E8$  region in view of the physical damage potential for the low-level or most sensitive of the transducer elements.

The neutral density values of 0.4–0.6 and 3.0–3.5 in FIG. 1 together with the 10% and 90% attenuations of the beamsplitting member 130 effectively divide the optical signal 122 into two components of dynamic range  $1E4$  each. The optical density attenuators 136 and 138 can be adjusted or selected in order to provide location adjustment of these ranges and to provide the slight degree of range overlap desired between the transducer elements 140 and 142 during receipt of optical signals in the mid-intensity range.

The use of a black body transducer for generating optical signals of large intensity variation, that is, signals affording good temperature resolution characteristics is described in the above-identified 1983 article published by Ray R. Dils. The 1983 Dils article is hereby incorporated by reference into the present specification. The Dils article also indicates that temperature measurement has been based on use of an optical fiber as a signal generator in addition to the herein described use of optical fiber as a signal transmission medium. The use of an optical fiber signal generator in the FIG. 1 apparatus is, of course, within the spirit of the present invention.

By way of explanation, it should be noted that the black body signal source 100 in FIG. 1 may be thought of in the nature of a transducer device, that is, a device which is heated in the work environ and as a result of this heating emits an intensity varying signal usable for measuring the work environ temperature. For the sake of terminology consistency however, the word "transducer" is herein, preferred for use in connection with the photodiode elements 140 and 142 in FIG. 1.

The optical passband of the spectrally selective elements in the FIG. 1 apparatus relates to a notable aspect of the present invention. The desired properties for the

bandpass filter 126 and the optical fiber array, the principal other spectrally selective element in the FIG. 1 apparatus, can be appreciated with the assistance of FIGS. 2, 3 and 4 in the drawings. The curves in FIG. 2, for example, show the relationship between spectral radiance or optical signal intensity and optical spectrum wavelength for a black body signal source operated at a series of different temperatures; the FIG. 2 temperatures 201, 203, etc. are measured in degrees Kelvin. FIG. 3 as indicated above shows the relationship between electrical output signal and optical input signal wavelength for the indium gallium arsenide transducer element preferred for use in the transducer element P1, 140 and P2, 142 in FIG. 1. The curves in FIG. 4 of the drawings show the relationship between optical signal wavelength and optical signal attenuation for one type of sapphire optical fiber usable in the fiber bundle 114 in FIG. 1. The spectral scales 200, 300 and 400 in each of FIGS. 2, 3, and 4 include a desirable portion of the optical spectrum for use in the FIG. 1 apparatus.

The spectral radiance or signal output scale 202 in FIG. 2 extends logarithmically over a dynamic range of  $1E12$ . Actually, however, some signal falling outside the range of FIG. 2 are of interest in the present invention, one representation of such signals is included in Table I at the end of this specification. The optical signal wavelength scale 200 in FIG. 2 shows portions of the near and far infrared spectrum also on a logarithmic scale. The black body temperatures in FIG. 2 extend between the 200° K. indicated at 201 and the 6000° K. indicated at 203. An operating band of choice for the FIG. 1 instrument is shown by the dotted lines 204, 208, and 212 in FIG. 2.

One aspect of the FIG. 2 curves concerns the change in optical signal dynamic range which results from operating a black body temperature transducer at different wavelengths along the scale 200—i.e., from limiting the spectral band of interest within the scale 200. At a wavelength of 50 micrometers, for example, the temperatures between 200° K. and 6000° K. involve a signal dynamic range of  $1E2$ , while at a wavelength of 10 micrometers a signal dynamic range slightly under  $1E4$  is generated. At a wavelength of 3 micrometers moreover, a dynamic range in the neighborhood of  $1E9$  is required to cover the temperatures between 200° and 6000° K.

In the past, wavelengths in the range of 0.6 to 0.8 micrometers have been employed for fiber optic probe temperature measuring instruments. At these wavelengths, as can be observed in FIG. 2, an optical signal dynamic range capability in the order of  $10^{16}$  and  $10^{13}$ , respectively, is needed in order to measure temperatures between 300° and 2300° K., the temperatures found in a possible turbulent combustion flame. A problem has therefore existed previously in that no known detector was possessed of such large dynamic range capability. In the dynamic range sense, therefore, the large output signal of a black body probe is desirable for achieving good temperature sensitivity and accuracy, but is somewhat troublesome when the need to cover wide temperature ranges is present.

Optical multiplexing as represented by the beamsplitting member 130 in FIG. 1 makes it feasible to overcome the dynamic range problem of a wide temperature range black body transducer signal through splitting the signal into multiple component signals each covering a  $1E3$ – $1E4$  dynamic range.

It can be therefore observed from FIG. 2 that because of dynamic range considerations as well as because of spectral attenuation characteristics discernible in FIG. 4 of the drawings a shift to somewhat longer wavelengths than the previous 0.6 to 0.8 micrometer wavelengths is desirable for a wide range fiber optic optical pyrometer apparatus.

From the combination of optical fiber attenuation characteristics shown in FIG. 4, photodiode transducer characteristics shown in FIG. 3, and blackbody characteristics shown in FIG. 2, an instrument operating in the spectral wavelength region of 1.6 micrometers can be observed to be desirable. At a 1.6 micrometer spectral wavelength, a dynamic range of  $1E8$  will cover a temperature range on the order of  $400^{\circ}$ – $2300^{\circ}$  K. with some accuracy falloff below  $500^{\circ}$  K. and will provide measurement feasibility for the variations observed in a turbulent flame combustion atmosphere. The dotted line 206 in FIG. 2 and the arrow 204, indicate the preferred 1.6 micrometer spectral operating wavelength in FIG. 2. The dotted lines 214 and 210, the arrows 212 and 208 show the extent of the signal dynamic range for a 1.6 micrometer spectral wavelength operating point in FIG. 2.

Actual photon flux values in watts for a black body device operated at temperatures between  $300^{\circ}$  K. and  $2300^{\circ}$  K. are shown in Table 1 at the end of this specification. As indicated by these photon flux values, a FIG. 1 instrument operated with a center optical spectrum wavelength of 1.6 micrometers involves a signal dynamic range of  $1E11$  to cover the temperature band of  $300^{\circ}$  K. to  $2300^{\circ}$  K. A large part of this dynamic range is, however, devoted to the low, or room temperature, end of this temperature band so that an instrument covering the temperature band of  $500^{\circ}$  K. to  $2300^{\circ}$  K. involves a signal dynamic range of  $1E6$ . The herein provided dynamic range of  $1E8$  therefore allows a lower temperature intermediate these  $300^{\circ}$  K. and  $500^{\circ}$  K. values. An instrument operating in the 0.7 micrometer wavelength region in the visible area of the spectrum would require a dynamic range of  $1E13$  to cover the  $300^{\circ}$ – $2300^{\circ}$  K. temperature band; clearly the selected 1.6 micrometer operating frequency and  $1E8$  dynamic range are preferable for an instrument of moderate sensitivity that is to be capable of measuring over a large range of temperatures.

The scales 300 and 302 in FIG. 3 indicate value of spectral wavelength and relative signal amplitude, respectively, for a preferred indium gallium arsenide photodiode transducer device. The line 306 indicates the location of the preferred 1.6 micrometer spectral operating wavelength and the point 308 in FIG. 3 indicates location of this desired 1.6 micrometer wavelength on the response curve 304 of the preferred indium gallium arsenide photodiode transducer device. Other transducer devices having usable output signal magnitudes in the 1.6 micrometer wavelength region could, of course, be used in the FIG. 1 apparatus as an alternate to the preferred indium gallium arsenide photodiode transducer.

The attenuation response of sapphire fiber elements usable in the high temperature optical fiber bundle 114 in FIG. 1 is shown in FIG. 4 of the drawings. In FIG. 4, spectral wavelengths are indicated along the scale 400 and attenuation values along the scale 402. In FIG. 4, the attenuation is shown to include two curves 404 and 406 lying on either side of an attenuation peak 405. The attenuation value in decibels is indicated along the scale

402 in FIG. 4 for a specified fiber length, near 1000 meters, of a specific sapphire fiber material. Fibropoil QSF200, which is manufactured by the Saphikon Division of Tyco Laboratories. The curve 406 portion of FIG. 4 and especially the point 412 and the lines 408 and 410 are of interest with respect to the operating point for the FIG. 1 apparatus—these lines and points relate to the 1.6 micrometer preferred wavelength. As indicated by the attenuation values along the scale 402 in FIG. 4, the sapphire fiber bundle portion 114 of the signal transmitting optical fibers 102 in FIG. 1 contributes significantly to attenuation of the optical signal; indeed only the indicated desirable characteristics of the sapphire fibers make use of such fibers attractive in the FIG. 1 apparatus.

The curves in FIG. 4 also indicate that the sapphire fibers in the bundle 114 contribute desirably to the optical wavelength selection achieved in the FIG. 1 apparatus. The curve portion 406 in FIG. 4, for example, indicates sharply increasing optical attenuation in the fiber bundle 114 at wavelengths of 1.5 micrometers and below; this curve actually therefore indicates the sapphire bundle to be a wavelength filter which together with the bandpass filter 126 in FIG. 1 defines the operating spectral region for the FIG. 1 apparatus. The bandpass filter 126 can be of such characteristics as to attenuate optical wavelengths lying outside the sharp attenuations shown in FIG. 4, wavelengths below 1.5 micrometers and above 1.8 micrometers, thereby assuring that only a small spectral band round the 1.6 micrometers is active in the FIG. 1 apparatus. The bandpass filter 126 can also be used to accommodate the presence of undesirably short lengths in the fiber bundle 114—lengths which are too short to achieve the desired optical signal attenuation.

FIG. 5 in the drawings shows a block diagram representation of an electronic system usable for processing the electrical signals generated by the photodiode transducer elements T1, 140 and T2, 142 in FIG. 1. These photo transducer elements are represented in electrical form at 504 and 506 in FIG. 5, and are shown symbolically to receive photons of optical energy 500 and 502. The FIG. 5 electronic system includes a pair of electronic signal preamplifiers 508 and 510 which feed the amplifier, sample and hold, and analog-to-digital converter modules 509, 511. The preamplifiers 508 and 510 are preferably of the junction field effect transistor (JFET) type having an input JFET device operated in the trans-impedance circuit configuration with high input impedance and low output impedance. The modules 509 and 511 which include the amplifiers 512 and 512, the sample and hold circuits 516 and 518, and the analog-to-digital converters 520 and 522 are available commercially as integrated circuit devices from suppliers such as Analog Devices, Inc. The modules 509 and 511 can, for example, be data acquisition modules identified as Analog Devices Incorporated part numbers DAS 1156. The sample and hold and analog-to-digital converter combination preferably provides 15 bit resolution with throughput rates in the range of 20 kilohertz for the FIG. 1 apparatus.

Digital signals provided by the analog-to-digital converters 520 and 522 are time sampled by the multiplexer 524 in FIG. 5, and transmitted to a digital computer 528 by way of a data bus 526. The output of the digital computer 528 is transmitted by a second data bus 530 to a display 532 which may include a cathode ray tube 534, or other display arrangements. The display 532 may

also include a keyboard for entering operator instructions and display selection information.

Since the two photodiode transducer elements T1, 140 and T2, 142 or their electrical representations at 504 and 506 in FIG. 5 are each responsive to only a predetermined intensity range of signal from the black body source 100, only one of the electrical signals received from these photodiode transducer elements is of interest in making a given temperature measurement. A high temperature work environ measurement producing large intensity signals, for example, will provide a usable, linear operating range, signal from the high temperature photodiode transducer element T2, 142 and also provide a larger but non-linear operating range signal from the low temperature photodiode transducer element T1, 140.

Selection between the signal generated by the photodiode element 506 and the signal generated by the photodiode element 504 is accomplished in the computer 528 in FIG. 5 using a signal amplitude discriminating algorithm. The discriminating algorithm in the computer 528 should provide the following capabilities:

- Selection of the signal representing transducer operation within the transducer linear range
- Exclusion of transducer signals falling above a predetermined linear range of transducer operation
- Selection of either one or an average of both transducer signals for intermediate intensity signals
- Exclusion of a transducer signal residing within the transducer noise background level.

A signal amplitude responsive algorithm is satisfactory for performing these selections.

Implementation of a computer algorithm performing these functions is of course, dependent upon the type of computer used at 528 and the operating system and programming language employed with the computer, a program of this type is, in any event within the capability of persons skilled in the computer art.

Dedicated hardware could, of course, be used to replace the computer 528 and the display 532, such hardware would include amplitude discriminating circuitry, data storage devices, and a display in the form of a light emitting diode alphanumeric character matrix or a liquid crystal matrix of the type commonly used in electronic wristwatches. A cathode ray tube display device could also be employed with such a dedicated hardware system. A significant portion of such hardware could also be adapted from commercially available temperature indicating instruments which operate with a thermocouple or other sensing devices.

The frequency domain response of the temperature measuring apparatus in FIG. 1 and FIG. 5 can extend into the kilohertz region and thereby enable use of the apparatus in the measurement of rapidly fluctuating or transient temperature conditions such as may exist in engine combustion, turbulent combustion, or sooty combustion environs. Thermal inertia in the black body signal source 100 and limited thermal conductivity in the optical fiber bundle 114 are the most limiting considerations in determining the frequency domain response of the FIG. 1 and FIG. 5 apparatus. Through the use of a frequency rolloff compensation algorithm in the computer 528, these limitations can be accommodated to a useful degree and enable higher frequency temperature measurement capability than has heretofore been available. Sampling frequency rates up to 20 kilohertz are, for example, achievable with the FIG. 1 and FIG. 5 apparatus. Since the maximum frequency requirement

for studying events in a turbulent flame has been found to lie in the region of 10 kilohertz, a 20 kilohertz response is more than adequate for such studies. Notwithstanding this range of overall system response, however, it should be realized that the naked frequency domain response of the black body signal source 100 can have a 250 millisecond time constant; the extension of responses in this range of time constants to the 20 kilohertz region is achieved with the use of frequency domain compensation in the computer 528.

Heretofore, the available photon transducers for the preferred 1.5 to 1.8 micrometers spectral wavelength region have been comprised of germanium, doped germanium, indium antimonide, and lead selenide. The addition of the preferred indium gallium arsenide transducer provides a noise equivalent power output from the transducer which is superior to previous detector types by more than an order of magnitude when measured in the non-cooled or 300° K. temperature environment. The quantum efficiency of indium gallium arsenide is on the order of 60% at the preferred 1.6 micrometer operating wavelength. The indium gallium arsenide photodiode transducer provides junction capacitances comparable to that of silicon PIN detectors and is therefore suitably low for high frequency domain temperature measurement operation.

Calibration of the FIG. 1 and FIG. 5 apparatus to provide absolute temperature measurement may be achieved by calibrating the electro-optical response function with the aid of a black body radiation source. Single point calibration can be used to allow computation of the absolute temperature using a transfer function relationship since the emissivity of iridium or one of the alternate black body materials is substantially temperature independent, as can be seen from the explanation for photon flux vs. temperature below. The FIG. 1 and FIG. 5 apparatus is capable of temperature measurements with resolution and accuracy exceeding 0.5 percent over the selected temperature range.

The use of a black body transducer in order to obtain increased temperature measurement sensitivity is based on a convolution of the optical fiber bandpass characteristics with Planck's black body radiation equation, such a convolution enables the measurement of temperature from a measurement of photon flux arriving at a photodiode transducer element. The applicable Planck equation has the form of

$$L(\lambda_0) = \frac{a\epsilon_0 c_1}{\lambda_0^5 [\exp(c_2/\lambda_0 T) - 1]} \quad [W/m]$$

where

- a = area of the cavity exit (m<sup>2</sup>)
- ε<sub>0</sub> = apparent emittance of the cavity
- c<sub>1</sub> = first radiation constant (3.7418 × 10<sup>-16</sup> W M<sup>2</sup>)
- c<sub>2</sub> = second radiation constant (1.43879 × 10<sup>-2</sup> m.K)
- λ<sub>0</sub> = wavelength in vacuum (m)
- T = temperature (K)
- λ<sub>0</sub> is herein selected to provide maximum temperature change sensitivity and low optical signal absorption in sapphire at elevated temperatures.

While the apparatus and method herein described constitute a preferred embodiment of the invention, it is to be understood that the invention is not limited to this precise form of apparatus or method, and that changes may be made therein without departing from the scope

of the invention, which is defined in the appended claims.

TABLE I

Black Body Probe Intensity Variation as a Function of Temperature with a Central Wavelength of 1600 nm and Halfwidth of 100 nm; W = Watts.			
T (°K.)	Intensity (W)	T (°K.)	Intensity (W)
300.0	0.32867E-10	350.0	0.19043E-08
400.0	0.41009E-07	450.0	0.45345E-06
500.0	0.31322E-05	550.0	0.15331E-04
600.0	0.57866E-04	650.0	0.17868E-03
700.0	0.47087E-03	750.0	0.10926E-02
800.0	0.22837E-02	850.0	0.43890E-02
900.0	0.78439E-02	950.0	0.13204E-01
1000.0	0.21107E-01	1050.0	0.32282E-01
1100.0	0.47525E-01	1150.0	0.67673E-01
1200.0	0.93596E-01	1250.0	0.12617E+00
1300.0	0.16624E+00	1350.0	0.21466E+00
1400.0	0.27221E+00	1450.0	0.33963E+00
1500.0	0.41759E+00	1550.0	0.50670E+00
1600.0	0.60750E+00	1650.0	0.72045E+00
1700.0	0.84593E+00	1750.0	0.98426E+00
1800.0	0.11357E+01	1850.0	0.13004E+01
1900.0	0.14784E+01	1950.0	0.16699E+01
2000.0	0.18748E+01	2050.0	0.20931E+01
2100.0	0.23247E+01	2150.0	0.25694E+01
2200.0	0.28270E+01	2250.0	0.30973E+01
2300.0	0.33802E+01		

We claim:

1. Large temperature range optical pyrometer apparatus comprising:

optical beamsplitting means for segregating photon flux optical signals into first and second component optical signals of predetermined segregated intensity range ratio;

optic means for transmitting photon flux optical transmission signals from adjacent an elevated temperature work environ to said beamsplitting means;

first optical attenuation means for generating from said first component optical signal a first attenuated optical signal of first intensity ratio relationship with said first component optical signal;

second optical attenuation means for generating from said second component optical signal a second attenuated optical signal of second intensity ratio relationship with said second component optical signal;

first optical-to-electrical transducer means, of smaller dynamic range capability than said photon flux energy optical signal, for generating first electrical signals amplitude responsive to said first attenuated optical signal intensity;

second optical-to-electrical transducer means of smaller dynamic range capability than said photon flux energy optical signal, for generating second electrical signals amplitude responsive to said second attenuated optical signal intensity; and

means responsive to the amplitude of a selected one of said first and second electrical signals for generating a pyrometer output temperature indication signal.

2. The apparatus of claim 1 further including optical filter means for limiting the spectrum of said first and second attenuated optical signals to a predetermined spectral band.

3. The apparatus of claim 2 wherein said optical filter means includes a limiting spectral response in said optic transmission means.

4. The apparatus of claim 3 wherein said optic transmission means limiting spectral response lies on one spectral wavelength side of said predetermined spectral

band and said optical filter means further includes an optical filter element of limited spectral response lying on the opposite spectral wavelength side of said predetermined spectral band.

5. The apparatus of claim 4 wherein said spectral band includes the spectral wavelength of 1.6 micrometers.

6. The apparatus of claim 1 further including a black body transducer element located within said work environ intermediate said environ and a work environ terminus of said optic means.

7. The apparatus of claim 6 wherein said black body transducer element is comprised of a metal taken from the group of platinum and irridium.

8. The apparatus of claim 7 wherein said black body transducer element includes a protective film of oxide material disposed over the metal surface adjacent said work environ.

9. The apparatus of claim 1 wherein said optic transmission means includes a transmission element comprised of sapphire.

10. The apparatus of claim 9 wherein said optic transmission means includes a high temperature sapphire transmission element adjacent said work environ and low temperature fiber optic means intermediate said sapphire transmission element and said beamsplitting means.

11. The apparatus of claim 1 wherein said first and second optical-to-electrical transducer means each include a transducer element comprised of indium gallium arsenide.

12. The apparatus of claim 1 wherein said means for generating a pyrometer output temperature indication signal includes selection means responsive to the amplitude of said first and second electrical signals for selecting between said electrical signals in generating said pyrometer output indication signal.

13. The apparatus of claim 1 wherein said beamsplitting means includes a beamsplitting pellicle member, said first component signal is transmitted through said pellicle member, said second component optical signal is reflected from said pellicle member and said second component reflected optical signal is of lesser intensity than said first component transmitted optical signal;

whereby said transmitted first component signal correlates with a low intensity, low temperature portion of the dynamic range of said pyrometer and said reflected second component signal, correlates with a high intensity high temperature portion of said dynamic range of said pyrometer.

14. The apparatus of claim 13 wherein said first optical attenuation means is of smaller attenuation capability than said second optical attenuation means;

whereby said second lower intensity component optical signal is attenuated by a greater degree than said first component optical signal and the portions of said pyrometer dynamic range correlating with said component signals are further segregated.

15. The apparatus of claim 2 wherein said spectral band is located at a spectral wavelength of limited optical signal intensity dynamic range

16. The apparatus of claim 15 wherein said optical-to-electrical transducer means includes a transducer element comprised of indium, gallium, and arsenic, said selected spectral band includes the wavelength of 1.6 micrometers, one of said attenuation means is capable of

15

attenuation greater than one thousand times and the other of said attenuation means is capable of attenuation less than one hundred times.

17. The method for optically measuring a wide band of work environ temperatures comprising the steps of: 5  
 transducing a work environ temperature into an intensity modulated black body radiance optical signal;  
 selecting a predetermined spectral band of said black body radiance signal as an intensity signal representation of said work environ temperature band; 10  
 splitting said intensity signal into a plurality of intensity range segregated optical signal components;  
 converting each of said component optical signals into an electrical signal, a plurality of said electrical signals each corresponding to a component optical signal and representing a range of work environ temperatures thereby resulting; and 15  
 generating a temperature indication signal from a selected sequence of said plural electrical signals. 20

18. The method of claim 17 further including attenuating each of said component optical signals by a differing predetermined amount in inverse correspondence with said segregated intensity ranges; 25

whereby the dynamic range of each said component signal converted into an electrical signal is similar and within the linear dynamic range of means performing said converting. 30

19. The method of claim 17 wherein said step of selecting a predetermined spectral band includes rejecting the black body spectral band of maximum signal dynamic range: 35

whereby optical signals of large dynamic range and transducer physical damage capability are excluded from said converting step and limited dynamic range converting is enabled.

20. The method of claim 19 wherein said step of splitting said intensity signal into a plurality of signal components comprises splitting said intensity signal into two signal components of dissimilar intensity range. 40

21. Apparatus for optically measuring a wide band of work environ temperatures comprising:

means for transducing a work environ temperature into an intensity modulated black body radiance optical signal; 45

means for selecting a predetermined spectral band of said black body radiance signal as an intensity analog signal representation of said work environ temperature band; 50

means for splitting said intensity analog signal into a plurality of intensity range segregated optical signal components;

means for converting each of said component optical signals into an electrical signal, a plurality of elec-

16

trical signals each corresponding to a component optical signal resulting; and

means for generating a temperature indication signal from selected of said plural electrical signals.

22. Apparatus for optically measuring fluctuating work environ temperatures in the range of 500 to 2300 degrees Kelvin comprising:

an irridium black body transducer member capable of being immersed in said work environ and of generating a black body radiance signal when heated by said environ;

an optical beamsplitter member capable of dividing a radiance signal sample into ten and ninety percent intensity components;

an optical transmission member including optically coupled sapphire fiber and glass fiber portions located intermediate said work environ and said beamsplitting members respectively, and capable of transmitting optical radiance signal samples therebetween;

optical filter means located in the path of said optical radiance signal sample for rejecting radiance signal spectral components external of a band between 1.5 and 1.8 micrometers of spectral wavelength;

a first neutral density attenuation member of density factor between four-tenths and six-tenths located in the ninety percent intensity component path of said beamsplitter;

a second neutral density attenuation member of density between three and three and one-half located in the ten percent intensity component path of said beamsplitter;

a first optical signal to electrical signal detector member comprised of a room temperature maintained gallium indium and arsenic compound photodiode capable of converting said four-tenths to six-tenths density attenuated beamsplitter ninety percent component into a first electrical signal; said detector member diode having a linear dynamic transducer range between 1E5 and 1E6;

a second optical signal to electrical signal detector member comprised of a room temperature maintained gallium indium and arsenic compound photodiode and capable of converting said three to three and one-half density attenuated beamsplitter ten percent component into a second electrical signal, said detector member diode having a linear dynamic transducer range between 1E5 and 1E6; and

means responsive to a selected one of said first and second electrical signals for generating a measured temperature indication.

23. The apparatus of claim 22 wherein said optical filter means is comprised of a first limited spectral passband residing in said optical transmission member and a filter member of second limited spectral passband.

• • • • •

60

65

## EVALUATION OF OPTICAL DIAGNOSTIC TECHNIQUES FOR HIGH-FREQUENCY TEMPERATURE MEASUREMENTS

V. Vilimpoc, L. P. Goss, and B. Sarka  
Systems Research Laboratories, Inc.  
2800 Indian Ripple Road  
Dayton, OH 45440-3696

A complete study of turbulent flames requires the use of diagnostic techniques capable of measurement rates in excess of the change in the scalar properties being measured. Nonintrusive techniques, in general, are not capable of such high measurement rates (in excess of 5 kHz). However, one such method which has been applied successfully for this purpose is thin-filament pyrometry.<sup>1</sup> This technique relies upon the blackbody emission of a thin ceramic filament for measurement of the temperature distribution.

The major advantages of this technique are high-frequency response, good spatial resolution, and high-sampling-rate capability. The method can be used to measure a temperature profile along a line or at a point. It has been applied successfully to the study of diffusion and premixed flames to obtain temperature profiles in both modes of operation.

The filament is made of ultrafine  $\beta$ -SiC with excess carbon.<sup>2</sup> The fiber diameter (10 - 20  $\mu\text{m}$ ) and thermal conductivity (10 kcal/m  $\cdot$  hr  $\cdot$   $^{\circ}\text{C}$  along the fiber axis at room temperature) allow the fiber to respond rapidly to temperature changes. The fiber has been verified experimentally to be graybody in radiometric terms, i.e., its emissivity (0.88) is not temperature dependent.

The optical arrangement for obtaining a temperature profile along a line is shown in Fig. 1. The rotating mirror and lenses image a different portion of the radiating fiber onto a single-element InGaAs detector. A LeCroy high-speed digitizer then digitizes the analog voltage output from the detector and sends the data to the computer for storage and further analysis. The HeNe and the PIN photodiode provide the necessary synchronization signal for proper digitization of the image. The effective rotation speed of the mirror used in this experiment is 1000 Hz, corresponding to a scan period of 1 ms, and the fiber image is recorded in a 200- $\mu\text{s}$  interval. Estimates of fiber response are between 1 and 2 ms; therefore, the time required to record the image is considered to be adequate. The intensity data are converted to temperature by calibration of the detector response against a known temperature. In the case of the hydrogen diffusion flame, the calibration intensity was obtained from a stoichiometric hydrogen flame. The detector response as a function of wavelength was obtained experimentally and convolved with an integrated blackbody-radiation curve to obtain a calibration curve for conversion of intensity to temperature for the particular detector (see Fig. 2).

In the case of a dynamic event where temperature fluctuates slowly relative to the rotation speed of the scanning mirror, a complete temporal history of the event can be obtained by this method. Several profiles at different elevations above an H<sub>2</sub>-N<sub>2</sub> diffusion flame are shown in Fig. 3. The flame is axisymmetric, and the fiber is located along the central plane of the flame. The evolution of the flame structure and physical processes governing it can be interpreted from this figure. Near the nozzle exit the core of unburnt fuel is surrounded by hot reacting gas which results from the combustion of the fuel with the co-annular flowing air. This reaction zone is well defined and steady near the nozzle due to the molecular-transport nature of the mixing process in this region. Because of the difference in velocities between the inner core of fuel and the co-annular flowing air, a shear layer is formed which has a velocity gradient which tends to transport the air into the fuel core and, thus, promote mixing. The combustng zone enlarges as more and more fuel undergoes combustion, resulting in a rise in temperature with increasing elevation. The increase in temperature, in turn, promotes the formation of a buoyancy-driven vortex whose velocity can be deduced from the spacings between the troughs and crests in the figure along the time axis. These buoyancy-driven vortices grow as a function of height and, at ~ 100 mm axial location, show signs of wrapping the flame surface back upon itself. These vortices are radially symmetric but axially nonsymmetric due to this expansion.

When temperature data at a point is desired, the rotating mirror in Fig. 1 can be replaced by a stationary mirror. The rate of data acquisition can be increased significantly for studying highly dynamic events. To assess the feasibility of this technique for studying turbulent flames, a premixed propane-air flame from a Bunsen burner was studied. The burner has a turbulence generator in the form of four protrusions into the jet stream about one diameter from the nozzle exit. In this case the inner cone exhibits highly turbulent fluctuation. The outline of the inner cone at different heights is imaged onto the detector. The intensity as a function of time at different elevations is shown in Fig. 4. The digitization rate in this case is 5000 Hz., and the period of observation is 200 ms. The turbulence fluctuation is near maximum close to the tip of the inner cone of the flame and decreases with further increase in elevation due to viscous damping. It can be seen from this figure that the fiber response was more than adequate for tracking the temperature fluctuations.

#### References

1. "Combustion Diagnostic Development and Application," SRL R&D Status Report 6890-1 under Contract F33615-85-C-2562, covering the period 16 September 1985 - 16 December 1985 (Systems Research Laboratories, Inc., Dayton, Ohio, 5 March 1986).
2. Dow Corning Corporation (Nippon Carbon Company, Ltd.), Midland, MI 48686-0994.

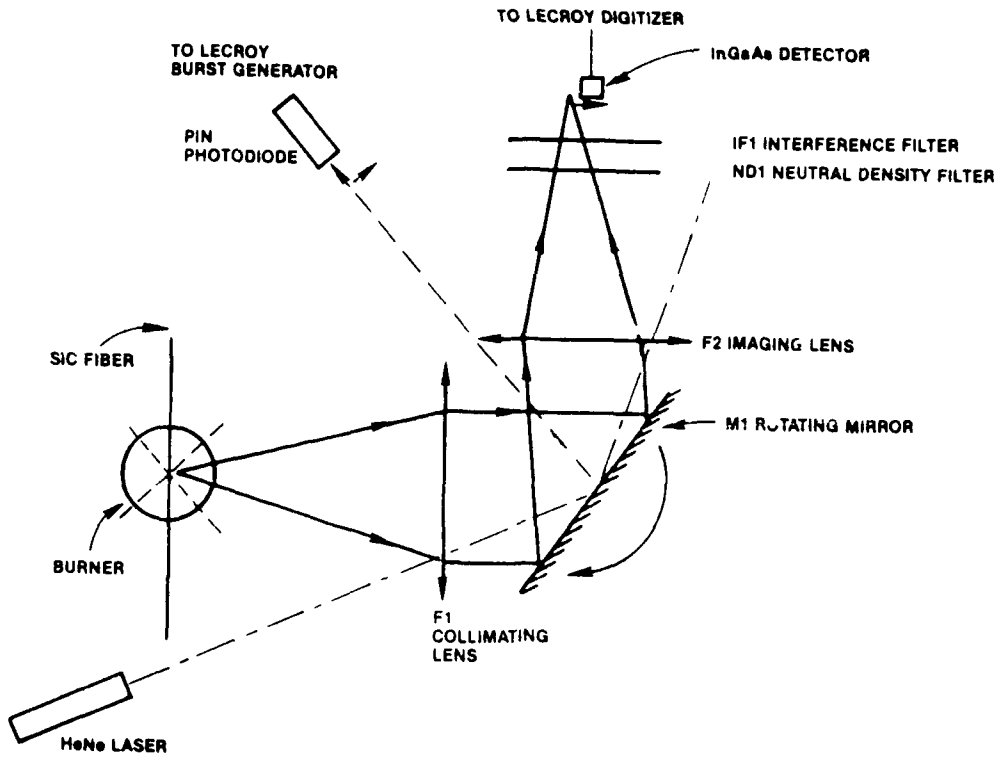


Figure 1. Thin-Fiber-Thermometry Optical Layout.

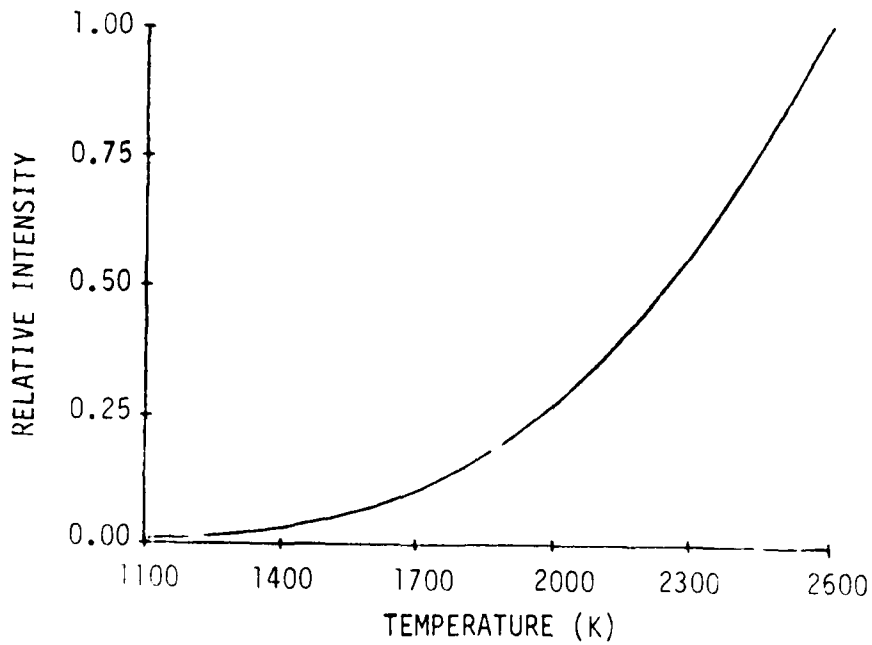


Figure 2. Relative Emission Curve from SiC Thin Filament as Detected by InGaAs Detector.

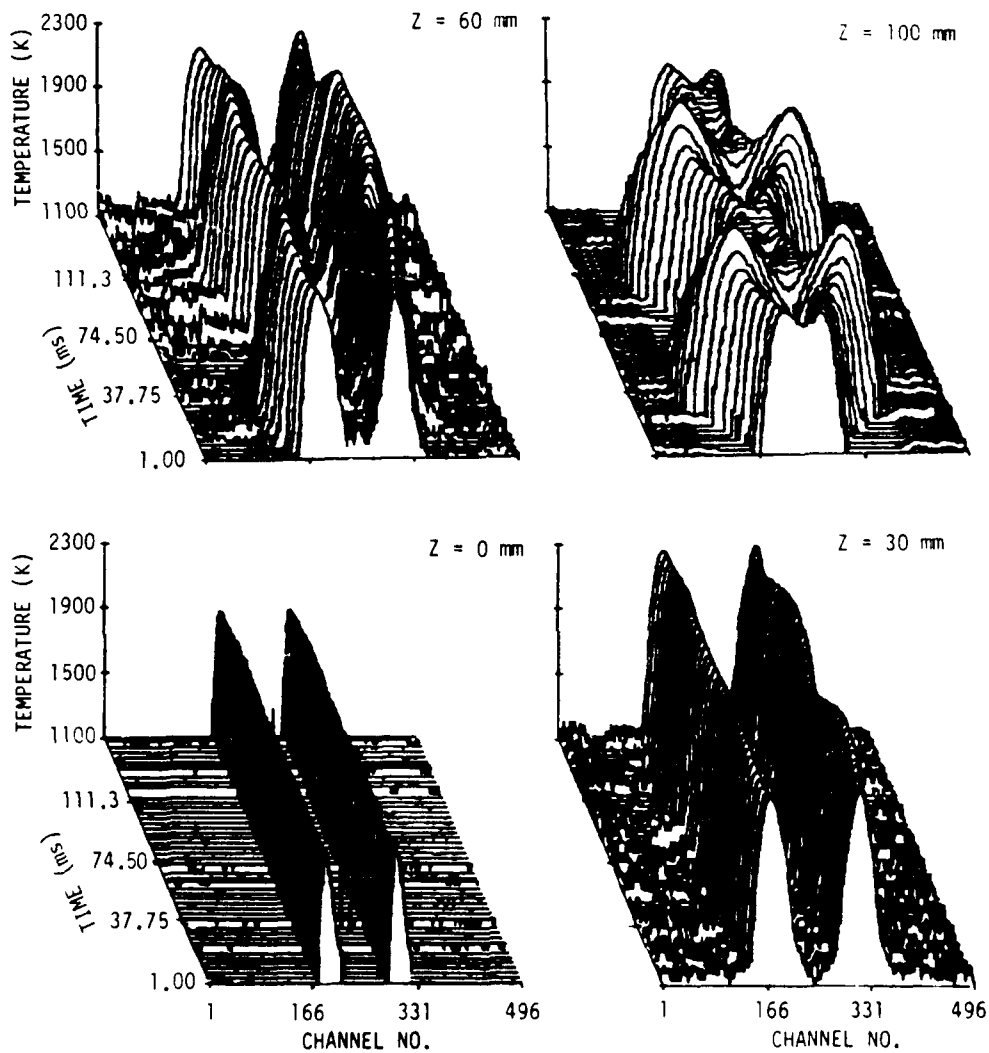


Figure 3. Temperature Profiles of Nitrogen-Diluted Hydrogen Diffusion Flame at Various Axial Locations (Z). Each Channel in X-Axis Corresponds to  $50 \mu$ .

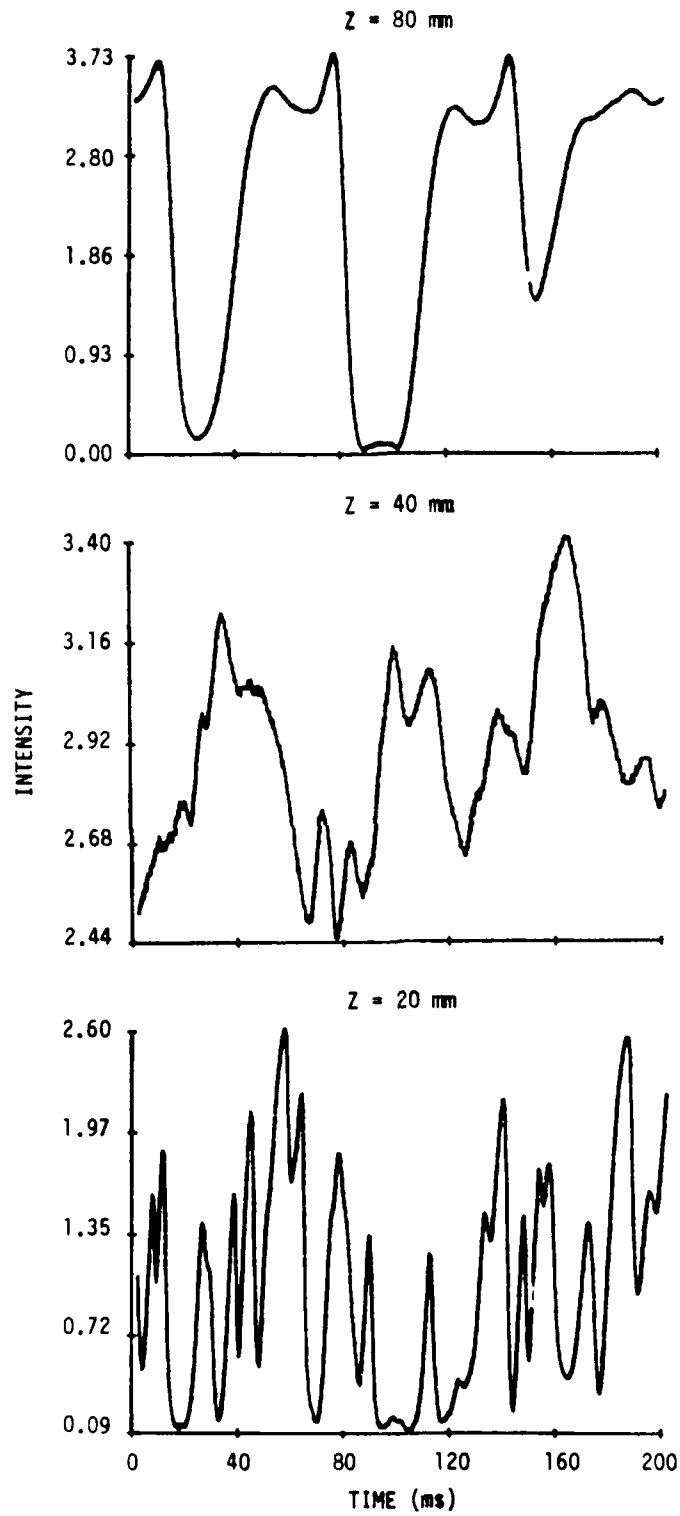


Figure 4. Time History of Fiber Emission from Propane-Air Premixed Flame at Different Axial Locations.

## Spatial temperature-profile measurements by the thin-filament-pyrometry technique

V. Vilimoc, L. P. Goss, and B. Sarka

Systems Research Laboratories, Inc., 2800 Indian Ripple Road, Dayton, Ohio 45440-3696

Received July 23, 1987; accepted October 30, 1987

A novel technique for making temperature measurements in combusting flows is described. This technique, thin-filament pyrometry, is based on the graybody emission of a small ceramic filament (15  $\mu\text{m}$ ), which is introduced into the flow field under study. The technique is applicable over the temperature range 1000–2600 K. The temporal response of the filament is a function of the velocity, constituents, and temperature of the flow field but under ambient conditions is  $\sim 750$  Hz (1/e). The emission from the filament can be recorded over the entire length of the filament, allowing the complete spatial temperature distribution to be recorded.

A complete study of turbulent flames requires the use of diagnostic techniques capable of measurement rates in excess of the change in the scalar properties under study. Nonintrusive techniques, with a few exceptions,<sup>1–3</sup> are incapable of such high measurement rates (in excess of 1 kHz). Probe techniques (i.e., small thermocouples and optical-fiber thermometers) can operate at high frequency rates but yield temperature data only at one spatial location, suffer from perturbations to the flow field, and/or require complicated compensation schemes.<sup>4,5</sup> In this Letter we describe a novel technique capable of moderate-frequency temperature measurements along a line. The technique, thin-filament pyrometry (TFP), relies on the graybody emission of a thin ceramic filament (SiC) in the wavelength range 0.8–1.8  $\mu\text{m}$  for measurement of the temperature distribution in a combusting flow field. The technique is limited to nonsooting flames since the emission from soot can interfere with the filament emission. The TFP technique is similar to a technique reported by Ferguson *et al.*,<sup>6</sup> in which the emission from a silica-coated platinum-platinum-13% rhodium thermocouple was monitored to determine flame temperatures. The major differences between the earlier study and the present one are the use of a  $\beta$ -SiC filament for emission and the fact that line rather than point measurements are being reported.

The filament is made of ultrafine  $\beta$ -SiC with excess carbon and is available commercially.<sup>7</sup> The filament diameter is nominally 15  $\mu\text{m}$ , and the thermal conductivity is 10 kcal/m h<sup>-1</sup> °C<sup>-1</sup> along the filament axis at room temperature. Because of its small size the filament can respond almost instantaneously to temperature changes in its surroundings. The response under ambient conditions was measured to be  $\sim 750$  Hz (1/e). This was determined by heating the filament with a chopped CO<sub>2</sub> laser beam and monitoring the heat-up and cool-down cycles of the filament. The thermal conductivity of the filament is  $\sim 40$  times lower than that of a platinum-platinum-rhodium wire, which drastically reduces the spread in the temperature pro-

file along the filament, resulting in high spatial resolution. Because the emissivity of the filament is large (0.88) (Ref. 8) and is a weak function of temperature and wavelength, the emittance can be directly related to the flame temperature.

Quantitative measurements with the filament require that its temperature response be calibrated or adequately predicted in order to establish a distinct relationship between filament-emission intensity and temperature. The equation describing the graybody emission from such a filament is well established. The Planck equation that describes the radiance for a graybody is

$$L(\lambda_0) = \frac{\epsilon(\lambda_0, T)C_1}{\lambda^5[\exp(C_2/\lambda_0 T) - 1]} \text{ (W/m sr)}, \quad (1)$$

where  $\epsilon(\lambda_0, T)$  is the emissivity of the filament,  $C_1$  is the first radiation constant,  $C_2$  is the second radiation constant,  $\lambda_0$  is the wavelength in vacuum, and  $T$  is the filament temperature. If Eq. (1) is to be used for quantitative measurement of the temperature of the filament, the emissivity of the filament must be known as a function of temperature, angle, and wavelength. The emissivity of SiC is reported in Ref. 8 to be a weak function of temperature, wavelength, and angle. To verify that this is indeed the case for the SiC filaments, the relative emissivity as a function of temperature was measured by a reflectance technique. The reflectance of the filament can be related to its emissivity by Kirchhoff's relationship

$$\epsilon(\theta, \phi) = 1 - \rho_h(\theta, \phi), \quad (2)$$

where  $\rho_h(\theta, \phi)$  is the hemispherical reflectance, which is the sum over all angles of the bidirectional reflectance-distribution function (BRDF). In order for Eq. (2) to hold, the reflectance from the surface at all angles must be measured or the surface must be uniformly illuminated with light from all directions and the reflectance measured at a fixed angle.

Of actual importance in the implementation of the TFP technique is the relative change in the emissivity

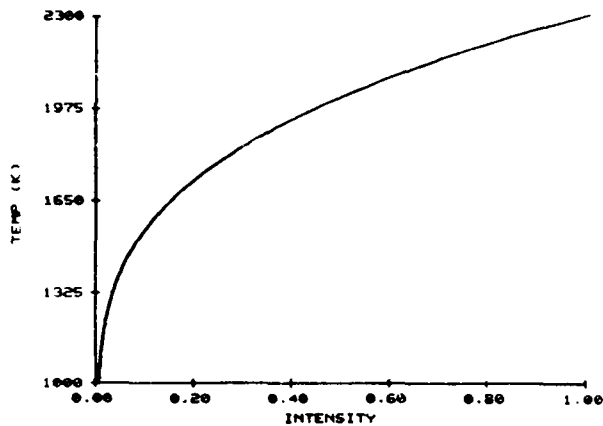


Fig. 1. Calculated emission curve of SiC filaments as function of temperature when InGaAs is used as the detector.

with  $T$  rather than the absolute value of the emissivity, since the filament can always be introduced into a flame of a known temperature for calibration. The relative change in the emissivity can be measured by monitoring a single near-normal angle, assuming that the BRDF is not a function of temperature. In this case, the emissivity was determined to be a constant and did not vary within the precision of the reflectance experiment, which was of the order of 1.0%. In order to monitor whether the BRDF was, in fact, a function of temperature, measurements at normal and at  $\pm 45$  deg were made. No change in the reflectance with temperature was observed. Because the emissivity does not vary with temperature, the graybody equations adequately describe the filament-emission intensity. In practice, however, a detector of limited spectral bandwidth (0.8–1.8  $\mu\text{m}$ ) is used to detect the emission; thus the graybody emission must be multiplied by the detector response to predict the filament response. The detected emission is described by

$$D_e(T) = k_e \int_0^{\infty} L(\lambda, T) R(\lambda) T_r(\lambda) d\lambda, \quad (3)$$

where  $L(\lambda, T)$  is the graybody function,  $R(\lambda)$  is the response function of the InGaAs photodiode,  $T_r(\lambda)$  is the transmission characteristics of the optics employed in the experiment, and  $k_e$  is an experimental constant that takes into account the collection efficiency of the optical system. As we stated above, the system is calibrated by placing the filament within a flame of known temperature (either a hydrogen-air diffusion flame or a propane-air premixed flame). The signal from this flame is then used to normalize the results from an unknown flow field. The resulting calibration curve is shown in Fig. 1. As can be seen from the figure, the detected emission varies greatly with temperature. Because of this variance along with the limited dynamic range of the digitization system (255 to 1), the temperature uncertainty can be large (especially at low temperatures). Assuming a 1% uncertainty in the intensity measurement, the temperature uncertainty at 1100 K is  $\sim 80$  K and at 2300 K is  $\sim 8$  K.

The temperature of the filament may be different from that of the surrounding gas because of radiation losses. Thus a detailed heat-balance analysis must be conducted for accurate prediction of the gas temperature. In general, the relationship between the gas temperature and the filament temperature is given by

$$T_g = T_f + \frac{\epsilon \sigma T_f^4}{h_c} \quad (4)$$

where  $T_g$  is the gas temperature,  $T_f$  is the filament temperature,  $\sigma$  is the Stefan-Boltzmann constant, and  $h_c$  is the heat-transfer coefficient. A similar equation was derived in Ref. 6. The results of such an analysis for the flame conditions reported herein indicate that the radiation correction varies from 30 K at 1200 K to 200 K at 2300 K.

The optical arrangement employed for obtaining filament emission along a line is shown in Fig. 2. The light from the filament is collimated by a lens ( $f/5$ ) and directed onto a rotating mirror, which sweeps the image of the filament through a focusing lens ( $f/2.5$ ) and across a single InGaAs diode detector. A LeCroy TR8818 transient recorder is used to digitize the analog signal from the detector and store it in an MM8103 ECL memory unit for subsequent transmission to a Modcomp Classic minicomputer for storage and analysis. By sweeping the image across a single detector, one can record the emission along the length of the wire as a function of time. The He-Ne laser and the P-I-N photodiode provide the necessary synchronization signals for proper digitization of the image. The image was swept by the detector at an effective rate of 1000 Hz. The image of a 6-cm length along the wire is recorded in 512 discrete samples during a 200- $\mu\text{sec}$  window at the rate of 2.56 MHz. This translates into an effective spatial resolution of 120  $\mu\text{m}$  per sample point. The spatial resolution obtained is a function of the magnification factor used in the imaging process and, hence, can be varied subject to the limitation imposed by the decreasing signal-to-noise ratio at higher magnification. Because of the limited spectral response of the InGaAs detector employed in these studies, only temperatures in excess of 1000 K could be

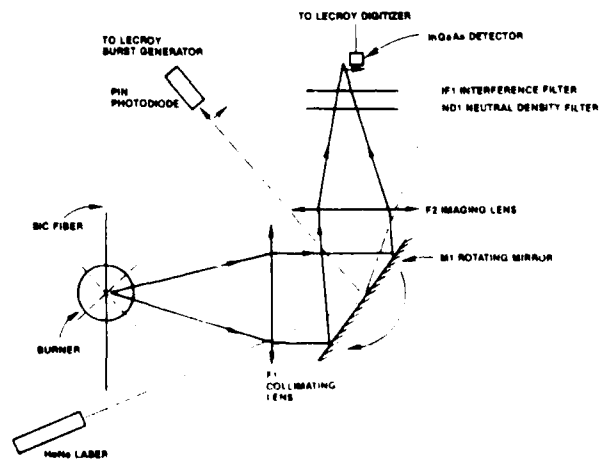


Fig. 2. Thin-filament-pyrometry optical layout.

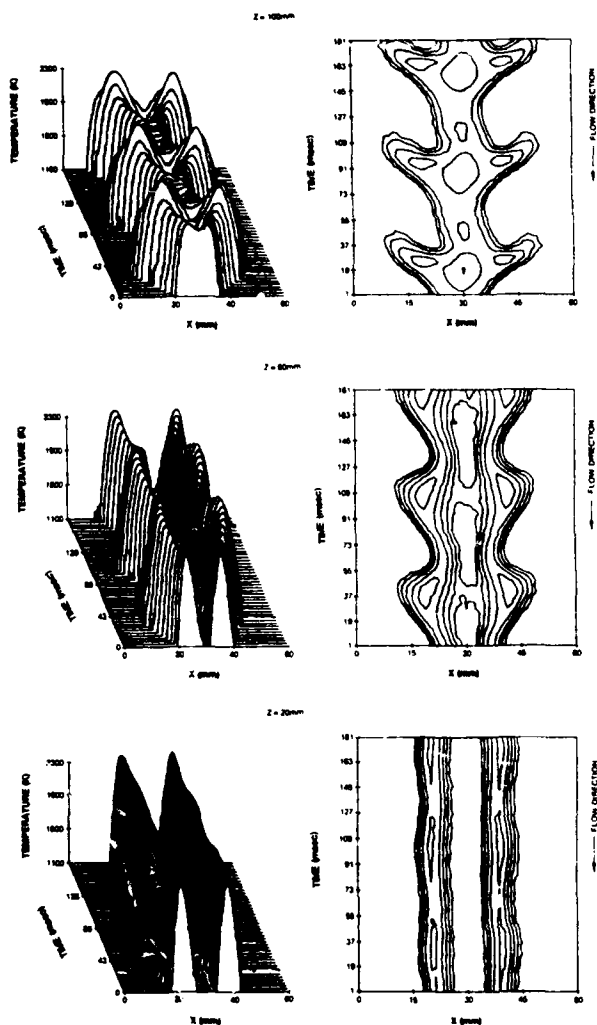


Fig. 3. Temperature profiles of nitrogen-diluted hydrogen-diffusion flame at various axial locations ( $Z$ ). Each channel in the  $X$  axis corresponds to  $120 \mu\text{m}$ .

measured. However, with a suitable choice of IR detector and optics, this lower temperature limit could be extended.

To demonstrate the capability of this technique in a dynamic flame environment, a hydrogen-nitrogen diffusion flame was profiled. The flame consisted of a 1-cm contoured jet surrounded by a coannular air jet. The hydrogen and nitrogen were mixed in the ratio 0.06 to 1. The adiabatic flame temperature for such a mixture was calculated to be  $\sim 2320$  K. These types of flame are known to exhibit large-scale buoyancy-driven structures that fluctuate in the range 10–20 Hz.<sup>9</sup> The filament was placed on the centerline of the diffusion jet and an axial profile of the flame made. The temporal-radial temperature profiles taken at various axial locations are displayed in Fig. 3. The evolution of the large-scale flame structures can be studied from

this figure. Near the nozzle exit, the core of unburned fuel is surrounded by a hot reacting cone, which results from the combustion of the fuel and the coflowing air. The reaction zone is well defined and steady near the nozzle exit owing to the molecular-transport nature of the mixing processes in this region. Because of the difference in the velocities of the fuel and air jets, a shear layer is formed, which tends to transport the air into the fuel jet and thus to promote mixing. The reaction zone enlarges as more and more air is mixed with the fuel and undergoes combustion, resulting in a rise in the temperature with increasing elevation from the nozzle exit. The adiabatic temperature of 2320 K is in good agreement with the observed peak temperature of 2315 K. The increase in temperature, in turn, promotes a density gradient, which results in the formation of a buoyancy-driven vortex whose frequency can be deduced from the temporal scans in Fig. 3. These buoyancy-driven vortices grow as they travel downstream and eventually wrap the flame surface back upon itself. The periodicity of the vortices is reproducible and was determined to be  $\sim 15.5$  Hz. These large-scale vortices are responsible for the growth of the reaction zone and the eventual collapse of the potential core at downstream axial locations.

In summary, thin-filament pyrometry offers the unique capability to record the temperature distribution of a flow field as a function of time along a line. The combination of small size, high emissivity, and low thermal conductivity of the ceramic filaments results in fast temporal response as well as good temperature sensitivity and spatial resolution.

This research was supported under U.S. Air Force contract F33615-85-C-2562.

## References

1. L. P. Goss, D. F. Grosjean, and B. Sarka, presented at the American Institute of Aeronautics and Astronautics/Society of Automotive Engineers/American Society of Mechanical Engineers 21st Joint Propulsion Conference, Monterey, California, July 8–10, 1985.
2. D. R. Ballal, T-H. Chen, and P. P. Yaney, presented at the 24th Aerospace Sciences Meeting, Reno, Nevada, January 6–9, 1986.
3. T. M. Dyer, *AIAA J.* 17, 912 (1979).
4. A. Ballantyne and K. N. C. Bray, in *Sixteenth Symposium (International) on Combustion* (Combustion Institute, Pittsburgh, Pa., 1977), p. 777.
5. R. R. Dils and D. A. Tichenor, presented at the Western States Section of the Combustion Institute 1984 Spring Meeting, Boulder, Colorado, April 2–3, 1984.
6. C. R. Ferguson and J. C. Keck, *J. Appl. Phys.* 49, 3031 (1978).
7. Nicalon, Silicon Carbide Fiber, Dow Corning Corporation, Midland, Mich. 48686-0995.
8. Y. S. Touloukian, ed., *Nonoxides and Their Solutions and Mixtures Including Miscellaneous Ceramic Materials*, Vol. 5 of *Thermophysical Properties of High Temperature Solid Materials* (Macmillan, New York, 1967), pp. 119–140.
9. A. W. Strawa and B. J. Cantwell, *Phys. Fluids* 28, 2317 (1985).

## SiC-BASED THIN-FILAMENT PYROMETRY: THEORY AND THERMAL PROPERTIES

V. VILIMPOC AND L. P. GOSS

*Systems Research Laboratories  
A Division of Arvin/Calspan  
2800 Indian Ripple Road  
Dayton, OH 45440-3696*

Blackbody radiation from a thin filament of  $\beta$ -SiC can be used to measure the spatial temperature distribution in a combusting flowfield. The technique, Thin-Filament Pyrometry, exhibits rapid temporal response and excellent spatial resolution because of the small diameter and low thermal conductivity of the filament. Factors which affect the accuracy, temporal response, and spatial resolution of the probe in a  $H_2$ - $N_2$  jet diffusion flame are presented.

### Introduction

Semiconductor materials are ideal candidates for spatial blackbody temperature probes. This class of materials has lower thermal conductivity than binary or tertiary metal alloys used in conventional thermocouples, is generally inert to oxidizing atmospheres, and exhibits relatively high emissivity. One such material,  $\beta$ -SiC, can be obtained commercially<sup>1</sup> in the form of a 15- $\mu$ m-diameter filament whose thermal conductivity (10 kcal/m hr  $^\circ$ C) is 40 times lower than that of Pt-PtRh wire. Because of the small size of the filament, the ratio of the circumferential to cross-sectional surface area is large; hence, the rate of heat transfer by convection and radiation is much higher than the rate of energy storage and axial-conduction heat transfer. As a result, the filament exhibits excellent spatial resolution and temporal response to transient heat input.

The technique, Thin-Filament Pyrometry (TFP), is similar to one reported by Ferguson, et al.,<sup>2</sup> in which the emission from a silica-coated platinum-platinum-13% rhodium thermocouple was monitored to determine flame temperature. The present study differs from the earlier work in that  $\beta$ -SiC was used as the emitter and that line rather than point temperature measurements were made.

### Theory

The Planck equation for graybodies which governs heat-transfer processes occurring via radiative exchange of energy is given by

$$L(\lambda, T) = \frac{\epsilon C_1}{\lambda^5 [\exp(C_2/\lambda T) - 1]} \quad (1)$$

where  $\epsilon$  is the apparent emissivity of the filament,  $C_1$  and  $C_2$  the first and second radiation constants, respectively,  $\lambda$  the wavelength in vacuum, and  $T$  the absolute filament temperature. Because it is a function of temperature and wavelength, the emissivity of the filament must be known or determined experimentally over the entire wavelength range of interest. The emissivity of SiC as a function of temperature and wavelength has been measured experimentally by a number of workers<sup>3-9</sup> and determined to be a very weak function of temperature and relatively constant for the wavelengths used in the present study. Because the filament is a graybody, Eq. (1) can be used to describe its emission as a function of temperature. Experimentally, the detector used to observe the emission will have a limited response over a range of wavelengths (900-1600 nm), and this factor must be taken into account. Equation (1) must then be multiplied by the detector response function and the transmission characteristics of the optics and integrated over the detector-response-wavelength bandwidth. The detected power is given by

$$D_T = k_{exp} \int_{\lambda_1}^{\lambda_2} L(\lambda, T) R(\lambda) T_r(\lambda) d\lambda \quad (2)$$

where  $L(\lambda, T)$  is the graybody response given by Eq. (1),  $R(\lambda)$  the detector-response function,  $T_r(\lambda)$  the transmission characteristics of the optics,  $\lambda_1$  and  $\lambda_2$  the lower and upper limits of the detector response, respectively, and  $k_{exp}$  an experimental constant which takes into account the efficiency of the

collection optics and the gain of the detector electronics. Technically, the constant  $k_{exp}$  is a function of the experimental system and should be determined for all collection angles employed. In reality, the emission is collected within  $\pm 5$  degrees of normal incidence, and the variation in the efficiency is quite small. Equation (2) relates the detected emitted power to the filament emission, the detector-response function, and the transmission characteristics. Thus, the emission from the filament at a known temperature can be used to calculate the relative emitted power. Subsequently, other temperatures can be calculated from Eq. (2) by normalization to the relative emitted power; therefore, the experimental constant need not be determined. Because of the nonlinear nature of the Planck equation, the observed filament emission is also nonlinear. A curve generated from Eq. (2) is shown in Fig. 1. At the low-temperature limit of the curve, the slope is very steep, indicating that a small change in emittance corresponds to a very large change in temperature. The lowest detectable signal corresponds to 1000 K, and the maximum temperature emission is at 2370 K. Because of the steep slope at low temperature, the measurement precision is 80 K. In contrast, at the high-temperature limit, the change in temperature with intensity is small while the intensity itself is large; thus, the measurement precision is improved to 8 K. The noise in the experimental system was determined to be 1% of full scale.

### Experimental

To verify the feasibility of the technique, a  $H_2-N_2$  jet diffusion flame was chosen for study.<sup>10</sup> This flame is ideally suited for study by the TFP technique due to the presence of large-scale buoyancy-driven structures (bulges) at relatively low Reynolds numbers.<sup>11</sup> Temperature measurements in these flames have been made traditionally by means of thermocouples and the CARS technique.<sup>12</sup> In both

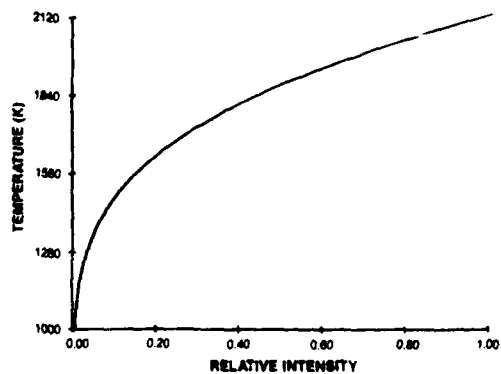


FIG. 1. Plot of Filament Temperature as Function of Intensity.

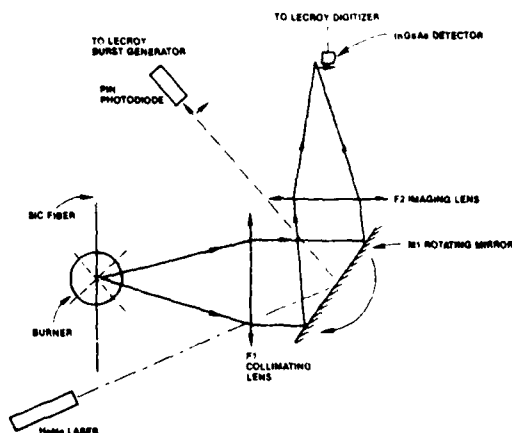


FIG. 2. Schematic Diagram of Experimental Arrangement for TFP Technique.

cases it is difficult to interpret the single point measurements due to the dynamic nature of these flames. A wealth of information can be obtained by the TFP technique due to its high-frequency response and good spatial resolution.

A schematic diagram of the experimental arrangement is shown in Fig. 2. The filament was stretched across the flame at the center of a 10-mm nozzle by a holder which supplied sufficient tension to prevent movement of the filament. The holder is made of two thin strips of flexible steel to which the filament is attached by means of tape. The emission from the filament was collimated by an  $f/5$  lens. A rotating multi-faceted mirror swept the collimated light from the filament, and an  $f/2.5$  lens formed an image of the filament at the detector plane. The InGaAs detector has an active element 80  $\mu m$  in diameter whose spectral bandwidth covers the region from 900 to 1600 nm. The mirror-detector combination converts a spatial scan into a temporal one. To synchronize the scanning and digitization of the detector signal, the output of a HeNe laser is reflected off the mirrors and collected by a PIN photodiode to produce a pulse which is used to activate the digitizer. The synchronization pulse from the PIN photodiode is delayed as needed and used to open a 200- $\mu s$  gate centered on the sweep of the filament image. The gate is used in conjunction with a pulse generator to send 512 pulses to the LeCroy digitizer. The output from the InGaAs detector is amplified and fed into a LeCroy TR8818 Transient Recorder. The digitized data are stored in a bank of LeCroy MM8103 ECL Memory Units. The digitization sequence continues until the memory is filled. The data are then transferred through a custom-built interface to a ModComp 7870 Classic Mini-computer for analysis. The digitization rate and gate-pulse width (200  $\mu s$ ) are set for a 1000-Hz sweep rate of the filament image. A 6-cm length of filament is recorded in 512

discrete samples which produces an equivalent spatial resolution of 120  $\mu\text{m}$  per sample point. The spatial resolution is a function of the magnification factor used in the imaging process, the period and number of digitization pulses, and the rotational speed of the scanning mirrors and, hence, can be varied subject to the constraint of decreasing signal-to-noise ratio at higher magnification. Because of the limited response of the InGaAs detector employed in the study, only temperatures in excess of 1000 K can be measured. However, with a suitable choice of IR detector and optics, this lower temperature limit can be extended. In the  $\text{H}_2\text{-N}_2$  flame studied, the longevity of the filament varied from 15 to 30 min. which permits a complete traverse of the flame to be made with one filament.

### Thermal Behavior of the Filament

#### Convective and Radiative Energy Balance:

The ability of the filament to measure flame temperature depends upon the rate at which heat can be transferred from the hot combustion gas to the filament. For the case of a small filament in a cross-flow, the rate of heat transfer by axial thermal conduction is negligible compared with that by convection and radiation.<sup>15</sup> Assuming steady-state conditions, the energy balance for the filament can be written as

$$hP(T_g - T_f) = \sigma\epsilon PT_f^4 \quad (3)$$

$$T_g = T_f + \frac{\sigma\epsilon T_f^4}{h} \quad (4)$$

where  $h$  is the heat-transfer coefficient,  $P$  the circumferential surface area, and  $\sigma$  the Stefan-Boltzmann constant. When Eq. (3) is rearranged into the form of Eq. (4), it is obvious that the last term on the right-hand side represents the difference between the gas and the filament temperature. This is a systematic error resulting from the temperature difference required to transfer energy to the filament by convection.

In order to determine the correction to the filament temperature, the heat-transfer coefficient must be found. This coefficient is a phenomenologically determined parameter which relates the following variables in a heat-transfer process: the fluid properties, the diameter of the cylinder, and the velocity of the fluid. It can be obtained from the following equations:

$$\text{Re} = \frac{dU}{\nu} \quad (5)$$

$$\text{Nu} = \frac{hd}{k} = c(\text{Re})^n \quad (6)$$

$$h = c(\text{Re})^n \frac{k}{d} \quad (7)$$

where  $\text{Nu}$  is the Nusselt number,  $\text{Re}$  the Reynolds number,  $k$  the thermal conductivity of the fluid,  $U$  the average velocity of the fluid,  $\nu$  the kinematic viscosity, and  $d$  the diameter of the cylinder. For the range of experimental conditions in the present study, the values of the parameters  $c$  and  $n$  are 0.800 and 0.280, respectively.<sup>13</sup> The fluid properties must be determined at the film temperature (average of filament and gas temperatures). Since the gas temperature is not known *a priori*, the temperature-correction procedure must be iterative in nature.

The algorithm used to correct for the radiative heat loss is discussed below. The filament temperature calculated via Eq. (2) is assumed to be the gas temperature. The mole fractions of the fuel, oxidant, and products are then calculated via an adiabatic-equilibrium program corresponding to this temperature. The mole fraction-weighted average transport properties are then calculated and used to obtain the Reynolds number and the Nusselt number according to the relationship in Eqs. (5) and (6), respectively. Since the quantity sought is the average heat-transfer coefficient, the volume average velocity (the ratio of the volume flow rate to the cross-sectional area of the nozzle) was used to calculate the Reynolds number. Provision could be made to use an actual velocity profile such as that obtained by LDV for this purpose. Once the Reynolds number is obtained, the heat-transfer coefficient  $h$  can be calculated and used in Eq. (4) to obtain the corrected gas temperature  $T_g$ . This temperature is then used in place of the assumed gas temperature to obtain the true thermodynamic-equilibrium gas composition. The entire process is then repeated to obtain a more accurate corrected gas temperature. The correct gas temperature can usually be obtained within two iterations of this process.

The above temperature-correction procedure was applied to the  $\text{H}_2\text{-N}_2$  jet-diffusion-flame data obtained with the experimental arrangement discussed above. A plot of  $T_f$  as a function of  $\Delta T$  is

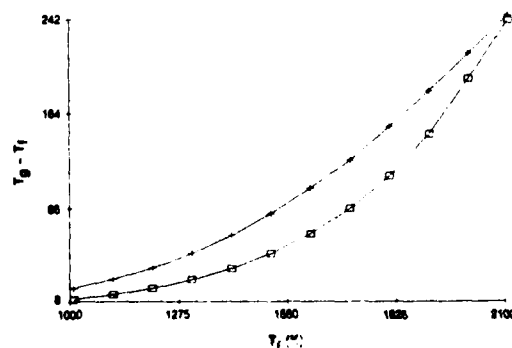


FIG. 3. Plot of Temperature Difference Due to Radiation as Function of Filament Temperature. + — Fuel-Lean Case, □ — Fuel-Rich Case.

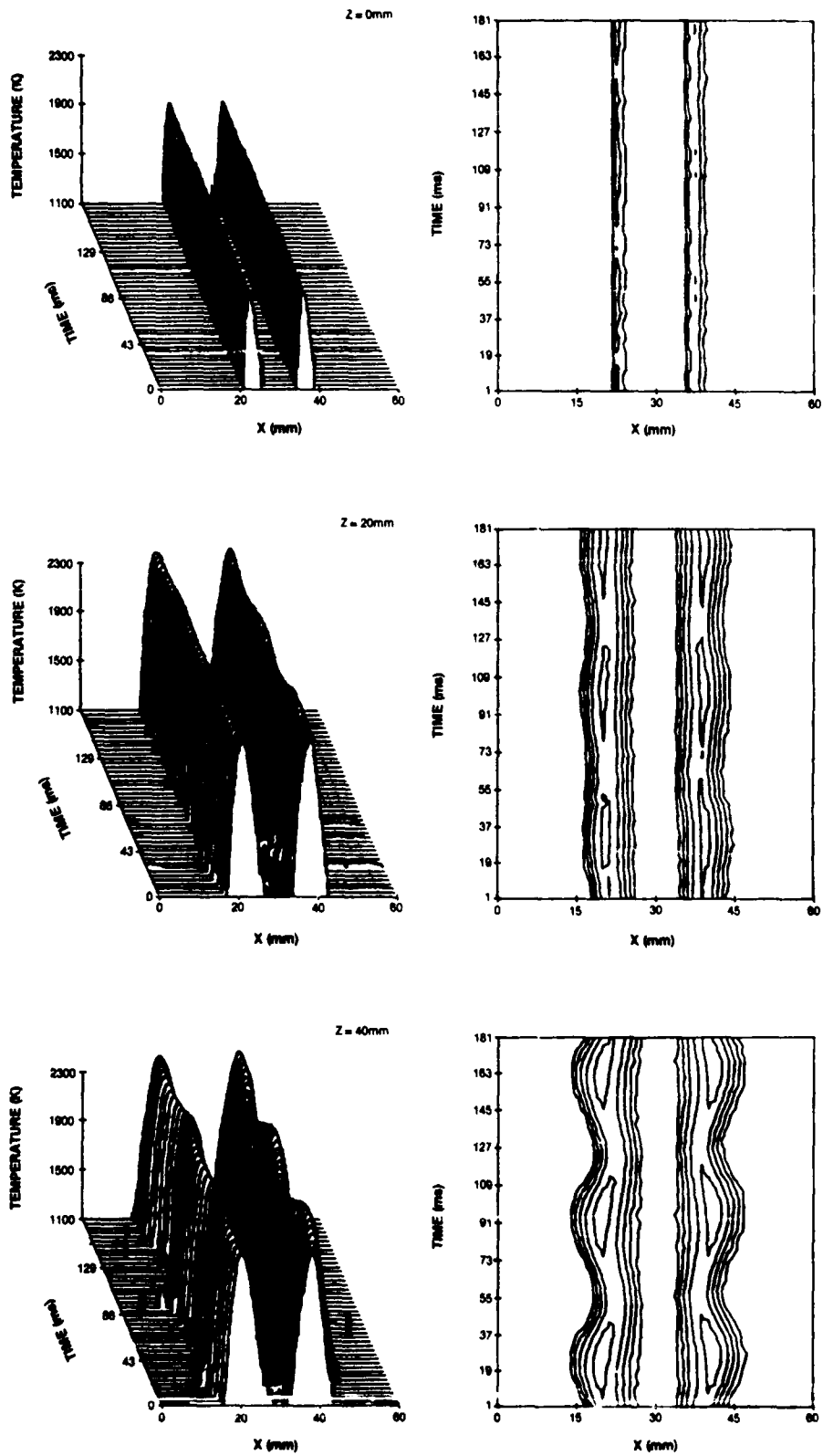


FIG. 4. Corrected Temperature Profiles at Different Axial Elevations.

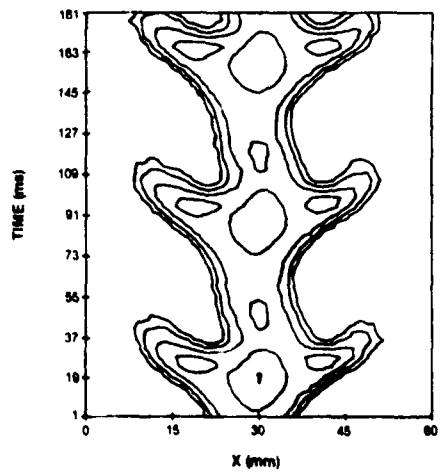
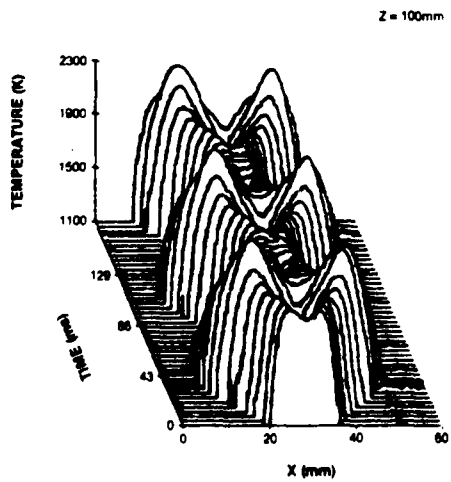
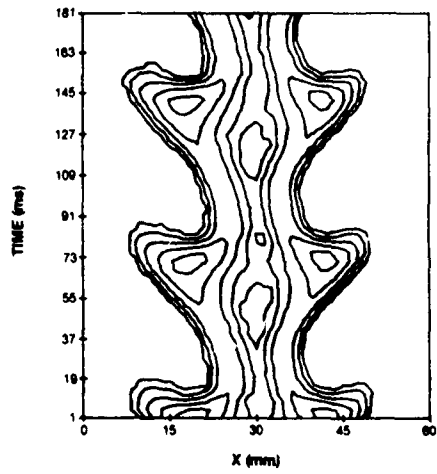
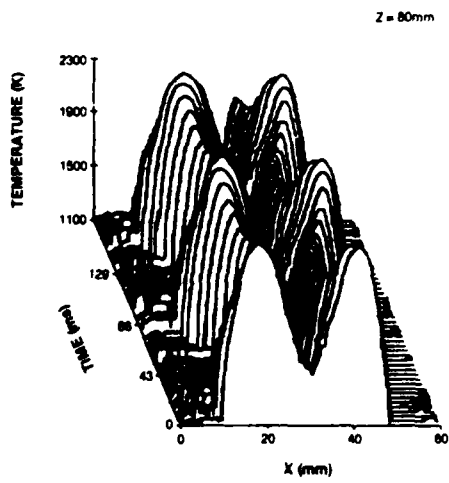
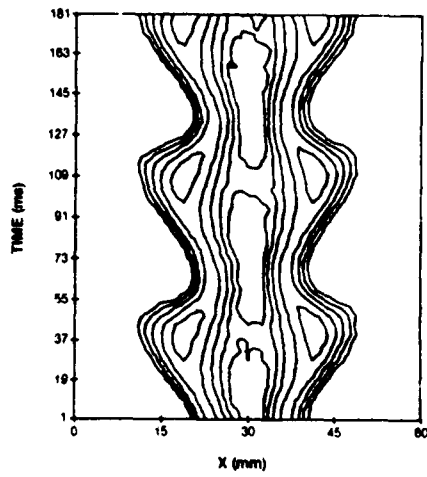
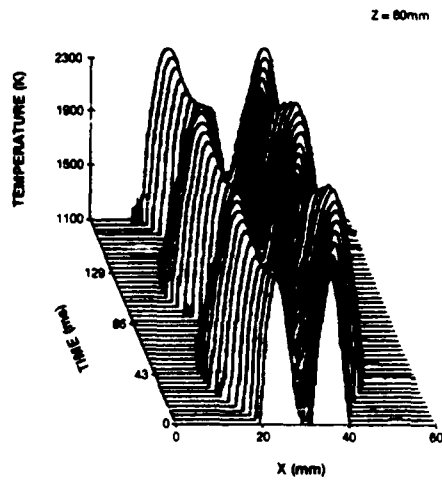


FIG. 4. (Continued)

shown in Fig. 3. Note that two values are possible for each  $T_f$ . At equilibrium the gas composition is a function of both space and temperature. Inside the reaction zone, an abundance of fuel will be present but relatively little oxidant because most of the oxidant will have been consumed during the transportation across the reaction zone. Conversely, on the annular-air side of the reaction zone, relatively little fuel will remain after combustion at the flame surface. Because the thermal properties of hydrogen differ greatly from those of air, the local composition of the gases must be taken into account when determining the heat-transfer properties of the filament.

Figure 4 shows the corrected temperature profiles at a few axial locations above the nozzle which were collected using the experimental arrangement described above. Note the spatial and temporal development of low-frequency oscillations in the temperature field.

#### Transient Response:

The temporal response of the filament to a rapid change in temperature is obtained by solving the energy equation as a function of time. This can be expressed as the rate of change in the internal energy of the filament (which is initially at a temperature  $T_f$ ) as it cools down by convection, conduction, and radiation to the surrounding gas temperature,  $T_\infty$ :

$$\rho C_p V \frac{dT_f}{dt} = hP(T_f - T_\infty) + \sigma \epsilon P T_f^4 + kA \frac{d^2 T_f}{dx^2} \quad (8)$$

where  $C_p$ ,  $k$ ,  $V$ , and  $\rho$  are the heat capacity, thermal conductivity, volume, and density of the filament, respectively,  $A$  the cross-sectional surface area, and  $t$  time. It can be shown that the contribution from conduction heat transfer is negligible as compared to that from the other mechanisms. Equation (8) should be integrated numerically since  $h$  is not a constant but changes with temperature. The relative importance of each mechanism in the various temperature regimes can be appreciated by inspection of Table I. The heat-transfer coefficients used

TABLE I  
Relative Contribution from Heat-Transfer Mechanisms

T (K)	$h(T_\infty - T_f)$ (cal/sec cm)	$\sigma \epsilon T_f^4$ (cal/sec cm)	$\frac{\sigma \epsilon T_f^4}{h(T_\infty - T_f)}$
1000	46.9	1.2	0.025
1400	81.0	4.6	0.056
1800	118.9	12.5	0.105
2000	142.6	19.1	0.134

are those from the inside flame surface and represent the worst-case situation for the present study. The data used here were obtained from Ref. 14. As can be seen from the table, the relative importance of radiative heat transfer increases with the absolute temperature of the filament. Neglecting the contribution from the radiative heat-transfer process and taking into account the initial condition  $T(0) = T_0$ , the time constant of the filament due to convection is as follows:

$$\tau = \frac{\rho C d}{4h} \quad (9)$$

or

$$1.8 \times 10^{-3} < \tau < 4.95 \times 10^{-4} \text{ sec}$$

for the lower and upper bounds of temperature as shown in Table I.

To confirm the calculation of the temporal response of the filament, the response was measured experimentally using a  $\text{CO}_2$  laser to heat the filament for a short period of time. The emission of the filament was then monitored with an InGaAs detector as a function of time. One heat-up and cool-down cycle is shown in Fig. 5. The experiment was performed in ambient air and, therefore, represents a lower limit to the filament response time. The  $1/e$  value taken from this curve corresponds to 1.5 ms, in good agreement with the previous calculation. The typical filament response is 700 Hz. Heiter, et al.,<sup>16</sup> also obtained results which indicate similar dependence of the time constant upon the velocity and the properties of the gas.

#### Thermal Spatial Resolution:

One of the major advantages of the TFP technique is the ability to measure temperature distri-

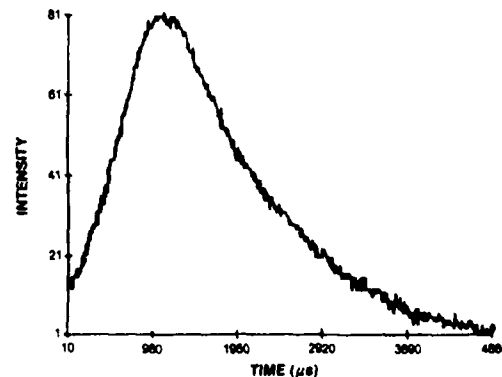


FIG. 5. Experimental Heat-Up and Cool-Down Cycle.

bution along the length of the filament. For each differential element of the filament to respond to the local gas temperature, the axial thermal diffusion must be small. To evaluate the magnitude of the thermal diffusion, an axial energy balance is performed. The analysis is based on the assumption that radiative heat transfer does not contribute significantly to the overall process. This assumption is made to simplify the mathematics involved but will not invalidate the result in view of the relative importance of each heat-transfer mechanism presented in Table I. The effect of not including the radiation term will be an overestimate to the diffusion length by an average of 5 to 15%. The analytical solution<sup>17</sup> obtained with the boundary conditions  $T = T_0$  at  $x = 0$  and  $dT/dx = 0$  at  $x = \ell$  is shown below:

$$\frac{d^2T}{dx^2} = m^2(T - T_\infty) \quad (10)$$

$$\Delta T = \frac{\cosh m(\ell - x)}{\cosh m\ell} \Delta T_i \quad (11)$$

where

$$m = \sqrt{\frac{4h}{kd}}$$

Using Eq. (10) and the assumption that the temperature on one end of the filament is held at 2370 K while the other end is at 300 K, the temperature profile along the filament can be generated and is plotted in Fig. 6. The distance over which axial thermal diffusion causes the temperature to decay from 2370 to 300 K is  $\sim 120 \mu\text{m}$ . Because of the low thermal conductivity and the relatively large circumferential surface area as compared to the cross-

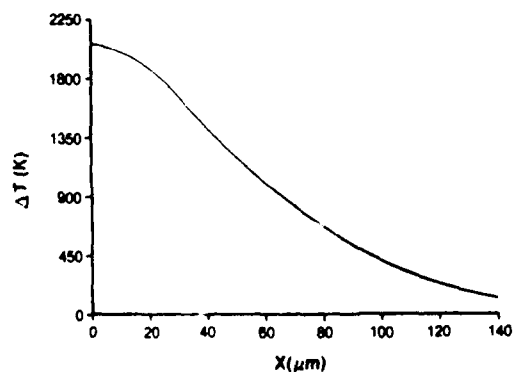


FIG. 6. Theoretical Axial-Temperature Profile Due to Thermal Diffusion.

sectional area, the hot zone is restricted to a small region adjacent to the hot surface. Therefore, very little degradation of the temperature profiles occurs along the filament axis.

### Conclusion

The TFP technique has been demonstrated to be capable of measuring temporal-spatial temperature distribution in a nonsmoking flame. It is characterized by its high spatial resolution, fast temporal response, and ability to measure the temperature distribution along a line rather than at a point. An examination of the thermal properties of the SiC filament indicates that axial thermal diffusion is very small but that a radiation correction must be made to arrive at the correct flame temperature. An algorithm presented for calculating the correction factor was shown to be dependent upon the gas velocity and properties.

### Acknowledgment

This work was performed under USAF Contract No. F33615-85-C-2562.

### REFERENCES

1. Dow Corning Corp. (Nippon Carbon Company, Ltd.), Midland, MI 48686-0994.
2. FERGUSON, C. R. AND KECK, J. C.: *J. Appl. Phys.* 49, 3031 (1978).
3. OLSON, O. H. AND MORRIS, J. C.: ARF. WADC-TR-56-222, III. AD-239-302.
4. BLAU, H. H., JR., CHAFFEE, E., JASPERSE, J. R. AND MARTIN, W. S.: Arthur D. Little, Inc. USAF. AFCRC-TN-60-165. AD-236-394.
5. BLAU, H. H., JR., MARCH, J. B., MARTIN, W. S., JASPERSE, J. R. AND CHAFFEE, E.: Arthur D. Little, Inc. USAF. APCRL-TR-60-416. AD-248-276.
6. MITCHELL, C. A.: *J. Opt. Soc. Am.* 52, 341 (1962).
7. WADE, W. R. AND SLEMP, W. S.: NASA TN-D-998. AD-272-614.
8. SCHATZ, E. A., GOLDBERG, D. M., PEARSON, E. G. AND BURKS, T. L.: Air Force Materials Laboratory. ASD-TDR-63-657, I. AD-423-743.
9. Thermophysical Properties of High Temperature Solid Materials, Vol. 5 - Nonoxides and Their Solutions and Mixtures Including Miscellaneous Ceramic Materials (Y. S. Touloukian, Ed.). pp. 118-140. MacMillan Co. 1967.
10. VILIMPOC, V., GOSS, L. P. AND SARKA, B.: Evaluation of Optical Diagnostic Techniques for High-Frequency Temperature Measurements.

- Paper presented at the 1987 Spring Technical Meeting of the Central States Section of The Combustion Institute. Argonne, IL. May 1987.
11. ROQUEMORE, W. M., GOSS, L. P., LYNN, W. F. AND CHEN, L. D.: Structure of Jet Diffusion Flames, Paper presented at the 1987 Spring Technical Meeting of the Central States Section of the Combustion Institute. Argonne, IL. May 1987.
  12. BALLAL, D. R., CHEN, T. H., SCHMOLL, W. J., GOSS, L. P. AND TRUMP, D. D.: Measurements of Joint PDFs and Scalar Fluxes in a Turbulent Flame Using an Integrated CARS-LDA System. Paper presented at the 1987 Spring Technical Meeting of the Central States Section of The Combustion Institute. Argonne, IL. May 1987.
  13. MORGAN, V. T.: Advances in Heat Transfer (T. F. Irvine, Jr., and J. P. Harnett, Eds.). Vol 11, p. 234. Academic Press. 1975.
  14. KRIETH, F.: Principles of Heat Transfer. Harper and Rowe. 1973.
  15. BRADLEY, C. AND MATTHEWS, K. I.: J. Mech. Eng. Sci. 10, 299 (1968).
  16. HEITOR, M. V., TAYLOR, A. M. K. P. AND WHITELAW, J. H.: Experimental Measurements and Techniques in Turbulent Reactive and Non-Reactive Flows, (R. M. C. So, J. H. Whitelaw, and M. Lapp, Eds.) AMD-Vol. 66. American Society of Mechanical Engineers. 1984.
  17. WELTY, J. R., WICKS, C. E. AND WILSON, R. E.: Fundamentals of Momentum, Heat, and Mass Transfer. p. 255. John Wiley and Sons. 1969.

## COMMENTS

*H. G. Semerjian, National Bureau of Standards, USA.* Is the dominant loss mechanism from the wire the radiation process? If so, how does this effect your evaluation of the response time? Isn't that a temperature dependent quantity, and is it evaluated at temperatures representative of combustion conditions?

*Author's Reply.* The response of the filament is dominated by the convective heat transfer between the surrounding gases and the filament surface. Radiation from the filament represents a loss term which prevents the filament from achieving the gas temperature. Because convective heat transfer is the dominant term, except under very low flow conditions, the response time of the filament is primarily determined by convection—not radiation. Only under extremely low flow conditions and at high temperatures does radiation become the major heat-transfer term. However, because the convective heat-transfer coefficient is a function of the Reynolds number of the flow, the response must be evaluated for each flow condition.

*P. E. Sojka, Purdue Univ., USA.* You state that the only disadvantage of your technique is that it cannot be used in sooty flames. However, it does not seem to be applicable to systems including halogenated compounds since they would form compounds which would attack the surface of the filament. Would you please comment.

*Author's Reply.* Any environment which is com-

prised of compounds which would attack the surface of the filament would greatly reduce the longevity of the filament and complicate the interpretation of the surface emission since both the emissivity and the filament diameter could be affected.

*R. Matthews, Univ. of Texas, USA.* What is the maximum temperature that can be measured with this technique?

*Author's Reply.* The maximum temperature measurable by the filament is ideally the melting temperature which is ~2673 K. However, it is unlikely that the filament would survive such a high temperature because of the decrease in tensile strength with increasing temperature. In a static oven, the upper temperature limit might be achieved; but under all but the lowest flow conditions, the filament would likely break before reaching this temperature.

*M. Lapp, Sandia National Laboratories, USA.* Are there any significant catalytic effects at the surface of your emitting probe that would cause it to indicate a temperature different from the surrounding gas phase?

*Author's Reply.* To the authors' knowledge, no significant catalytic effects have been reported in the literature.

# Thin-Filament Pyrometry: A Novel Thermometric Technique for Combusting Flows

L. P. Goss

V. Vilimpoc

B. Sarka

W. F. Lynn

Systems Research Laboratories,  
A Division of Arvin/Calspan,  
Dayton, OH 45440-3696

*A novel technique is described for making temperature measurements in a combusting flow. The technique, Thin-Filament Pyrometry, is based on the blackbody emission of a small ceramic filament (15  $\mu\text{m}$ ), which is introduced into the flow field under study. Because the emission along the entire length of the filament is recorded, the complete spatial temperature distribution is measured. The temporal response of the filament is  $\sim 700$  Hz under ambient conditions. To demonstrate the capabilities of the technique in a combusting flow, a  $\text{H}_2$ - $\text{N}_2$  jet diffusion flame was studied. The evolution of the large-scale buoyancy-driven structures at low Reynolds numbers was followed by this technique.*

## Introduction

Over the past decade, significant effort has been expended to develop nonintrusive laser-based diagnostic techniques capable of measuring velocity, temperature, and species concentration in combusting environments. This effort has culminated in the development of techniques such as Laser-Doppler Velocimetry (LDV), Laser-Induced Fluorescence (LIF), Spontaneous Raman Scattering (SRS), and the nonlinear Raman scattering techniques, i.e., Coherent Anti-Stokes Raman Spectroscopy (CARS) [1]. These methods have been most successfully applied to point measurements in flames. Recently, the LIF techniques have been extended to two-dimensional measurements [1]. All of these techniques suffer from the complexity of the optical and laser systems and the sheer cost of building, operating, and maintaining them. The simplicity and low cost of probe techniques such as thermocouples and gas-sampling probes have fostered their continued use. Probes, however, are known to perturb the flow fields in which they are placed, often resulting in anomalous observations. This problem furnished the initial driving force for the development of laser-based techniques. The ideal technique would actually combine the advantages of both types of techniques and be relatively simple, easy to implement, inexpensive, and non-perturbing. This paper describes a technique that offers a majority of these desirable qualities: Thin-Filament Pyrometry (TFP).

TFP combines the advantages of low cost, ease of implementation, and nonperturbing qualities to the measurement of temperature in a combusting environment. The technique has the added advantage that the temperature is measured along a line rather than at a single point, as is the case with most probe techniques. The TFP technique relies upon the

blackbody emission of a thin ceramic filament (SiC) in the wavelength range 0.8 to 1.8  $\mu\text{m}$  for measurement of the temperature distribution in a combusting flow field. The emission is recorded spatially along the length of the filament, allowing the radial temperature distribution to be evaluated. The filament is made of ultrafine  $\beta$ -SiC with excess carbon and is available commercially [2]. The filament diameter ranges from 10 to 20  $\mu\text{m}$  (nominally, 15  $\mu\text{m}$ ), and the thermal conductivity is relatively low:  $\sim 10$  kcal/m h $^\circ\text{C}$  along the filament axis at room temperature. The thermal conductivity of the filament is  $\sim 40$  times lower than that of Pt-PtRh wire, which drastically reduces the spread in the temperature profile along the filament. Because of its small size, the filament can respond quickly to temperature changes in its surroundings. The high emissivity that is constant over the temperature range of interest allows the quantitative conversion of filament intensity to gas temperature.

The TFP technique is similar to a method reported by Ferguson et al. [3], in which the emission from a silica-coated platinum-platinum-13 percent rhodium thermocouple was monitored to determine flame temperature. The major differences between the earlier study and the present one are the use of a  $\beta$ -SiC filament for emission and the fact that line rather than point measurements were made.

Confirmation of the above attributes along with a demonstration of the application of the technique to a  $\text{H}_2$ - $\text{N}_2$  diffusion flame will be discussed in this paper. Also included will be a detailed analysis of the thermal properties of the filament in a flame environment. This probe should become an important tool in the study of turbulent flame systems.

## Theory

In order to relate the emission of the SiC filament to the temperature of the gas, the response of the filament to a temperature change must be calibrated or adequately predicted.

Contributed by the International Gas Turbine Institute and presented at the 33rd International Gas Turbine and Aeroengine Congress and Exhibition, Amsterdam, The Netherlands, June 5-9, 1988. Manuscript received by the International Gas Turbine Institute January 7, 1988. Paper No. 88-GT-28.

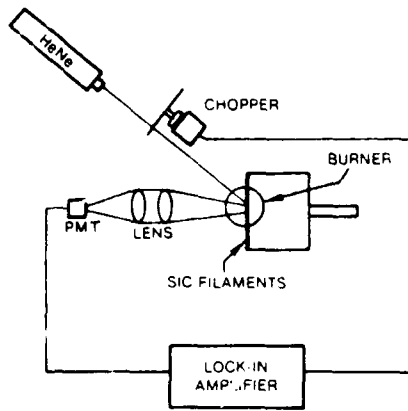


Fig. 1 Experimental arrangement for measuring relative emissivity of SiC filaments by reflectance

The  $\beta$ -SiC is reported in the literature to be a graybody and has a relatively high emissivity (0.88) [4]. The filament behavior is, thus, adequately described by the Planck blackbody equation given by

$$L(\lambda, T) = \frac{\epsilon(\lambda, T)C_1}{\lambda^5[\exp(C_2/\lambda T) - 1]} \quad [\text{W/m}] \quad (1)$$

where  $\epsilon$  is the apparent emissivity of the filament,  $C_1$  the first radiation constant,  $C_2$  the second radiation constant,  $\lambda$  the wavelength in a vacuum, and  $T$  the filament temperature. If equation (1) is to be used for the quantitative measurement of the temperature of the filament, the emissivity of the filament must be evaluated over the entire wavelength and temperature range of interest. Because it is a graybody, the emissivity does not vary with wavelength. The temperature effect on the emissivity, however, must be evaluated experimentally. The conventional approach to calibrating the emissivity of a material is to heat the material to a known temperature, measure its emittance, and compare the emittance to that of a blackbody at the same temperature. Due to the small size of the filament, this approach is quite difficult. Therefore, the reflectance of the filament was measured instead. The relationship between the reflectance and the emissivity of a material is given by Kirchoff as

$$\begin{aligned} \epsilon(\theta, \phi) &= 1 - \int \rho(\theta, \phi, \theta', \phi') d\theta' d\phi' \\ &= 1 - \rho_h(\theta, \phi) \end{aligned} \quad (2)$$

where  $\epsilon(\theta, \phi)$  is the directional emissivity,  $\rho(\theta, \phi, \theta', \phi')$  the bidirectional reflectance distribution function (BRDF), and  $\rho_h(\theta, \phi)$  the directional hemispherical reflectance. In general, the required reflectance accuracy for a desired emissivity accuracy is given by the following relation:

$$\frac{\Delta \rho_h}{\rho_h} = \frac{\epsilon}{1 - \epsilon} \frac{\Delta \epsilon}{\epsilon} \quad (3)$$

where the  $\theta, \phi$  index has been dropped. For a highly emissive sample such as the SiC filament, with emissivity of 0.88, the error in the emissivity measurement based on a 1 percent error in the reflectance is 0.13 percent. Thus, reflectance measurements - if conducted properly - can be a very accurate indicator of the emissivity (especially for highly emissive materials). The concern with the SiC filament was not in measuring the absolute emissivity at all temperatures but rather in establishing whether the emissivity remained constant, which reduced the problem to measuring the relative change in the emissivity rather than the absolute value. This was accomplished with the experimental arrangement shown in Fig. 1. The chopped output from a HeNe laser was directed onto a bundle of SiC filaments, the scatter from which was monitored by a PMT and lock-in amplifier. The filaments were then heated by a

propane torch to a temperature of  $\sim 2200$  K. The reflectance was monitored during the heatup of the filament and after it reached its maximum temperature. Several times the reflectance was observed to remain constant throughout this process to within an experimental error of  $\sim 1$  percent. Assuming that the BRDF of the filament did not vary with temperature, this experiment established an upper bound of  $\sim 0.13$  percent in the variation of the emissivity of the SiC over the 300-2200 K temperature range. The emissivity is, thus, assumed to be constant for purposes of evaluating the filament temperature from the observed emission.

It should be noted that equation (2) relates the emissivity to the hemispherical reflectance—not the bidirectional reflectance. In the present experiments the bidirectional reflectance rather than the full hemispherical reflectance is measured. It is assumed that the hemispherical is proportional to the directional reflectance and, thus, that the reflectance distribution function does not vary with temperature. Measurements with collection angles at normal and  $\pm 45$  deg were examined to verify that this was the case.

Because the emissivity is constant with wavelength and temperature, equation (1) can be evaluated for predicting the filament emission characteristics. Experimentally the emission is detected over a limited spectral region with a detector that has a varying response to the wavelength of the emission. Equation (1) must then be multiplied by the detector response and integrated over this region. The detected signal is given by

$$D_{\text{exp}} = k_{\text{exp}} \int_{\lambda_1}^{\lambda_2} L(\lambda, T) R(\lambda) T_r(\lambda) \quad (4)$$

where  $L(\lambda, T)$  is the blackbody response given by equation (1),  $R(\lambda)$  the detector response,  $\lambda_1$  and  $\lambda_2$  the limits of the detector response,  $T_r(\lambda)$  the transmission characteristics of the optics employed in the experiment, and  $k_{\text{exp}}$  an experimental constant that takes into account the efficiency of the collection optics and the gain of the detector electronics. The experimental constant  $k_{\text{exp}}$  is removed by normalizing the observed signal to the signal at a known temperature. To evaluate equation (4), one must know the detector-response function  $R(\lambda)$ . The response function for the InGaAs detector employed in these studies is shown in Fig. 2(a). By integrating the response function and the blackbody function over the limits of the detector bandwidth, the emission from the filament can be determined. Figure 2(b) displays the relative intensity as a function of temperature for the experimental setup. The calculated intensity has been normalized to the emission corresponding to the maximum temperature of a  $\text{H}_2$  diffusion flame. Notice that the data have been plotted in this figure with intensity as the independent variable and temperature as the dependent variable. This facilitates the conversion of the measured intensity to a temperature. The curve in Fig. 2(b) was fitted by a power-series expansion of  $I$  with temperature as the dependent variable. The experimentally measured intensity from an unknown flow field is converted to a temperature by first normalizing the observed intensity to a flame of known temperature such as a stoichiometric propane-air flat flame or pure-hydrogen diffusion flame and then employing the coefficients of the power series with the normalized intensity to determine a temperature.

Because of the nonlinear nature of the Planck equation, the observed filament emission is nonlinear. At the low temperature limit of the curve [Fig. 2(b)], the slope is very steep, indicating that a small change in the emittance corresponds to a very large change in the temperature. The experimental detection system, which will be discussed in more detail in a later section, has a dynamic range of 256 to 1. The lowest detectable signal is  $\sim 1000$  K with the maximum temperature set at 2370 K. Because of the steep slope at low temperature, the precision of the measurement is  $\sim 80$  K. In contrast, at the high-temperature limit, the change in temperature with intensity is small

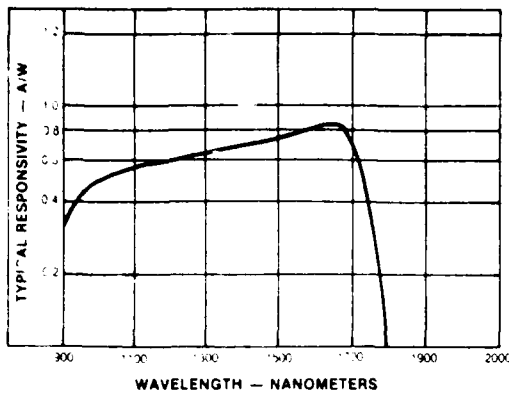


Fig. 2(a) Spectral response of InGaAs detector (from "RCA Technical Publication for C-30980E InGaAs Photodiode")

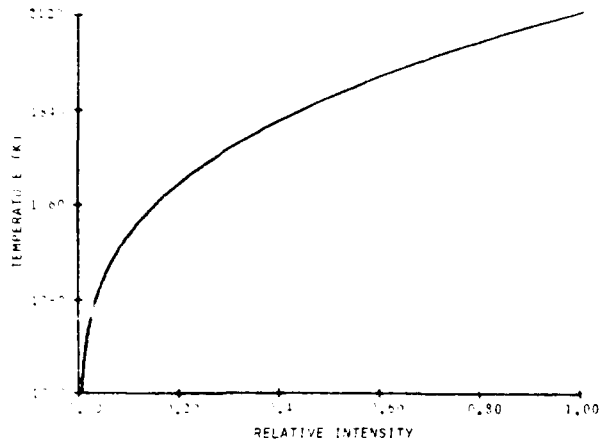


Fig. 2(b) Relative filament emission as a function of temperature

and the intensity itself is large; thus, the measured precision is improved to  $\sim 8$  K. The high-temperature limit is determined by the survivability of the filament ( $\sim 2400$  K). The noise in the experimental system was determined to be  $\sim 1$  percent of full scale.

Throughout the above discussion, it has been assumed that the filament temperature is the same as that of the surrounding gases. At high temperatures a correction to the filament temperature must be made in determining the gas temperature. The source and magnitude of this correction are discussed in the next section.

### Thermal Properties of SiC Filament

The discussion on the thermal properties of the SiC filament is divided into four parts, which treat convective heat transfer properties, transient heat response, axial thermal conductivity, and heat-balance and radiation corrections.

**Convective Heat Transfer Properties.** The convective heat transfer coefficients of the SiC filament are determined from its Nusselt number. For the case of a small filament in a crossflow, the Nusselt number is given by

$$\text{Nu} \approx \frac{hD}{k} = c(\text{Re})^n \quad (5)$$

where

$$\text{Re} = \frac{vD}{\nu} \quad (6)$$

$h$  is the heat transfer coefficient,  $D$  the filament diameter,  $k$  the thermal conductivity of the surrounding gases,  $v$  the ve-

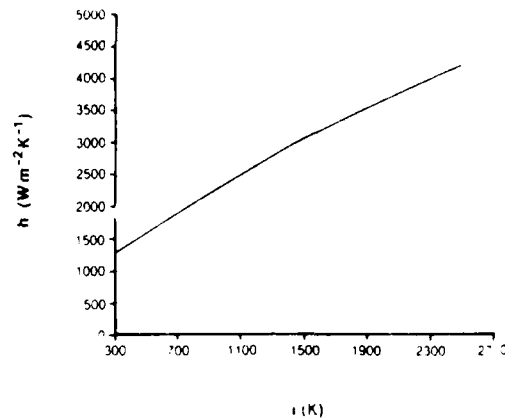


Fig. 3 Heat transfer coefficient for SiC filament in 2-m/s  $H_2$  flame

locity of the gases,  $\nu$  the kinematic viscosity of the gases, and  $c$  and  $n$  fitted parameters based upon the Reynolds number

$$h = c(\text{Re})^n \frac{k}{D} \quad (7)$$

Because of the small filament diameter ( $15 \mu\text{m}$ ), the Reynolds number is small, varying from 0.03 to 1 for the experimental conditions reported in this paper. The generally accepted  $c$  and  $n$  quantities in this case are 0.80 and 0.280, respectively [5]. The heat transfer coefficient for a 1-m/s hydrogen diffusion flame is shown in Fig. 3, assuming  $H_2O$  and air to be the predominant constituents. The thermal conductivity and kinematic viscosity for the flame were taken from [6]. The heat-transfer coefficients are quite large, ranging from a low of  $\sim 1300 \text{ W m}^{-2} \text{ K}^{-1}$  to over  $4000 \text{ W m}^{-2} \text{ K}^{-1}$ . The large coefficients are primarily due to the small diameter of the filament. Intuitively, because of the large  $h$ , the response of the filament to a heat transient should be quite fast.

**Transient Heat Response.** The response of the filament to a transient heat pulse is determined in a manner similar to that in the case of a small thermocouple. The net change in the internal energy of the filament must be equal to the net heat flow from the filament (neglecting the radiation-loss term), which is written as

$$-C\rho_f V dT = hA_s(T - T_\infty) d\theta \quad (8)$$

where  $C$  is the heat capacitance of the filament,  $\rho_f$  the density of the filament,  $V$  the volume of the filament,  $A_s$  the surface area of the filament, and  $d\theta$  the change in time. Subject to the initial condition  $T(0) = T_0$ , equation (8) has the general solution

$$\frac{T - T_\infty}{T_0 - T_\infty} = \exp - \frac{hA_s}{C\rho_f V} \theta \quad (9)$$

The time constant of the filament is given by

$$\tau = \frac{C\rho_f V}{hA_s} \approx 1.59 \times 10^{-3} \text{ s} \quad (10)$$

for a gas temperature of 2370 K at a velocity of 1 m/s.

To confirm the calculation of the filament temporal response, the response was measured experimentally using a  $CO_2$  laser to heat the filament for a short period of time. The emission of the filament was monitored with an InGaAs detector and recorded. A heat-up and cool-down cycle is shown in Fig. 4. This cycle was recorded under ambient conditions and, thus, represents a lower limit to the filament response time. The  $1/e$  value taken from this curve corresponded to  $\sim 1.5$  ms, in good agreement with the previous calculation. The filament response is  $\sim 700$  Hz. As the velocity and tem-

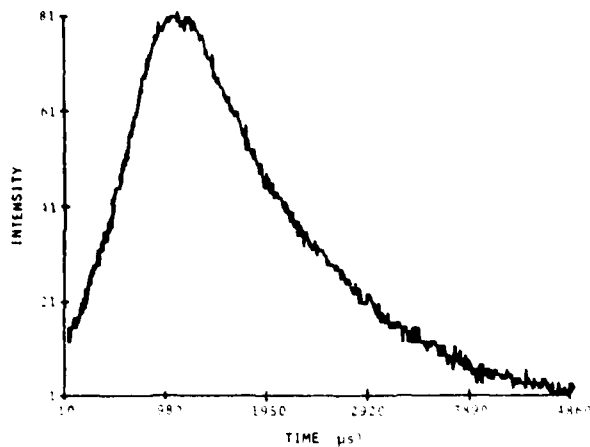


Fig. 4 Response of SiC filament to CO<sub>2</sub> laser heat pulse

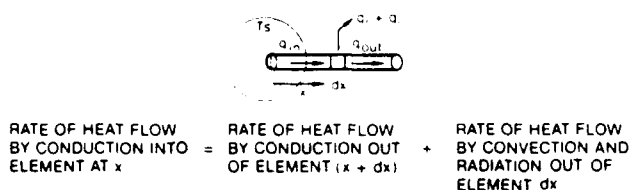


Fig. 5(a) Model for evaluation of axial thermal conductivity of SiC filament

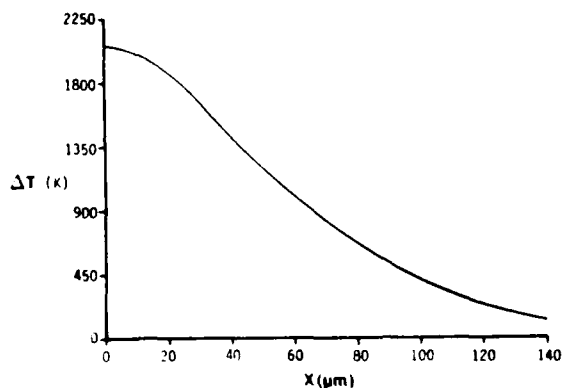


Fig. 5(b) Axial temperature distribution for SiC filament against 2800 K surface

perature increase, the filament response should improve because of increased heat transfer to the surroundings.

**Axial Thermal Conductivity.** One of the major advantages of the TFP technique is the ability to measure the temperature distribution along the length of the filament. For the measured temperature distribution to correspond to the real temperature distribution of the gas, the spatial flow of heat along the filament axis must be small. The axial heat flow is evaluated as shown in Fig. 5(a). Assuming that the filament is in contact with a flame surface at a temperature  $T_s$ , the rate of heat flow by conduction into the element  $x$  must be equal to the rate of heat flow out of the element  $x + dx$  by conduction, convection, and radiation. Neglecting the radiation term, the heat-balance equation is given by

$$-kA_s \frac{dT}{dx} = -kA_s \frac{dT}{dx} + \frac{d}{dx} \left[ -KA_s \frac{dT}{dx} \right] dx + hC_s dx (T - T_\infty) \quad (11)$$

where  $C_s$  is the circumference of the filament. Equation (11) reduces to

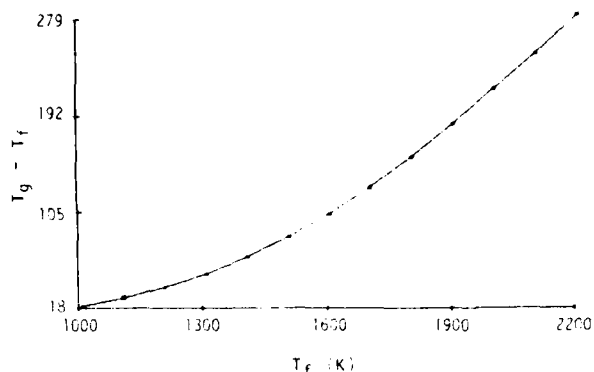


Fig. 6 Radiation-loss term for 2-m/s H<sub>2</sub> flame:  $T_f$  = filament temperature;  $T_g$  = gas temperature

$$\frac{d^2T}{dx^2} = m^2(T - T_\infty) \quad (12)$$

where

$$m = \sqrt{\frac{hC_s}{kA_s}} \quad (13)$$

Equation (12), when subject to the boundary conditions  $T = T_0$  at  $x = 0$  and  $dT/dx = 0$  at  $x = l$ , has the general solution

$$\Delta T = \frac{\cosh m(l-x)}{\cosh ml} \Delta T_i \quad (14)$$

where  $l$  is the length of the filament,  $x$  the distance from the hot surface,  $\Delta T = T - T_\infty$ , and  $\Delta T_i = T_0 - T_\infty$ . Assuming that the initial temperature is 2370 K at the hot flame surface while the filament temperature is 300 K at its end, Fig. 5(b) displays the temperature distribution adjacent to the hot flame surface. Because of the low thermal conductivity and the large convective heat transfer at the filament surface, the temperature distribution is restricted to a small region near the hot surface. This thermal conduction along the filament axis is, thus, expected to have only a small effect upon the observed temperature distribution.

**Heat Balance and Radiation Corrections.** As stated in the theoretical section, the temperature of the filament can be different from that of the surrounding gas. This difference can be obtained from the full heat balance of the filament. The convective heat input from the surrounding gas must equal the radiative heat output due to the filament emission and the conductive heat output along the filament axis, which is written as

$$hA_s(T_g - T_f) = \sigma \epsilon A_s T_f^4 + kA_s \frac{dT}{dx} \quad (15)$$

Because the ratio of the circumferential to cross-sectional surface area is large, the axial heat transfer can be ignored, resulting in

$$hA_s(T_g - T_f) = \sigma \epsilon A_s T_f^4 \quad (16)$$

Rearranging and solving for the gas temperature yields

$$T_g \approx T_f + \frac{\sigma \epsilon T_f^4}{h} \quad (17)$$

The second term on the right-hand side of equation (17) is the correction factor, which relates the measured filament temperature to the surrounding gas temperature. For the experimental conditions reported in this paper, the correction term is plotted in Fig. 6. As the temperature increases the blackbody emission increases as  $T^4$ . The convective heat transfer increases only as  $T$ ; thus, the correction term becomes large as the temperature increases. At 1000 K, the correction is small,  $\sim 20$

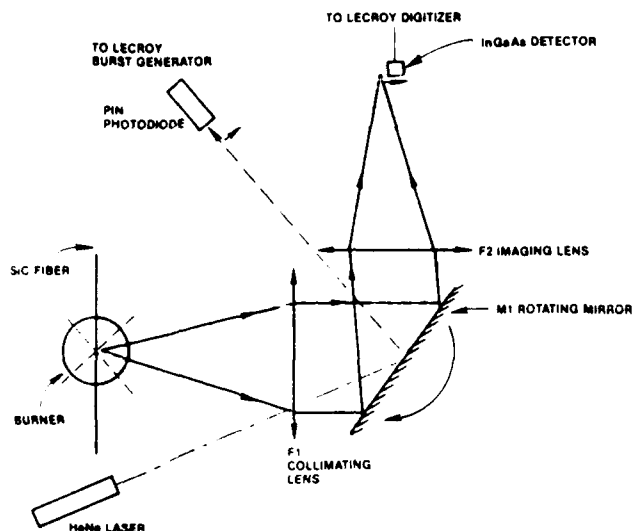


Fig. 7(a) Optical layout of filament-imaging system

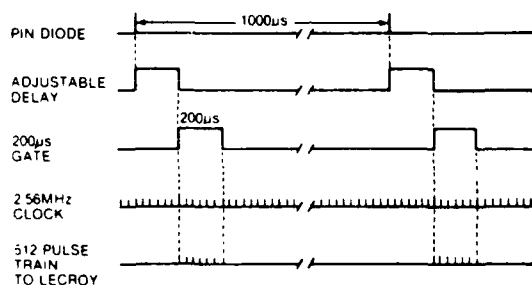


Fig. 7(b) Timing diagram of synchronizing and digitizing electronics for filament-imaging system

K; but at 2370 K it is  $\sim 276$  K. The correction term (or radiation-loss term) is dependent upon the flow conditions and constituents as well as the temperature due to the heat transfer coefficient in the denominator. Thus, the correction term must be evaluated each time the flow conditions or fuel types are changed.

## Experimental

The experimental arrangement for the TFP technique is displayed in Fig. 7. The system can be broken out into the optical and electronic subsystems, which will be discussed separately. The optical arrangement is shown in Fig. 7(a). The filament is suspended across the flame by a holder, which supplies just enough tension to keep the filament from sagging but not so much as to cause it to break at higher temperatures, where its tensile strength is reduced. The filament emission is collimated by lens f1 (f/5, 10-cm-dia) and directed toward a spinning mirror assembly, which consists of a ten-facet wheel rotating at speeds up to 500 Hz. Because each of the ten facets of the wheel acts as an individual mirror ( $\sim 2$  cm<sup>2</sup> area), the effective scan speed of the wheel is ten times its rotating speed (up to 5000 Hz). The reflected radiation from the wheel is swept through a focusing lens f2 (f/2.5, 10-cm-dia) onto a single InGaAs detector (80- $\mu$ m-dia), which is sensitive to radiation in the spectral bandwidth shown in Fig. 2(a). As the wheel rotates, the image of the filament is swept past the detector. The mirror-detector combination thus acts to convert a spatial scan into a temporal one. The combination of high-f-number lenses and the small-area rotating mirror increased the depth of field and field of view. To ensure that the response of the optical system was not angularly dependent, the filament and

flame were traversed across the optical axis. No variation in signal was observed in the field of view of interest. The output from a HeNe laser is reflected off the rotating wheel onto a pin diode to produce a pulse that can be used to synchronize the scanning and the digitizing electronics.

A timing diagram of the digitizing electronics is shown in Fig. 7(b). The output signal from the InGaAs detector is amplified and fed into a LeCroy TR8818 Transient Recorder. The synchronization pulse from the pin diode is delayed as needed and used to open a 200- $\mu$ s gate centered on the sweep of the filament image. The delay from the synchronizing pulse allows the image signal to be moved inside the gate for optimum placement. This gate is used in conjunction with a pulse generator to send 512 pulses to the LeCroy digitizer. At the leading edge of each of these pulses, the signal from the InGaAs detector is digitized and stored in the MM8103 ECL Memory Unit. The rate of digitization during the 200- $\mu$ s gate is 2.56 MHz. The digitization sequence continues with subsequent scans until the memory is completely filled. The data are then transferred through a custom-built interface to a ModComp 7870 Classic Minicomputer for analysis. The digitization rate and gate pulse width are set for a 1000-Hz sweep rate of the filament image. A 6-cm length along the filament is recorded in the 512 discrete samples, translating into an effective spatial resolution of 120  $\mu$ m per sample point.

The advantages of using a rotating mirror in association with a single detector rather than a scanning array of detectors include the increased flexibility and lower cost of the system. Since a single detector is employed, detectors that are not presently available in array form, i.e., the InGaAs detector, can be used. This is also important for future work where the temperature range will possibly be extended by use of IR detectors.

Analysis of the digitized data consists of unpacking the 8-bit data from the LeCroy into 16-bit data for the ModComp; ratioing the measured intensity to a calibrated intensity at a known temperature; converting the ratioed intensity to temperature employing the fitted, calculated curve shown in Fig. 2(b); and correcting the filament temperature for radiation losses. The reduced data can then be plotted either multidimensionally or as contours, as demonstrated in the Results Section. The calibrated intensity usually is determined by measuring a H<sub>2</sub> diffusion flame and noting the maximum intensity corresponding to a temperature of 2382 K.

The LeCroy TR8818 Transient Recorder is a high-speed 8-bit system having a dynamic range of 256 of 1. Experimentally, the filament emission from the flame was surveyed to determine the area of maximum temperature. The signal from this region was then adjusted to the maximum allowed by the digitizer in order to take full advantage of the limited dynamic range. As a result of this limited range and the wavelength response of the InGaAs detector, temperatures below 1000 K are not detected. A wider temperature range is possible by employing IR detectors, but care must be taken to minimize the interference from the hot flame gases in the IR region.

## Results and Discussion

Recent studies on the structure of jet diffusion flames have demonstrated the presence of large-scale buoyancy-driven structures (bulges) at relatively low Reynolds numbers [7, 8]. These structures can expand to several jet diameters in width and display an 8-20 Hz repetition. Laser-sheet-lighting visualization techniques, in conjunction with high-speed photography, have added greatly to the understanding of the dynamics of these flames [8]. Temperature measurements in these flames have been made traditionally with thermocouples and, more recently, by means of the CARS technique [9]. In both cases it is complicated to interpret point temperature measurements due to the dynamic nature of these flames. A wealth of in-

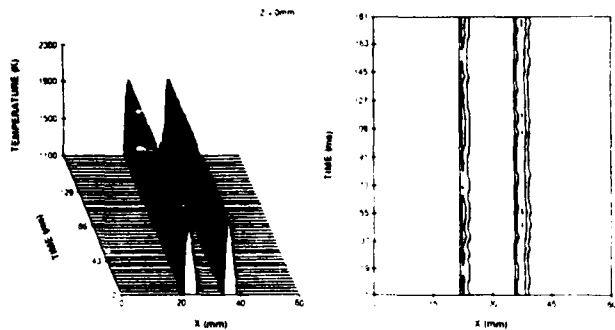


Fig. 8 Imaging scans of SIC filament in  $H_2-N_2$  jet diffusion flame at axial location 0 mm above nozzle exit

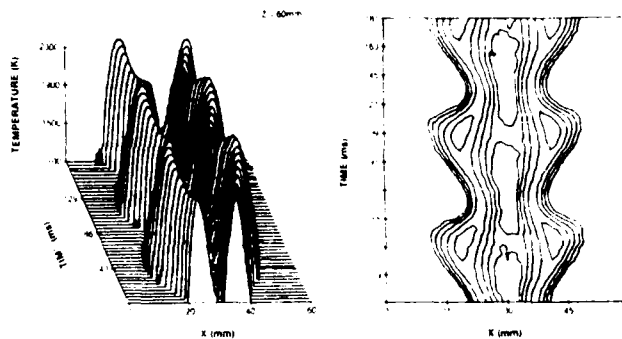


Fig. 11 Imaging scans of SIC filament in  $H_2-N_2$  jet diffusion flame at axial location 60 mm above nozzle exit

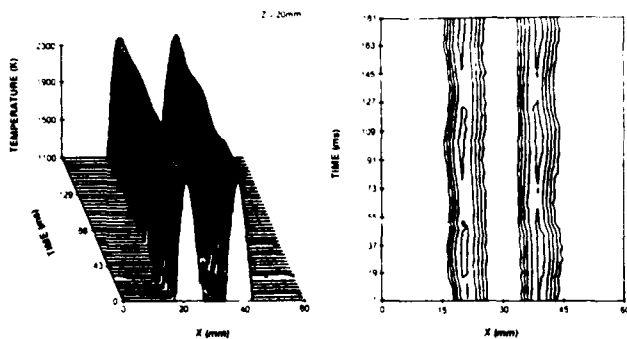


Fig. 9 Imaging scans of SIC filament in  $H_2-N_2$  jet diffusion flame at axial location 20 mm above nozzle exit

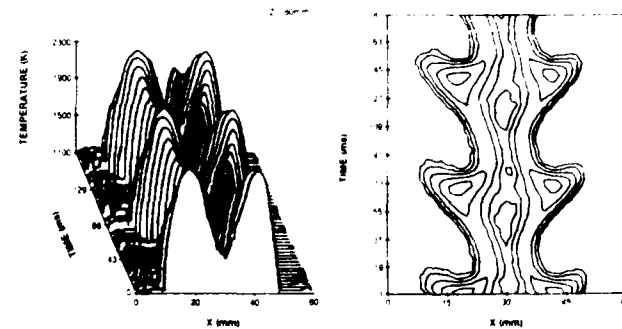


Fig. 12 Imaging scans of SIC filament in  $H_2-N_2$  jet diffusion flame at axial location 80 mm above nozzle exit

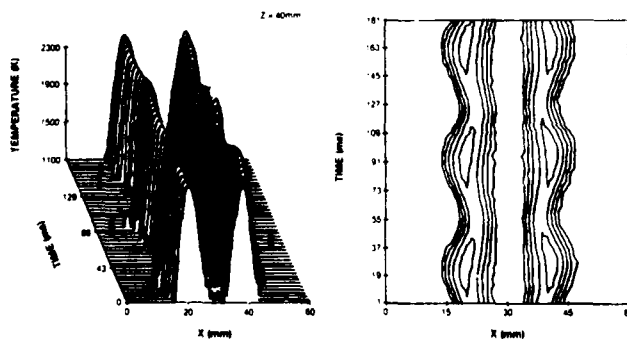


Fig. 10 Imaging scans of SIC filament in  $H_2-N_2$  jet diffusion flame at axial location 40 mm above nozzle exit

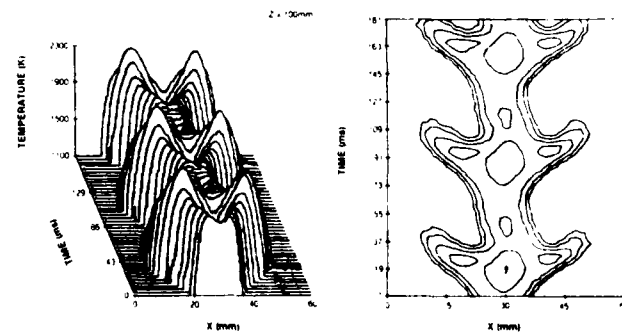


Fig. 13 Imaging scans of SIC filament in  $H_2-N_2$  jet diffusion flame at axial location 100 mm above nozzle exit

formation concerning the temperature field dynamics, however, can be obtained using the TFP technique. Because the temperature measurement is made along the width of the flame and because the filament response is much higher than the variation in the flame, the temporal and spatial temperature field dynamics can be studied.

To demonstrate this point, a  $H_2-N_2$  jet diffusion flame was chosen for study. This flame is ideal for study by the TFP technique due to the dynamics discussed above and the lack of sooting, the emission from which could interfere with the filament emission. The burner consists of a 1-cm contoured jet surrounded by a coannular air jet. The contour of the fuel jet was constructed in such a way as to yield a flat-top velocity profile. The coannular jet is ~25 cm in diameter and is characterized by a low-turbulence flat velocity field ~5 cm/s. The  $H_2$  and  $N_2$  were mixed in the ratio of 8 to 1 by volume and had an exit velocity of ~3 m/s. The adiabatic flame temperature for such a mixture is calculated to be 2320 K. The filament was suspended along the central axis of the axisymmetrical jet flame, and the flame was translated up or down to obtain radial profiles at several axial locations. The filament emission was scanned at the rate of 1000 Hz with a spatial resolution of ~120  $\mu\text{m}$ . The emission was recorded and converted to

temperatures, as explained earlier. The temperature data at several axial locations of the jet diffusion flame are shown in Figs. 8-13. The reader should keep in mind that the displayed temperature fields represent the movement of the flame structure past a single axial location as a function of time. The y axis in the plots is time—not space (as in a photograph of the flame).

The evolution of the large-scale buoyancy-driven structures can be traced from these plots. Near the nozzle exit (Fig. 8), the fuel jet is surrounded by a hot reacting cone, which results from the combustion of fuel and coflowing air. The flame structure is well defined and displays little indication of low-frequency oscillations or flicker. The temperature is below the adiabatic calculated temperature due to heat loss to the nozzle and the small size of the reaction zone.

At the 20-mm axial location (Fig. 9), the flame temperature is very near the calculated adiabatic temperature. The flame has increased in size radially, and the hot temperature zones have increased in size. The increase in hot-zone size is probably due to the high diffusivity of the  $H_2$  molecule and the extremely broad flammability limits. This width has been confirmed by

CARS measurements [10]. Notice at this location that a low-frequency oscillation of the outer flame boundary is occurring. This is the initial development of the large-scale buoyancy-driven structures. At the 40-mm axial location (Fig. 10), the jet has radially expanded further and the flame oscillation has increased markedly in amplitude. Notice that while the outer boundary oscillations are distinct, the inner flame boundary (between the hot temperature zone and the cold jet) exhibits only a small hint of oscillation. The flame or hot zone is acting to dampen the buoyancy-induced oscillations due to the high viscosity of this zone.

At the 60-mm axial location (Fig. 11), the jet flame has more than doubled its width and the oscillations that were nearly sinusoidal at the 40-mm location are now much more complex, having taken on a bell-like shape. The unburnt jet fuel is still present at this height.

At 80 mm (Fig. 12), the expansion of the flame continues, with the bulges showing signs of possibly wrapping and entraining the outside air. Sheet-light studies of this flame at this location indicate that associated with this bulging is a vortex structure in the surrounding air. The vortex tends to grow with the flame bulge and acts to entrain air into the flame. The interplay between the bulge and the coexisting vortex structure is responsible for the flame characteristics observed in these studies.

At the 100-mm axial location (Fig. 13), the temperature field shows the continued evolution of the flame bulge, which strongly displays the massive air entrainment. The flame is three times its original size at the 0-mm location. The cold central jet, which was visible through the 60-mm location, has undergone periodic combustion with the entrained air, coincident with the periodic entrainment of air into the central jet by the outside vortex, as can be seen from the oscillation of temperature in the central part of the jet. Above the 100-mm location, the surrounding coflowing-air jet field has decayed to the point where room disturbance is beginning to affect the flame structure. Thus, higher profiles were not attempted. The start and continued evolution of low-frequency buoyancy-driven structures are clearly evident from the temperature fields measured by the TFP technique. The temporal as well as spatial dynamics of the changing structure are captured by the rotating-mirror imaging system. This technique, in conjunction with laser-sheet-lighting techniques, should greatly enhance the understanding of the dynamics of jet diffusion flames. The advantages of the technique outweigh the disadvantages of restricted temperature range, limitation to low-sooting flames, and limited upper response of  $\sim 1000$  Hz.

## Conclusions

In conclusion, a novel thermometric technique (TFP) has been demonstrated to be capable of measuring the temporal-

spatial temperature distributions in nonsooting flames. The technique is characterized by its high spatial resolution of  $\sim 200$   $\mu\text{m}$ , its fast temporal response of  $\sim 1000$  Hz, and its ability to measure the radial temperature distribution along a line rather than just at a point. An examination of the thermal properties of the SiC filament employed for the technique indicates that it displays little axial heat conduction but requires that a radiation correction be made at high temperatures. Studies on a  $\text{H}_2$ - $\text{N}_2$  jet diffusion flame indicate that the evolution of the large-scale buoyancy-driven structures associated with this flame can be studied. Future efforts will be concentrated on combining this technique with dynamic visualization techniques to obtain a more detailed picture of the dynamics of jet diffusion flames.

## Acknowledgments

This work was performed under USAF Contract No. F33615-85-C-2562. The authors wish to thank Dr. L. D. Chen for supplying the adiabatic flame calculations, Dr. W. M. Roquemore for encouragement and support, and Dr. R. S. Tankin for discussions on the thermal properties of the filament.

## References

- 1 So, R. M. C., Whitelaw, J. H., and Lapp, M., eds., *Measurements and Techniques in Turbulent Reactive and Non-Reactive Flows*, ASME, New York, 1984, and reference therein.
- 2 Dow Corning Corporation, Nippon Carbon Company, Ltd., Midland, MI 48686-0994.
- 3 Ferguson, C. R., and Keck, J. C., "Hot-Wire Pyrometry," *J. Appl. Phys.*, Vol. 49, No. 3031, 1978.
- 4 "Properties of Silicon Carbide," in: *Thermophysical Properties of High Temperature Solid Materials, Vol. 5—Nonoxides and Their Solutions and Mixtures Including Miscellaneous Ceramic Materials*, Y. S. Touloukian, ed., MacMillan Co., New York, 1967, pp. 118-140.
- 5 Morgan, V. T., "The Overall Convective Heat Transfer from Circular Cylinder," in: *Advances in Heat Transfer*, T. F. Irvine, Jr., and J. P. Harnett, eds., Academic Press, New York, 1975, Vol. 11, p. 234.
- 6 Kreith, F., *Principles of Heat Transfer*, 3rd ed., Harper and Row, New York, 1973.
- 7 Chen, L. D., and Roquemore, W. M., "Visualization of Jet Flames," *Comb. Flame*, Vol. 66, No. 81, 1986.
- 8 Chen, L. D., and Roquemore, W. M., "Two Dimensional Visualization and Single Point Frequency of Low Reynolds Number Jet Flames," in: *ICALEO '86, Arlington, VA, Vol. 85—Flow and Particle Diagnostics*, Laser Institute of America, Toledo, OH, 1986, pp. 16-23.
- 9 Roquemore, W. M., Goss, L. P., Lynn, W. F., and Chen, L. D., "Structure of Jet Diffusion Flames," presented at the 1987 Spring Technical Meeting of the Central States Section of the Combustion Institute, May 11, 1987, Argonne, IL.
- 10 Systems Research Laboratories, Inc., "Combustion Diagnostic Development and Application," SRL R&D Status Report 6890-5 under Contract No. F33615-85-C-2562 covering the period 17 Sept.-16 Dec. 1986, Dayton, OH, 1987.

## 2.4 FLAME VISUALIZATION

In the early development of advanced laser-based nonintrusive diagnostics, the major emphasis was placed on precise point-wise measurements in flames. Data from these measurements typically included average, rms, and pdf distributions of the scalar and vector quantities. Profiling of the flame was achieved one spatial point at a time; thus, a time-averaged picture of the flame was obtained. For dynamic flame systems, this is a severe drawback and has spurred the development of multi-point visualization techniques. Several multi-dimensional measurement techniques have been developed and evaluated by SRL's Optical Diagnostics Group. One of the earliest and most widely applied methods was the reactive Mie scattering (RMS) technique. This flame-visualization technique employs the reaction of  $\text{TiCl}_4$  with water vapor to form  $\text{TiO}_2$  seed particles. The seed particles formed in this manner are used to scatter light within a laser sheet, allowing an instantaneous two-dimensional snapshot of the flame flow structure to be captured. An image of the Mie scattering from the particles in the laser light sheet can be recorded by still photography, cine photography, or CCD cameras. If the technique is used in conjunction with a high-repetition-rate laser system (i.e., a copper-vapor laser), then the evolution of the flame-flow structure can be studied as a function of time. The development of this technique was discussed in detail in a review paper entitled, "Development of Laser Diagnostics for Combustion Research," which was presented at the 1986 Spring Technical Meeting of the Central States Section of the Combustion Institute (see p. 5). Several applications of the technique to jet-diffusion-flame studies are discussed in Volume 2 of this report.

Another technique which has been employed for two-dimensional flame visualization is the Rayleigh scattering technique. This method relies upon the Rayleigh scattering of gases in a laser light sheet for visualization of density-temperature variations in a flowfield. A paper which discusses the development and evaluation of the technique is entitled, "Multi-Dimensional Scalar Measurements in a  $\text{H}_2\text{-CH}_4$  Diffusion Flame," and was presented at the 1988 Spring Technical Meeting of the Central States Section of the Combustion Institute (see p. 116).

The incorporation of multiple filaments and a two-dimensional camera into the TFP technique allowed two-dimensional temperature visualization to be achieved. This extension of the TFP technique was discussed in a paper entitled, "Two-Dimensional Temperature and Velocity Measurement Techniques in a Sooty Jet Diffusion Flame,"

which was presented at the 1990 ASME Fluids Engineering Division Meeting (see p. 122).

Combinations of the visualization techniques are possible and allow additional information to be obtained. An example of this approach is given in the paper entitled, "Statistical OH-Zone Structure of Turbulent Hydrocarbon Jet Flames: Results of RMS/OH-PLIF Techniques," which is now being reviewed for publication in *Combustion Science and Technology* (see p. 125). In this paper the interaction of flame surface and fuel-jet vortices is examined in detail by the RMS technique and planar laser-induced fluorescence (PLIF) of the OH radical.

# Turbulent Flame Visualization Using Thin-Filament Pyrometry at High Sampling Rates

T. H. Chen, L. P. Goss, D. D. Trump, B. Sarka, V. Vilimpc, and M. E. Post  
*Systems Research Laboratories, Inc.*  
*A Division of Arvin/Calspan*  
*Dayton, OH 45440-3696*

W. M. Roquemore  
*Wright Research and Development Center/Aero Propulsion and Power Laboratory*  
*Wright-Patterson AFB, OH 45433-6563*

## ABSTRACT

The application of Thin-Filament Pyrometry (TFP) to the characterization and visualization of turbulent diffusion flames is described. The TFP technique has high spatial resolution, fast temporal response, and the ability to measure the temperature distribution along a line. The major thrust of this paper is the demonstration of the impact of the high-speed temperature sampling of TFP upon the understanding of turbulent flame propagation. Because of the rapid sampling, the dynamic, time-varying features of the flame can be characterized quantitatively. In addition, the simplicity of the technique allows combination with other methods to achieve simultaneous measurements.

## NOMENCLATURE

$a_1, a_5$ : amplitude of peak  
 $a_2, a_6$ : location of peak  
 $a_3, a_7$ : ( $\times 2.354 =$ ) width of peak  
 $a_4$  : background  
 $d$  : diameter of fuel tube  
 $L$  : length scale of radial flame-surface motion  
 $S$  : strain rate ( $= v'/L$ )  
 $t$  : time  
 $T$  : temperature  
 $U_j$  : jet exit velocity  
 $v$  : radial velocity ( $= dy/dt$ )  
 $v'$  : root mean square (rms) value of radial velocity (velocity scale of radial flame-surface motion)  
 $y$  : radial ordinate  
 $z$  : axial ordinate

## INTRODUCTION

Turbulent flame propagation has been studied experimentally by various advanced optical techniques including visualization (1-4). While detailed information on complicated flame structures has been obtained, the evolution of flame/flow interactions remains undetermined because of the low sampling rates of the optical techniques employed. Although, high-repetition-rate lasers and fast, intensified 2-D cameras are available for measuring and visualizing the turbulent reaction process (5), the expense involved in acquiring and operating these systems is rather high. Another disadvantage of the high-speed optical techniques such as Rayleigh scattering is that the signal is weak. In the present paper, a low-cost alternative--a physical probe with optical signal sampling--is introduced and illustrated.

The Thin-Filament-Pyrometry (TFP) technique relies upon the blackbody radiation from a thin filament placed in the flame. The emission from the filament is a strong function of temperature; because of this strong emission, line scans can be made at a rate of more than 3,000 scans/sec. Thus, time-varying properties (6)--essential elements for understanding flame/flow interactions--can be measured. In addition, because of the simplicity of the TFP technique, it can be combined with other methods and is free from particle noise. This advantage allows the filament to be applied to the measurement of the flame temperature in a lightly particle-laden environment.

In the present paper, the development of the TFP technique and its application to the visualization and characterization of turbulent diffusion flames are described. For visualization, the technique is utilized at high sampling rates to trace the development of the temperature

field along a line. For quantitative characterization of the propagation of turbulent flames, an accurate, automated data-processing method has been developed. With this scheme, the length and velocity scales can be measured directly. The data treatment employed in this study is directly applicable to other high-sampling-rate techniques such as Rayleigh scattering.

## TECHNICAL DEVELOPMENTS

### Filament and Optical Arrangement

The thin-filament pyrometer used in this experiment was described in detail previously (7). Special features of the pyrometer include its high spatial resolution, fast temporal response, and ability to measure the temperature distribution along a line rather than at a point. The thermal properties of the filament and the calibration procedure for obtaining the temperature from the measured blackbody radiation are also described in Ref. 7. In the present study, the filament was utilized to trace the motion of the flame. The signal strength was measured, but the true temperature was not calculated, thus avoiding a complicated calibration procedure.

The filament has a diameter of  $\sim 10 \mu\text{m}$  and is held by a "U"-shaped steel stripe under proper tension. The span of the holder is  $\sim 12 \text{ cm}$ , which covers the flame diameter. When placed in the flame, the filament becomes visibly "hot red" from blackbody radiation. This radiation was imaged onto a single InGaAs photodiode detector through the use of a rotating mirror as demonstrated in Fig. 1. The line image of the filament radiation was sequentially digitized into 512 time steps during each scan of the mirror. For a fixed optical layout, the physical length observed can be adjusted by changing the mirror scan rate and the digitization rate. This scanned length divided by 512 yields the pixel resolution. Since this study covered a range of flow

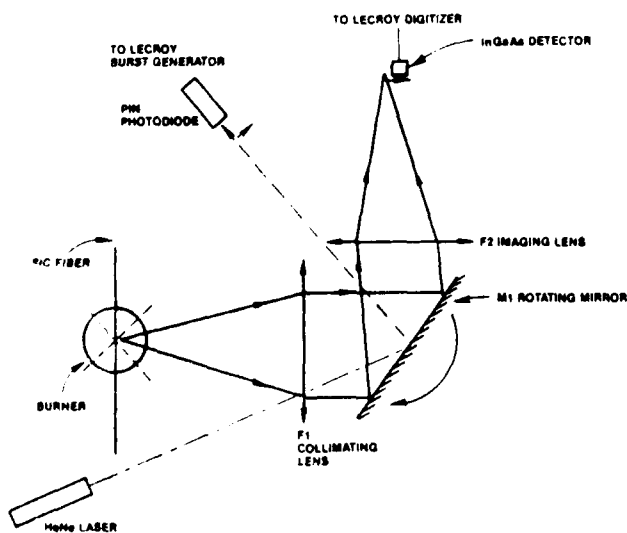


Fig. 1 Optical layout of filament-imaging system

conditions, the pixel resolution was varied from 60 to 150  $\mu\text{m}$ . Use of a single detector not only reduces the cost but also allows one flexibility in choosing a detector--even if not available in array form--to expand the coverage of the temperature range of interest (7). Efforts involved in maintaining the optical alignment are minimal.

### Data-Acquisition Hardware

Because of the high-sampling-rate requirement, the success of applying this pyrometer to the study of flames relies heavily upon the design of the fast electronic interfaces. The function of the first interface is to acquire the signal and that of the second is to transfer data into the host computer. Those two interfaces and the system hardware are shown schematically in Fig. 2.

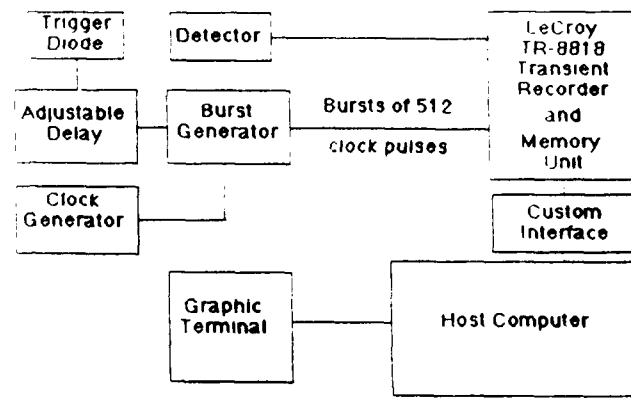


Fig. 2 Block diagram of system hardware

A minimum scan rate ranging from 1000 to 3000 Hz is required to cover the dominant jet-shear-layer frequency which was measured by LDA to be in the range 150 - 600 Hz. To achieve this high sampling rate, a LeCroy TR8818 Transient Recorder was used. This high-speed 8-bit system has a dynamic range of 1. The output signal from the InGaAs detector is amplified and fed into the MM8103 ECL Memory Unit of the transient recorder. The rise-time of the overall detector circuitry in this setup was 1  $\mu\text{sec}$ . Therefore, during the gated time period, 512 bytes of data were digitized at a selected rate in the range 2.5 - 4 Mbyte/sec. To ensure the completion of the sampling of 512 bytes, a counter was utilized in association with the gate.

Because of the continuous acquisition of massive amounts of data, another interface is needed for extracting the data from the transient recorder and feeding the information into the host computer. To satisfy this need, an interface was custom built which is capable of transferring data from the transient recorder to the ModComp 7870 Classic Minicomputer (host computer) at a rate of  $>1 \text{ MHz}$ . The current hardware configuration has two independent channels. This allows data acquisition of the signal from two adjacent filaments. In addition, the simplicity of the TFP method allows integration with other

scalar measurement techniques, the signals from which can be acquired by the second channel.

### Data Analysis

A natural limitation on the amount of data which can be acquired for a selected measurement location is the availability of the computer memory. For the current study 750 line images were acquired at each axial location to complete a data file. Multiple files could be taken at the same location if needed. It was found that even under liftoff flame conditions, the flame could be described as flamelet-like in nature. Since the filament intercepts the flame surface on both sides of the fuel jet, its emission appears as two near-Gaussian peaks separated by the width of the jet and superimposed on a small background. This type of peak and the background can be fit with the composite function (8)

$$F(y) = a_1 \exp\{-0.5 [(y - a_2) / a_3]^2\} + a_4 + a_5 \exp\{-0.5 [(y - a_6) / a_7]^2\} \quad (1)$$

where the amplitude of the two peaks is given by  $a_1$  and  $a_5$ , their location by  $a_2$  and  $a_6$ , their width by  $a_3$  and  $a_7$ , and their background by  $a_4$ . This fitting process improves the accuracy with which the peak (presumably the flame location) is located and avoids the difficulty associated with selecting a convention for determining the width. In Eq. (1),  $y$  is of the same dimension as the pixel number which can then be converted to the physical dimension through the known pixel resolution. It was crucial to ensure that each flame surface was covered by at least 20 to 40 pixels. An example of the measured signal along the filament and the fitted function is plotted in Fig. 3. The fact that the two peaks are not equal is an

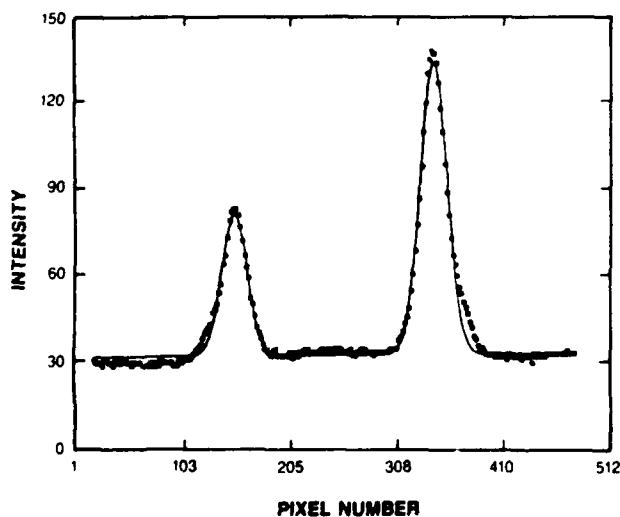


Fig. 3 Flame profile captured by TFP technique (dots) and fitted curve (solid line)

indication that the flame is asymmetric. This is expected because the jet becomes asymmetrical starting at a location two jet diameters downstream due to the development of azimuthal instabilities (9).

The fitting process allows the motion of the flame surface to be captured, even if its movement is less than the size of a single pixel which is  $\sim 60 - 150 \mu\text{m}$ . This improvement in spatial resolution is important to the fractal evaluation of the flame surface. The fitted function is stored for each scan; these functions form a time series which provides a record of the instantaneous flame position, radial flame velocity, and flame thickness. Figure 4 is an example of the captured flame position as a function of time. The flame trace shows the small-scale wiggle of the flame motion and the richness of the frequency content. Although the precision of tracking the flame surface is in the  $100\text{-}\mu\text{m}$  region, the statistical error arises due to the limited number of samples. For example, 750 samples will yield an uncertainty of  $\sim 4\%$ , which is  $1/\sqrt{750}$ . This uncertainty is believed to be the major source of experimental error in this study.

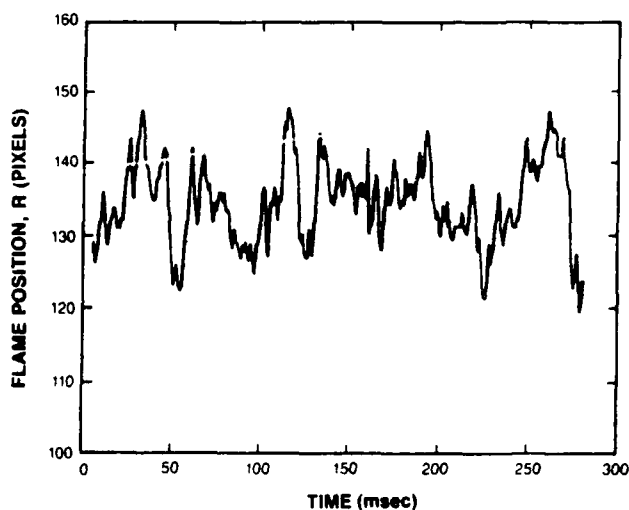


Fig. 4 Trace of flame surface as function of time

In addition to improving the accuracy of tracking the flame movement, the fitting provides a direct method for automating the data-processing tasks. The drawback of this fitting process is that it is time consuming; the fitting of each profile containing 512 pixels requires, on the average, 3 sec of CPU time of the host computer. For a file having 750 scans,  $\sim 45 \text{ min.}$  is needed, whereas the entire file might be acquired in  $< 1 \text{ sec.}$  during data acquisition. However, the automated data processing can be accomplished without operator interaction.

### EXPERIMENTAL

A short, tapered 5-mm-id nozzle was used as the fuel jet in forming a jet diffusion flame. A 25-cm duct

confined the annular air flow. Propane and methane were used as fuels; these fuels were issued at jet velocities such that the flame condition ranged from lifting to near blowout. The corresponding jet velocities ranged from 20 to 80 m/sec. Although the filament is durable and does not break even for a flame with higher jet speed, it experiences severe vibration which affects signal collection. Therefore, the filament was used only as a visualization tool for flames having jet speeds of  $> 60$  m/sec. If measurements are required at high jet speeds, then the span of the filament holder can be shortened; however, this may interfere with the flowfield.

The locations chosen for the temperature measurement were in the near-field range from the flame base to the end of the blue-flame zone. In this regime the shear layer and flame surface interact strongly. Deformation of the flame surface under the influence of the vortical shear layer can be examined in this region.

## RESULTS AND DISCUSSION

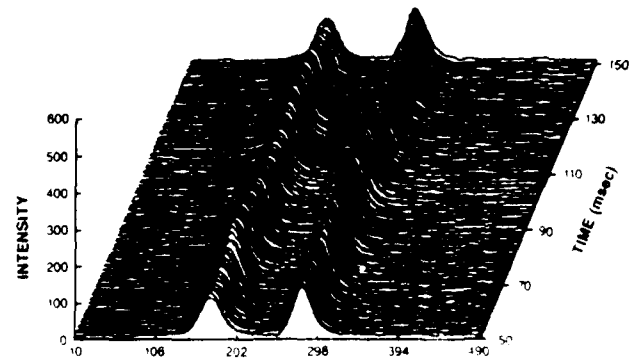
### Direct Flame Visualization

In the study of turbulent flame propagation, local extinction is a fascinating phenomenon which intrigues many theoretical and experimental researchers. TFP provides a movie-like picture of the temperature structure along a line. Since this technique offers high speed sampling capability, the transition of unsteady flame propagation can be observed. Figures 5 (a) and (b) are three dimensional plots of the thin-filament temperature data for propane and methane flames under attached conditions. Results for the attached propane flame are shown in Figs. 5(a) and (b) for the positions  $z = 20$  and  $40$  mm, respectively. Results for the methane flame are shown in Fig. 5(c) for the position  $z = 40$  mm.

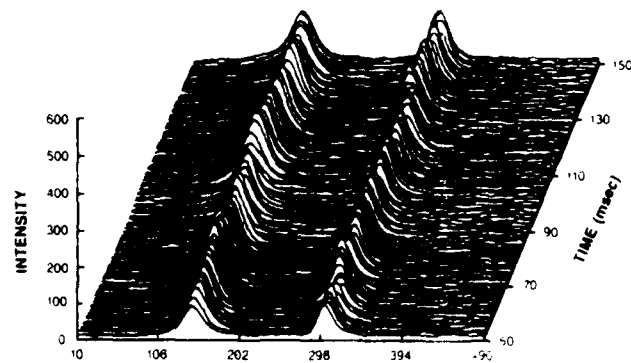
It is observed that the propane-flame surface is continuous at both  $z = 20$  and  $40$  mm. In the case of methane, the flame surface is also continuous at  $z = 20$  mm; since the TFP results are similar to those shown in Fig. 5(a), they are not displayed. Beginning at the position  $z = 40$  mm,  $z/d = 8$ , the methane-flame surface is no longer continuous; holes  $\sim 10$  mm in diameter appear which are similar to those found by other investigators (2,4). With a very small increase in jet velocity or small disturbance, the methane flame splits at  $z \sim 40$  mm. In this type of direct display, the signal-analysis technique described previously is not needed. Such direct temperature visualization provides qualitative information on flame-surface motion without the complication of detailed data analysis. In addition, since TFP is a line measurement technique, the occurrence of the instantaneous discontinuity of the flame surface can be observed.

### TFP Combined with Other Techniques

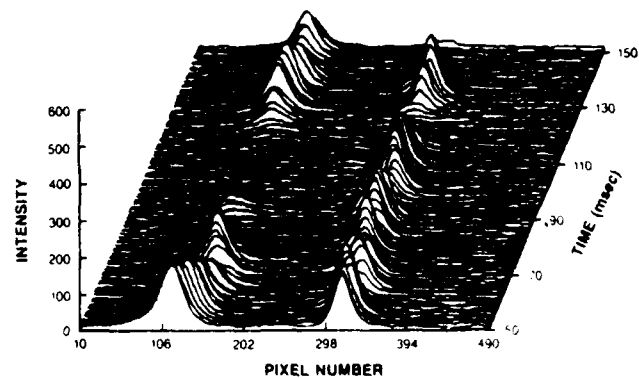
In addition to direct flame visualization, TFP can be combined with other visualization techniques to provide simultaneous comparison of the information obtained



(a)



(b)



(c)

Fig. 5 Three-dimensional plot of TFP results for propane flame at (a)  $z = 20$  mm and (b)  $z = 40$  mm and methane flame at (c)  $z = 40$  mm

by means of different methods. For example, TFP and the Reactive Mie Scattering (RMS) technique have been successfully integrated by Goss, et al. (10), in their study of propane diffusion flames. In the RMS technique as used here, a cw argon-ion laser beam is directed through the flamelet about the same axial location as the filament and parallel to it. The  $TiO_2$  particles from the reaction of

TiCl<sub>4</sub> with H<sub>2</sub>O serve as the marker which reflects the laser light. The resulting Mie scattering along the laser beam is scanned by the rotating mirror used in the TFP system and then fed into a separate detector. The signal is amplified and fed into the second channel of the LeCroy Transient Recorder used in the TFP system.

Figure 6 presents the temperature contour obtained by TFP which is associated with the RMS results taken simultaneously. The minimum value of the temperature contour is 1200 K. The results clearly show that inside the reaction zone of the diffusion flame where the temperature is > 1200 K, Mie scattering drops substantially. These results further demonstrate that caution should be exercised while applying the RMS technique to the visualization of the flame (4). In addition, application of TiO<sub>2</sub> particles for flame diagnostics such as LDV velocity measurements may suffer from biasing due to the drop in the Mie scattering. Finally, TFP directly traces the high-temperature region which is ideal for flame visualization.

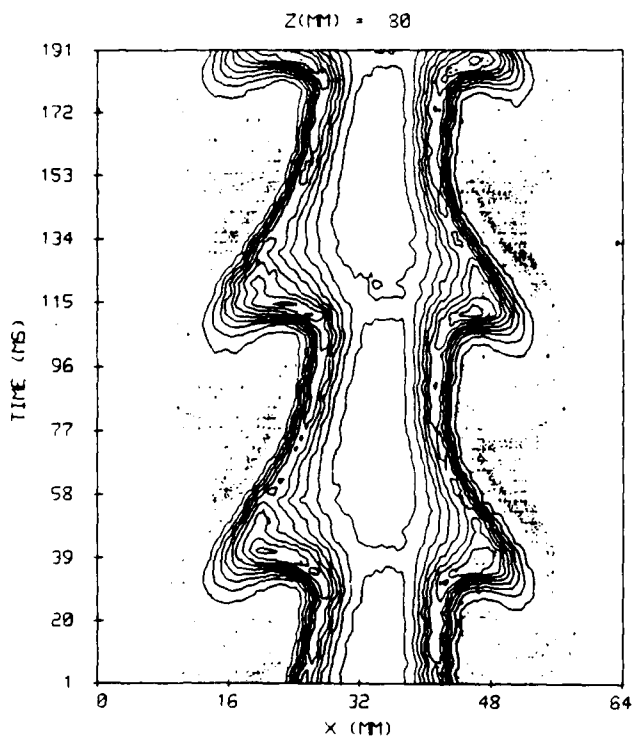


Fig. 6 Simultaneous TFP and RMS measurements of 1-cm propane flame with  $U_j = 3$  m/sec

#### Direct Measurement of Flame Propagation

The dynamic features of turbulent flame propagation can be quantitatively described by means of length and velocity scales. In conventional experiments where direct flame-surface tracking is not possible, these scales are derived from velocity measurements of the flow field. The velocity measured under that circumstance, however,

does not necessarily characterize the flame motion. In the TFP technique, these two scales result from direct tracking of the motion of the flame surface. Application of the turbulent Prandtl number required in other techniques is not needed for data reduction with this technique.

From the TFP results, a series of radial flame surface positions  $y(t_i)$  and root-mean-square (rms) values  $y'$  can be determined;  $y'$  is defined as the integral length scale,  $L$ . The time derivative of the flame position,  $dy(t)/dt$ , is the instantaneous radial velocity,  $v$ , of the flame surface. The mean value of the radial velocity is zero; however, the rms value  $v'$  is not zero and represents the turbulent velocity scale. These two important scales associated with the propagation of the flame surface were measured directly and are shown in Figs. 7 and 8 (11,12). In this experiment, both the methane and the propane flames were operated under critical liftoff velocities. At these velocities, the flame could be attached or lifted. Comparing the results for the attached and lifted flames indicates that both the length and velocity scales increase dramatically after the flame lifts. At the critical liftoff velocity, the methane flame displays larger length and velocity scales than the propane flame. This indicates that the flame/flow interaction for the methane flame is stronger than that for the propane flame. This strong interaction causes the methane flame to display holes, as observed by direct TFP visualization.

From the measured values of  $L$  and  $v'$ , the strain rate which is the ratio of  $v'$  to  $L$  can be derived. It is important to measure this quantity because it allows the flame-stretching concepts to be examined. The measured strain rate for the flame conditions shown in Figs. 7 and 8 is given in Fig. 9. Here, the measured strain rate displays a relatively constant value ranging from ~300 to 500 1/sec, which compares favorably with the results of other researchers (13-15).

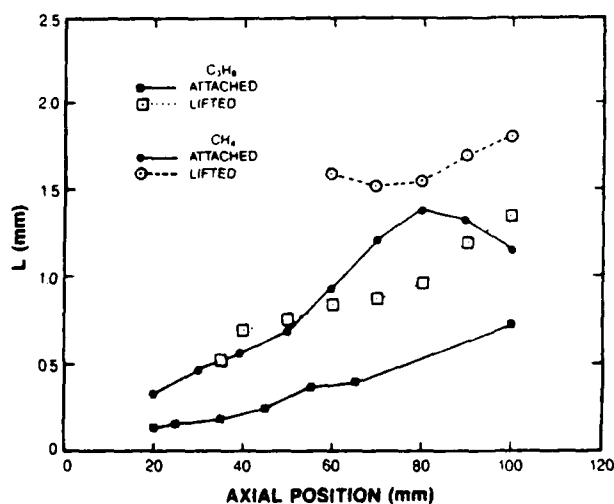


Fig. 7 Measured length scale of radial flame-surface motion

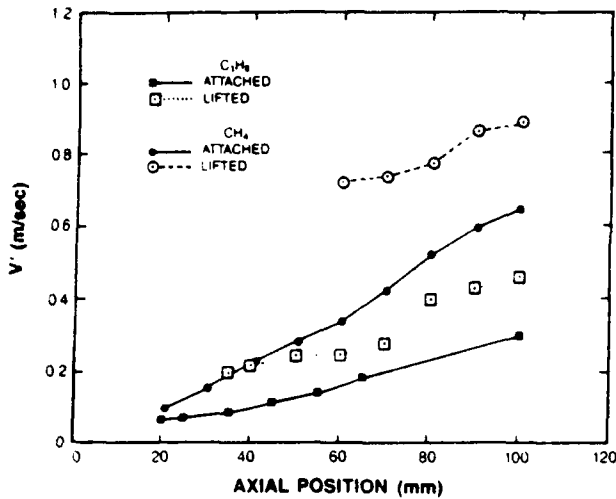


Fig. 8 Measured velocity scale of radial flame-surface motion

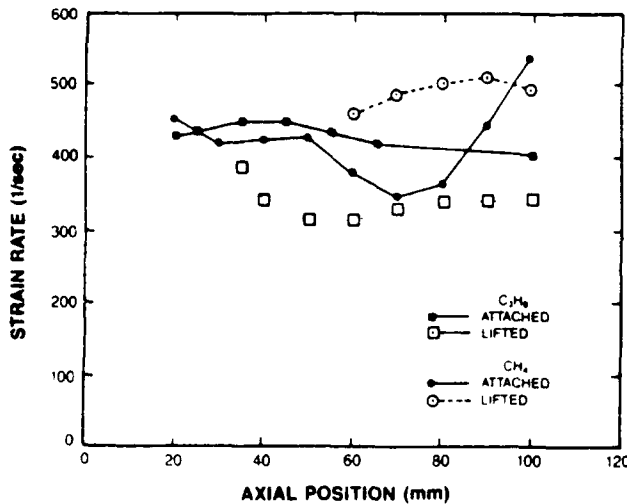


Fig. 9 Measured strain rate,  $S = v'/L$

### Karlovitz Number

In the study of flame stabilization, either the Damkohler or the Karlovitz number is often used as one of the stability criteria (16-17). The definition of these numbers can be related to the ratio of the length scale,  $L$ , to the velocity scale,  $v'$ . In the definition of the Damkohler number,  $L$  and  $v'$  must be related to the velocity flowfield which may be considered the origin or "input" of the disturbance of the flame. In the definition of the Karlovitz number,  $L$  and  $v'$  are associated with the motion of the flame surface which is the result or "output" of the flow disturbance. The relationship between "input" and "output" could be a complicated function of parameters such as Reynolds number, geometry, and flame type. These facts must be considered when making the decision to use one of the above criteria

to study flame extinction. If the generalized flame behavior under certain conditions, e.g., near extinction, is of interest, then the measurement of the "output" of the flame would seem to be a more direct approach.

Figures 7 and 8 show measured  $L$  and  $v'$  directly associated with the flame-surface motion; these scales can be utilized for derivation of the Karlovitz number. The derived Karlovitz number for methane and propane flames under critical flame conditions ranges from 0.75 to 1.2. These values agree well with the results of Lewis and von Elbe (18). Considering that the results were obtained from different combustion systems using various experimental techniques, this fair agreement indicates that under the local extinction condition, the flame may exhibit universal behavior, regardless of conditions such as the type of the flame and geometry.

### CONCLUSION

Through visualization and characterization of turbulent jet flames, the length and velocity scales were found to increase dramatically after flame lifting. The flame/flow interaction for the methane flame is stronger than that for the propane flame presumably due to density effects. As a result, the methane jet flame is more likely to experience holes, which poses a modeling problem. In addition, the Karlovitz number measured near the flame-base zone under lifting conditions agrees with the results for other types of flames. This indicates that under conditions of local extinction, the flame may exhibit universal behavior. Therefore, a natural extension of this research is examination of the turbulent combustor flowfield in a simulated combustor. This effort, which is currently being undertaken, should at least provide the information on similarities and differences between a simple jet diffusion flame and a realistic combustor flame.

### ACKNOWLEDGEMENT

This work was supported in part by and performed at the Wright Research and Development Center/Aero Propulsion and Power Laboratory under Contract No. F33615-85-C-2562. Technical assistance from M. Whitaker, J. Sturud, and C. Obringer is appreciated.

### REFERENCES

1. Dibble, R. W., Long, M. B., and Masri, A., *Progress in Astronautics and Aeronautics*, Vol. 105, 1985, p. 99.
2. Schefer, R. W., Namazian, M., and Kelly, J., "Structure Characteristics of Lifted Turbulent-Jet Flames," *Twenty-Second Symposium (International) on Combustion*, The Combustion Institute, 1988.
3. Hanson, R., "Combustion Diagnostics: Planar Imaging Techniques," *Twenty-First Symposium (International) on Combustion*, The Combustion Institute, 1984, pp. 1677-1691.

4. Roquemore, W. M., Chen, L. D., Goss, L. P., and Lynn, W. F., "The Structure of Jet Diffusion Flames," *Lecture Notes in Engineering*, Vol. 40, *Turbulent Reactive Flows*, Borghi, R., and Murthy, S. N. B., eds., Springer-Verlag, New York, 1989, pp. 49-63.
5. Shepherd, I. G., Hubbard, G. L., and Talbot, L., "The Dynamic Structure of Turbulent V-Shaped Premixed Flames," *Twenty-First Symposium (International) on Combustion*, The Combustion Institute, 1984, pp. 1377-1383.
6. Haworth, D. C., Drake, M. C., Pope, S. B., and Blint, R. J., "The Importance of Time-Dependent Flame Structures in Stretched Laminar Flamelet Models for Turbulent Jet Diffusion Flames," *Twenty-second Symposium (International) on Combustion*, The Combustion Institute, 1988.
7. Goss, L. P., Vilimpc, V., Sarka, B., and Lynn, W. F., "Thin-Filament Pyrometry: A Novel Thermometric Technique for Combusting Flows," *Journal of Engineering for Gas Turbines and Power*, Transactions ASME, Vol. 111, January 1989, pp. 46-52.
3. Bevington, P. R., *Data Reduction and Error Analysis for the Physical Sciences*, McGraw-Hill Book Company, New York, 1969.
9. Cohen, J., and Wygnanski, I., "The Evolution of Instabilities in the Axisymmetric Jet, Part 1," *Journal of Fluid Mechanics*, Vol. 176, 1987, pp. 191-219.
10. Goss, L. P., Vilimpc, V., Lynn, W. F., and Sarka, B., "Simultaneous TFP and RMS Measurements on an H<sub>2</sub> Jet Diffusion Flame," Poster presented at the Twenty-Second Symposium (International) on Combustion, Seattle, WA, 1988.
11. Chen, T. H., Goss, L. P., Talley, D., and Mikolaitis, D., "Stabilization Zone Structure in Jet Diffusion Flames from Liftoff to Blowout," AIAA Paper 89-0153 presented at the AIAA 27th Aerospace Sciences Meeting, Reno, NV, 1989.
12. Chen, T. H., and Goss, L. P., "Flame Lifting and Flame/Flow Interactions of Jet Diffusion Flames," AIAA Paper 89-0156 presented at the AIAA 27th Aerospace Sciences Meeting, Reno, NV, 1989.
13. Dixon-Lewis, G., David, T., Gaskett, P. H., Fukutani, S., Jinno, H., Miller, J. A., Kee, R. J., Smooke, M. D., Peters, N., Effelsberg, E., Warnatz, J., and Behrendt, F., "Calculation of the Structure and Extinction Limit of a Methane-Air Counterflow Diffusion Flame in the Forward Stagnation Region of a Porous Cylinder," *Twentieth Symposium (International) on Combustion*, The Combustion Institute, 1984, pp. 1893-1904.
14. Tsuji, H., "Counterflow Diffusion Flames," *Progress in Energy and Combustion Science*, Vol. 8, 1982, p. 93.
15. Lewis, G. S., Cantwell, B. J., Vandsburger, U., and Bowman, C. T., "An Investigation of the Interaction of Laminar Non-Premixed Flame with an Unsteady Vortex," *Twenty-Second Symposium (International) on Combustion*, The Combustion Institute, 1988.
16. Barlow, R. S., Dibble, R. W., Chen, J. -Y., and Lucht, R. P., "Effect of Damkohler Number on Super-equilibrium OH Concentration in Turbulent Nonpremixed Jet Flames," AIAA Paper 89-0061 presented at the 27th Aerospace Sciences Meeting, Reno, NV, 1989.
17. Williams, F. A., *Combustion Theory*, Addison-Wesley Publishing Company, New York, 1965.
18. Lewis, B., and von Elbe, B., *Combustion, Flames and Explosions of Gases*, 3rd ed., Academic Press, Inc., New York, 1987.

## MULTI-DIMENSIONAL SCALAR MEASUREMENTS IN A H<sub>2</sub>-CH<sub>4</sub> DIFFUSION FLAME

L. P. Goss, W. F. Lynn, B. Sarka, and D. D. Trump  
Systems Research Laboratories  
A Division of Arvin/Calspan  
2800 Indian Ripple Road  
Dayton, OH 45440-3696

In the early development of advanced laser-based nonintrusive diagnostics, the emphasis was on precise point-wise measurements in flames. Techniques such as Raman,<sup>1</sup> CARS,<sup>2</sup> LIF,<sup>3</sup> and LDV<sup>4</sup> allow point-wise measurements of temperature, radial species concentration, and velocities in flame environments. Data from these measurements typically include average, rms, and pdf distributions of the scalar and vector quantities. Profiling of the flame is achieved one point at a time; thus, an average picture of the flame is obtained. For dynamic flame systems, this has been a severe drawback and has spurred the development of multi-point measurement techniques.

Multi-dimensional techniques which have been reported to date include Planar Laser-Induced Fluorescence (PLIF) for measuring radical species concentration and temperature,<sup>5</sup> Rayleigh imaging for measuring density and/or temperature,<sup>6</sup> Lorentz-Mie imaging for studying the mixing properties of jets,<sup>7</sup> and Thin-Filament Pyrometry (TFP) for measuring temperature along the length of a SiC filament placed in a flame.<sup>8</sup> In this paper the use of Rayleigh imaging to capture the temperature field of a low-Reynolds-number jet diffusion flame is reported. Recent studies of such flames<sup>8,9</sup> employing both the reactive-Mie-scattering visualization technique and the TFP technique have shown the presence of large-scale buoyancy-driven vortices which act to modulate the flame surface and are believed to be primarily responsible for flame flicker. Rayleigh imaging may prove to be a valuable tool in understanding these structures.

Because Rayleigh is an elastic scattering process, the intensity of the scattered signal is typically much larger than that of other light-scattering techniques such as Raman or CARS which have been employed for flow diagnostics. The relatively large Rayleigh scattering cross section allows the use of commercially available detectors and laser sources for two-dimensional measurements. The effective Rayleigh cross section  $\sigma_e$  of a gas mixture is given by the sum of the mole-fraction-weighted cross section of the individual constituents<sup>10</sup>

$$\sigma_e = \sum_i \chi_i \sigma_i \quad (1)$$

where  $\chi_i$  is the mole fraction of the gas  $i$  and  $\sigma_i$  is the Rayleigh cross section of the gas observed at 90 deg. The Rayleigh image intensity observed from a uniform laser sheet is given by

$$I_R(x,y) = k I_0 N(x,y) \sigma_e(x,y) \quad (2)$$

where  $I_R$  is the observed signal from volume element  $x,y$ ,  $N$  the number of molecules in this volume element,  $\sigma_e$  the effective cross section for this element,  $k$  a calibration constant for the collection optics, and  $I_0$  the intensity of the incident laser sheet.

The number density of the flame can be related to the flame temperature through the Ideal Gas Law. Thus, if a flame is employed whose Rayleigh-scattering cross section does not vary with temperature, then the observed Rayleigh signal is inversely proportional to the temperature. By comparing the observed Rayleigh signal at room temperature to that of a combusting flowfield, the temperature of the flowfield can be determined by

$$\frac{I_R(\text{flow})}{I_R(\text{room})} \propto \frac{T(\text{room})}{T(\text{flow})} \quad (3)$$

Equation (3) is valid only for a flame in which the effective Rayleigh cross section does not vary appreciably from product to reactant. A wide variety of binary mixtures of hydrocarbons and hydrogens which satisfy the cross-section constraint mentioned above<sup>1</sup> has been reported. The binary mixture employed for the present study contained 31% methane and 69% hydrogen, and its effective Rayleigh cross section varies less than 2% when undergoing combustion.

The experimental apparatus employed for this study is shown in Fig. 1. The doubled output from a Quanta-Ray DCR-I Nd:YAG laser is used to form a 6-cm-high by 1-mm-thick light sheet. Approximately 200 mJ of doubled output is used to form the sheet. The light sheet is placed through the center of an axisymmetric jet diffusion flame. A Photometrics, Ltd., image-intensified camera system is employed to capture the Rayleigh image of the flame at a 90-deg. angle to the light sheet. The camera consists of a Varo image intensifier (utilizing an S20 photocathode) which is coupled to a Thompson 384 x 576 CCD array by a tapered fiber-optic bundle. The camera is controlled by a 68010-based Photometrics DIPS 1000 Controller System. A Princeton Instruments Model PG10 Pulse Generator is used to gate the camera intensifier about the firing of the Nd:YAG laser. A 10- $\mu$ s gate is employed to eliminate unwanted emission from the flame. The synchronization between the laser firing and the camera exposure is controlled by a custom-built interface. To maintain maximum pulse power, the laser is allowed to free run at a 10-Hz rate. Upon acknowledgement by the DIPS 1000 that an exposure is required, the interface waits for the next laser-flashlamp discharge; 250  $\mu$ s after this event, the Q-switch is fired and the exposure made. The interface then acknowledges to the DIPS 1000 that an exposure has been made and that digitization and transfer can take place.

The 376 x 584 camera frame is digitized by a low-noise ADC having 12-bit resolution and stored in the video RAM of the DIPS 1000 for analysis or archival. Analysis of the data consists of correcting each image for non-zero background and scattered laser light and then ratioing the signal from the unknown flowfield to a room-temperature image.

The burner employed is the same as that reported in Ref. 9; therefore, only a brief discussion of it will be given here. The burner system consists of an inner fuel jet surrounded by an annular-air jet. The

fuel nozzle employed in this study was a special tapered 1-cm nozzle designed to produce a flat velocity field. A fuel mixture of 31% methane and 69% hydrogen was employed to minimize changes in the Rayleigh cross section upon burning. The velocity of the fuel jet was  $\sim 3$  m/s at its exit, with the annular-air-flow velocity being  $\sim 0.15$  m/s. The annular-air flow was employed primarily to minimize room-air disturbances on the flame.

Visualization studies of the  $H_2$ - $CH_4$  jet diffusion flame under the above conditions indicate the presence of large toroidal vortices. In general, these vortices which are associated with low-Reynolds-number jet diffusion flames result from an instability in the outer shear layer formed between the faster-moving fuel jet and the slower-moving annular jet. The impact of these vortices upon the flame structure at low and moderate fuel velocities is significant.<sup>8,9</sup> The outer vortices are believed to be responsible for the flame flicker as defined by the oscillation of the luminous flame surface. The flame is pulled radially outward as the toroidal vortices rotate. This results in the formation of a bulge in the flame surface, as demonstrated in the two-dimensional Rayleigh images shown in Figs. 2 - 4. To an observer in the laboratory, the oscillating flame has a flickering appearance due to the upward convective motion.

The appearance and evolution of the flame bulge is depicted in the Rayleigh images of Fig. 2 - 4. Figure 2 displays the temperature-field image recorded  $\sim 1$  cm above the fuel-jet nozzle. The total area of the image is  $\sim 6 \times 6$  cm<sup>2</sup>. The thick reaction zones of this flame are believed to be due to the high molecular diffusivity of the hydrogen molecule and its broad flammability range. The formation of the bulge can be seen at the top of Fig. 2. The cold central core of fuel is clearly visible in the figure.

Figure 3 displays the Rayleigh image of the flame at a location 7 cm above the jet nozzle. The growth of the flame bulge with axial location is clearly demonstrated. Large amounts of cold air are being entrained into the flame surface by the bulges and associated air vortices (not depicted). The cold central jet is still visible in this flame region.

Figure 4 displays the Rayleigh image of the flame at a location 12 cm above the jet nozzle. The extent of wrapping of the flame bulge can be observed from this image. The flame has increased to approximately three times its size at the nozzle exit. The cold central jet which was visible through the 13-cm region has now undergone extensive preheating and some combustion, as evidenced by the appearance of the dark inner core. The Rayleigh image at this location gives a more complete picture of the temperature field than that from the TFP technique because of the 1000-K lower limit of the TFP.

In conclusion, a two-dimensional Rayleigh imaging technique has been developed and employed to examine a  $H_2$ - $CH_4$  jet diffusion flame. The temperature images clearly demonstrate flame bulging (pinching and stretching) due to the interaction of the flame surface and outer toroidal vortices.

### Acknowledgement

This effort was supported by USAF Contract No. F33615-85-C-2562.

### References

1. M. Lapp and D. L. Hartley, "Raman Scattering Studies of Combustion," Combust. Sci. Technol. 15, 199 (1976).
2. A. C. Eckbreth and J. H. Stufflebeam, "Considerations for the Application of CARS to Turbulent Reacting Flow," in Experimental Measurements and Techniques in Turbulent Reactive and Nonreactive Flows, AMD-Vol. 66 (R. M. C. So, J. H. Whitelaw, and M. Lapp, Eds.) (American Society of Mechanical Engineers, New York, 1984), p. 11.
3. Laser Probes for Combustion Chemistry (D. R. Crosley, Ed.), ACS Symposium Series 134 (American Chemical Society, Washington, D. C., 1980).
4. P. O. Witze, "A Critical Comparison of Hot-Wire Anemometry and Laser Doppler Velocimetry for I. C. Engine Applications," Trans. SAE 86, 1012 (1977), Paper No. 770220.
5. R. K. Hanson, B. Hiller, E. C. Rea, Jr., P. M. Seitzman, G. Kychakoff, and R. D. Howe, "Laser Based Diagnostics for Flow-field Measurements," in Experimental Measurements and Techniques in Turbulent Reactive and Nonreactive Flows, AMD-Vol. 66 (R. M. C. So, J. H. Whitelaw, and M. Lapp, Eds.) (American Society of Mechanical Engineers, New York, 1984), p. 1.
6. D. C. Forquette, R. N. Zurn, and M. B. Long, "Two Dimensional Rayleigh Thermometry in Turbulent Nonpremixed Methane-Hydrogen Flame," Combust. Sci. Technol. 44, 307 (1986).
7. M. Winter, J. K. Lam, and M. B. Long, "Techniques for High-Speed Digital Imaging of Gas Concentrations in Turbulent Flows," Exp. Fluids 5, 177 (1987).
8. V. Vilimpoc, L. P. Goss, and B. Sarka, "Evaluation of Optical Diagnostic Techniques for High-Frequency Temperature Measurements," Paper presented at the 1987 Spring Technical Meeting of the Central States Section of the Combustion Institute, Argonne, IL, May 11-12, 1987.
9. W. M. Roquemore, L-D. Chen, L. P. Goss, and W. F. Lynn, "The Structure of Jet Diffusion Flames," Paper presented at the United States - France Joint Workshop on Turbulent Reactive Flows held in Rouen, France, July 6-10, 1987.
10. C. M. Penny, "Light Scattering in Terms of Oscillator Strength and Refractive Indices," J. Opt. Soc. Am. 59, 34 (1969).
11. R. W. Dibble and R. E. Hollenback, "Laser Rayleigh Thermometry in Turbulent Flames," in 18th Symposium (International) on Combustion (The Combustion Institute, Pittsburgh, PA, 1981), p. 1489.

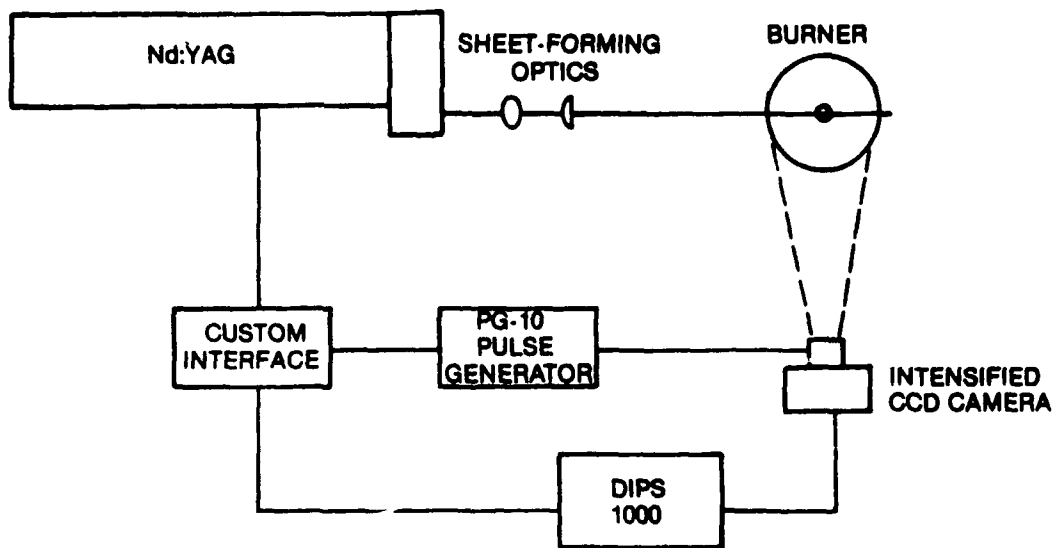


Figure 1. Schematic Diagram of Two-Dimensional Rayleigh Imaging System.

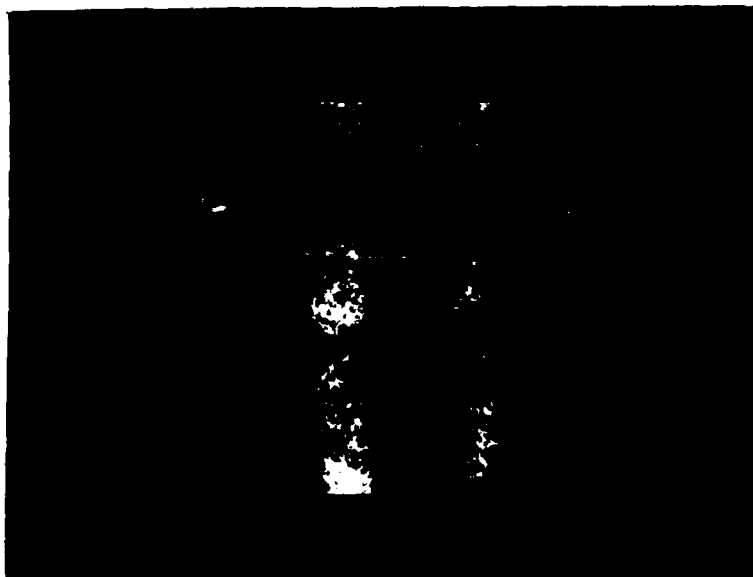


Figure 2. Rayleigh Image of H<sub>2</sub>-Methane Diffusion Flame at Location 1 cm Above Nozzle Exit.

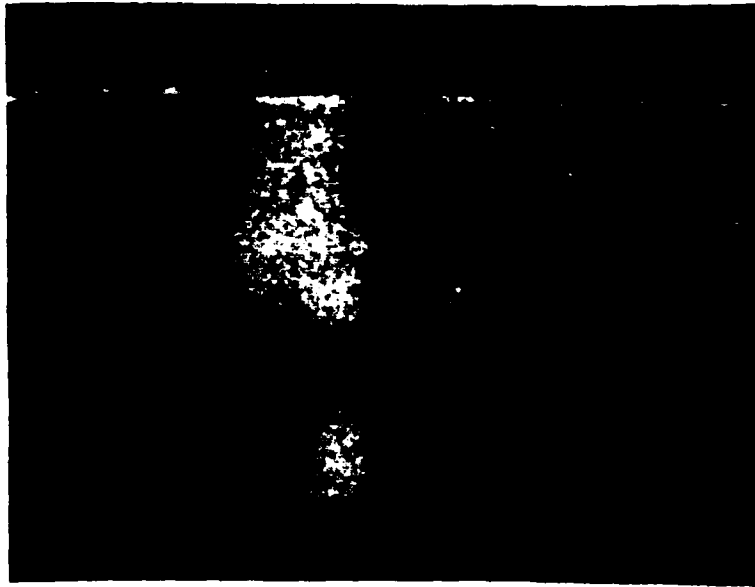


Figure 3. Rayleigh Image of H<sub>2</sub>-Methane Diffusion Flame at Location 7 cm Above Nozzle Exit.

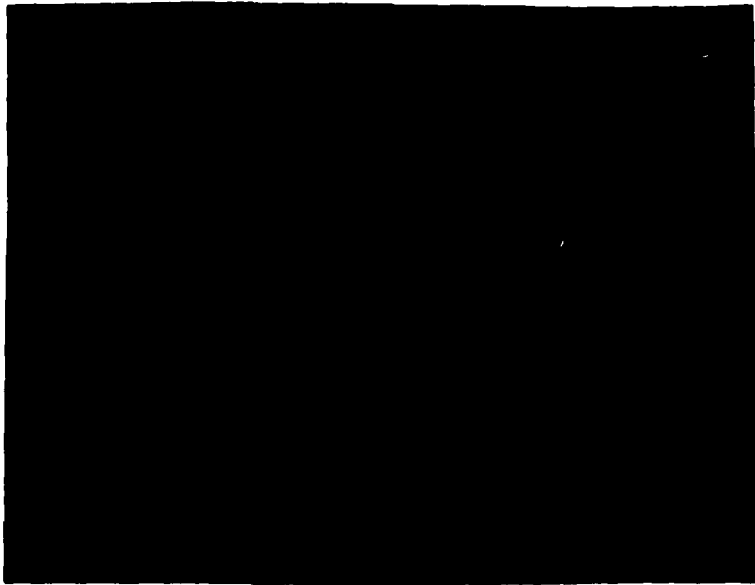


Figure 4. Rayleigh Image of H<sub>2</sub>-Methane Diffusion Flame at Location 12 cm Above Nozzle Exit.

## TWO-DIMENSIONAL TEMPERATURE AND VELOCITY MEASUREMENT TECHNIQUES IN A SOOTY JET DIFFUSION FLAME

V. Vilimpec, L. P. Goss, M. E. Post, B. Sarka, and D. D. Trump

Systems Research Laboratories, Inc.  
A Division of Arvin/Calspan  
2800 Indian Ripple Road  
Dayton, OH 45440-3696

### ABSTRACT

In a jet diffusion flame, strong interaction between velocity and temperature gradients gives rise to the formation of periodic large-scale buoyancy-driven structures. To understand and model such a dynamic process, the temperature and velocity history for the entire cycle must be available. Thin-filament pyrometry was used in conjunction with a CCD camera to obtain instantaneous temperature profiles, and two-color particle-imaging velocimetry was employed to map the velocity field in a sooty propane jet diffusion flame.

### THIN-FILAMENT-PYROMETRY TECHNIQUE

Thin-filament pyrometry (TFP) is a radiometric technique which utilizes the blackbody emission from a SiC fiber for the measurement of temperature. SiC has thermal conductivity (10 kcal/m hr °C [1]) which is ~ 40 times lower than that of Pt-Pt-Rh wire. It also possesses a fast response time due to its small size (15- $\mu$ m nominal diam.). Successful application of the TFP technique in this laboratory to the study of non-sooting jet diffusion flames was reported previously [2-4].

### Experimental

In an effort to extend this technique to the mapping of an instantaneous two-dimensional temperature field in a sooty jet diffusion flame, a CCD camera was used to capture images of 10 filaments suspended vertically above a propane-nitrogen flame anchored on a contoured nozzle. The nozzle used in the experiment has a diameter of 23 mm, with a 7-deg. tapered exit section. The fuel used was a mixture of propane and nitrogen in equal mass fractions, flowing at an exit velocity of 10 cm/sec.

Co-flowing annular air at an exit velocity of 15 cm/sec from a 250-mm-diam. annulus stabilized and reduced the outside disturbance to the flame system. The imaging system consists of a Photometrics Model 200 CCD camera system with a 384 x 576 pixel image format, each pixel being ~ 25  $\mu$ m in diam., and a computer controllable shutter from Uniblitz.

It was determined through observation of the flame that the formation and movement of the large-scale structures are repetitive and cyclic in nature. A silicon photodiode detected periodic signals from the structures and produced signals which could then be employed to initiate the image-acquisition sequence. After receipt of the photodiode trigger pulse, a time delay was generated

internally by the control computer; thus, a sequence of images was obtained at different times in the cycle. The period for a complete cycle of the flame-bulge formation is ~ 60 ms. A sequence of 14 images was taken for each of six phases in the cycle, with the initial sequence having a 10-ms delay and the final sequence having a 60-ms delay from receipt of the photodiode trigger pulse. Each image consisted of an ~ 10 x 25 cm region in which the lowest filament was suspended 50 mm above the nozzle and each of the other nine filaments was located 20 mm from its nearest neighbors. The images in each sequence were then subjected to identical image-processing procedures to extract the filament intensity data. These data were converted to temperature and then averaged to smooth out small variations.

### Data Analysis

An intensity plot in a direction parallel to the filaments is shown in Fig. 1. Note the almost uniform soot emission to either side of the filament. The approach used to compensate for soot emission was to approximate as closely as possible the soot intensity in a direction normal to the filament and subtract this

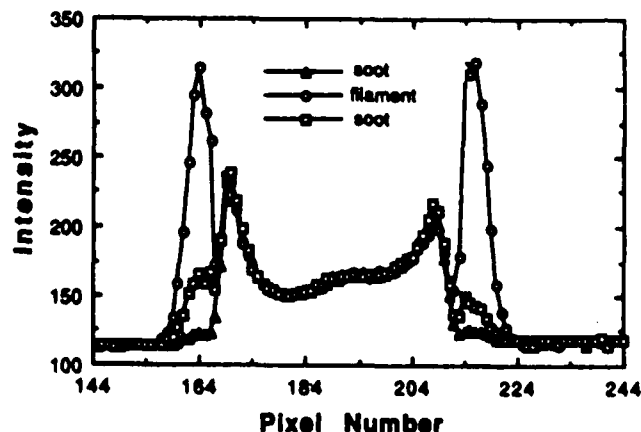


Fig. 1. Intensity (vertical axis) plot of filament and its two adjacent neighbors (horizontal scale represents distance along filament length)

intensity from the actual intensity at corresponding spatial locations. At locations where only soot is present, the interpolated intensity and the actual intensity are identical; therefore, the resultant subtracted intensity would be zero. Along the filaments, sums of the soot and the filament intensities will be higher than the interpolated soot intensity; the subtracted intensity would then represent only the filament intensity.

Because the filament may not necessarily lie along a given column of image data, an automated search to find the actual filament locations was made by searching for maxima in the derivative image. In practice, the filament intensity typically spread over three to four columns in width due to the limited resolution of the imaging system. Once the locations of the filaments were known, the intensity values needed to construct the polynomials were obtained from the pixels adjacent to the filament. To approximate the soot emission, fourth-order least-squares polynomial coefficients were obtained by regression analysis of the actual data. The data used to compute the fitting polynomial coefficients and the resultant interpolation are shown in Fig. 2. The filament center is located at Column 211. The data for the polynomial fit are obtained from Columns 200-206 and 215-221. A fourth-order polynomial is used to construct the intensity profile of the soot background, from Columns 200-221, which is then subtracted from the actual intensity at the corresponding locations. The resultant subtracted intensity values for the eight columns centered on the filament are summed to account for the image-blooming effect of the detector.

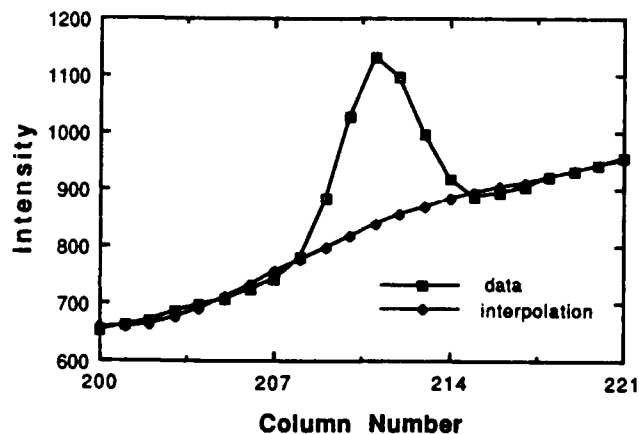


Fig. 2. Data used in regression analysis to form fourth-order polynomial ( $\square$ ) and resulting interpolation ( $\circ$ )

To convert the filament intensity obtained into temperature, pure hydrogen was substituted for the propane-nitrogen fuel mixture. The average maximum-intensity value obtained from the hydrogen jet diffusion flame was then assigned a temperature value corresponding to the adiabatic equilibrium flame temperature, and the intensity data for the propane flame were scaled by the known hydrogen-flame temperature and converted to temperature data through the use of Planck's equation. The calculated temperature profiles were then corrected, by the method outlined in Ref. 2, for the minor heat loss due to convection. Temperature profiles obtained by means of this technique are superimposed on the average of 14 images, as shown in Fig. 3. Note the expansion and contraction of high-temperature zones following the passage of the large-scale structures. At most locations in the flame, excellent data were obtained, revealing the essential features of the temperature fields under study.

#### TWO-COLOR PARTICLE-IMAGING VELOCIMETRY

In complex flowfields, i.e., recirculating flows, it is important to obtain an instantaneous two-dimensional picture of the entire flowfield rather than be restricted to a pointwise time-averaged map. For low to moderate velocity flowfields, particle-tracking

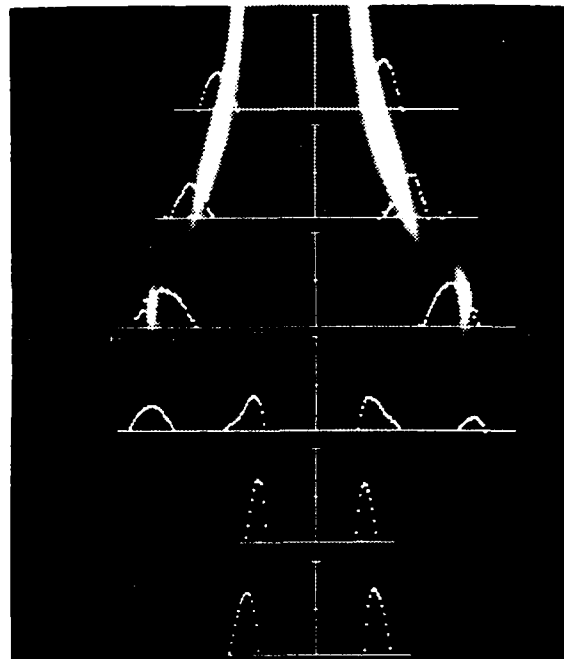


Fig. 3. Center portion of jet diffusion flame with resultant temperature profiles superimposed on filament locations (note incipient formation of large-scale structures)

methods are efficient, offering a wide velocity range and allowing two-dimensional measurement of the velocity flowfield [5].

#### Experimental

The experimental arrangement for two-color particle-imaging velocimetry (PIV) measurements is shown in Fig. 4. Two separate Nd:YAG lasers are used in forming the different-color light sheets for exposing the position of the particles in the seeded flowfield. The green-laser light sheet is formed from the doubled output of a Nd:YAG laser (Quanta-Ray DCR 1A) at 532 nm. The red-laser light sheet at 607 nm is formed by using the frequency-doubled output of a Nd:YAG laser (Quanta-Ray DCR 3A) to pump a dye laser. The combined laser sheets were ~ 10 cm in height and 1 mm in thickness in the test area. The time separation between the green- and red-laser sheets was 500  $\mu$ sec. The seed (alumina of 1- $\mu$  nominal size) was injected into both the fuel and the annular air.

A Nikon 35-mm format camera was used to record the Mie scattering from the seeded flowfield. A macro zoom lens operating at an  $f/8.4$  aperture was employed for the images reported in

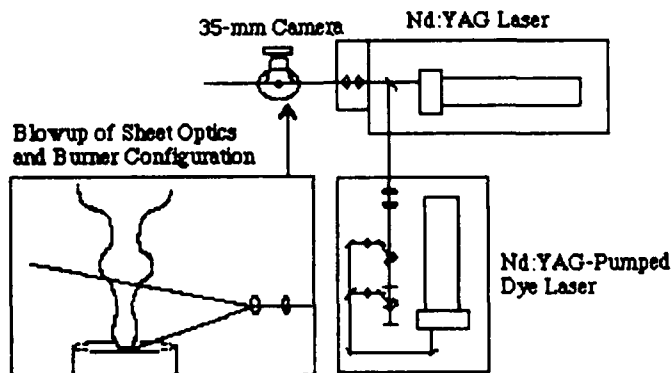


Fig. 4. Experimental arrangement for two-color particle-imaging velocimetry

this study. This lens-aperture combination resulted in a magnification factor of 0.39. To reduce the contribution of the soot emission of the flame, a Uniblitz high-speed camera shutter operating at a 1/500-sec. exposure was employed. The 100 - 400 ASA color film used to record the two-color PIV images was processed commercially. The experimental arrangement for the jet diffusion flame was described previously.

### Image Analysis

The analysis procedure consists of 1) digitizing the color negative with a CCD array, 2) determining the spatial locations of the digitized particle images, 3) constructing a correlation map from which the most probable displacement vector can be determined, and 4) using this information in a tracker which identifies green/red-particle vector pairs from the digitized image.

The color film was digitized by a 384 x 576 CCD camera using a film projector to enlarge a section of the film onto the camera. The digitized film sections typically covered a 1.5-sq.-cm area of the recorded image. Each section of the enlarged image was digitized twice--first with a green filter for identifying the green-particle image and the second time with a red filter for identifying the red-particle images. The unique color coding helps remove directional ambiguities since the red image occurs after the green.

A correlation-histogram map is constructed from the green-and red-particle images. As green/red-particle pairs having the same velocity--and thus displacement--are mapped onto correlation space, peaks are built up on this map. The maximum of this map corresponds to the most probable displacement from the center coordinate. To determine the individual velocity vectors, a tracker must be employed.

The tracker functions by first starting from each green-particle image, adding the most probable vector displacement, and searching for the corresponding red-particle pair. If there is a red particle at the projected coordinates, then a velocity match is made and a vector drawn. If no red particle is found at these coordinates, a small window is opened around the target coordinates. This window is expanded incrementally to a selected percentage of the vector length.

The processed two-color PIV image for the 2.54-cm propane jet is shown in Fig. 5. The initial velocity of the fuel jet was ~ 0.15 m/sec at the nozzle exit. As the fuel jet progressed downstream, the velocity of the jet decayed, approaching zero at ~ 1.5 diameters downstream. The development of the stagnation zone was due to the high density of the propane fuel which overcame the initial momentum of the fuel jet. Just above this stagnation zone the fuel jet accelerated due to the proximity of the fast hot-burning gases. Notice that these hot regions displayed a much higher velocity than the cold central fuel jet. This high velocity was believed to be due to the buoyancy effect which would accelerate the hot (low density) combusting gases. The gases in the combusting zone reach a velocity of ~ 3 m/sec. Notice, also, how the cooler outer air was entrained into the flame at downstream locations. This process acted to mix burning fuel with air and, thus, sustain combustion at downstream locations.

### CONCLUSIONS

Application of the TFP technique to the study of a sooty flame has been demonstrated. Furthermore, by spacing filaments over the height of the flame and using a CCD array detector, instantaneous two-dimensional temperature profiles were obtained. Through application of the two-color PIV technique to the same flame, an instantaneous two-dimensional velocity map was obtained. Although not employed in this study, concurrent application of the techniques can be used to obtain simultaneous temperature profiles and velocity fields; this can be an invaluable tool in the analysis of temporally and spatially dependent phenomena.

### ACKNOWLEDGEMENT

The research reported herein was supported by and performed at the Wright Research and Development Center, Aero Propulsion

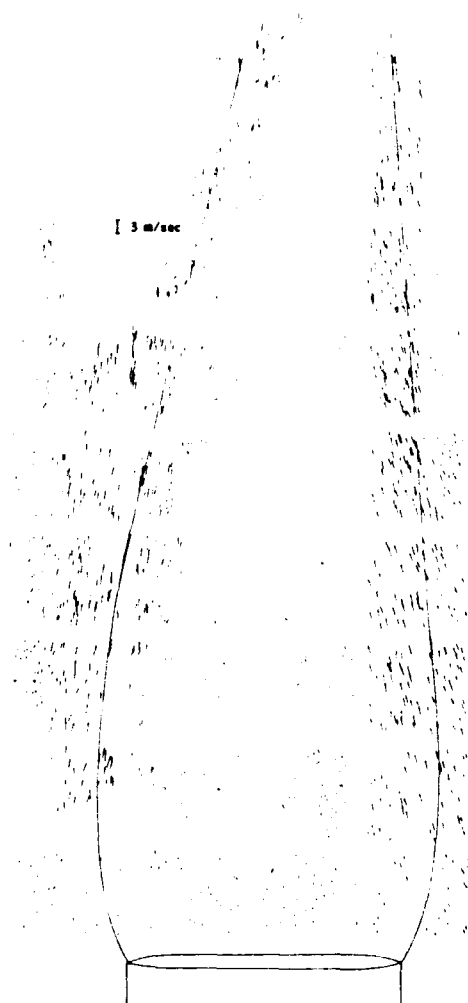


Fig. 5. Outline of jet diffusion flame with superimposed velocity vectors

and Power Laboratory, Wright-Patterson Air Force Base, Ohio, under Contract F33615-85-C-2562. The authors are grateful to Dr. W. M. Roquemore, Dr. C. D. MacArthur, and Mr. S. W. Kizimis for helpful discussions.

### REFERENCES

1. Nicalon, Silicon Carbide Fiber, Dow Corning Corporation, Midland, MI 48686-0995.
2. Goss, L. P., Vilimpc, V., Sarka, B., and Lynn, W. F., "Thin-Filament Pyrometry: A Novel Thermometric Technique for Combusting Flows," *Transactions of the ASME, Journal of Engineering for Gas Turbines and Power*, Vol. 111, Jan. 1989, pp. 46-52.
3. Vilimpc, V., Goss, L. P., and Sarka, B., "Spatial Temperature-Profile Measurements by the Thin-Filament Pyrometry Technique," *Optics Letters*, Vol. 13, Feb. 1988, pp. 93-95.
4. Vilimpc, V., Sarka, B., Kizimis, S., Fernandez, M., and Roh, W., "Study of Oscillations in  $H_2-N_2$  Diffusion Flame Using Thin-Filament Pyrometry and FFT Frequency-Domain Analysis," Presented at the 1988 Spring Technical Meeting of the Central States Section of the Combustion Institute, Indianapolis, IN, May 2-3, 1988.
5. Goss, L. P., Post, M. E., Sarka, B., and Trump, D. D., "Two-Color Particle Velocimetry," Presented at the International Congress on Applications of Laser and Electro-Optics (ICALEO '89), Livermore, CA, 15-20 October 1989.

**Statistical OH-Zone Structures of Turbulent Hydrocarbon Jet Flames:  
Results of RMS/OH-PLIF Techniques\***

**Tzong H. Chen and Larry P. Goss  
Systems Research Laboratories, Inc.  
A Division of Arvin/Calspan  
2800 Indian Ripple Road  
Dayton, OH 45440-3696  
(513) 252-2706**

**Abstract**

Joint Reactive-Mie-Scattering (RMS) and Planar-Laser-Induced-Fluorescence (PLIF) techniques have been employed to study the impact of jet-shear-layer development upon flame behavior. Images of the complete penetration of the shear-layer vortex through the flame surface have been successfully captured utilizing these planar imaging techniques. Studies of these images have indicated that the degree of flame/flow interaction varies with respect to a wide range of flame conditions and results in the observation of several different types of flame zones--flamelets, multiple flamelets, thick flame zones, and local extinction. The probability of observing the different types of flame behavior was measured, and the results are presented. Analysis of the probability data indicates that the root-mean-square (rms) flame-surface fluctuation,  $L$ , provides a proper length scale for correlating the statistical behavior of the flame. Significant changes in the flame behavior were observed to occur at two critical values of  $L$ --the minimal thermal thickness ( $\sim 1$  mm) and the nozzle diameter (5 mm).

**KEY WORDS:** Flame, Stabilization, Measurement, OH, PLIF, Probability.

---

\*A version of this paper was presented at the AIAA 28th Aerospace Sciences Meeting as AIAA Paper No. 90-0159.

## INTRODUCTION

Information on the detailed flame/flow interaction is an important key to understanding flame-stabilization mechanisms for jet flames under attached or lifted flow conditions. Three different theories (Pitts, 1988) have been applied in attempts to explain flame lifting: 1) the laminar flamelet mode (Peters and Williams, 1983), 2) the premixed combustion mode (Vanquickenborne and van Tiggelen, 1966), and 3) the large-scale structural-mixing model (Broadwell and Breidenthal, 1982; Dahm and Dibble, 1988; Miake-Lye and Hammer, 1988). Although these models were established through sound experimental and theoretical efforts, under many circumstances they are contradictory. Disagreement between the various theories may be due, in part, to the vast differences in the turbulence states of mixing and combustion processes in the jet flowfield which result from the development of large-scale vortices. As an example, earlier work of Shekarchi *et al.* (1988) indicated that the flame lifting begins at the nozzle mouth, regardless of the fuel, for a taper nozzle jet exhibiting a flat velocity profile. However, it has been experimentally observed that this is *not* the case for a methane flame (Chen and Goss, 1989); the observed difference in lifting characteristics between the methane and propane flames in this study was attributed to the difference in the degree of interaction of the flame surface and the vortices initiated from the fuel jet. Thus, a thorough statistical characterization of this interaction can aid the understanding of flame-lifting mechanisms.

Two important aspects of large-scale vortices have opposite effects upon flame stabilization: 1) promotion of fuel-air mixing which stabilizes the flame, and 2) stretching and penetration of the flame zone which destabilizes the flame. The weight of these counter-effects may be determined by means of associated scales such as the thickness of the combustible mixing zone, the size of the large-scale structure, and the thickness of the OH zone which provides a potential source of reignition. Studies of the stabilization effect have received more attention; however, due to the availability of laser diagnostics, considerable interest has now been shown in the destabilization effect. This study is concerned with the destabilization effects of large-scale vortices as imaged by planar-laser-imaging techniques.

The Planar-Laser-Induced-Fluorescence (PLIF) (Hanson, 1986) and Reactive-Mie-Scattering (RMS) (Roquemore *et al.*, 1989) techniques were employed in the present study to characterize the flame/flow interactions of turbulent jet flames. For the PLIF technique, the OH-radical fluorescence was utilized. The existence of the OH radical is an indicator of ongoing combustion processes and can mark the area of the thermal zone. For the RMS technique, TiO<sub>2</sub> seed particles formed by the reaction of TiCl<sub>4</sub> with water were used for Mie scattering. When properly introduced into the fuel jet, TiCl<sub>4</sub> forms TiO<sub>2</sub> in the fuel-mixing layer. By tracking the vortex motion with Mie scattering and marking the flame zone by OH fluorescence, the impact of large-scale structures upon flame behavior can be observed. By statistically analyzing the experimentally observed OH profiles, the thickness of the thermal zone, the magnitude of the flame fluctuation, and the probability of observing flamelets, thick flame zones, and holes can be determined. This analysis allows evaluation of the dependence of the statistical flame properties upon the degree of flame/flow interaction. A proper representation of the degree of flame/flow interaction will be described.

## EXPERIMENTAL

### Flow Conditions

The fuel jet employed in this study consisted of a short, tapered 5-mm-id nozzle surrounded by a 25-cm annular air duct. The contraction ratio of the contoured nozzle, 20 to 1, was designed to yield a flat exit-velocity profile. The exit velocity of the annular air flow was fixed at 15 cm/sec. The fuels employed for this study included propane and methane, with jet velocities ranging from flame liftoff to near blowout. The critical liftoff velocity for the propane flame was measured to be 19.5 m/s and that for the methane flame, to be 29.0 m/s. Under the critical liftoff condition, the flame can be either attached or lifted. The measurement locations were chosen in the near-field region from the flame base up to 60 jet diameters downstream,  $x/d = 60$ . In this region the fuel-jet shear layer and flame surface interact strongly, allowing the deformation of the flame surface to be studied.

## Diagnostic Techniques

The optical setup utilized in this study for joint RMS/OH-PLIF measurements is shown in Fig. 1. A Quanta-Ray DCR-3:PDL:WEX laser system was employed to produce the UV radiation required to excite the (0,1) transition of the OH radical. The UV beam of 283-nm wavelength was passed through sheet-forming optics and directed through the flame zone. Laser-induced fluorescence from the OH radical was observed at right angles to the laser sheet by an intensified two-dimensional CCD camera (Photometrics CC200). The 384 x 576 pixel density of the CCD camera combined with the optical arrangement resulted in a 98- $\mu\text{m}$ /pixel spatial resolution which allowed observation of a 37.5 x 55 mm area of the flame.

Joint RMS/OH-PLIF measurements were made by introducing a small amount of  $\text{TiCl}_4$  into the gaseous fuel.  $\text{TiCl}_4$  reacts with water formed as a combustion byproduct to produce small seed particles which can scatter laser light. Care was taken to ensure that the seed concentration would be maintained at a low level such that the OH-fluorescence signal would not be overwhelmed by the Mie-scattering signal. In this arrangement the Mie-scattering and OH-PLIF signals are observed simultaneously by a single camera system. For independent OH-PLIF measurements, a spike filter with 30% efficiency centered at 314 nm, half-width of 10 nm, was used to filter out the Mie scattering from the dust particles and soot. For most flame conditions tested, the flame base was blue in color and soot emission was not observed to be a problem.

## Dissipation Calculation

One of the natural candidates for examining the degree of flame/flow interaction is measurement of the scalar dissipation involved in the combustion process. The presence of the OH radical marks the thermal zone which--for the case of a diffusion flame--includes the reaction zone. The absence of the OH radical in a cross section of the flame surface thus represents possible flame extinction. Calculation of the dissipation of the OH radical was carried out for the experimental OH images as (Namazian *et al.*, 1988; Long and Yip, 1988):

$$\chi = 2D [(\delta S/\delta x)^2 + (\delta S/\delta y)^2] \quad (1)$$

where D is the diffusion coefficient, S the measured OH signal,  $\delta$  the differential operator, and x and y the ordinates of horizontal and vertical direction, respectively.

### Probability Analysis and Signal Detectability

For constructing a statistical description of the flame properties, hundreds of scalar measurements are required. In the case of two-dimensional imaging techniques, this can constitute a problem due to the massive amount of data required (443 KBytes of information per image). To solve this problem, a line image system was employed. In this case the laser-excitation beam is mildly focused into a cylinder or line, the fluorescence from which is captured by a 1024-element intensified-diode-array system. For each flame condition, several axial locations were chosen for measurement. At each location 750 line images were acquired and stored for analysis.

Because the laser-excitation line intercepts the jet-flame axis perpendicularly, it crosses the flame zone twice. Since the radial flame fluctuation is small compared to the jet-flame diameter, disappearance of the OH fluorescence signal cannot be due to drifting of the flame. Absence of the OH signal in an area where the flame surface should be located can be due to either flame extinction or hole formation. Except for hole formation, the experimentally observed thermal zones were of three types: thin flamelets (~ 1 mm in thickness), thick flame zones (> 3 mm), and multiple flame zones (combination of multiple thin or thick zones). For data-presentation purposes, multiple flamelets were considered to be a thick flame.

By counting the number of times each of these zones was observed, one could determine the probability of their occurrence:

$$\text{Probability} = (\text{event count}) / N_i \quad (2)$$

where  $N_i$  is the number of line images collected (750 in this study).

Although this type of analysis does not require quantitative temperature information, the signal-detectability limit must be considered. To ensure that the OH signal would not disappear due to insufficient laser power or inefficient detectability, several measures were taken. First, the Nd:YAG laser was operated at full power. Measurements of the OH signal intensity as a function of laser power indicated that the OH fluorescence was in the saturated regime for the line-measurement conditions studied. For the optical setup utilized in this study, the linear OH fluorescence exists only under very low power conditions--less than 50% of full power. Second, results from the line-OH measurements, when compared with temperatures measured by thin-filament pyrometry (TFP) (Chen and Goss, 1989; Chen *et al.*, 1989), indicated that the OH signal was detected only in a region where the temperature was above ~ 1000 K. Therefore, when the local flame temperature was higher than the ignition temperature and the fuel-air mixture was combustible, the OH radical existed and could be detected by the optical setup employed.

## RESULTS AND DISCUSSION

### Local Extinction and Non-Flamelet Behavior

Evidence of discontinuities (or holes) in the flame sheet of jet diffusion flames has been reported by several groups (Roquemore *et al.*, 1989; Eickhoff *et al.*, 1985; Schefer *et al.*, 1988; Takahashi *et al.*, 1982). The existence of holes in the flame surface is thought to result from the penetration of the flame by vortices formed by the fuel jet. Since flame-stabilization behavior is linked to the evolution of these vortices (Pitts, 1988; Miake-Lye and Hammer, 1988), an experimental investigation was initiated to study these flame/vortex interactions.

Figure 2 is a joint RMS/OH-PLIF image taken in the near field of an attached  $\text{CH}_4$  diffusion flame at the critical liftoff velocity. The vortex penetration through the flame surface can be seen clearly in this figure. The flame surface, indicated by the outer OH fluorescence, displays an area of local extinction corresponding to the size of the penetrating vortex which

is marked by the Mie scattering associated with the fuel jet. In this particular case the propagation of the flame surface is passive and dominated by the vortex motion which is driven by the fuel jet. For most jet diffusion flames, the separation of the flame surface from the shear layer (Roquemore *et al.*, 1989; Masri *et al.*, 1984) is well defined. However, this separation is not so well defined in the methane as in the propane flame, resulting in a stronger flame/flow interaction for the former. In addition, the density of the methane jet is lower than that of the co-flowing air; thus, the shear-layer vortex has a higher probability of spinning out and interacting with the flame. As a result, the methane flame displays a higher probability of hole formation than the propane flame at the critical liftoff jet velocity. The high probability of hole formation at a location  $\sim 60$  mm downstream causes the methane flame to split before complete lifting occurs. This observation was confirmed by the probability data which will be presented in the next section.

Seven large vortices can be identified in the RMS/OH-PLIF image displayed in Fig. 2. The flame surface is distorted by only three of these. The other four have little effect due to their greater separation from the surface which reduces the strength of the interaction. As a result, the flame surface fluctuates at a frequency which is lower than that of vortex passage. This result is consistent with those of previous studies which found that the flame surface fluctuates in the frequency range  $\sim 50$  to 125 Hz. Based upon the liftoff height, jet exit velocity, and flame-crossing frequency, the values of the Strouhal number for this flame were determined to be  $\sim 0.10 - 0.15$  (Chen *et al.*, 1989).

As can be seen from Fig. 2, the OH-zone thickness remains fairly constant,  $\sim 1$  mm, at the flame base for both the propane and methane flames operating under the critical liftoff condition. This slow growth of the thermal zone was also observed by Schefer *et al.* (1988). The OH zone thickness for the laminar propane and methane flames was also experimentally measured, and the smallest value was found to be 1 mm. As the jet velocity increases beyond flame liftoff, the interaction between the flame and the vortex layer becomes stronger, resulting in an increase in the probability that local extinction (hole) will occur at the flame surface. In

this case, the flame attempts to stabilize at a downstream location where the interaction is weaker. Under the near-blowout condition, the flame base is stabilized far downstream where fuel-air mixing is nearly complete. This results in a premixed combustion zone which is thick in nature and tends to wrap around the vortices. In this region tribrachial flames (Buckmaster and Matalon, 1988) may exist, which can also contribute to a thick thermal zone. The measured thickness of the OH zone near the flame base under this condition varies from ~ 10 to 30 mm which compares favorably with previous temperature results (Chen and Goss, 1989).

Figures 3-5 depict planar OH images and their associated dissipation at the base of a lifted methane flame operated under near-blowout conditions. Under these conditions 1-mm-thick flamelets can still be observed, but the probability of observing them is lower. The observed flame-base structures fall into three categories. The first, shown in Fig. 3, is a simple flame tip. The second is a thick vortical structure, as shown in Fig. 4. Inside the thick thermal zone, two small non-burning zones can be observed, corresponding to pockets which are extremely fuel-rich (Barlow, 1989). The third type of flame base, shown in Fig. 5, is characterized by two distinct islands of combustion located outside the main flame base. The associated dissipation map, shown in Fig. 5(b), indicates that the dissipation rate is maximized at the interface between these islands. The wedge shape of this maximum-dissipation area suggests that the local extinction here may be due to excessive stretching.

#### Probability of Observing Flamelets, Holes, and Thick Zones

The flames shown in Figs. 4 and 5 would display multiple OH-signal peaks if observed by a line CCD detector. The presence of such peaks was reported in an earlier study (Chen *et al.*, 1989). The multiple flame zones in this case were classified as thick flames, as was mentioned previously. In addition to the thick zone, flamelets and holes can also be observed at different downstream locations. The probability of observing these events is shown in Figs. 6-9 for methane and propane flames under the critical liftoff condition. Figures 6, 7, 8, and 9 display data for the attached methane flame, the lifted methane flame, the attached propane flame,

and the lifted propane flame, respectively. The probability of observing thin flamelets is highest at the flame base. Further downstream, the probability of observing holes and thick OH zones increases. The methane flame displays a higher probability of developing holes than the propane flame, as explained previously. The coexistence of thin flamelets, holes, and thick flame zones is indeed challenging to the modeling community (Haworth *et al.*, 1989; Chen and Kollmann, 1989; Corea and Gulati, 1989).

Comparison of Figs. 6 and 7 leads to the conclusion that under the critical liftoff condition, flamelets, thick flame zones, and holes have the same probability of occurring in attached and lifted flames. This is primarily due to the fact that the exit velocities are the same. This conclusion can also be drawn from the propane-flame results displayed in Figs. 8-9. At the 300-mm downstream location, the probability of observing holes approaches that of observing flamelets for the flow conditions presented in Figs. 6-9. Data for the methane flame, having an exit velocity of 40 m/s, are plotted in Fig. 10. As the jet velocity is increased, the flame/flow interaction is observed to become stronger. The probability of observing holes is higher than that of observing flamelets at the 225-mm downstream location. For a methane flame having an exit velocity of 60 m/s, the corresponding location is ~ 175 mm.

The effect of the changing scales upon flame stabilization can be appreciated by examining Fig. 6 which shows that at  $\cong 60$  mm, there is a local high probability that holes will be observed and, thus, a low probability that the flame will be observed. Eventually, with a small increase in velocity from the critical liftoff value, flame necking will occur at this location. The probability of holes being displayed at this location may be at the local maximum; however, the highest probability of holes being observed occurs farther downstream, as shown in Figs. 6-10. The reason for local splitting of the methane flame at ~ 60 mm but not at other locations having higher probabilities of displaying holes (local quenching) may be related to the variety of scales, each of which is changing with respect to space and time. Near the nozzle exit mixing is incomplete, and the mixing layer and the flammable zone are thin. As a result the measured flame zone is thin, ~ 1 mm. The size of the vortex at this location can be as large

as 5 mm, which is larger than the thickness of the flame and can completely penetrate the flame, as shown in Fig. 2. Under these conditions the flame can be quenched and is not reignited easily. Farther downstream, however, more efficient mixing is achieved which results in a thick mixing layer and flammable zone. Thus, in this region the probability of holes being displayed increases (which may be due to the increasing importance of large buoyancy instability structures); however, since the probability of reignition is also greater, the flame will not split at these locations.

### Correlation of Statistical Properties and the Degree of Flame/Flow Interactions

As the flow is perturbed by large structures in the jet shear layer, the flame surface fluctuates about its stationary (reference) position. The rms value of the flame-surface fluctuation can be measured from the line-OH profiles. This rms flame fluctuation is denoted by  $L$  which is a length scale corresponding to the degree of the flame/flow interaction. A similar approach was employed in earlier studies to determine the degree of flame/flow interaction (Chen and Goss, 1989; Chen *et al.*, 1989).

The probability data, as discussed in the previous section, indicated that at the critical liftoff velocity, the methane flame has a higher probability of displaying holes than the propane flame. This is due to the stronger flame/flow interaction in the methane-flame case. However, the thermal time scale--the ratio of laminar flame thickness and laminar flame speed--for the methane and propane flames is approximately the same (1/430 and 1/400 sec, respectively). Therefore, if the degree of flame/flow interaction is the same, the probability of displaying holes or local extinction should be the same. To pursue this hypothesis, the probability of observing flamelets and holes was plotted as a function of the rms flame fluctuation,  $L$ ; the results are displayed in Fig. 11.

Data for the propane and methane flames under critical liftoff conditions, both attached and lifted, are summarized in Fig. 11. In addition, data for methane flames in operation beyond the flame-lifting condition and having jet exit velocities of 40, 50, and 60 m/s are included. For

the wide range of flame conditions studied, the maximum rms flame fluctuation was observed to be  $< 7$  mm for the flame in the 300-mm downstream range ( $x/d < 60$ ). Under the same flame condition, the flame/flow interaction becomes stronger ( $L$  becomes larger) as the downstream location increases. At a given downstream location, the flame/flow interaction becomes stronger with increasing jet exit velocity. Therefore, use of  $L$  as the independent variable inherently includes the fuel-type, fuel-velocity, and downstream-distance dependence of the flame/flow interaction. Figure 11 indicates that the probability of observing flamelets decreases with increasing  $L$ , while the probability of observing holes increases with increasing  $L$ . Indeed, the probability data which represent a wide range of flame conditions fall within a relatively narrow band when plotted in this manner.

A detailed examination of Fig. 11 indicates that there are two important values of  $L$  with which the statistical properties of the flame behavior change dramatically. The first is the minimum thermal thickness, measured to be  $\sim 1$  mm; while the second is the nozzle diameter of the jet (5 mm). When  $L$  is smaller than 1 mm, the probability of observing flamelets and holes is constant, 1 and 0, respectively. This implies that when interaction is small such that  $L$  remains less than the minimal thermal thickness, the flame displays thin-flamelet behavior and no local extinction occurs. When  $L$  is larger than 1 mm, the probability of observing flamelets decreases linearly, while that of observing holes increases linearly. When the value of  $L$  reaches  $\sim 5$  mm, the probability of observing holes becomes greater than that of observing flamelets.

## CONCLUSIONS

Hydrocarbon jet diffusion flames under liftoff to near-blowout conditions have been characterized using joint RMS/OH-PLIF techniques. The shear-layer zone observed by the RMS technique and the flame zone revealed by line and planar OH imaging display many degrees of interaction. As a result three types of OH zones--thin, multiple, and thick--are observed. In addition, local flame extinction through the flame surface has been observed and

may be governed by strong convection, dissipation, strain, and heat-loss mechanisms.

The statistical description of various types of OH zones under a wide range of flow conditions has been given. From a statistical viewpoint, the following conclusions have been drawn:

- For both the methane and propane flames, the thinnest flamelets observed are  $\sim 1.0$  mm. Near the flame blowout condition, the thermal thickness of the flame base may be as large as 30 mm.
- Local extinction inside a thick thermal zone and small pockets of combustion located outside the main flame zone are observed near the flame base when the flame is operated under near-blowout conditions.
- The flame/flow interaction is stronger for the methane than for the propane flame under the critical liftoff condition. Consequently, the methane flame has a higher probability of displaying holes.
- Good correlation was observed between the rms flame fluctuation,  $L$ , and the probability of displaying holes and flamelets for the methane and propane flames. The statistical analysis indicates that when the value of  $L$  approaches the nozzle diameter, the probability of observing holes in the flame surface is higher than that of observing flamelets. If the interaction is small, such that  $L$  remains less than 1 mm (the minimal thermal thickness), the flame displays thin-flamelet behavior and no local extinction occurs.

## ACKNOWLEDGEMENT

This work was supported by and performed at the Wright Research and Development Center/Aero Propulsion and Power Laboratory under Contract No. F33615-85-C-2562. The authors are indebted to Dr. W. M. Roquemore for support and discussions concerning this work. The authors wish to thank Drs. R. Dibble, J. Driscoll, D. Mikolaitis, W. Shyy, F. Takahashi, and D. Talley for the discussion regarding the structure of the lifted flame base. Technical assistance from D. D. Trump and M. Whitaker is appreciated.

## REFERENCES

- Barlow, R. (1989). Sandia National Laboratories., Private communication.
- Broadwell, J. E., and Breidenthal, R. E. (1982). A simple model of mixing and chemical reaction in a turbulent shear layer. *J. Fluid Mech.* **125**, 397.
- Buckmaster, J., and Matalon, M. (1988). Anomalous Lewis number effects in tribrachial flames. In *Twenty-Second Symposium (International) on Combustion*, The Combustion Institute, Pittsburgh, Pennsylvania, pp. 1527-1535.
- Chen, J-Y., and Kollmann, W. (1989). PDF modeling of chemical nonequilibrium effects in turbulent nonpremixed hydrocarbon flames. In *Twenty-Second Symposium (International) on Combustion*, The Combustion Institute, Pittsburgh, Pennsylvania, pp. 645-653.
- Chen, T. H., and Goss, L. P. (1989). Flame lifting and flame/flow interactions of jet diffusion flames, AIAA Paper No. 89-0156.
- Chen, T. H., Goss, L. P., Talley, D., and Mikolaitis, D. (1989). Stabilization zone structure in jet diffusion flames from liftoff to blowout. AIAA Paper No. 89-0153.
- Correa, S. M., and Gulati, A. (1989). Non-premixed turbulent CO/H<sub>2</sub> flames at local extinction conditions. In *Twenty-Second Symposium (International) on Combustion*, The Combustion Institute, Pittsburgh, Pennsylvania, pp. 599-606.
- Dahm, W. J. A., and Dibble, R. W. (1988). Combustion stability limits of coflowing turbulent jet diffusion flames, AIAA Paper No. 88-0538.
- Eickhoff, H., Lenze, B. and Leuckel, W. (1985). Experimental investigation on the stabilization mechanism of jet diffusion flames. In *Twentieth Symposium (International) on Combustion*, The Combustion Institute, Pittsburgh, Pennsylvania, pp. 311-318.
- Hanson, R. K. (1986). Combustion diagnostics: planar imaging techniques. In *Twenty-First Symposium (International) on Combustion*, The Combustion Institute, Pittsburgh, Pennsylvania, pp. 1677-1691.

- Haworth, D. C. Drake, M. C., Pope, S. B., and Blint, R. J. (1989). The importance of time-dependent flame structures in stretched laminar flamelet models for turbulent jet diffusion flames. In *Twenty-Second Symposium (International) on Combustion*, The Combustion Institute, Pittsburgh, Pennsylvania, pp. 589-597.
- Long M. B., and Yip, B. (1988). Measurement of three-dimensional concentrations in turbulent jets and flames. In *Twenty-Second Symposium (International) on Combustion*, The Combustion Institute, Pittsburgh, Pennsylvania, pp. 701-709.
- Masri, A. R., Starnner, S. H., and Bilger, R. W. (1984). Transition and transport in the initial region of a turbulent diffusion flame. In Bowen, J. R. (Ed.), *Dynamics of Flames and Reactive Systems*, American Institute of Aeronautics and Astronautics, Washington, D. C., Vol. 95 of *Progress in Astronautics and Aeronautics*, pp. 293-304.
- Miake-Lye, R. C., and Hammer, J. A. (1988). Lifted turbulent jet flames: a stability criterion based on the jet large-scale structure, In *Twenty-Second Symposium (International) on Combustion*, The Combustion Institute, Pittsburgh, Pennsylvania, pp. 817-824.
- Namazian, M., Schefer, R. W., and Kelly, J. (1988). Scalar dissipation measurements in the developing region of a jet. *Comb. Flame* 74, 147.
- Peters, N., and Williams, F. A. (1983). Liftoff characteristics of turbulent jet diffusion flames. *AIAA J.* 21, 423.
- Pitts, W. M. (1988). Assessment of theories for the behavior and blow out of lifted turbulent jet diffusion flames. In *Twenty-Second Symposium (International) on Combustion*, The Combustion Institute, Pittsburgh, Pennsylvania, pp. 809-816.
- Roquemore, W. M., Chen, L-D., Goss, L. P., and Lynn, W. F. (1989). Structure of jet diffusion flames. In Borghi, R., and Murthy, N. B. (Eds.), *Turbulent Reactive Flows (Lecture Notes in Engineering)*, Springer-Verlag, New York, Vol. 40, pp. 49-63.
- Schefer, R. W., Namazian, M., and Kelly, J. (1988). Structural characteristics of lifted turbulent-jet flames. In *Twenty-Second Symposium (International) on Combustion*, The Combustion Institute, Pittsburgh, Pennsylvania, pp. 833-842.

- Shekarchi, S., Savas, O., and Gollahalli, S. R. (1988). Structure of a split gas flame. *Comb. Flame* 73, 221
- Takahashi, F., Mizomoto, M., and Ikai, S. (1982). Transition from laminar to turbulent free jet diffusion flames. *Comb. Flame* 48, 85.
- Vanquickenborne, L. V., and van Tiggelen, A. (1966). The stabilization mechanism of lifted diffusion flames. *Comb. Flame* 10, 59.

## FIGURE CAPTIONS

- Fig. 1. **Optical arrangement of joint RMS/OH-PLIF systems.**
- Fig. 2. **Image of penetration of vortex through surface of  $\text{CH}_4$  diffusion flame under critical liftoff condition; flame surface is marked by OH fluorescence and jet, by Mie scattering.**
- Fig. 3. (a) **First type of flame base of  $\text{CH}_4$  diffusion flame under near-blowout condition.**  
(b) **Dissipation map of OH image shown in (a).**
- Fig. 4. (a) **Second type of flame base of  $\text{CH}_4$  diffusion flame under near-blowout condition; local extinction found inside thick thermal zone.**  
(b) **Dissipation map of OH image shown in (a).**
- Fig. 5. (a) **Third type of flame base of  $\text{CH}_4$  diffusion flame under near-blowout condition; island of combusting zone located away from main thermal zone.**  
(b) **Dissipation map of OH image shown in (a).**
- Fig. 6. **Plot of probability of observing flamelets, thick flame, and holes for attached  $\text{CH}_4$  flame under critical liftoff condition.**
- Fig. 7. **Plot of probability of observing flamelets, thick flame, and holes for lifted  $\text{CH}_4$  flame under critical liftoff condition.**
- Fig. 8. **Plot of probability of observing flamelets, thick flame, and holes for attached  $\text{C}_3\text{H}_8$  flame under critical liftoff condition.**
- Fig. 9. **Plot of probability of observing flamelets, thick flame, and holes for lifted  $\text{C}_3\text{H}_8$  flame under critical liftoff condition.**
- Fig. 10. **Plot of probability of observing flamelets, thick flame, and holes for lifted  $\text{CH}_4$  flame with exit velocity of 40 m/s.**
- Fig. 11. **Correlation between rms flame fluctuation,  $L$ , and probability of observing flamelets and holes for wide range of flame conditions.**

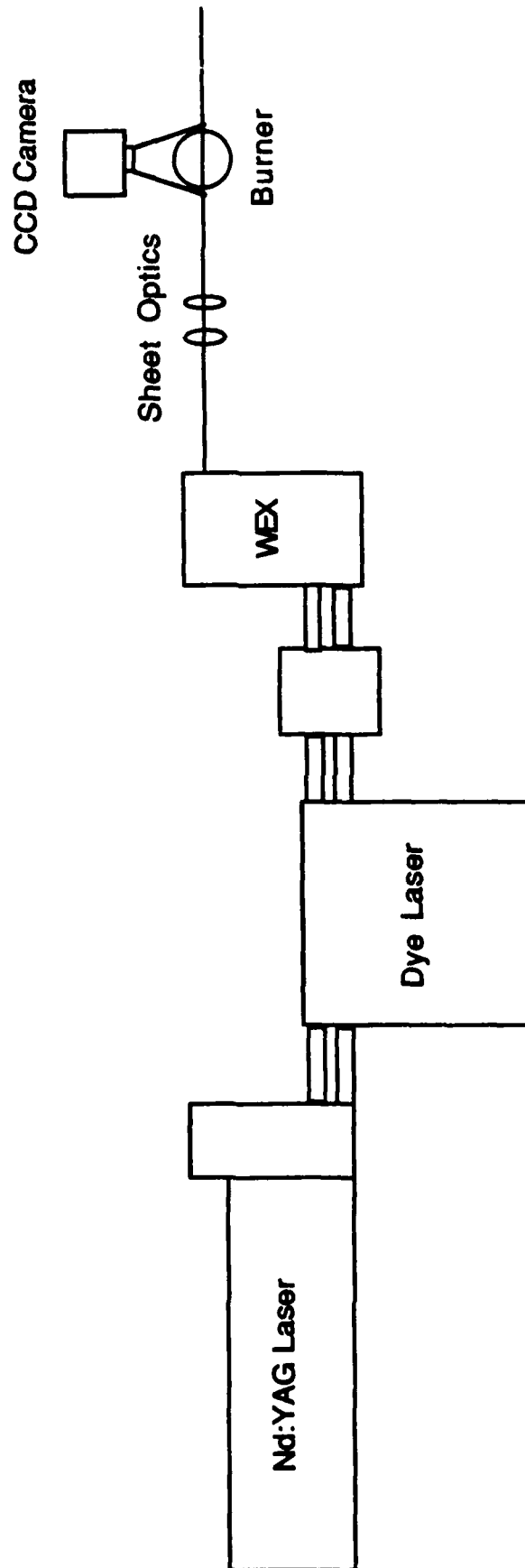
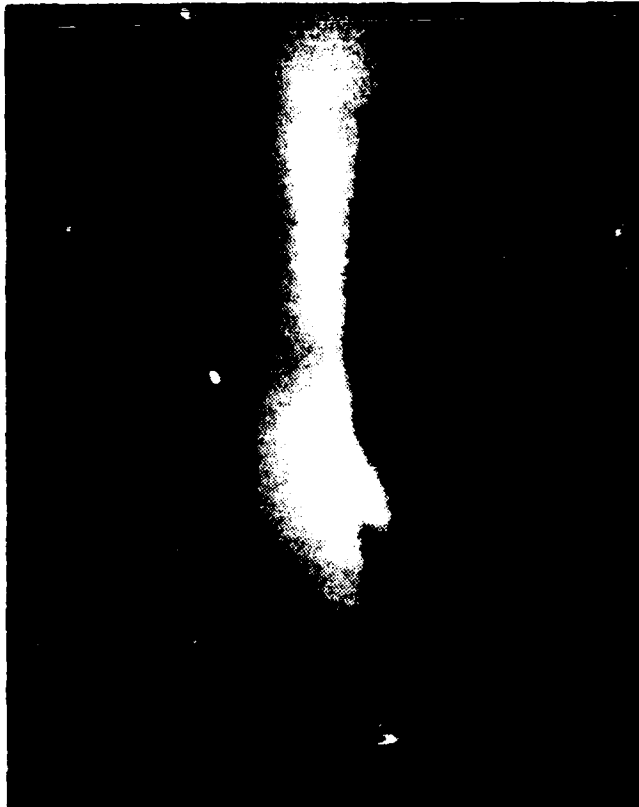


Figure 1  
T. H. Chen



10 mm

Figure 2  
T. H. Chen



(a)



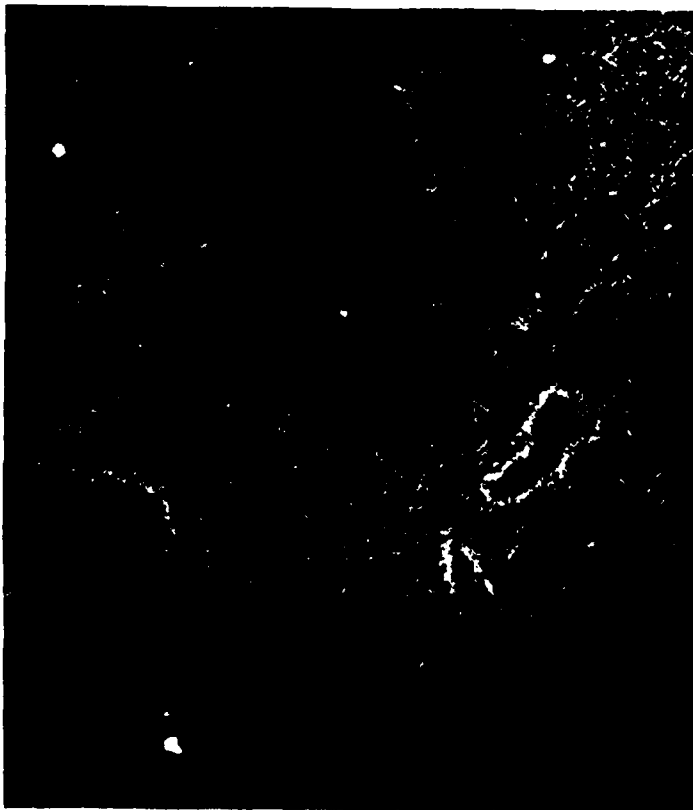
10 mm

(b)

Figure 3  
T. H. Chen



(a)

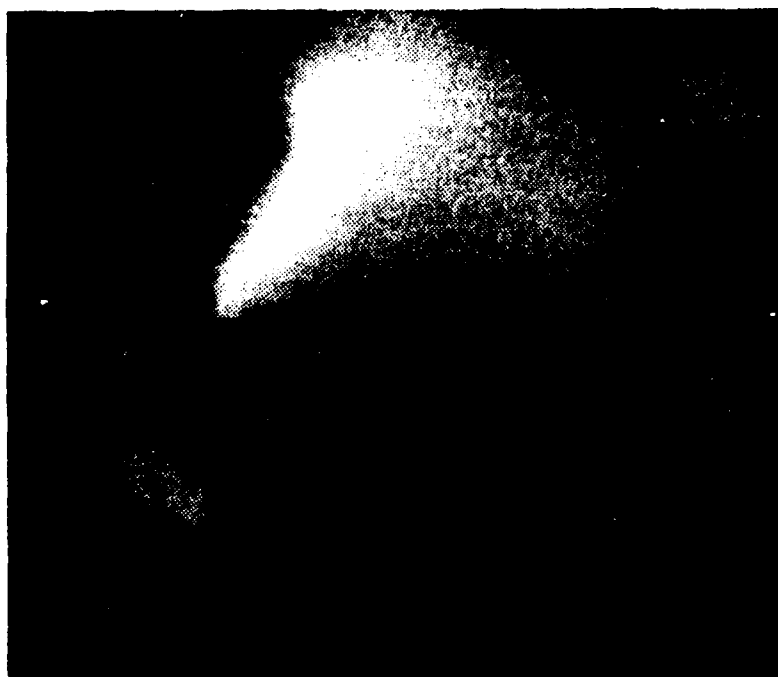


10 mm

(b)

144

Figure 4  
T. H. Chen



(a)



10 mm

(b)

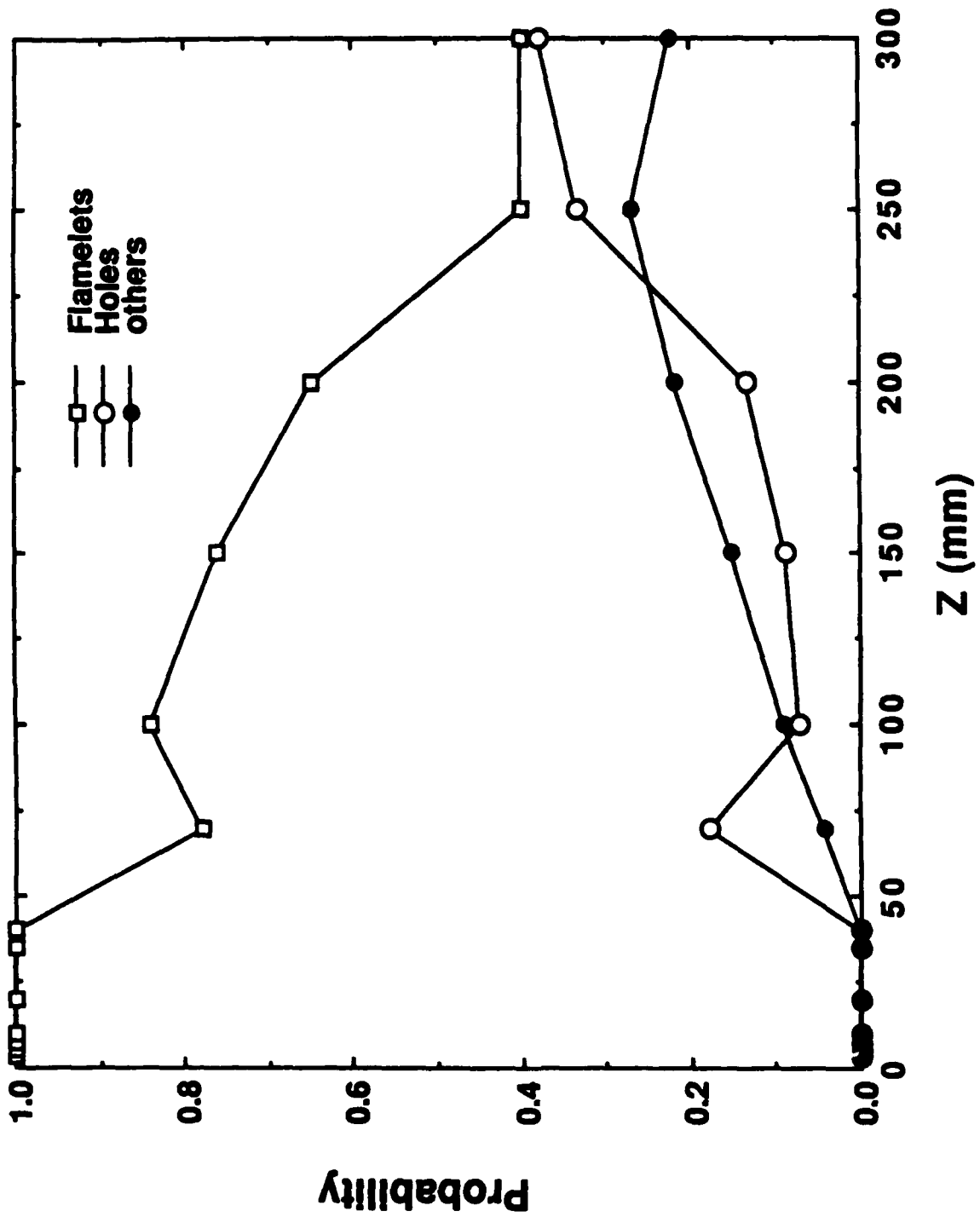


Figure 6  
T. H. Chen

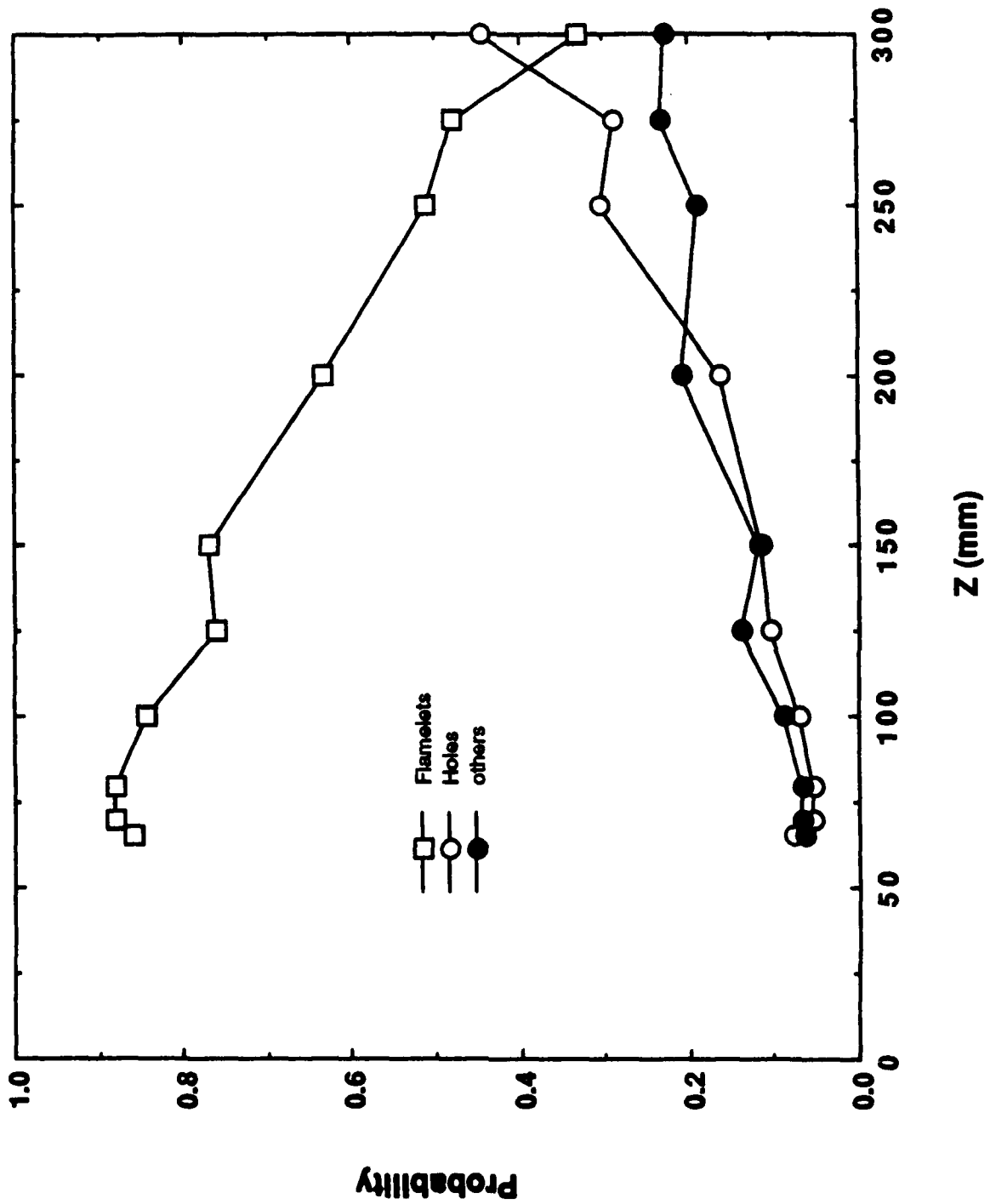


Figure 7  
T. H. Chen

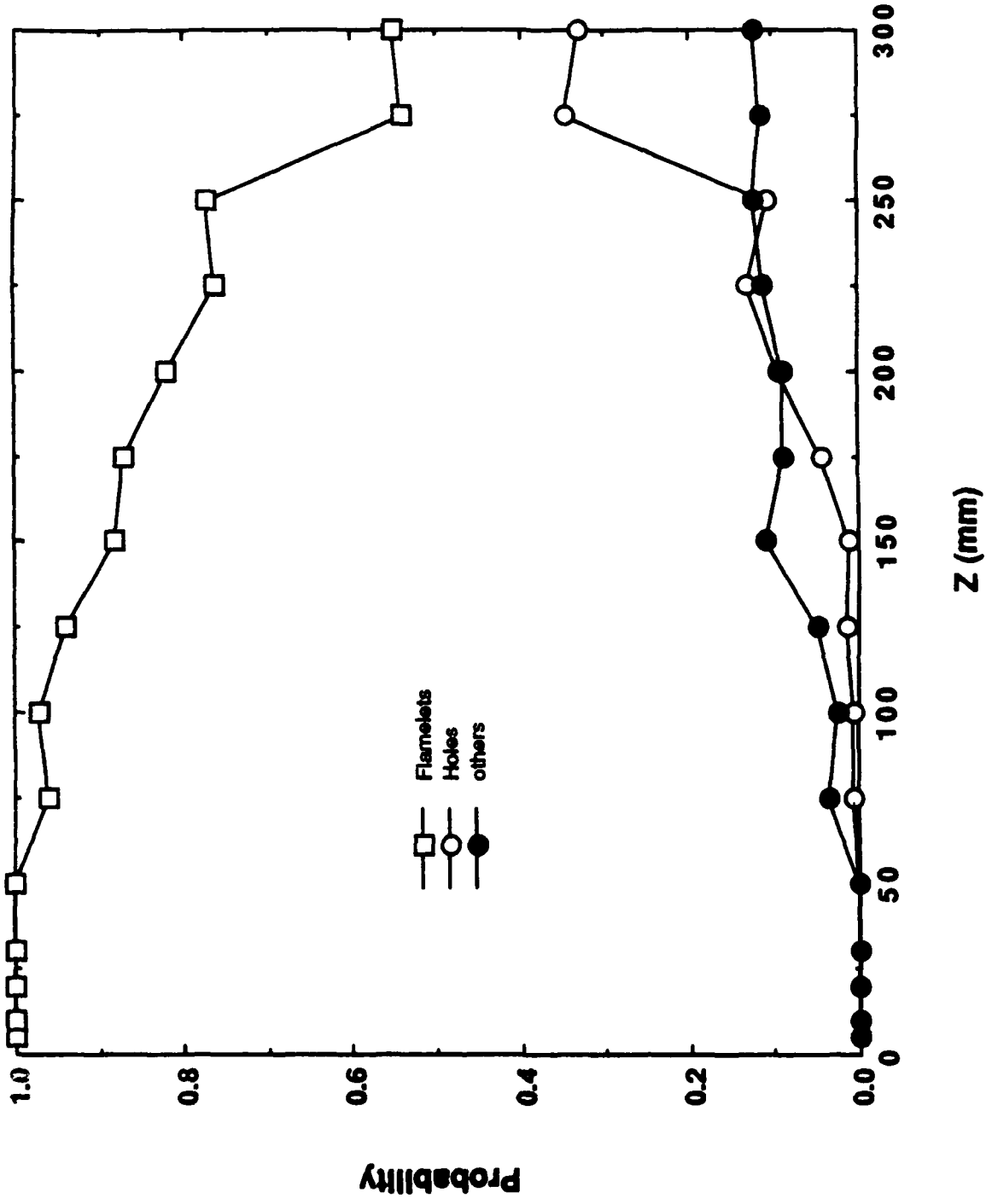


Figure 2  
T. H. Cren

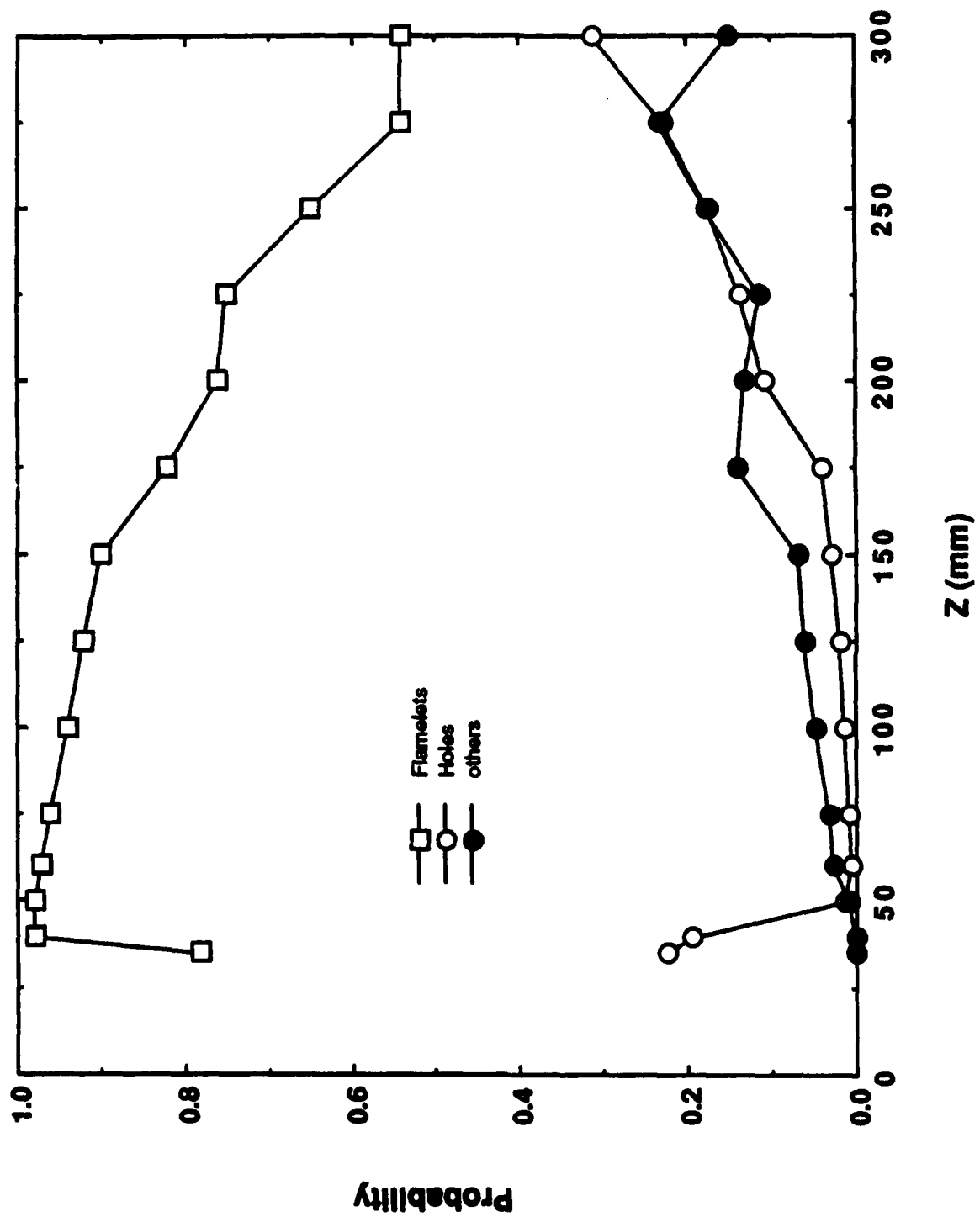


Figure 9  
T. H. Chen

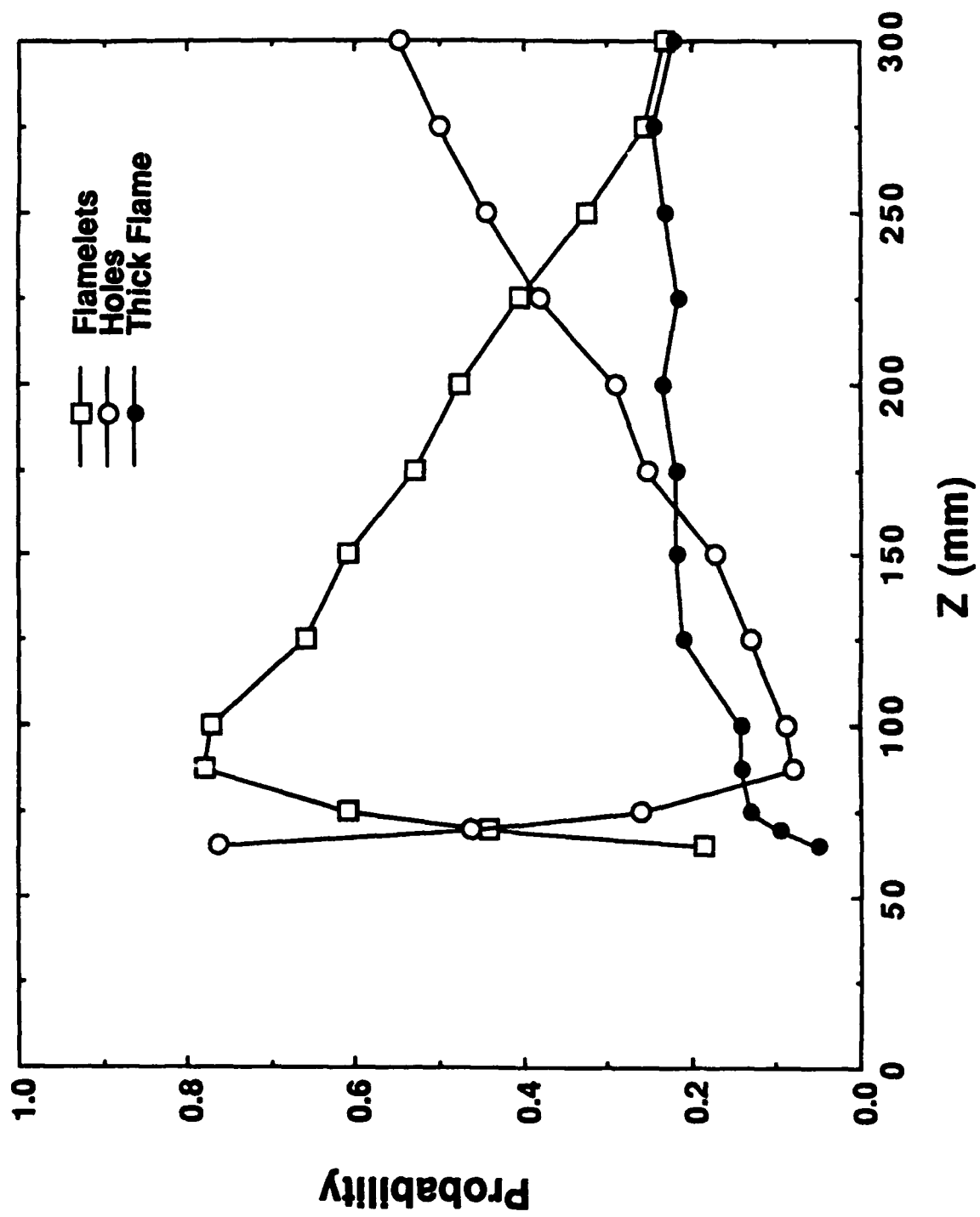


Figure 10  
T. H. Chen

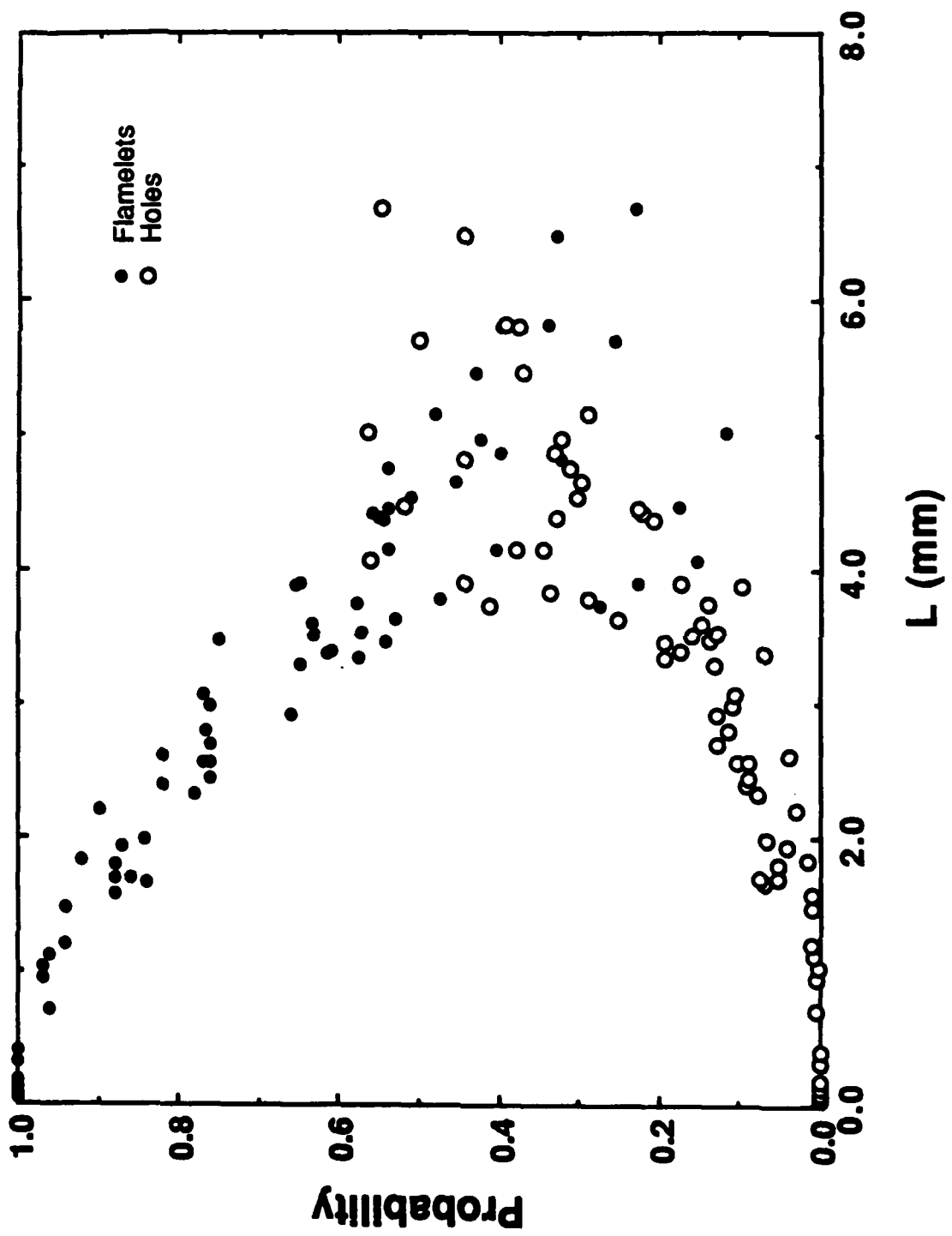


Figure 11  
T. H. Chen

## 2.5 TWO-COLOR PARTICLE-IMAGING VELOCIMETRY

A novel method for determining two-dimensional velocity flowfields has been developed. The technique, two-color particle-imaging velocimetry (PIV), is similar to existing PIV techniques except that two different-color laser sources are used to form the light sheets required for exposing the position of the particles. A green-colored laser sheet (formed by a doubled Nd:YAG laser) and a red-colored laser sheet (formed by a Nd:YAG-pumped dye laser) are employed sequentially to expose the particle positions which are then recorded on ordinary 35-mm color film. Analysis of the resulting images consists of digitizing the exposed film with color filters to separate the green- and red-particle image fields and processing the digitized images with velocity-displacement software. The two-color PIV technique has the advantage that direction as well as particle displacement is uniquely determined because the green-particle image occurs before the red-particle image by a known time increment. Development and evaluation of the two-color PIV technique is discussed in two papers entitled, "A Novel Technique for Blade-to-Blade Velocity Measurements in a Turbine Cascade," which was presented at the AIAA/ASME/SAE/ASEE 25th Joint Propulsion Conference (see p. 153) and "Two-Color Particle-Imaging Velocimetry," which was presented at the 1989 International Conference on Applications of Lasers and Electro-Optics (see p. 164).



**AIAA-89-2691**

**A Novel Technique for Blade-to-  
Blade Velocity Measurements in  
a Turbine Cascade**

L. P. Goss, M. E. Post,  
D. D. Trump, and B. Sarka  
Systems Research Laboratories, Inc.  
A Division of Arvin/Calspan  
2800 Indian Ripple Road  
Dayton, OH 45440-3696

C. D. MacArthur and G. E. Dunning, Jr.  
Aero Propulsion and Power Laboratory  
Wright Research and Development Center  
Wright-Patterson Air Force Base, OH 45433-6563

**AIAA/ASME/SAE/ASEE  
25th Joint Propulsion Conference  
Monterey, CA / July 10-12, 1989**

For permission to copy or republish, contact the American Institute of Aeronautics and Astronautics  
370 L'Enfant Promenade, S.W., Washington, D.C. 20024

# A NOVEL TECHNIQUE FOR BLADE-TO-BLADE VELOCITY MEASUREMENTS IN A TURBINE CASCADE

L. P. Goss,\* M. E. Post,\*\* D. D. Trump,† and B. Sarkat †

System Research Laboratories, Inc.

A Division of Arvin/Calspan

2800 Indian Ripple Road

Dayton, OH 45440-3696

C. D. MacArthur‡ and G. E. Dunning, Jr.‡‡

Aero Propulsion and Power Laboratory

Wright Research and Development Center

Wright-Patterson Air Force Base, OH 45433-6563

## Abstract

A novel method for determining two-dimensional velocity flowfields has been developed. The technique, two-color particle-image velocimetry (PIV), is similar to existing PIV techniques except that two different-color laser sources are used to form the light sheets required for exposing the position of the particles. A green-colored laser sheet (formed by a doubled Nd:YAG laser) and a red-colored laser sheet (formed by a Nd:YAG-pumped dye laser) are employed sequentially to expose the particle positions which are then recorded by ordinary 35-mm color film. Analysis of the resulting images consists of digitizing the exposed film with color filters to separate the green- and red-particle image fields and processing the digitized images with velocity displacement software. The two-color PIV technique has the advantage that direction, as well as particle displacement, is uniquely determined because the green-particle image occurs before the red-particle image by a known time increment. This technique is, thus, applicable to complex flowfields (i.e., recirculating), where the normal 180-deg. directional ambiguity of single-color techniques can be troublesome. Velocity measurements utilizing the two-color PIV technique on a turbine-cascade test section have been made and are discussed.

## Introduction

The most common approach to making velocity measurements in a flowfield involves the use of a

\*Chief Scientist, Member AIAA

\*\*Research Physicist

†Project Engineer

††Electrical Engineer

‡Project Engineer

‡‡Turbine Design Engineer

laser Doppler velocimeter (LDV). An LDV functions by measuring the frequency of the Doppler burst created as a small particle traverses a laser fringe pattern. The frequency of the burst is directly related to the spacing of the fringes and the velocity of the particle. Because of the accuracy of this form of velocity measurement and the nonperturbing nature of the technique, LDV methods have become an important tool in the study of complex flowfields. However, the restricted measurement area limits LDV techniques to point measurements. In complex flows (i.e., recirculating), it is important to obtain a two-dimensional instantaneous picture of the entire flowfield rather than a time-averaged pointwise map. Several techniques have been reported in the literature which have the capability to determine the two-dimensional flowfield. These techniques can be divided into three categories: particle-tracking schemes,<sup>1-8</sup> time-of-flight techniques,<sup>9-11</sup> and Laser Doppler methods.<sup>12-15</sup> For low-to-moderate velocity flowfields, particle-tracking techniques are effective, offering a wide velocity range and allowing a two-dimensional measurement of the velocity flowfield.

Particle tracking or particle image velocimetry (PIV) is basically an extension of speckle photography which has been employed extensively in solid mechanics. The PIV technique involves 1) double pulsing a particle-laden flowfield, 2) recording the scattered light either by conventional photography or holography, and 3) processing the photographs to obtain velocity information. While the first two steps are relatively simple to implement, the data analysis is typically complex and requires computerized image processing. The experimental technique consists of seeding the air flow with particles 0.2 to 5  $\mu\text{m}$  in size and employing a high-peak-power short-pulse laser (ruby, Nd:YAG, or copper vapor) to form a laser light sheet. The Mie scattering from the seed particle is imaged onto a conventional or electronic camera for recording. For the range of velocities encountered in the flowfield, the time delay

is chosen such that a maximum displacement of  $\sim 1$  mm is observed.

Two different approaches have been taken in analyzing double-pulsed particle images. The first is an optical-correlation method called the Young's fringe technique.<sup>1</sup> This method makes use of an interrogation laser which traverses the positive film of the photograph. If the double exposures are sufficiently close, then a series of Young's fringes will be formed. The magnitude of the velocity is proportional to the separation of the particle images which, in turn, is inversely proportional to the fringe-pattern spacing; the direction of the velocity is perpendicular to the fringe orientation. The drawbacks of this analysis approach are the 180-deg. directional ambiguity associated with the fringes and the extended time required for analysis. Although phase-shifting techniques have been proposed in the literature for removing the directional ambiguity, they are typically difficult to implement and control accurately.<sup>5-7</sup> The second analysis approach involves direct computation of the correlation of the particle field rather than optical determination. In this approach the average particle displacement is determined by constructing a correlation map or histogram of the particle field from which the most probable displacement vector can be determined. Computationally, histogram correlation techniques can be quite fast; however, with these techniques and also with single-color PIV images, a 180-deg. directional ambiguity is observed. This ambiguity is removed with the addition of color.

This paper introduces a novel two-color PIV technique designed to remove directional ambiguities and allow measurements to be made in complex flow systems (i.e., turbine cascades). The technique consists of employing small particles to seed a gas stream exiting a nozzle or passing through a test section. A laser sheet (green) formed by passing the output from a doubled Nd:YAG laser through a cylindrical lens is used to illuminate the seed particles in the flowfield. After a short time delay (ranging from a few microseconds for high-velocity flow systems to milliseconds for low-velocity flow systems), a second laser sheet (red) from a Nd:YAG-pumped dye laser is pulsed to illuminate the flowfield a second time. Any particles remaining in the plane of the laser sheets produce a "displacement-vector" pair which is made up of a green- and a red-particle image. The Mie scattering from the seeded particles is recorded on 100-400 ASA color film which is processed by direct digitization. The unique color coding helps to remove directional ambiguities associated with single-color techniques because the red image appears after the green image.

Although this is a conceptually simple technique, the details of aligning the laser sheets, illuminating the area of interest, sequencing the firing of the lasers at a selected time interval, recording the image of the light scattered by the seed particles,

digitizing the captured image, and processing the green/red-particle-image pairs to determine velocity vectors present complex and challenging problems. The analysis procedure in simplest terms consists of identifying "displacement-vector" pairs of green and red dots. This is accomplished by determining the coordinates of the green- and red-particle images, finding the most probable vector displacement between pairs, and identifying green/red particle pairs which are separated by the most probable vector displacement to within a specified percentage. Each of these tasks is described below.

### Theory of Particle-Tracking Velocimetry

As mentioned in the previous section, particle-tracking methods involve 1) multiply exposing a particle-laden flowfield with a sheet of laser light, 2) recording the Mie-scattered light either by conventional photography or holography, and 3) processing the photographs to obtain velocity information. Each step in this process requires careful consideration if the technique is to predict two-dimensional flowfields accurately.

For particle imaging the exposure resulting from a particle in a laser light sheet of energy  $W$  and area  $\Delta y \Delta z$  is given by<sup>4</sup>

$$\epsilon = \frac{4}{\pi k^2 d_e^2 \Delta y \Delta z} \int \sigma^2 d\Omega \quad (1)$$

where  $k = 2\pi/\lambda$ ,  $W$  is the collection angle of the lens system,  $\sigma$  the Mie-scattering cross section of the particle,  $\lambda$  the wavelength of the laser light sheet, and  $d_e$  the nominal image diameter given by

$$d_e = (m^2 d_p^2 + d_s^2)^{1/2} \quad (2)$$

where

$$d_s = 2.44 (m + 1) f\# \lambda \quad (3)$$

with  $m$  being the magnification of the image,  $d_p$  the particle diameter,  $f\#$  the ratio of the focal length to the lens diameter, and  $\lambda$  the wavelength of the laser source. The "diffraction-limited" blur image of the lens is given by  $d_s$ . For small seed particles the particle image recorded on film is actually the blur image and, thus, represents a lower limit to the image size--which is important in determining the resolution of the velocity measurement.

Adrian,<sup>4</sup> has calculated the Mie-scattering contribution to Eq. (1) and generated the family of curves for normalized exposure,  $f\#$ , and particle size shown in Fig. 1. Normalizing the exposure to the light-sheet energy density allows comparison with experimental conditions other than those reported in

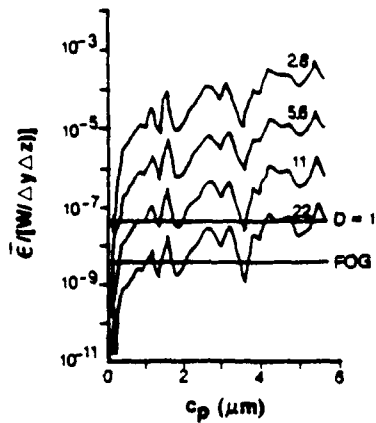


Fig. 1. Nondimensional exposure ( $\epsilon$ ) as function of particle size ( $c_p$ ) for various  $f\#$  collection optics.

Ref. 4. The minimum exposure level of the film is given by the inverse of the ASA speed rating in  $\text{erg}/\text{cm}^2$ . For 100-ASA film, the minimum exposure corresponds to  $1 \times 10^{-5} \text{ J/m}^2$ . In order to compare this value with the family of curves in Fig. 1, the exposure must be normalized to the energy density of the laser light sheet. Because of the high speeds in the test chamber of these studies, a combination of a Nd:YAG laser (green sheet) and a Nd:YAG-pumped dye laser (red sheet) was employed. Assuming an energy level of 200 mJ/pulse from these lasers in a 10 cm x 1 mm sheet, the energy density available is  $\sim 2000 \text{ J/m}^2$ . With the minimum exposure or fog level for 100-ASA film, the normalized exposure,  $\epsilon$ , is  $\sim 5 \times 10^{-9}$ . Since a density of one is considered to be an adequate exposure level, the optimum exposure ( $\epsilon$ ) level with these laser systems is  $\sim 5 \times 10^{-8}$ . Superimposing this level on the family of curves generated by Adrian (see Fig. 1) indicates that submicron particles can be captured with a 5.6  $f\#$  lens.

The precision of particle-tracking or PIV methods requires determination of the smallest displacement which can be accurately measured by the film (resolving power of the film). In order to understand the resolving capability of the film, one must examine the modulated transfer function (MTF) which is a measure of the ability of the film to resolve accurately line pairs separated by a given distance. The function is defined by

$$\text{MTF} = \frac{I_{\text{max}} - I_{\text{min}}}{I_{\text{max}} + I_{\text{min}}} \quad (4)$$

where  $I_{\text{max}}$  is the intensity maximum of adjacent line pairs (or particle images) and  $I_{\text{min}}$  the minimum intensity between the line pairs. As the line pairs per millimeter of the input image increases, a point is reached where the lines are no longer distinct and overlapping (cross-talk) occurs. For example, 100-ASA film exhibits an MTF value which

corresponds to a resolution of 300 line pairs/mm. This color film is, thus, capable of resolving a 6- $\mu\text{m}$  particle separation. However, the particle-image size given by Eq. (2) represents the ultimate limit to the velocity resolution since no two particles can be resolved closer than their diameter. The recorded particle diameter for an  $f/8.4$  lens with a magnification of 0.4 is  $\sim 30 \mu\text{m}$ .

Assuming that the maximum velocity of the cascade test section is 340 m/sec and that a spatial resolution of 1 mm is required, the time separation between sequential pulses would be  $\sim 3 \mu\text{sec}$ . The minimum velocity would correspond to the minimum particle spacing,  $\sim 30 \mu\text{m}$ , divided by the pulse separation, 3  $\mu\text{sec}$ , which would correspond to  $\sim 10 \text{ m/sec}$  or  $\sim 3\%$  of the full-scale velocity limit. Achievement of a lower minimum velocity with a double-pulsed system would require a longer time separation between pulses, which would result in a lower spatial resolution. The requirement for a 3- $\mu\text{sec}$  separation between pulses cannot be achieved with a single double-pulsed Nd:YAG system. The double-pulsed Nd:YAG laser used in the present study has a minimum separation between pulses of 26  $\mu\text{sec}$ , with a maximum of  $\sim 250 \mu\text{sec}$ . Thus, two separate Nd:YAG lasers were required for the cascade measurements.

The two-color FIV technique utilizes color to remove directional ambiguities and reduce tracking errors. However, because the Young's-fringe analysis approach cannot distinguish between the different color particle fields, an alternative correlation-tracker analysis approach was developed. The analysis procedure consists of 1) digitizing the color negative with a CCD array, 2) determining the spatial locations of the digitized particle images, 3) constructing a correlation map from which the most probable displacement vector can be determined, and 4) using this information in a tracker which identifies green/red particle-vector pairs from the digitized image.

#### Determination of Particle Coordinates

In order to take full advantage of the resolution available with the color film on which images are recorded, an enlarger was used to subdivide the image for analysis. The position of the enlarger was controlled with an automated x,y,z traversing mechanism that could set the position of the enlarger to within 20  $\mu\text{m}$  in any direction. Each section of the enlarged image was digitized twice using a CCD camera system. The first digitized image was taken with a green filter to identify the green-particle images, and the second digitized image was taken with a red filter to identify the red-particle images. These digitized images were processed in an identical manner to determine the coordinates of the green and red particles.

A typical digitized image displays peaks associated with the particles superimposed on a slowly varying background. In order to simplify procedures for finding the coordinates of each particle, components of the background, which are constant or slowly varying over the scale of the particle size, are removed by application of a two-dimensional Laplacian operator to the digitized image. This operator basically acts as a spatial-frequency filter passing high-frequency (small-size) components of the image but suppressing low-frequency (background) components. The particle images can be further enhanced above the background and film noise if the step size of the Laplacian operator is approximately the particle size. Next, the processed image is scanned in two dimensions for local maxima, and a series of tests is performed to identify those local maxima which correspond to particles. In brief, particles are identified by finding local maxima which 1) are above a threshold value, 2) do not constitute a peak shoulder, 3) have a local average intensity above a threshold value, and 4) have an estimated diameter within a specified range.

The four-step process is briefly described here. The first step involves scanning the digitized image (enhanced by the Laplacian operator) with an 8 x 8 box. The maximum value of the pixel intensity in this box is determined; if the maximum is above a preset threshold value, it is selected as a candidate peak. In the second step, a test is performed to determine whether the candidate peak is a shoulder or secondary peak in the near vicinity of a larger peak (some particles are relatively flat topped, having two or three local maxima of which only the largest is desired). If the peak is indeed a real peak and not a shoulder of an adjacent peak, then the third step is implemented. In this third step, the intensities of all pixels in the box centered on the candidate peak are averaged and compared to a threshold value. The reason for calculating the average intensity value is that peaks from particles are typically composed of a group of pixels of relatively high intensity. Although background noise spikes of high intensity may satisfy conditions for the first and second steps, they are not accompanied by a group of similarly intense neighbors. In the final step, a weighted average is performed using the intensities and coordinates of the box centered on the candidate peak to determine the "center of mass" of the particle. Starting from the "center of mass" coordinates, the particle diameter is then estimated by making a pixel count in four outward directions (at 90-deg. intervals) to the points where intensity is either one-half the peak maximum or one-half the threshold value. If the diameter is less than 1 or 2 pixels, the peak is probably due to a scratch or pinhole flaw in the negative. If the diameter is greater than 16 pixels, the peak is probably an object in the test section. If the diameter

is in the 3- to 16-pixel range, the candidate peak is selected as a particle peak.

Figures 2 and 3 illustrate a digitized segment of a double-pulsed particle flowfield and the particle centers determined by the particle-location software, respectively.

#### Determination of Most Probable Vector Displacement

Methods for determining the most probable displacement (correlation) for vector pairs in a section of the image (beginning with the simplest and moving to the most mathematically complex) include: 1) vector comparison, 2) histograms, and 3) Fourier transforms. Generally speaking, as the number of particles in a digitized image increases, the simple methods become very time consuming. For less than 50 green/red pairs, vector comparison is simple and relatively fast. For more than 50 green/red pairs, histogram techniques require less computer time than the vector-comparison methods. As the number of green/red-particle pairs increases, the Fourier transform approach becomes the technique of choice.

Vector Comparison. The simplest approach to determining the most probable velocity vector in a region of the digitized image is to calculate the velocity vector between every possible combination of green and red images. Each of the vector pairs is put into a probability distribution function (pdf) and the peak value of the pdf determined. The peak of the pdf represents the vector value repeated most often and is the most probable vector displacement. In performing this comparison, it is advisable that the bin size of the velocity pdf be ~ 5% of the total width which allows for any velocity fluctuations which may have occurred in the digitized region. This method is ideally suited for low particle density where it is computationally efficient. Since the time for analysis scales as the square of the number of particle images, high-density particle images can be quite slow to process.

Histograms. The histogram approach to particle correlation is the method adopted for this study and, therefore, will be discussed in detail. The cross correlation between the green- and red-particle images is given by

$$c(\xi, \psi) = \sum_x \sum_y g(x, y) r(x-\xi, y-\psi) \quad (5)$$

where  $c(\xi, \psi)$  is the two-dimensional correlation map,  $g(x, y)$  the digitized green image,  $r(x, y)$  the digitized red image, and the limits of summation are over the pixel dimensions of the digitized image. The correlation in this form is computationally intensive since



Fig. 2. Digitized segment of two-color PIV image obtained with green filter.



Fig. 3. Particle coordinates determined by peak-locator software for digitized segment of two-color PIV image depicted in Fig. 2.

it represents a double summation of the entire digitized image. In the histogram approach a correlation histogram map is constructed from the green- and red-particle images; the maximum of these images contains the most probable displacement vector. The method is displayed schematically in Fig. 4. The software for this analysis functions by first finding an initial particle image in the green digitized image.

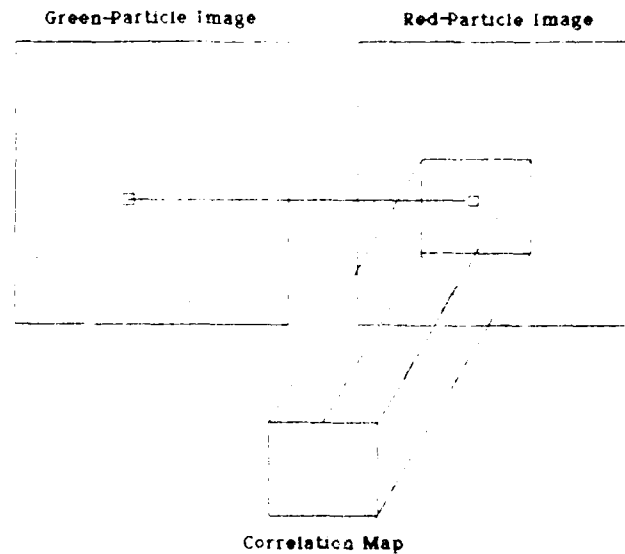


Fig. 4. Schematic diagram of mapping from image to correlation space for two-color PIV technique. For each green particle, a 120 x 120 area of red-particle image centered on green-particle coordinates is summed into correlation map.

The exact location of the green particle is determined and used for mapping. A 120 x 120 pixel area of the red-particle image centered about the green-particle coordinates is then copied into a histogram map (correlation space). This procedure is then repeated for all the green-particle images and their associated surrounding fields in the red-particle images. This process is represented mathematically by

$$H(\xi, \psi) = \sum_n g(x_c, y_c) r(x_c - \xi, y_c - \psi) \quad (6)$$

where  $H(\xi, \psi)$  is the correlation histogram,  $g(x_c, y_c)$  the center coordinates of the green-particle images,  $r(x_c - \xi, y_c - \psi)$  the red particle images surrounding the green particle being mapped, and the summation is over all green-particle images. Because the double summation of Eq. (5) over all  $x$  and  $y$  pixels has been replaced with a single summation over the number of green particles, Eq. (6) is computationally more efficient and results in a cross-correlation map.

As green/red-particle pairs having the same velocity, and thus displacement, are mapped onto correlation space, peaks are built up on this map. The maximum of this map corresponds to the most

probable displacement from the center coordinate, illustrated in Fig. 5(a). If only a single-color image had been used instead of a two-color image, the resulting correlation map would have been symmetric and centered about a large self-correlation peak at the center of the map, illustrated in Fig. 5(b). This would have resulted in a 180-deg. directional ambiguity which would have had to be resolved by phase

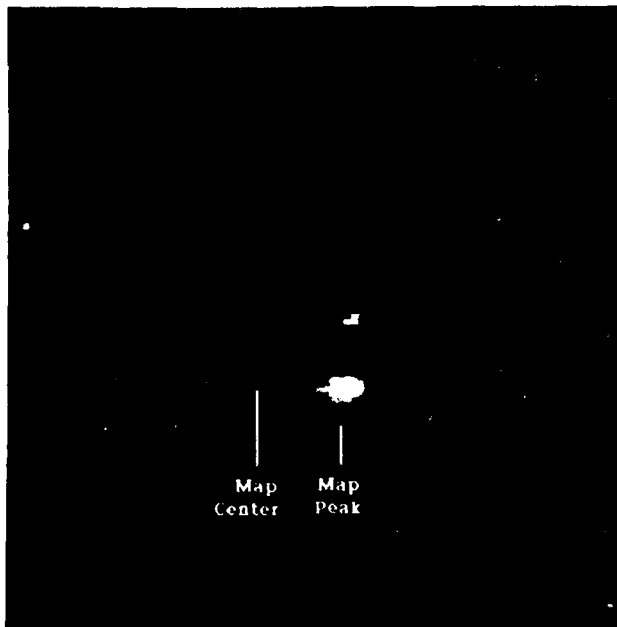


Fig. 5(a). Correlation map of two-color PIV double-pulsed image. Notice absence of self-correlation center peak.



Fig. 5(b). Correlation map of single-color PIV double-pulsed image. Notice self-correlation peak at center of map and symmetry of secondary peaks.

shifting or by having an *a priori* knowledge of the flowfield. Because only the red-particle images were mapped into the histogram map with respect to the green, neither the self-correlation peak nor the symmetry and associated 180-deg. directional ambiguity is observed. Thus, both displacement and directional information are determined from the histogram map. The analysis software determines the direction and displacement by searching for the maximum. The displacement is then determined from the maximum to the center. This corresponds to the most likely velocity and direction averaged over the  $x,y$  array which was examined. To determine the individual velocity vectors, a tracker must be employed. The task of the tracker now, however, is simplified because the average velocity and direction have been determined, thus reducing the angles and displacements over which it must track.

The drawback of all correlation techniques is the requirement for a statistically significant number of particle pairs for determining the most probable velocity vector. If the sampled area over which the correlator is used for analysis contains too few particle pairs, then the resulting correlation can be erroneous. The time required to obtain a correlation histogram on a  $384 \times 576$  pixel array is  $\sim 30$  sec. Normally, the digitized  $384 \times 576$  image is subdivided into fourths or sixteenths, depending upon the particle density and the variation of the velocity field over which correlation maps with subsequent tracking are constructed. The tracker which follows the correlation is extremely fast,  $\sim 10$  sec. The correlation-histogram technique functions best for images in which a large number of velocity pairs is sampled.

**Fourier Transforms.** The Fourier transform is the most mathematically rigorous method for estimating the most probable vector displacement. The computational burden of Eq. (5) can be reduced by use of the convolution theorem of Fourier transforms. The equivalent cross correlation using Fourier transforms is given by

$$c(x, y) = \text{IFT} \{ \text{FT} [ g(x, y) ] \cdot \text{FT} [ r(x, y) ] \} \quad (7)$$

where IFT denotes the inverse Fourier transform and FT the Fourier transform. Thus, the cross correlation of the green and red images can be formed by taking the inverse Fourier transform of the product of the Fourier transform of each image. Although this process involves two two-dimensional Fourier transforms and one two-dimensional inverse transform, it requires less time than the full correlation method because of the efficiency of Fast-Fourier-Transform algorithms. Since the cross correlation determined by Eq. (7) is independent of the number of particles present in the image, the computation time is the same for sparse and for densely seeded flowfields. The histogram approach, however,

is dependent upon particle density and, for the densities recorded in the experimental test section, was computationally more efficient.

### Tracker--Matching Green/Red Pairs

Once the coordinates of the green- and red-particle images have been determined and the most probable displacement vector calculated from the correlation histogram, the individual velocity vectors of green/red-particle pairs can be identified in a relatively short time. A tracker routine was developed to permit one to use the average velocity and directional information obtained from the correlation map and find green/red-particle pairs which fit this value within a preset uncertainty. The tracker functions by first starting from each green-particle image, adding the most probable vector displacement, and searching for the corresponding red-particle pair. If there is a red particle at the projected coordinates, then a velocity match is made and a vector drawn. If no red particle is found at these coordinates, a small "box" is opened around the target coordinates. This "box" is expanded incrementally to a selected percentage of the vector length. Figure 6 is a graphical representation of this process. The number and size

of increments should be kept relatively small (usually three increments or less with a maximum size of 50% of the vector length at the last increment). If the number and size of increments becomes too large, the number of erroneous matches may become large. Generally, good results are obtained with three increments, with the maximum increment being 20% of the vector length. The tracker portion of the analysis is very efficient, normally requiring < 30 sec on a full 384 x 576 digitized image for processing. The combination of a correlator and tracker was found to be the most efficient and effective approach to determining velocity vectors in the two-color images recorded in this study.

### Experimental

The experimental arrangement for two-color PIV measurements is shown in Fig. 7. Two Nd:YAG lasers are used in forming the different-color light sheets for exposing the position of the particles in the seeded flowfield. The green-laser-light sheet is formed from the doubled output of a Nd:YAG laser (Quanta-Ray DCR 1A) at 532 nm (this laser is capable of a single pulse in excess of 200 mJ). The second laser employed for the red-laser-light sheet is a broadband dye laser. The frequency-doubled output of a Nd:YAG laser (Quanta-Ray DCR 3A) is used to pump a dye laser consisting of an oscillator/amplifier combination which operates in a broadband mode for maximum conversion efficiency and output power. The dye laser is capable of over 100 mJ/pulse at 607 nm. The outputs from both the dye and

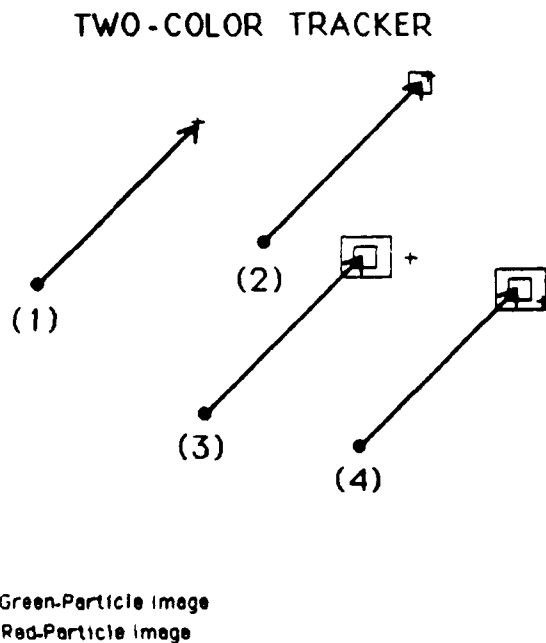


Fig. 6. Schematic illustration of two-color PIV tracker. Most probable velocity vector is drawn from each green-particle image (●) to locate corresponding red-particle image (+). Case (1) depicts exact match. Case (2) depicts match obtained with first uncertainty box. Case (3) depicts no match. Case (4) depicts match obtained with second uncertainty box.

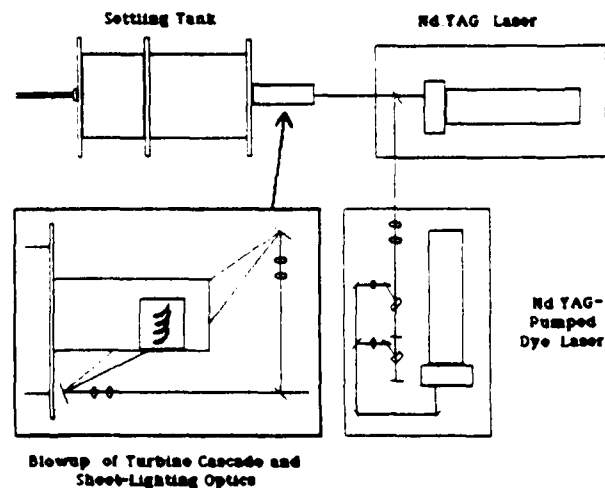


Fig. 7. Schematic of experimental arrangement for two-color PIV technique on turbine-cascade test section. Both a Nd:YAG and a Nd:YAG pumped dye laser are employed for sheet lighting the test section. Forward and backward light sheets are used to expose the test section.

Nd:YAG lasers are combined by a dichroic mirror, split into two equal parts by a beamsplitter, and directed into sheet-forming optics. These optics consist of a cylindrical lens which spreads the laser beams two dimensionally and a plano-convex lens which controls the beam waist of the laser sheets. Two separate laser sheets of nearly equal intensity are required for lighting the turbine-cascade test section because of the limited optical access. The laser sheets are ~10 cm in height and 1 mm in thickness in the test section.

Synchronization of the two laser systems presented a special problem because of the difference in repetition rates between the two Nd:YAG laser systems (10 and 20 Hz). In the present setup the lamp output from the 20-Hz DCR 3 (dye) laser is frequency halved by a divided-by-two circuit and used to fire the flashlamps of the DCR 1 laser at 10-Hz. The internal Q-switch circuitry of the DCR 1 laser is used to control the actual lasing of the 10 Hz laser. The Q-switch output from the DCR 1 is delayed by a pulse generator and feed into the Q-switch input of the DCR 3, thus firing the laser Q-switch at a fixed time delay after the DCR 1. This time delay is normally set to  $5 \mu\text{sec} \pm 20 \text{ nsec}$ . With this electronic arrangement, the DCR 3 laser discharges its flashlamps at a 20-Hz rate but fires its Q-switch at a 10-Hz rate.

A Nikon 35-mm-format camera was used to record the Mie scattering from the seeded flowfield. A macro zoom lens operating at an  $f/8.4$  aperture and a shutter speed of 0.125 sec. was employed for the images reported in this study. This lens-aperture combination resulted in a magnification factor of 0.39. The shutter speed ensured that at least one double-pulse exposure would be obtained for every shutter opening, reducing the need for camera synchronization electronics. If the flowfield emits a background light which will not allow the use of a low-speed shutter (i.e., a sooty flame or hot test section), then a high-speed shutter which can be synchronized to the laser firing must be employed. Color film of 100 - 400 ASA was used to record the two-color PIV images; the film was processed commercially.

The color film was digitized using the setup shown in Fig 8. A film projector was used to enlarge a section of the film onto a  $384 \times 576$  Thompson CCD array camera (Photometrics, Ltd.) which digitized and stored the information for later analysis. Each section of the film was digitized twice--once with a green-color filter and then with a red-color filter. The digitized film sections typically covered a  $1.5 \text{ cm}^2$  area of the recorded image. This corresponded to a pixel resolution of  $\sim 20 \mu\text{m}$  which was considered to be adequate for capturing the particle images. The 35-mm film was typically divided into 36 segments for digitization; these were stored on magnetic tape for analysis.

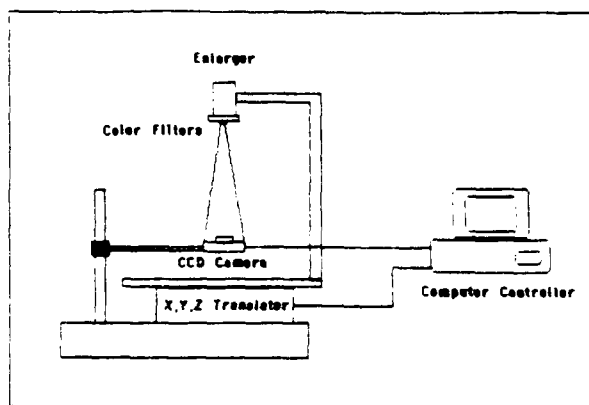


Fig. 8. Schematic of digitization system for two-color PIV images.

The turbine-cascade test section (Fig. 9) consisted of four aluminum airfoils representative of the high-pressure-turbine, first-stage-nozzle guide-vane row of commercial transport engines. The vanes were one-half engine scale, having a chord of 3.66 cm and a span of 2.54 cm. Design turning was 72-deg. and the pitch spacing was 2.54 cm. Seeded, dry-air flow entered the cascade from a rectangular channel which was 28 cm in length and had a cross section of  $23 \text{ cm}^2$ . The total throat area of the cascade was  $\sim 5 \text{ cm}^2$ . Each passage throat area was  $1.61 \text{ cm}^2$ . The cascade was operated at an inlet total-to-exit static pressure ratio of 2.15. Flow conditioning was provided upstream of the inlet channel by a large stagnation plenum containing screening and honeycomb flow straighteners. Access for the laser light sheets was provided by constructing one wall of the inlet channel and one of the exit tailboards of Plexiglas. Photographing the center passage of the cascade was done through a Plexiglas sidewall.

## Results and Discussion

Analysis of the two-color PIV images was discussed in the theoretical section, and only a brief review will given here. The color negative is first

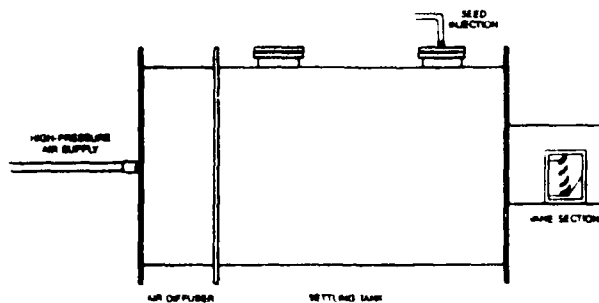


Fig. 9. Experimental turbine-cascade test section employed for high-speed-flow studies.

divided into 36 sections which are digitized twice to distinguish color. Each green/red digitized section is then analyzed separately. The initial step of this analysis is to locate the center coordinates of the green and red-particle images. Second, the digitized section (384 x 576) is subdivided into four or sixteen segments depending upon the particle density and velocity variation from which correlation histograms are constructed for each segment. The final step in the analysis involves a particle tracker which uses the most probable displacement vectors determined from the correlation histogram of each segment to find green/red-particle velocity pairs. The reduced velocity vectors are then stored for statistical analysis and graphics display.

A two-color PIV image which was taken on the turbine-cascade test section is shown in Fig. 10. A 5- $\mu$ sec time separation between the green and red laser sheets was used for this photograph. The air flow is from left to right in the photograph. The seed employed in this study was plasma-produced alumina (Zyp Coatings, Inc.) consisting of 5- $\mu$ m hollow microballoons with an effective aerodynamic drag of



Fig. 10. Two-color PIV image obtained in turbine-cascade test section. Time delay between laser pulses of 5  $\mu$ sec was employed for photograph.

less than 1  $\mu$ m. The hollow microballoons were chosen for this study to maximize particle visibility without sacrificing aerodynamic response. The seed is injected into the settling chamber just prior to exiting the test section. The air flow in this case is  $\sim$  80 m/sec upon exiting the settling chamber.

The processed two-color PIV vectors for the photograph shown in Fig 10 are displayed in Fig. 11. The length of the vectors depicted in this plot indicates the speed of the air flow. Analysis of the two-color PIV image indicates that the air entering the turbine test section was flowing at a rate of  $\sim$  80 m/s. However, as the air entered the passages between the turbine blades, it initially slowed to  $\sim$  60 m/s and then continuously accelerated to  $\sim$  340 m/s at the tip of the blades. The acceleration of the flow near the surface of the blade can be easily visualized in this plot.

In order to achieve consistent and reliable results, it was desirable to focus on a region sufficiently small that the velocity would be essentially constant, but sufficiently large that a significant number of green/red particle pairs would be present. A typical



Fig. 11. Processed velocity-vector map for turbine cascade.

image had a field of view of  $\sim 60 \times 90$  mm. This view were digitized into regions of  $\sim 10 \times 15$  mm which was further divided into fourths or sixteenths, depending upon the particle density and variation in velocity field. The subdivision of the sections into sixteenth regions was especially important in the areas near the blades where the velocity was accelerating rapidly. Even though the two-color PIV technique allows determination of speed and direction with only one green/red-particle pair, statistically it is desirable to have a minimum of ten pairs.

### Summary

In summary, the two-color PIV technique consists of 1) acquiring an image of green/red particle positions, 2) separating the green from the red particles, 3) finding the coordinates of the particles, 4) determining the most probable vector displacement for green/red pairs, and 5) matching green/red pairs which are within a specified percentage of the most probable vector displacement. The two-color PIV technique has the advantage that direction as well as particle displacement is uniquely determined because the green-particle image occurs before the red one by a known time increment. The technique is, thus, applicable to complex flowfields (i.e., recirculating), where the normal 180-deg. directional ambiguity of single-color techniques can be troublesome. Velocity measurements using the two-color PIV technique in a turbine-vane cascade test facility indicated that the large changes in direction and flow speed associated with these flowfields can be tracked by this technique.

### References

1. R. Meynart, *Appl. Opt.* **19**, 1385 (1980).
2. R. Meynart, *Appl. Opt.* **22**, 535 (1983).
3. C. S. Yao and R. J. Adrian. *Appl. Opt.* **23**, 1687 (1984).
4. R. J. Adrian and C. S. Yao. *Appl. Opt.* **24**, 44 (1985).
5. R. J. Adrian, *Appl. Opt.* **25**, 3855 (1986).
6. C. C. Landreth, R. J. Adrian, and C. S. Yao, "Double-Pulsed Particle Image Velocimetry with Directional Resolution for Complex Flows," Tenth Biennial Symposium on Turbulence, 1986.
7. J. M. Coupland, C. J. D. Pickering, and N. A. Halliwell. *Appl. Opt.* **23**, 11 (1987).

8. D. L. Ruess, R. J. Adrian, C. C. Landreth, D. T. French, and T. D. Fansler. "Instantaneous Planar Measurements of Velocity and Large-Scale Vorticity and Strain Rate in an Engine Using Particle-Image Velocimetry," SAE International Congress and Exposition, SAE Technical Paper 890616, 1989.
9. B. Hiller, R. A. Booman, C. Hassa, and R. K. Hanson, *Rev. Sci. Instrum.* **55**, 1964 (1984).
10. R. B. Miles, J. Connors, E. Markovitz, P. Howard, and G. Roth, *Phys. Fluids A*. **1**, 389 (1989).
11. L. R. Boedeker, *Opt. Lett.* **14**, 473 (1989).
12. B. J. Hiller, J. C. McDaniel, J. E. C. Read, and R. K. Hanson, *Opt. Lett.* **8**, 474 (1983).
13. J. C. McDaniel, B. Hiller, and R. K. Hanson, *Opt. Lett.* **8**, 51 (1983).
14. B. Hiller and R. J. Hanson, *Opt. Lett.* **10**, 206 (1985).
15. B. Hiller and R. K. Hanson, *Appl. Opt.* **27**, 33 (1988).

## Two-Color Particle Velocimetry

L. P. Goss, M. E. Post, D. D. Trump, and B. Sarka  
Systems Research Laboratories, Inc.  
*A Division of Arvin/Calspan*  
2800 Indian Ripple Road  
Dayton, OH 45440-3696 USA

### Abstract

A novel method for determining two-dimensional velocity flowfields has been developed. The technique, two-color particle-image velocimetry (PIV), is similar to existing PIV techniques except that two different-color laser sources are used to form the light sheets required for exposing the position of particles in a seeded flowfield. A green-colored laser sheet (formed by a doubled Nd:YAG laser) and a red-colored laser sheet (formed by a Nd:YAG-pumped dye laser) are employed sequentially to expose the particle positions which are recorded on 35-mm color film. Analysis of the resulting images involves digitizing the exposed film with color filters to separate the green- and red-particle image fields and processing the digitized images with velocity-displacement software. The two-color PIV technique has the advantage that direction, as well as particle displacement, is uniquely determined because the green-particle image occurs before the red one by a known time increment. Velocity measurements utilizing the two-color PIV technique on a propane jet diffusion flame have been made and are discussed.

### Introduction

In complex flowfields (i.e., recirculating flows), it is important to obtain an instantaneous two-dimensional picture of the entire flowfield rather than a time-averaged pointwise map. Several techniques have been reported in the literature which have the capability to determine the two-dimensional velocity of a flowfield. These techniques can be divided into three categories: particle-tracking schemes,<sup>1-8</sup> time-of-flight techniques,<sup>9-11</sup> and Laser Doppler methods.<sup>12-15</sup> For low-to-moderate velocity flowfields, particle-tracking techniques are efficient, offering a wide velocity range and allowing a two-dimensional measurement of the velocity flowfield. Particle tracking or particle-image velocimetry (PIV) is basically an extension of speckle photography which has been employed extensively in solid mechanics. The PIV technique consists of 1) double pulsing a particle-laden flowfield, 2) recording the scattered light either by conventional photography or holography, and 3) processing the photographs to obtain velocity information. While the first two steps are relatively simple to implement, the data analysis is typically complex and requires computerized image processing.

This paper introduces a novel two-color PIV technique designed to remove directional ambiguities, allowing measurements to be made in complex flow systems. The technique consists of employing small particles to seed a gas stream exiting a nozzle or passing through a test section. A laser sheet (green), formed by passing the output from a doubled Nd:YAG laser through a cylindrical lens, is used to illuminate the seed particles in the flowfield. After a short selected time interval (ranging from a few

microseconds for high-velocity flow systems to milliseconds for low-velocity flow systems), a second laser sheet (red) from a Nd:YAG-pumped dye laser is pulsed to illuminate the flowfield a second time. Any particles remaining in the plane of the laser sheets produce a "displacement-vector" pair comprised of a green- and a red-particle image. The Mie scattering from the seeded particles is recorded on 100-400 ASA color film and processed by direct digitization. The unique color coding helps to remove directional ambiguities associated with single-color techniques because the red image occurs after the green one.

### Image Analysis

The two-color PIV technique utilizes color to remove directional ambiguities and reduce tracking errors. However, because the standard Young's-fringe<sup>1</sup> analysis approach cannot distinguish between the different-color particle fields, an alternative correlation-tracker analysis approach was developed. The analysis procedure consists of 1) digitizing the color negative with a CCD array, 2) determining the spatial locations of the digitized particle images, 3) constructing a correlation map from which the most probable displacement vector can be determined, and 4) utilizing this information in a tracker which identifies green/red-particle vector pairs from the digitized image.

### Determination of Particle Coordinates

In order to take full advantage of the resolution available with the color film on which images were recorded (~ 300 line pairs/mm), an enlarger was employed to subdivide the image for analysis. An automated x,y,z traversing mechanism was used to set the position of the enlarger to within 20  $\mu\text{m}$  in any direction. Each section of the enlarged image was digitized twice using a CCD camera system. The first digitized image was taken with a green filter for identifying the green-particle images and the second with a red filter for identifying the red-particle images. These digitized images were processed in an identical manner to determine the coordinates of the green and red particles.

A typical digitized image displays peaks associated with the particles superimposed on a slowly varying background. In order to simplify the procedures for determining the coordinates of each particle, components of the background which are constant or slowly varying over the scale of the particle size are removed by applying a two-dimensional Laplacian operator to the digitized image. This Laplacian operator basically acts as a spatial-frequency filter, passing high-frequency (small-size) components of the image but suppressing low-frequency (background) components. The particle images can be further enhanced above the background and film noise if the step size of the Laplacian operator is approximately the particle size. Next, the processed image is scanned in two dimensions for local maxima, and a series of tests is performed to identify those local maxima which correspond to particles. In brief, particles are identified by finding local maxima which 1) are above a threshold value, 2) do not constitute a shoulder, 3) have a local average intensity above a threshold value, and 4) have an estimated diameter within a specified range.

## Determination of Most Probable Vector Displacement

Several methods have been used to determine the most probable displacement (correlation) for vector pairs in a section of the image. Beginning with the simplest and moving to the most mathematically complex, these include 1) vector comparison, 2) histograms, and 3) Fourier transforms. The histogram (correlation-map) approach to particle correlation was found to be computationally efficient; therefore, this method was chosen for the present study and will be discussed in detail here. The cross correlation between the green- and red-particle images is given by

$$c(\xi, \psi) = \sum_x \sum_y g(x, y) r(x - \xi, y - \psi) \quad (1)$$

where  $c(\xi, \psi)$  represents the two-dimensional correlation map,  $g(x, y)$  the digitized green image,  $r(x - \xi, y - \psi)$  the digitized red image, and the limits of summation are over the pixel dimensions of the digitized image. The correlation in this form is computationally intensive since it represents a double summation of the entire digitized image. In the histogram approach, a correlation-histogram map is constructed from the green- and red-particle images; the maximum of this map contains the most probable displacement vector. The method is displayed schematically in Fig. 1. The software for this analysis functions by first finding an initial particle image in the green digitized image. The exact location of the green particle is determined and used for mapping. A 120 x 120 pixel area of the red-particle image centered about the green-particle coordinates is then summed into a histogram map (correlation space). This procedure is repeated for all the green-particle images and their associated surrounding fields in the red-particle images. This process is represented mathematically by

$$H(\xi, \psi) = \sum_n g(x_c, y_c) r(x_c - \xi, y_c - \psi) \quad (2)$$

where  $H(\xi, \psi)$  represents the correlation histogram,  $g(x_c, y_c)$  the center coordinates of the green-particle images,  $r(x_c - \xi, y_c - \psi)$  the red-particle images surrounding the green particle being mapped, and the summation is over all green-particle images. Because the double summation of Eq. (1) over all  $x$  and  $y$  pixels has been replaced with a single summation over the number of green particles, Eq. (2) is computationally more efficient and results in a cross-correlation map.

As green/red-particle pairs having the same velocity--and thus displacement--are mapped into correlation space, peaks are built up on the map surface. The maximum of this map corresponds to the most probable displacement from the center coordinate, illustrated in Fig. 2. If a single-color image had been used instead of a two-color image, the resulting correlation map would have been symmetric and centered about a large self-correlation peak at the center of the map. This would have resulted in a 180-deg. directional ambiguity which would have had to be resolved by phase shifting or by having an *a priori* knowledge of the flowfield. Because only the red-particle images were mapped into the histogram with respect to the green, neither the self-correlation peak nor the symmetry and associated 180-deg. directional ambiguity is observed. Thus, both displacement and directional information are determined from the histogram map. The analysis software determines the direction and displacement by searching for the maximum. The displacement is then determined from the maximum to the center. This corresponds to the most likely velocity and direction averaged over

the x,y array which was examined. To determine the individual velocity vectors, a tracker must be employed. The task of the tracker is simplified because the average velocity and direction have been determined, thus reducing the angles and displacements over which it must search.

#### Determination of Vector Pairs (Tracker)

Once the coordinates of the green- and red-particle images have been determined and the most probable displacement vector calculated from the correlation histogram, the individual velocity vectors of green/red-particle pairs can be identified in a relatively short time. A tracker routine was developed to permit one to use the average velocity and directional information obtained from the correlation map to find green/red-particle pairs. The tracker functions by first starting from each green-particle image, adding the most probable vector displacement, and searching for the corresponding red particle. If there is a red particle at the projected coordinates, then a velocity match is made and a vector drawn. If no red particle is found at these coordinates, a small *window* is opened around the target coordinates. This *window* is expanded incrementally to a predetermined percentage of the vector length. Figure 3 is a graphical representation of this process. If the number and size of the window increments become too large, the number of erroneous matches may become large. Generally, good results are obtained with three window increments, the maximum increment being 20% of the vector length. The tracker portion of the analysis is very efficient, normally requiring < 30 sec to process a full 384 x 576 digitized image. The combination of a correlator and tracker was found to be the most efficient and effective approach to determining velocity vectors in the two-color images recorded in this study.

#### Experimental

The experimental arrangement for two-color PIV measurements is shown in Fig. 4. Two separate Nd:YAG lasers are used in forming the different-color light sheets for exposing the position of the particles in the seeded flowfield. The green laser light sheet is formed from the doubled output of a Nd:YAG laser (Quanta-Ray DCR 1A) at 532 nm. This laser is capable of a single pulse in excess of 200 mJ. The second laser employed for the red-laser-light sheet is a broadband dye laser. The frequency-doubled output of a Nd:YAG laser (Quanta-Ray DCR 3A) is used to pump a dye laser consisting of an oscillator-amplifier combination which operates in a broadband mode for maximum conversion efficiency and output power. The dye laser is capable of over 100 mJ/pulse at 607 nm. The outputs from both the dye and Nd:YAG lasers are combined by a dichroic mirror and directed into sheet-forming optics. These optics consist of a cylindrical lens which spreads the laser beams two dimensionally and a plano-convex lens which controls the beam waist of the laser sheets. The laser sheet in the test area was ~ 10 cm high and 1 mm thick.

Synchronization of the two laser systems presented a special problem because of the different repetition rates of the two Nd:YAG laser systems (10 and 20 Hz). In the present setup the lamp output from the 20-Hz DCR 3 (dye) laser is frequency-halved by a divided-by-two circuit and used to fire the flashlamps of the DCR 1 laser at 10 Hz. The internal Q-switch circuitry of the DCR 1 laser is used to control the actual lasing of the 10-Hz laser. The Q-switch output from the DCR 1 is delayed by a pulse generator and feed into the Q-switch input of the DCR 3, thus firing the laser Q-switch at a fixed

time delay after the DCR 1. This time delay is normally set to  $500 \mu\text{sec} \pm 20 \text{ nsec}$ . With this electronic arrangement, the DCR 3 laser discharges its flashlamps at a 20-Hz rate but fires its Q-switch at a 10-Hz rate.

A Nikon 35-mm-format camera was used to record the Mie scattering from the seeded flowfield. A macro zoom lens operating at an  $f/8.4$  aperture was employed for the images reported in this study. This lens-aperture combination resulted in a magnification factor of 0.52. To reduce the contribution of the soot emission of the flame, a Uniblitz high-speed camera shutter operating at a 1/500-sec. exposure was employed. Synchronization of the camera shutter with the laser firing was controlled by custom built timing electronics. Color film of 100-400 ASA was used to record the two-color PIV images; the film was processed commercially.

The color film was digitized by a  $384 \times 576$  Thompson CCD array camera (Photometrics, Ltd.) and a film projector was used to enlarge a section of the film onto the camera. Each section of the film was digitized twice--first with a green-color filter and then with a red-color filter. The digitized film sections typically covered a  $1.5 \text{ cm}^2$  area of the recorded image (which was  $\sim 54 \text{ cm}^2$ ). This corresponded to a pixel resolution of  $\sim 20 \mu\text{m}$  which was considered to be adequate for capturing the particle images. The 35-mm film was generally divided into 36 segments for digitization; these were stored on magnetic tape for analysis.

The experimental arrangement for the jet diffusion flame consisted of a 22.5-mm-diam. round central jet surrounded by a 254-mm-diam. annular coflowing air jet. The velocity of the central fuel jet and annular air was  $\sim 30 \text{ cm/sec}$ . The fuel used in this study was propane diluted with 50%-by-mass nitrogen. This flame has been studied experimentally by means of the reactive Mie scattering (RMS) and thin-filament-pyrometry (TFP) techniques in which visualization and temperature profiles, respectively, were obtained; these profiles were compared with numerical predictions of Davis, *et al.*<sup>16-17</sup> Experimental as well as numerical evidence indicates that the low-velocity propane jet is unusual in that a stagnation (weak-recirculation) zone is established approximately two diameters downstream of the nozzle. This stagnation zone is caused by the high density of propane which tends to overcome the weak momentum of the fuel jet, eventually stopping the upward fuel flow. The flame develops downstream from the stagnation zone due to the acceleration effects of buoyancy. The flowfield is, thus, relatively complex and provides a good test for two-dimensional velocity methods which can distinguish direction.

A 500- $\mu\text{sec}$  time separation was used between the green-and red-laser sheets for this study. If a maximum velocity in the flowfield of  $3 \text{ m/sec}$  is assumed, the minimum spatial resolution at this velocity is  $\sim 1.5 \text{ mm}$ . The lowest observable velocity is determined by the minimum detected particle separation divided by the time separation between laser pulses. For the collection optics and film used in this study, the smallest detectable particle separation was  $\sim 15 \mu\text{m}$ ; thus, the smallest detectable velocity was  $\sim 0.03 \text{ m/sec}$ . The seed, alumina of  $\sim 1 \mu\text{m}$  nominal size, was injected into both the fuel jet and coannular air jet just prior to exiting the tubes.

## Results and Discussion

Analysis of the two-color PIV images was discussed in the theoretical section and will be reviewed here only briefly. The color negative is first divided into 36 sections which are digitized twice to distinguish color. Each green/red digitized section is then analyzed separately. The initial step of this analysis involves locating the center coordinates of the green- and red-particle images. Next, the digitized section (384 x 576) is subdivided into four or sixteen segments (depending upon the particle density and velocity variation), from which correlation histograms are constructed. The final step in the analysis involves a particle tracker which uses the most probable displacement vectors determined from the correlation histogram of each segment to find green/red-particle velocity pairs. The reduced velocity vectors are then stored for statistical analysis and graphic display.

In order to achieve consistent and reliable results, it was desirable to focus on a region sufficiently small that the velocity would be essentially constant, but sufficiently large that a significant number of green/red-particle pairs would be present. A typical image had a field of view of  $\sim 60 \times 90$  mm. This view was digitized into  $\sim 10 \times 15$  mm regions which were further divided into fourths or sixteenths, depending upon the particle density and variation in velocity field. The subdivision of the sections into sixteen regions was especially important in areas where the velocity was changing rapidly. Although the two-color PIV technique allows determination of speed and direction with only one green/red-particle pair, statistically a minimum of ten pairs is desirable.

The processed two-color PIV image for the 22.5-mm propane jet is shown in Fig. 5. The initial velocity of the fuel jet was  $\sim 30$  cm/sec at the nozzle exit. As the fuel jet progressed downstream, its velocity decayed, approaching zero at  $\sim 1.5$  diameters downstream. The development of the stagnation zone was due to the high density of the propane fuel which overcame the initial momentum of the fuel jet. Just above this stagnation zone, the fuel jet accelerated due to the proximity of the fast, hot-burning gases. Notice that these hot regions displayed a velocity which was much higher than that of the cold central fuel jet. This high velocity was thought to be due to the buoyancy effect which accelerates the hot (low-density) combusting gases. The gases in the combusting areas reach a velocity of  $\sim 3$  m/sec. Notice that the cooler outer air was entrained into the flame at downstream locations. This process acted to mix burning fuel with air and, thus, sustain combustion at downstream locations.

The existence of the stagnation zone and flowfield acceleration due to buoyancy have been qualitatively demonstrated using the RMS flow-visualization technique on this jet diffusion flame.<sup>16</sup> Numerical results of Davis, *et al.*,<sup>16-17</sup> have confirmed the importance of the role of buoyancy in giving this flame its unique character. Future work on this flame will be directed toward obtaining velocity vorticity in this flowfield.

## Summary

In summary, the two-color PIV technique involves 1) acquiring an image of green/red particle positions, 2) separating the green particles from the red ones, 3) finding the coordinates of the particles, 4) determining the most probable vector displacement for green/red pairs, and 5) matching green/red pairs which are within a specified percentage of the most probable vector displacement. The two-color PIV technique has the

advantage that direction, as well as particle displacement, is uniquely determined because the green-particle image occurs before the red one by a known time increment. The technique is, thus, applicable to complex flowfields (i.e., recirculating), where the normal 180-deg. directional ambiguity of single-color techniques can be troublesome. Velocity measurements using the two-color PIV technique on a propane jet diffusion flame indicated that the large change in flow speed and direction associated with these flowfields can be measured by this technique.

#### Acknowledgement

This work was supported by and performed at the Wright Research and Development Center/Aero Propulsion Laboratory under Contract No. F33615-85-C-2562. The authors are indebted to Drs. W. M. Roquemore and C. D. MacArthur for support and discussions concerning this work and to M. Whitaker for editorial assistance.

#### References

1. Meynard, R. (1980). **Appl. Opt.** 19: 1385.
2. Meynard, R. (1983). **Appl. Opt.** 22: 535.
3. Yao, C. S. and R. J. Adrian (1984). **Appl. Opt.** 23: 1687.
4. Adrian, R. J., and C. S. Yao (1985). **Appl. Opt.** 24: 44.
5. Adrian, R. J. (1986). **Appl. Opt.** 25: 3855.
6. Landreth, C. C., R. J. Adrian and C. S. Yao (1986). "Double-Pulsed Particle Image Velocimetry with Directional Resolution for Complex Flows." Tenth Biennial Symposium on Turbulence.
7. Coupland, J. M., C. J. D. Pickering and N. A. Halliwell (1987). **Appl. Opt.** 23: 11.
8. Ruess, D. L., R. J. Adrian, C. C. Landreth, D. T. French and T. D. Fansler (1989). "Instantaneous Planar Measurements of Velocity and Large-Scale Vorticity and Strain Rate in an Engine Using Particle-Image Velocimetry." SAE International Congress and Exposition. SAE Technical Paper 890616.
9. Hiller, B., R. A. Booman, C. Hassa and R. K. Hanson (1984). **Rev. Sci. Instrum.** 55: 1964.
10. Miles, R. B., J. Connors, E. Markovitz, P. Howard and G. Roth (1989). **Phys. Fluids A.** 1: 389.
11. Boedeker, L. R. (1989). **Opt. Lett.** 14: 473.

12. Hiller, B. J., J. C. McDaniel, J. E. C. read and R. K. Hanson (1983). **Opt. Lett.** 8: 474.
13. McDaniel, J. C., B. Hiller and R. K. Hanson (1983). **Opt. Lett.** 8: 51.
14. Hiller, B., and R. K. Hanson (1985). **Opt. Lett.** 10: 206.
15. Hiller, B., and R. K. Hanson (1988). **Appl. Opt.** 27: 33.
16. Davis, R. W., E. F. Moore, L-D. Chen, V. Vilimpoc, L. P. Goss and W. M. Roquemore (May, 1989). "Numerical/Experimental Study of the Dynamic Structure of a Buoyant Jet Diffusion Flame." 1989 Spring Technical Meeting of the Central States Section of The Combustion Institute.
17. Davis, R. W., E. F. Moore, L-D. Chen, V. Vilimpoc, L. P. Goss and W. M. Roquemore (May, 1989). "Preliminary Results of Numerical/Experimental Study of a Buoyant Jet Diffusion Flame." Paper submitted to **Combust. Flame**.

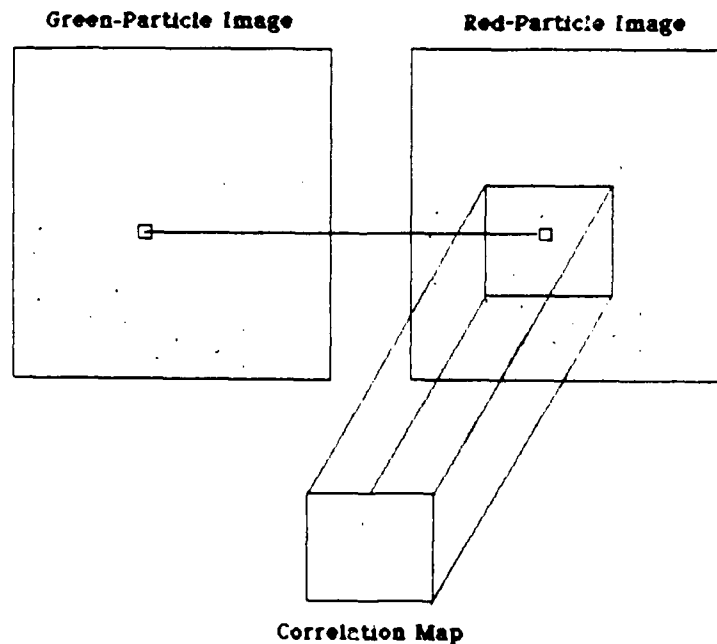


Fig. 1. Schematic Diagram of Mapping from Image to Correlation Space for Two-Color PIV Technique. For each green particle, 64 x 64 area of red-particle image centered on green-particle coordinates is summed into correlation map.

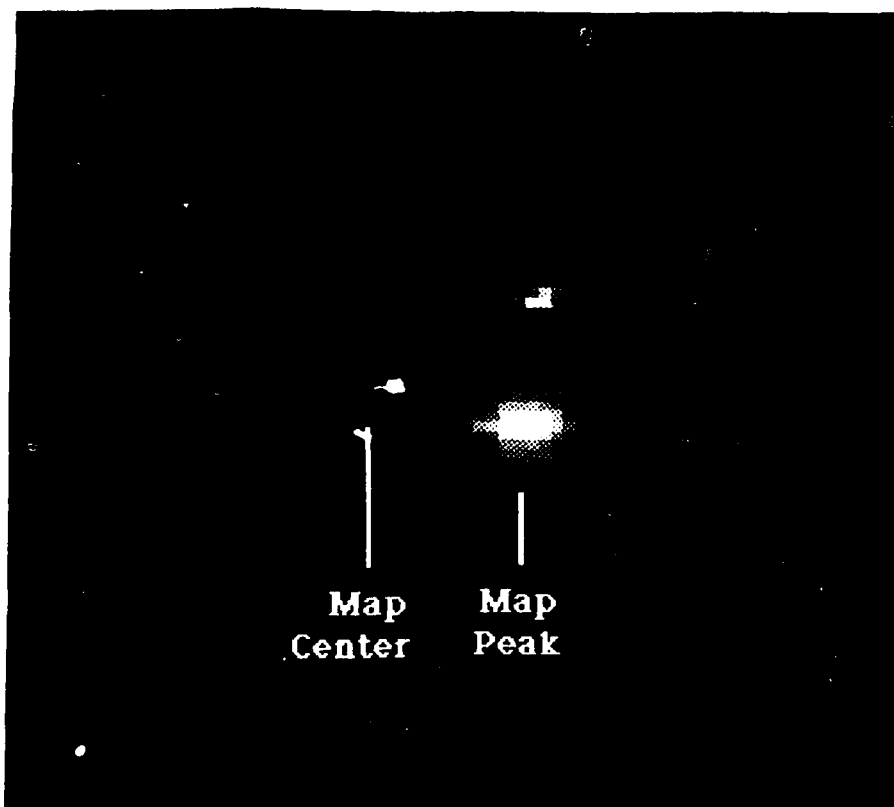


Fig. 2. Correlation Map of Two-Color PIV Double-Pulsed Image. Notice absence of self-correlation center peak.

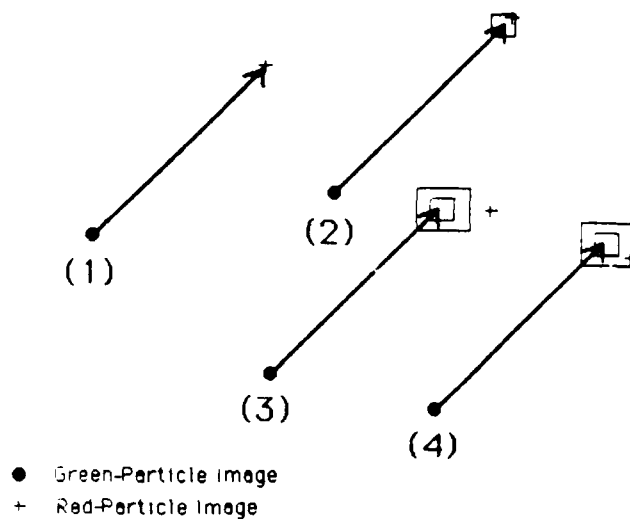


Fig. 3. Schematic illustration of Two-Color PIV Tracker. Most probable velocity vector is drawn from each green-particle image (●) to locate corresponding red-particle image (+). Case (1) depicts exact match; Case (2), match obtained with first uncertainty box; Case (3), no match; Case (4), match obtained with second uncertainty box.

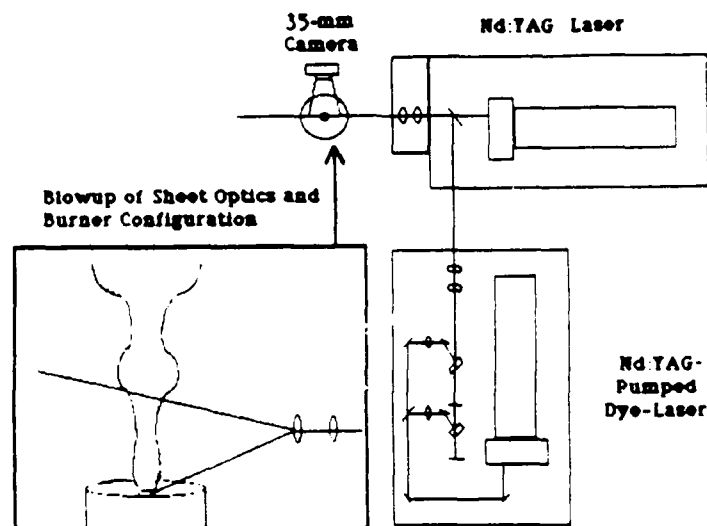


Fig. 4. Schematic Diagram of Experimental Arrangement for Two-Color PIV Technique on Propane Jet Diffusion Flame. Both a Nd:YAG and a Nd:YAG-pumped dye laser are employed for sheet lighting the flame.



Fig. 5. Processed Velocity-Vector Map of Propane Jet Diffusion Flame. Solid line in flow represents visible flame surface.

## 2.6 SPRAY-DIAGNOSTIC DEVELOPMENT

In the initial stage of this contractual effort, the primary instrument for performing combustion diagnostics was the hardened CARS system. This system has continued to be proficient in allowing combustion-temperature information to be obtained. During the course of this contract, the capabilities of this system have been further developed and expanded to include operation within a droplet-laden, liquid-fuel spray-flame environment. Experimental studies such as those described in the paper entitled, "Effect of Droplet Induced Breakdown on CARS Temperature Measurements," which was presented at the 1988 Fall Meeting of the Western States Section of the Combustion Institute (see p. 176), were performed for extension of the CARS technique to spray-flame diagnostics.

Early attempts at obtaining unambiguous two-dimensional velocity information led to the development of a scanned-laser-velocimetry technique which is described, along with two similar techniques, in the paper, "Applications of Laser-Sheet-Lighting Techniques to Multiple-Point Velocity Measurements in Mixing Flows," which was presented at the International Conference on Applications of Lasers and Electro Optics '86 (see p. 186).

The acquisition of an Aerometrics, Inc., two-component phase Doppler particle analyzer (PDPA)\* greatly expanded the available diagnostic techniques, allowing size and velocity measurements to be made in a liquid-spray environment. With this instrument, the diameter and/or two-velocity components of an individual droplet can be measured--even in very dense spray environments. During the initial familiarization with and development of this capability, several instrument problems were encountered and analyzed. One such problem involving an unstable frequency-shifting scheme is described in a paper, "Investigation of Velocity and Turbulence Intensity Measurement Limitations of the Phase Doppler Particle Analyzer," which was presented at the 1988 Spring Technical Meeting of the Central States Section of the Combustion Institute (see p. 194).

---

\*W. D. Bachalo and M. J. Houser, "Development of the Phase/Doppler Spray Analyzer for Liquid Drop Size and Velocity Characterizations," AIAA Paper 84-1199, Presented at the 20th Joint Propulsion Conference, Cincinnati, Ohio, 1984.

The study of spray behavior on its most basic level (i.e., single-drop reaction) required the development of several pieces of specialized test equipment, the most challenging being a source of individual liquid droplets. "The Development of a Water-Cooled Droplet-on-Demand Generator," which was presented at the Third Annual Conference on Liquid Atomization and Spray Systems (see p. 201), describes the successful technique which has been employed during the course of droplet-diagnostic applications.

The culmination of the hardened-system combustion-diagnostic development came with the integration of the PDPA into the hardened CARS system. The combined instrument as described in the paper, "An Integrated Spectroscopic-Interferometric Instrument for Spray Combustion Diagnostics," (see p. 206) provides a non-intrusive capability with which to measure simultaneously gas temperature and velocity as well as droplet size and velocity in liquid-spray flames.

# Effect of droplet-induced breakdown on CARS temperature measurements

Derek Dunn-Rankin, Gary L. Switzer, Cindy A. Obringer, and Tom A. Jackson

This research examines the potential for coherent anti-Stokes Raman scattering (CARS) to provide reliable gas temperature measurements in the presence of liquid droplets. The droplets cause dielectric breakdown by focusing the CARS laser beams. This breakdown produces a plasma that can disrupt or obscure the CARS signal. Specifically, we examine the influence of laser induced breakdown on the CARS signal, and we determine the importance of droplet position relative to the CARS focal volume and droplet concentration on the reliability of CARS temperature measurements in droplet-laden flows. In addition, we propose a reliable data reduction procedure to minimize the disruptive influence of laser induced breakdown on CARS temperatures.

## I. Introduction

### A. Background

Proper characterization of spray combustion flows requires spatially resolved maps of droplet size, droplet velocity, droplet composition, gas velocity, gas species concentration, and gas temperature. In addition, it is important to determine these properties without disturbing the flow field. Several nonintrusive optical diagnostic techniques have been designed and employed for this purpose (Roquemore *et al.*,<sup>1</sup>). For example, McDonnell *et al.*<sup>2</sup> and Mao *et al.*<sup>3</sup> report Phase Doppler Particle Analyzer (PDPA) measurements of droplet size, droplet velocity, and gas velocity in a spray flame. Comparable nonintrusive temperature measurements in liquid spray flames have not been reported. Our eventual goal is to provide these temperature measurements, in addition to measurements of the flow field and the droplet field, by combining CARS thermometry with PDPA interferometry. Toward this goal, the present paper concentrates on resolving difficulties of CARS thermometry in droplet laden flows.

### B. CARS in Particle Laden Environments

CARS is a nonlinear spectroscopic technique for measuring the energy spectrum from an ensemble of

molecules. Through quantum mechanics, the energy spectrum is a predictable function of temperature. CARS thermometry determines temperature by comparing the measured energy spectrum to calculated spectra using temperature as the fitting parameter. Because CARS thermometry relies on spectral fitting, disruption of the measured energy spectrum by scattered light has potentially serious consequences for the accuracy of the temperature measurements. Fortunately, in particle laden environments, CARS thermometry has significant advantages over other nonintrusive thermometric techniques such as Rayleigh scattering or spontaneous Raman scattering. The CARS signal is coherent so that spatial filtering prevents most of the light scattered by particles from entering the detector. In addition, CARS is an inelastic scattering process, and consequently the signal is spectrally separated from the pump and probe laser beams. Spectral filtering further eliminates particle-scattered background radiation. Eckbreth *et al.*<sup>4</sup> present a review of CARS spectroscopy and further advantages of CARS thermometry in hostile measurement environments.

Utilizing the inherent background rejection capability of CARS, several researchers have reported nonintrusive temperature measurements in combustion flows with solid particles present. Eckbreth and Hall<sup>5</sup> have demonstrated reliable temperature measurements in sooting flames. Goss and Trump<sup>6</sup> have combined a laser Doppler anemometer (LDA) with a CARS system, and have successfully measured temperature with titanium dioxide LDA seed particles in the flow. These efforts have shown that small particles ( $<1 \mu\text{m}$ ) do not significantly affect the collection and analysis of CARS signals. However, Beiting,<sup>7</sup>

Derek Dunn-Rankin is with University of California, Irvine, Department of Mechanical Engineering, Irvine, California 92717; Gary L. Switzer is with Systems Research Laboratories, Dayton, Ohio 45440-3696, the other authors are with AFWAL Aero-Propulsion Laboratory, Wright-Patterson Air Force Base, Ohio 45433-6563.

Received 13 December 1988

Lucht,<sup>8</sup> Noda *et al.*,<sup>9</sup> and Switzer *et al.*<sup>10</sup> (1989) showed significant dielectric breakdown, and disruption of CARS signals with large particles (1–100  $\mu\text{m}$ ) present. Taylor,<sup>11</sup> using relatively low laser energy intensity, did not have breakdown problems during collinear CARS measurements in a coal gasifier. Both Beiting and Lucht demonstrated qualitatively that breakdown can be minimized by reducing laser power, but they did not present a systematic study of breakdown during CARS measurements.

### C. Potential Effects of Particle Induced Breakdown on CARS Signals

Laser energy density of  $\sim 10^{12}$  W/cm<sup>2</sup> at a wavelength of 532 nm causes laser induced breakdown of clean air at standard temperature and pressure. For a Gaussian spatial intensity profile, and a triangular temporal profile, this energy density corresponds to the peak intensity in a 200-mJ, 10-ns laser pulse focused to 0.1-mm diam beam waist. To maximize the CARS signal, most researchers operate near this threshold energy level. However, large particles in the sample volume reduce the breakdown threshold energy by 1–2 orders of magnitude. Consequently, any large particle in the CARS interaction volume will produce a breakdown.

The plasma generated by laser breakdown affects the CARS signal in several ways: (1) the bright plasma discharge produces a background signal that obscures the CARS signal; (2) the nonresonant CARS signal generated in the plasma competes with the resonant CARS signal, making analysis of the spectrum difficult; (3) the plasma prevents CARS generation by absorbing laser radiation. Switzer *et al.*<sup>10</sup> and Lucht<sup>8</sup> reported difficulties with (1) and (2), Beiting<sup>7</sup> reported difficulties with (2). Although (3) has been reported in high density plasmas, it has not been significant for plasmas generated during CARS measurements in particle laden combustion systems.

The present work examines the effect of droplet induced laser breakdown on CARS temperature measurements. There are three objectives in the study: (1) determine the influence of droplet induced breakdown on the CARS spectrum, and how that influence affects the temperature fit of the experimental spectrum, (2) explore software tests to extract valid CARS temperature measurements from spectra affected by breakdown events, and (3) determine the droplet number density and spatial region where droplet breakdown has significant effects.

## II. Experiments

### A. Experimental Apparatus

Figure 1 is a schematic diagram of the experimental apparatus. The apparatus includes a CARS system, droplet generating hardware and electronics, an imaging system to visualize droplets, a PIN diode to record laser induced breakdown (LIB), and a propane burner and heat pipe to supply high temperature gas to the sample volume.

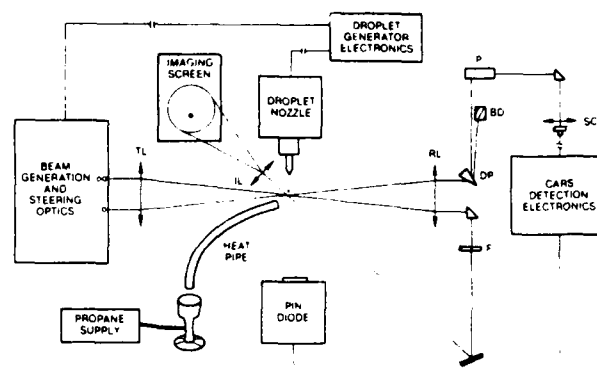


Fig. 1. Schematic diagram of the experimental apparatus: TL-transmitting lens, IL-imaging lens, RL-receiving lens, F-neutral density filter, DP-dispersing prism, BD-beam dump, P-periscope, SC-sample collection optics.

### (1) CARS System

The CARS system uses the second harmonic (532 nm) of a pulsed Nd:YAG laser (Spectra-Physics DCR-2) as its primary photon source. Part of the 532-nm light pumps a Rhodamine 590 dye laser oscillator to generate a broadband ( $150\text{-cm}^{-1}$ ) Stokes laser beam peaked at 607 nm. The peak of the dye laser output is concentration tuned to probe the N<sub>2</sub> Q-branch. The remaining 532-nm beam is split into a pair of pump beams. A 500-mm focal length lens combines the two pump beams and the one Stokes beam in an interaction volume  $\sim 2$  mm long and 500  $\mu\text{m}$  in diameter. The interaction volume was measured by scanning a small nitrogen gas jet near the beam crossing, and recording the variation in the CARS signal amplitude. Switzer and Goss<sup>12</sup> describe this nitrogen jet scanning technique. Each pump beam contains  $\sim 47$  mJ of energy, and the Stokes beam contains  $\sim 30$  mJ of energy. Assuming a 10-ns laser pulse, and uniform spatial and temporal intensity, these energies indicate an average intensity of  $6 \times 10^9$  W/cm<sup>2</sup>. Dispersing prisms separate the CARS signal beam from the pump beams, and focusing optics converge the CARS energy onto the face of an optical fiber. The fiber transmits the CARS signal to a spectrometer. A Tracor Northern TN-1710 DARSS linear array detector collects the spectrum and passes it to a ModComp computer for analysis. Additional details of the CARS system have been reported by Switzer and Goss.<sup>12</sup>

### (2) Droplet Generators

We study the effect of laser induced breakdown on CARS measurements using three droplet sources: a drop-on-demand piezoelectric generator, a pressure atomizer, and a capillary breakup droplet stream generator. The droplet generators mount on a 3-D translation stage to place droplets or spray at different positions relative to the CARS focal volume. All of the measurements use water as the droplet fluid, and the droplets travel perpendicular to the laser beam direction.

The drop-on-demand droplet generator consists of a

glass nozzle encased in a cylindrical piezoelectric element. The generator produces droplets ( $\sim 65 \mu\text{m}$  diameter) when the piezoelectric element squeezes fluid out of the glass nozzle. A high-voltage pulser, triggered by a function generator, drives the piezoelectric element with  $\sim 75\text{-}\mu\text{s}$ , 50-V pulses. The function generator is synchronized to the 10-Hz laser firing to ensure that a droplet is present during the 8-ns Nd:YAG laser pulse. A gravity-feed reservoir supplies the nozzle with liquid. The droplet generator can be a stable source of mono-sized droplets at frequencies from 10–500 Hz, but we had difficulty with its reliability. We used this droplet generator only for room temperature experiments because it did not perform adequately at high temperature.

The pressure atomizer is a Delavan, 45°, 0.5-gal/h nozzle. We operated this nozzle at three pressures (30 psi, 40 psi, and 50 psi) to produce different droplet size distributions and number densities. An Aerometrics phase Doppler particle analyzer measured the droplet size and number density. The Sauter mean diameter ( $D_{32}$ ) for the droplet size distributions using 30-, 40-, and 50-psi pressures were 65, 56, and 45  $\mu\text{m}$ , respectively. The pressure atomizer was used for room temperature CARS measurements only. We attempted to heat the surrounding air with a heat pipe from a propane/air burner, but unfortunately, the heat pipe did not provide sufficient quantities of high temperature air, and the spray cooled the air to nearly room temperature.

The capillary breakup droplet steam generator is similar to the commercially available Bergland-Liu droplet generator (TSI Incorporated). The generator forces a stream of fluid through a 50- $\mu\text{m}$  pinhole while oscillating the stream with a piezoelectric element. At the proper frequencies the oscillation causes the fluid stream to break up into mono-sized droplets  $\sim 80 \mu\text{m}$  in diameter. We used this droplet generator both at room temperature and in heated air. Unlike the spray, the single droplet stream did not affect the air temperature significantly. A propane/air burner provided the high temperature (800-K) gas via a heat pipe. We also translated the droplet stream along the laser beam axis to determine the effects of droplet position on laser induced breakdown.

### B. Experiment Summary

Each experiment consists of 400 single shot CARS measurements. For each shot the reduced data contains the following: (1) *temperature*, the temperature fit to the experimental CARS spectrum; (2) *peak*, the peak amplitude of the CARS signal; (3) *baseline*, the average of 10 baseline pixels representative of the background intensity seen by the spectrometer; and (4) *breakdown*, the intensity of the laser breakdown recorded by a PIN diode with a very wide field of view. The PIN diode collects the breakdown signal 90° from the laser beam axis. The baseline pixels collect the breakdown noise from on-axis. In this work, the signal to noise ratio (SNR) is defined  $\text{SNR} = (\text{peak} - \text{baseline})/\text{baseline}$ .

The results include CARS temperature measurements in the following droplet environments:

(a) single drops from the drop-on-demand generator in room temperature air at different locations along the CARS laser beam axis,

(b) single drops from the capillary breakup drop generator in heated air at different locations along the CARS laser beam axis, and

(c) a spray of fluid drops from a pressure atomizer in room temperature air centered above the CARS focus; different atomizing pressure and different heights above the focus provide different droplet size and number density conditions.

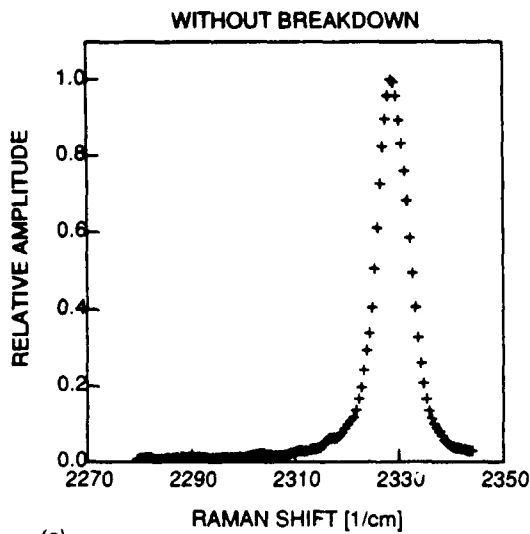
## III. Results and Discussion

### A. Effect of Droplet Breakdown on the CARS Signal

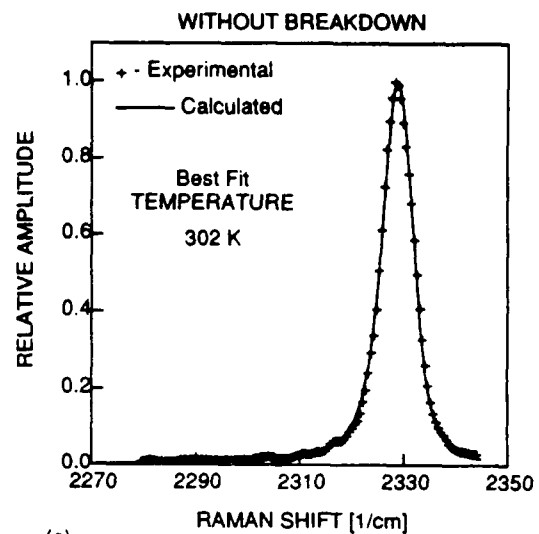
Several recent articles detail the physical processes of LIB of liquid droplets (Chang *et al.*,<sup>13</sup> Zhang *et al.*,<sup>14</sup> Hsieh *et al.*,<sup>15</sup> Chýlek *et al.*,<sup>16</sup> Zheng *et al.*,<sup>17</sup>). LIB in water droplets does not result from absorption, but rather the droplet acts as a lens, focusing the incident radiation just outside the shadow face of the droplet and inside the droplet, just within the shadow face. At high laser energy, breakdown first occurs in the gas outside the droplet, soon followed by breakdown within the droplet. The breakdown inside the droplet forms a highly absorbing plasma that absorbs incoming radiation. The absorption sustains a detonation wave that ejects plasma from the droplet at  $\sim 10 \text{ km/s}$ . The plasma forms in the first few nanoseconds of the laser pulse.

Figure 2 demonstrates the effect of droplet breakdown on CARS measurements by comparing a room temperature CARS spectrum without droplet breakdown to a CARS spectrum with droplet breakdown. The breakdown reduces the peak amplitude of the CARS signal, and increases the baseline amplitude. This combination substantially degrades the SNR of the measurement, making temperature fitting difficult. Figure 3 shows the temperature fits for the two spectra of Fig. 2. Without breakdown, the CARS fit is accurate, and produces a temperature close to room temperature. With breakdown, however, the CARS fitting routine tries to accommodate the lifted baseline and reduced peak by adding a hot band to the calculated spectrum. Adding a hot band produces a very high, incorrect temperature.

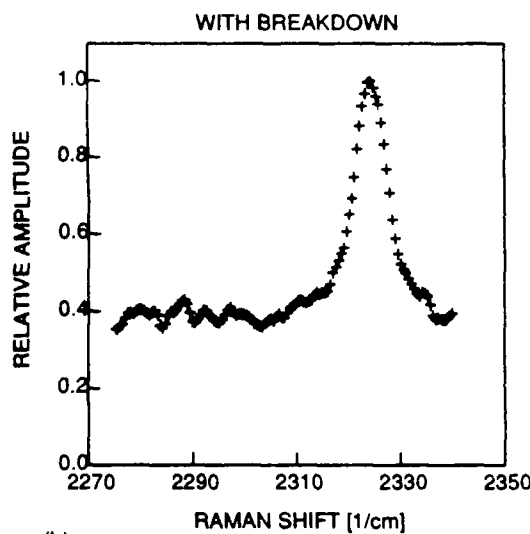
Figure 4 shows the average CARS temperature as a function of signal to noise ratio. Three cases are shown in the figure: single drops in heated air, with the drops falling through the focus of the CARS interaction volume; single drops in room temperature air, with the drops falling through the focus of the CARS interaction volume; and a spray in room temperature air, with the spray centered above the CARS interaction volume. The drop-free temperature range is centered about the average CARS temperature with no droplets present. The range includes  $\pm 1$  standard deviation of the drop-free temperatures. All of the curves show an incorrectly high temperature for low



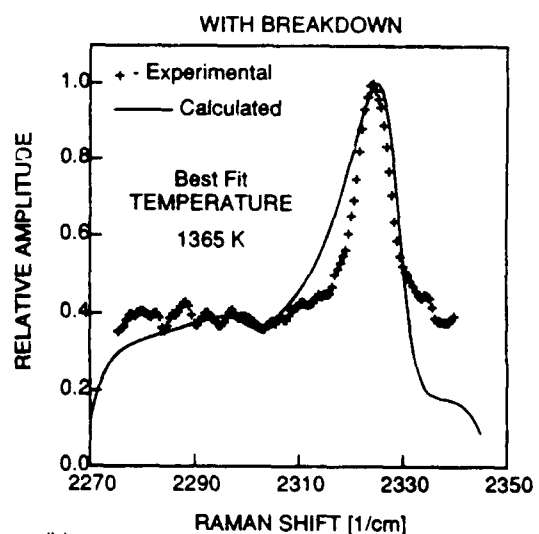
(a)



(a)



(b)



(b)

Fig. 2. Comparison between a CARS signal without droplet breakdown (a) and a CARS signal with droplet breakdown (b).

Fig. 3. Temperature fit to the experimental spectra of Fig. 2: (a) fit to CARS signal without droplet breakdown, (b) fit to CARS signal with droplet breakdown.

SNR, and an accurate temperature for high SNR. The cutoff between low and high SNR is  $\sim 20$ .

Figure 5 shows the average baseline level and the average breakdown intensity as a function of SNR for the three cases shown in Fig. 4. The baseline level decreases rapidly with increasing SNR, while the breakdown intensity decreases more slowly. The difference between the baseline and breakdown variation with SNR results from droplet position variations. Droplets at the edge of the CARS sample volume may produce a relatively intense breakdown, but the collection optics spatially discriminate against plasma discharge from the fringe of the sample volume. This discrimination is particularly apparent in the spray case, where the spark intensity is nearly independent of SNR. In the spray, droplets far from the CARS collection volume cause dielectric breakdown, but be-

cause they are out of the collection optics view, the breakdown does not affect the CARS signal significantly. We discuss droplet position in a later section.

#### B. Effect of Droplet Breakdown on CARS Temperature Measurements

The results of the preceding section indicate that reliable average temperature measurements can be obtained by utilizing only CARS spectra with a high SNR. Unfortunately, however, even with a high ( $>30$ ) SNR, the RMS temperature with droplets present is larger than the droplet-free RMS temperature. To improve our measurements of RMS temperature, we eliminate the influence of dielectric breakdown noise before we attempt a temperature fit. If the baseline lift is caused by plasma enhanced nonresonant back-

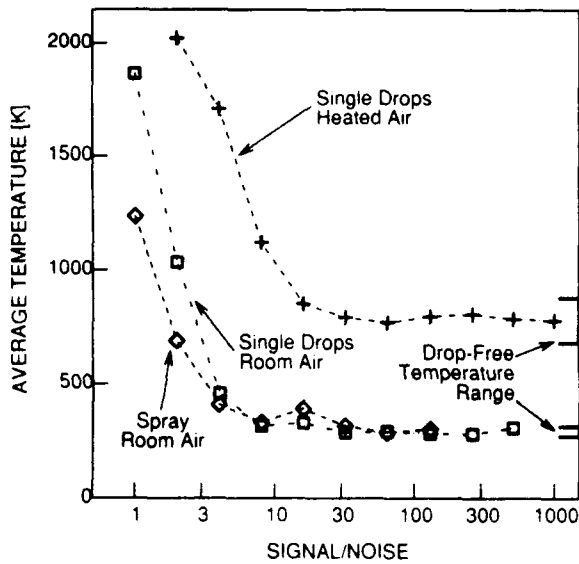
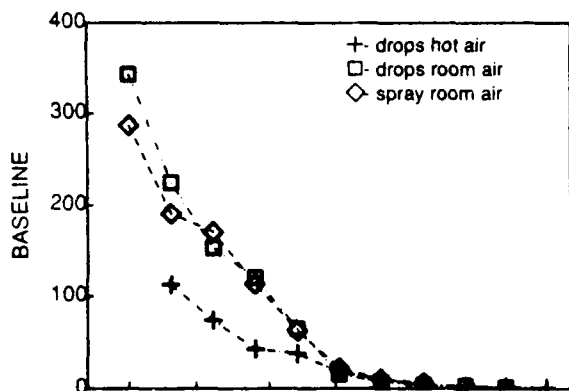
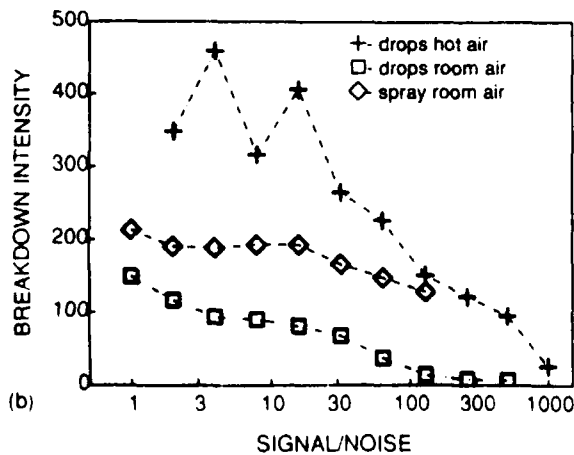


Fig. 4. Average CARS temperature as a function of SNR for single drops in heated air, single drops in room temperature air, and a spray in room temperature air.



(a)



(b)

Fig. 5. Average baseline intensity (a) and average breakdown intensity (b) as a function of SNR.

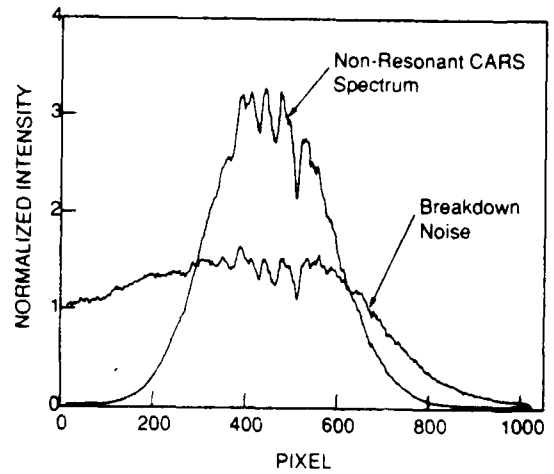


Fig. 6. Comparison between a normalized non-resonant reference spectrum and a normalized breakdown noise spectrum. The spectra are normalized to unit area.

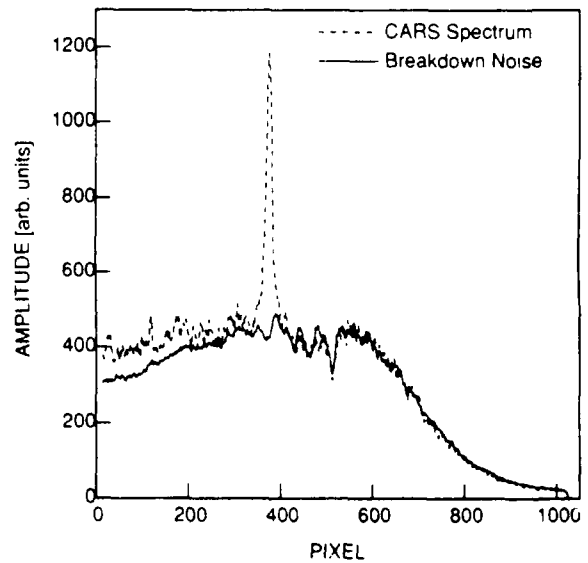
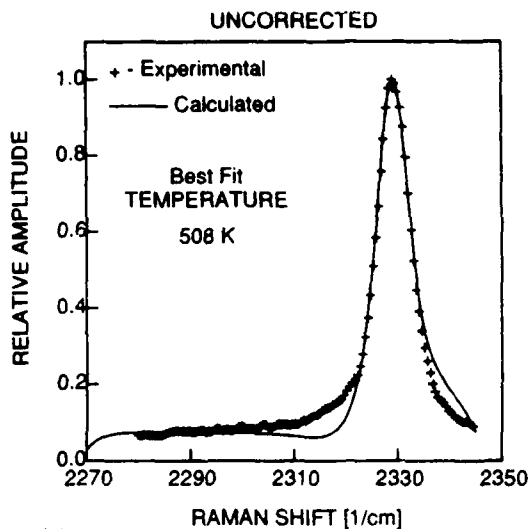


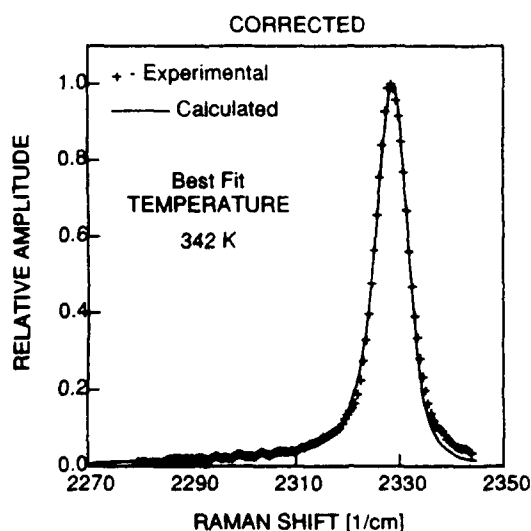
Fig. 7. Comparison between a CARS spectrum influenced by droplet breakdown and a breakdown noise spectrum with no CARS generation.

ground, as suggested by Beiting<sup>7</sup> we must subtract a normalized nonresonant background. If the baseline lift is caused by stray light from plasma recombination, then we must subtract a normalized breakdown noise spectrum.

Figure 6 compares a normalized nonresonant reference spectrum to a normalized breakdown noise spectrum. The spectra are normalized to unit area. The noise spectrum is taken with the dye laser beam blocked to prevent CARS generation. The nonresonant spectrum is spectrally narrower than the noise spectrum. Figure 7 shows that the breakdown noise spectrum matches very closely the baseline structure of a CARS spectrum influenced by droplet breakdown. For our experiments, therefore, the dominant source of



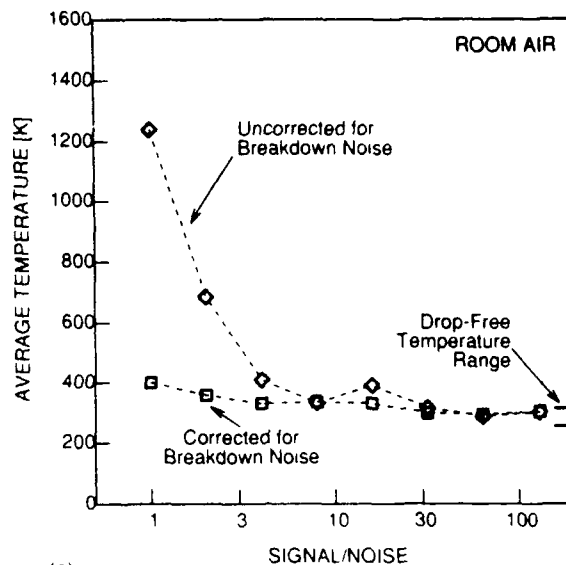
(a)



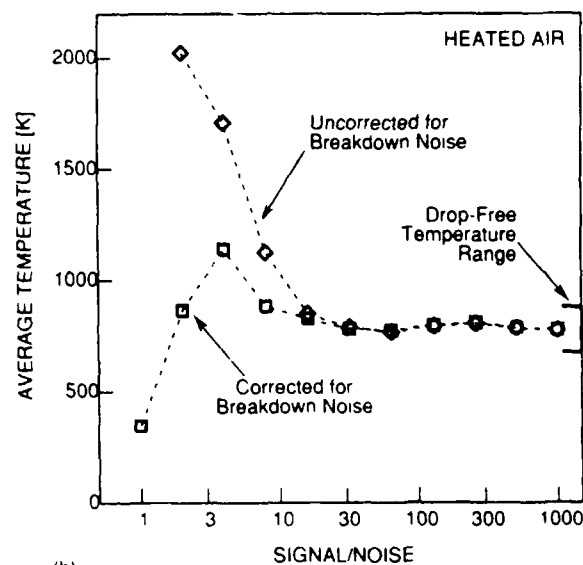
(b)

Fig. 8. Comparison between the CARS temperature fit to an uncorrected spectrum (a) and the CARS temperature fit to a corrected spectrum (b).

baseline lift comes from breakdown noise rather than from an enhanced nonresonant CARS contribution. This dominance may depend on droplet composition and on the gas environment. For example, hydrocarbons have large nonresonant susceptibilities (Farrow *et al.*,<sup>18</sup>) which may increase the nonresonant contribution, and as noted earlier, Beiting<sup>7</sup> found a dominant nonresonant contribution when breakdown was caused by irradiation of solid flyash particles. It is also possible that our droplet breakdown occurs later in the laser pulse than does the breakdown in flyash (Beiting<sup>7</sup>) and coal (Lucht<sup>6</sup>). With a late breakdown, most of the CARS signal is generated before a nonresonant signal from the plasma occurs. Because our intensifier gate is quite wide (1  $\mu$ s), light from the plasma



(a)



(b)

Fig. 9. Average temperature as a function of SNR for spectra uncorrected and corrected for droplet breakdown noise: (a) measurements in a room temperature spray, (b) measurements with single drops in heated air.

recombination can be added to the signal after the laser pulse ends.

Based on the results shown in Fig. 7, we correct our experimental spectra for breakdown noise by subtracting a normalized breakdown spectrum from the raw data before we attempt a temperature fit. Beiting<sup>19</sup> used a similar method to analyze CARS signals contaminated by coherent interference. The normalization factor is  $(S_{p10} - S_b)/(B_{p10} - B_b)$ .  $S$  is the measured CARS signal and  $B$  is an average breakdown spectrum. The subscript  $p10$  refers to an average of 10 pixels and subscript  $b$  refers to the absolute baseline of the DARSS detector. Initially, we chose to average the first 10 pixels of the DARSS, however, these pixels did not accurately monitor the level of the breakdown

noise. In Fig. 7, for example, the largest deviation between the signal baseline and the average breakdown spectrum occurs in the first few pixels. Consequently, we determine  $S_{p10}$  from an average of 10 pixels located near the second hot band of the nitrogen CARS spectrum. At high temperatures, the second hot band contributes to the CARS signal, requiring a modified choice of pixels to average. Figure 8 compares the temperature fit between an uncorrected and a corrected room temperature CARS spectrum. While the corrected room temperature is a little high, it is within the temperature uncertainty typical of low temperature CARS measurements.

Figure 9 compares the variation of temperature with SNR for corrected and uncorrected spectra. The figure shows results from measurements in a room temperature spray [Fig. 9(a)] and from measurements with single drops in heated air [Fig. 9(b)]. In Fig. 9(a), the correction procedure greatly improves the average temperature for spectra with SNR between 1 and 10. For SNR > 10, however, the signal is relatively good already, and the correction procedure adds little improvement. For the heated air case, Fig. 9(b), the correction procedure improves the average temperature for SNR between 3 and 10, but the improvement is

not as substantial as in the room temperature case. As in Fig. 9(a), there is little difference between the corrected and uncorrected results for SNR > 10.

The results of Fig. 9 indicate that spectral correction and conditional measurements based on SNR can produce reliable mean temperatures from CARS signals affected by droplet breakdown. However, the figure also indicates that droplet breakdown results in slightly higher mean temperatures than are measured in drop-free environments. For example, corrected spectra from room temperature spray measurements with SNR > 10 produce a mean temperature ~30 K (10%) higher than occurs in the drop-free temperature measurement. Similarly, corrected spectra from heated air with single drops with SNR > 10 produce a mean temperature ~25 K (3%) higher than occurs in the drop-free temperature measurement.

Figures 10 and 11 present temperature distributions for CARS measurements in a room temperature spray (Fig. 10) and with single drops in heated air (Fig. 11). The bottom distribution in each column is the temperature distribution without droplets present. The remaining histograms compare corrected and uncorrected temperature distributions for three SNR. For SNR > 5, the temperature distribution for uncorrected

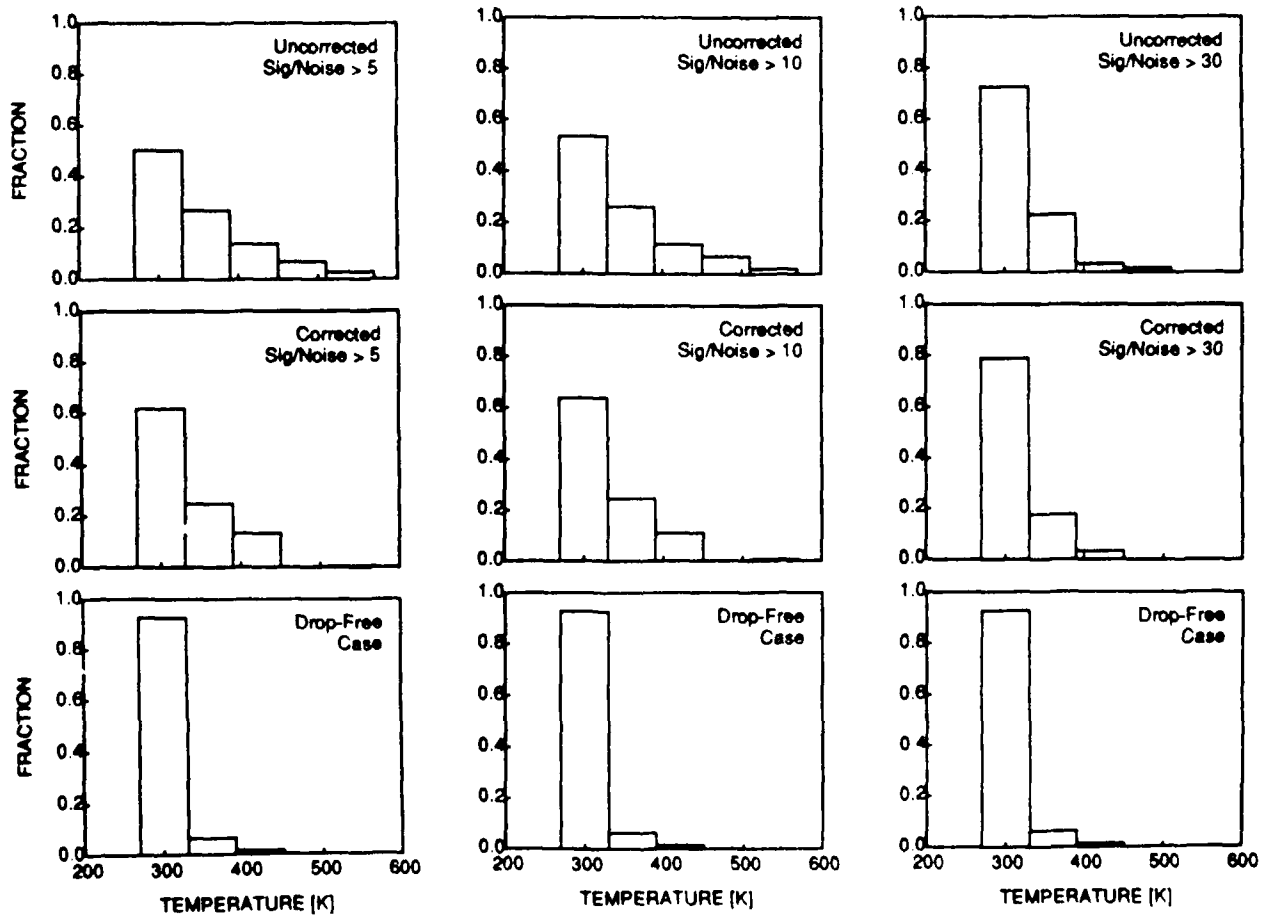


Fig. 10. Temperature distributions for CARS measurements in a room temperature spray. The bottom histogram in each column is the temperature distribution without droplets present. Distributions of uncorrected and corrected temperatures for three SNRs are shown.

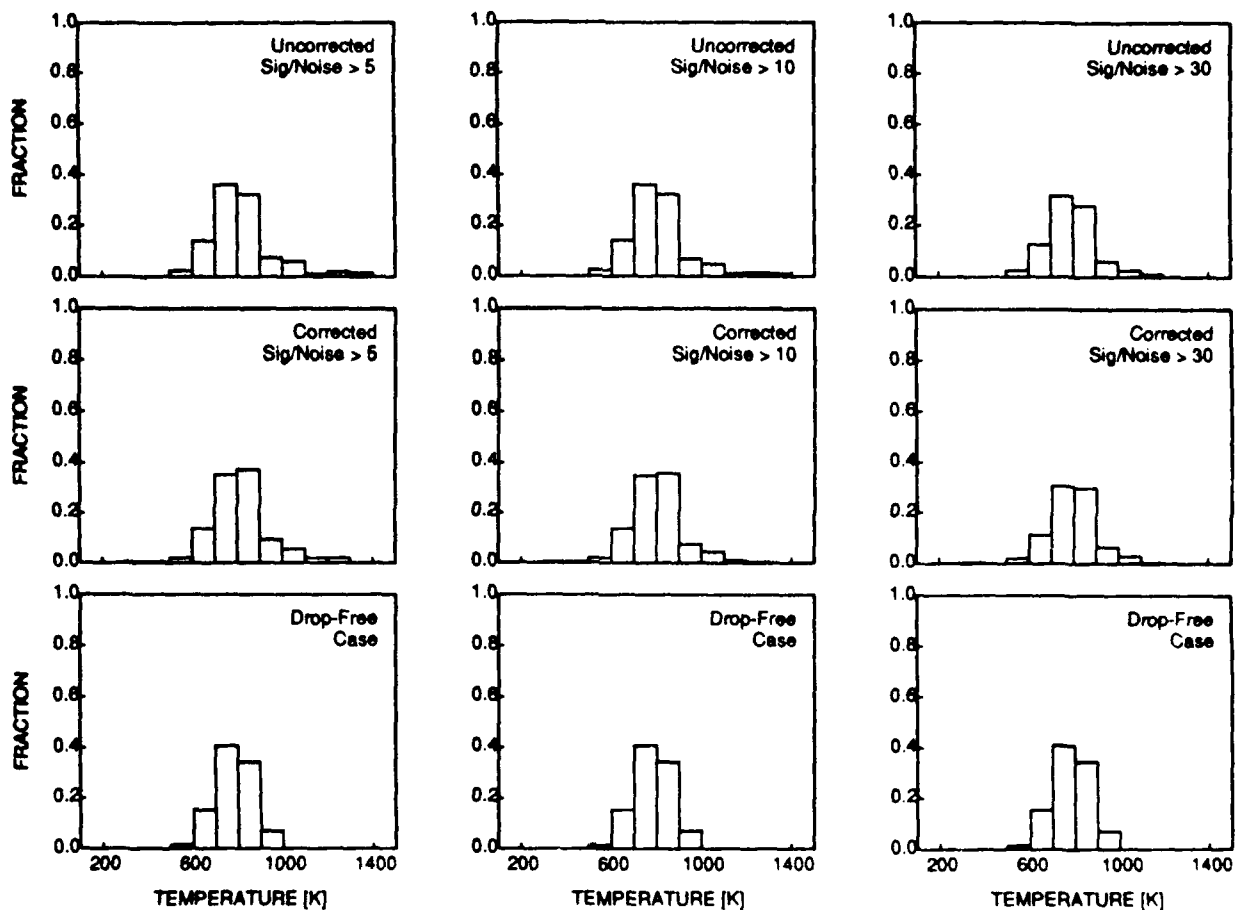


Fig. 11. Temperature distributions for CARS measurements with single drops in heated air. The bottom histogram in each column is the temperature distribution without droplets present. Distributions of uncorrected and corrected temperatures for three SNRs are shown.

spectra is much broader than the distribution for drop-free measurements. The temperature distribution from corrected spectra is narrower than the uncorrected distribution but still does not reproduce the drop-free distribution. Increasing the SNR condition improves the temperature distribution, however even for  $SNR > 30$ , the corrected temperature distribution does not reproduce the drop-free temperature distribution. The results from single drops in heated air (Fig. 11) demonstrate the same behavior as the distributions of Fig. 10. In heated air, however, there is little difference between distributions from corrected and uncorrected spectra.

Figures 10 and 11 show that CARS measurements in droplet laden flows produce a broader temperature distribution than measurements made in drop-free environments. The broadening is on the high temperature side of the distribution, and occurs because CARS spectra influenced by breakdown can be interpreted as high temperature spectra. The broadening is most severe at room temperature where the CARS spectra have few features to fit. Temperature measurements of corrected spectra in a room temperature spray with  $SNR > 10$  have a standard deviation of 58 K compared to 29 K for measurements in drop-free room air. For

single drops in heated air, corrected spectra with  $SNR > 10$  produce a temperature standard deviation of 128 K compared with 100 K for drop-free heated air.

### C. Effect of Droplet Position on CARS measurements

Figure 12 shows the fraction of CARS measurements that result in a valid temperature as a function of axial droplet position relative to the CARS focus. For this figure, the fraction is the number of temperatures within  $\pm 1$  standard deviation of the drop-free temperature divided by the number of measurements containing a noticeable breakdown event. Both the room air experiments and the heated air experiments indicate that the valid fraction is relatively insensitive to axial droplet position when the droplet is near the CARS focus ( $\approx \pm 2$  mm). With droplets in the near-focus region, we obtain valid temperatures in 30–40% of the measurements. The droplets travel across the narrow dimension of the CARS sample volume. Valid measurements occur when droplets break down above and below the sample volume because the collection optics spatially discriminate between the CARS signal and the plasma discharge. A similar discrimination does not occur with droplets at the axial edges of the sample volume because the collection optics are nearly

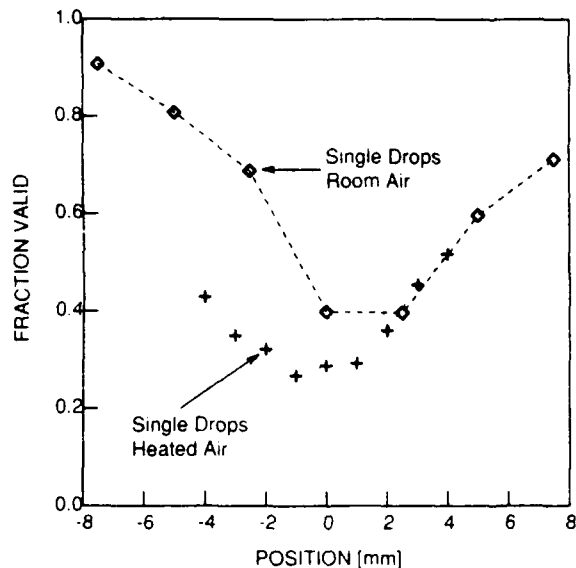


Fig. 12. Fraction of CARS measurements resulting in valid temperature measurements as a function of droplet position relative to the CARS focus. Valid measurements are within  $\pm 1$  standard deviation of drop-free temperature.

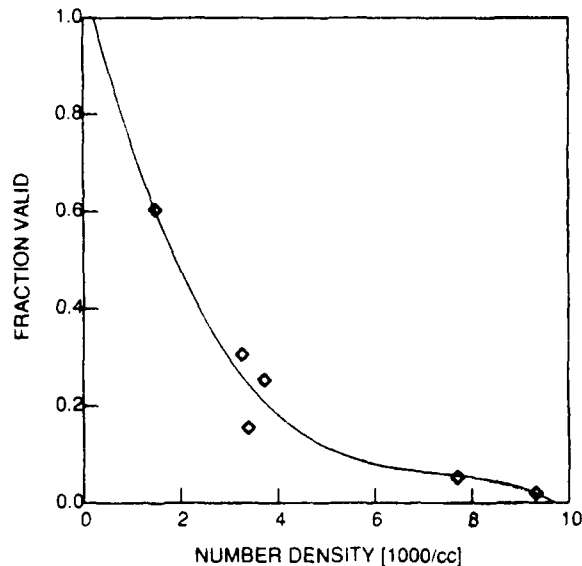


Fig. 13. Fraction of measurements in a room temperature spray that result in valid temperatures as a function of droplet number density. Valid temperatures are within  $\pm 1$  standard deviation of drop-free temperature measurements. The number density is measured with a phase-doppler particle analyzer.

on-axis and therefore insensitive to axial position variations. Our results suggest that a droplet breakdown will disrupt the CARS measurement if it is near the beam axis and in the primary CARS interaction volume.

From the above information and Poisson statistics we can estimate the upper bound on particle number density that will result in 40% valid temperature measurements. The number of particles in the CARS sample volume can be described with a Poisson distribution. The mean of the Poisson distribution is the product of the particle number density  $N$  and the probe volume  $V_p$ . Our CARS system has  $V_p \approx 0.4 \text{ mm}^3$  based on the interaction volume dimensions measured with a nitrogen jet. For  $N = 2500$  particles/cc, a particle will be present in the sample volume in 60% of the measurements. From this calculation, we expect that 2500 particles/cc is the number density limit for 40% valid temperature measurements. Figure 13 shows valid fraction as a function of particle number density from our CARS temperature measurements in a water spray. The solid line is a least squares cubic fit to the data. The experiments suggest 2500 particles/cc as the number density producing 40% valid measurements, in agreement with our estimate.

#### D. Minimizing the Effect of Droplet Breakdown on CARS Measurements

Our results suggest the following methods to minimize the effect of breakdown on CARS temperature measurements:

(1) Reduce laser power: reducing laser power decreases the size of the region with sufficient energy to generate breakdown. Unfortunately reducing laser

power also reduces the CARS signal. It is possible to compensate for the decrease in laser power with an increased interaction volume at the expense of degraded spatial resolution.

(2) Minimize optics field of view: restricting the optics field of view ensures that breakdown events outside the CARS interaction volume will not affect the CARS signal.

(3) Reduce detector gate time: the entire CARS signal is collected in less than 10 ns, while the plasma recombination occurs on the microsecond time scale. Gating the detector in a narrow time window around the CARS laser pulse will reduce the breakdown noise. Reducing the detector gate time will not reduce the nonresonant contribution to the noise. The detector gate time can be difficult to reduce in practice as it is often limited by detector hardware and shot-to-shot jitter.

(4) Software corrections and conditional sampling: CARS spectra that have been affected by breakdown noise can be improved by subtracting a normalized background characteristic of the breakdown. In addition, conditionally sampling the measurements to include only spectra with a high SNR allows accurate temperature measurements in droplet laden flows.

#### IV. Conclusions

Our experiments suggest the following conclusions:

Droplets that breakdown near the center of the CARS interaction volume influence the CARS signal by decreasing the peak signal intensity, and by raising the background intensity. There is little evidence of noise due to the plasma enhanced nonresonant CARS

signal that has been observed in similar experiments using solid particles rather than droplets to produce LIB.

LIB leads to inaccurate temperatures because the CARS fitting routine tries to fit the elevated background by enhancing the first nitrogen hot band. Subtracting a background spectrum characteristic of LIB improves the temperature fit. The improvement is more pronounced for low temperature spectra than for high temperature spectra.

Background subtracted CARS spectra with a high SNR provide reasonably accurate mean and RMS temperatures in droplet laden flows.

Droplets that generate breakdown plasma far from the CARS interaction volume do not influence the CARS measurement. Spatial filtering by the collection optics discriminates fairly well between the CARS signal and the plasma discharge.

Results from CARS measurements in sprays are very similar to results from CARS measurements with single droplets in the sample volume. It is likely, therefore, that the LIB process is a single droplet event. Our CARS sample volume ( $\sim 1 \text{ mm}^3$ ) and 40% validation rate requires a particle number density less than 2500 particles/cc.

The authors appreciate the important insights provided by Larry Goss of Systems Research Laboratory. This research is sponsored by the Air Force Office of Scientific Research/AFSC, United States Air Force, under Contract F49620-87-R-0004.

#### References

1. W. M. Roquemore, *et al.*, "Development of Laser Diagnostics for Combustion Research," Invited paper of the Central States Section/The Combustion Institute Spring Meeting, NASA Lewis Research Center, May 5-6, 1986.
2. V. G. McDonell, C. P. Wood, and G. S. Samuelsen, "A Comparison of Spatially-Resolved Drop Size and Drop Velocity Measurements in an Isothermal Chamber and a Swirl-Stabilized Combustor," in *Proceedings Twenty-first Symposium (International) on Combustion* (The Combustion Institute, Pittsburgh, PA 1986), p. 685.
3. C. P. Mao, G. Wang, and N. A. Chigier, "An Experimental Study of Air-Assist Atomizer Spray Flames," in *Proceedings Twenty-first Symposium (International) on Combustion* (The Combustion Institute, Pittsburgh, PA 1987), p. 665.
4. A. C. Eckbreth, P. A. Bonczyk, and J. F. Verdieck, "Review of Laser Raman and Fluorescence Techniques for Practical Combustion Diagnostics," Environmental Protection Agency Report EPA-600/7-77-006 (1977).
5. A. C. Eckbreth and R. J. Hall, "CARS Thermometry in a Sooting Flame," *Combust. and Flame* **36**, 87-98 (1979).
6. L. P. Goss and D. D. Trump, "Simultaneous CARS and LDA Measurements in a Turbulent Flame," AIAA Paper AIAA-84-1458, 20th Joint Propulsion Conference, Cincinnati, Ohio, June 11-13 (1984).
7. E. J. Beiting, "Coherent Interference in Multiplex CARS Measurements: Nonresonant Susceptibility Enhancement due to Laser Breakdown," *Appl. Opt.* **24**, 3010-3017 (1985).
8. R. P. Lucht, "Coherent Anti-Stokes Raman Scattering Measurements in Coal-Particle-Laden Flames," Sandia National Laboratories Technical Report SAND88-8721 (1988).
9. M. Noda, A. Gierulski, and G. Marowsky, (1987) "CARS-Studies of Coal and Coal-Water-Mixture Combustion," Paper 7C-109, Joint Meeting of the Western States and Japanese Sections/The Combustion Institute, Honolulu, Hawaii, November 22-25, 1987.
10. G. L. Switzer, T. A. Jackson, C. A. Obringer, and J. S. Stutrud, "An Integrated Spectroscopic-Interferometric Instrument for Spray Combustion Diagnostics," Western States Section/The Combustion Institute Fall Meeting, Sandia National Laboratories, Livermore, CA, October 23-24, 1989.
11. D. J. Taylor, "CARS Concentration and Temperature Measurements in Coal Gasifiers," Los Alamos National Laboratory Report LA-UR-83-1840 (1983).
12. G. L. Switzer and L. P. Goss, (1982) "A Hardened CARS System for Temperature and Species Concentration Measurements in Practical Combustion Environments," *Temperature: Its Measurement and Control in Science and Industry—Vol. 5*, J. F. Schooley, Ed. (Publ. City, 1982) p 583.
13. R. K. Chang, J. H. Eickmans, W.-F. Hsieh, C. F. Wood, J.-Z. Zhang, and J.-B. Zheng, "Laser Induced Breakdown in Large Transparent Water Droplets," *Appl. Opt.* **27**, 2377-2385 (1988).
14. J.-Z. Zhang, J. K. Lam, C. F. Wood, B.-T. Chu, and R. K. Chang, "Explosive Vaporization of a Large Transparent Droplet Irradiated by a High Intensity Laser," *Appl. Opt.* **26**, 4731-4737 (1987).
15. W.-F. Hsieh, J.-B. Zheng, C. F. Wood, B. T. Chu, and R. K. Chang, "Propagation Velocity of Laser-Induced Plasma Inside and Outside a Transparent Droplet," *Opt. Lett.* **12**, 576-578 (1987).
16. P. Chýlek, M. A. Jarzembki, V. Srivastava, R. G. Pinnick, J. D. Pendleton, and J. P. Cruncheon, "Effect of Spherical Particles on Laser Induced Breakdown of Gases," *Appl. Opt.* **26**, 760-762 (1987).
17. J.-B. Zheng, W.-F. Hsieh, S.-C. Chen, and R. K. Chang, "Temporally and Spatially Resolved Spectroscopy of Laser Induced Plasma from a Droplet," *Opt. Lett.* **13**, 559-561 (1988).
18. R. L. Farrow, R. P. Lucht, and L. A. Rahn, "Measurements of the Nonresonant Third-Order Susceptibilities of Gases using Coherent Anti-Stokes Raman Spectroscopy," *J. Opt. Soc. Am. B* **4**, 1241-1246 (1987).
19. E. J. Beiting, "Multiplex CARS Temperature Measurements in a Coal-Fired MHD Environment," *Appl. Opt.* **25**, 1684-1692 (1986).

Application of Laser-Sheet-Lighting Techniques to  
Multiple-Point Velocity Measurements in Mixing Flows

Gary L. Switzer, Larry P. Goss, Darryl D. Trump, and Benjamin Farka

Systems Research Laboratories, Inc.  
2800 Indian Ripple Road, Dayton, OH 45440-3696

Abstract

The techniques of particle-streak and pulsed-laser velocimetry were investigated to determine their applicability in obtaining two-dimensional velocity information. As a result of these investigations, a third technique--scanned-laser velocimetry--was developed. In each method particles are seeded into combusting and noncombusting flows and their movement within a sheet of laser light photographically recorded. Analysis of the particle tracks provides velocity as well as valuable flow-visualization information.

Introduction

Various techniques have been proposed for obtaining two-dimensional velocity measurements in flowing-gas systems. Among these, particle-streak velocimetry,<sup>1</sup> pulsed-laser velocimetry,<sup>2</sup> speckle velocimetry,<sup>3</sup> and laser-induced fluorescence<sup>4</sup> share certain limitations, which can affect their usefulness, i.e., requirements for seeding with particles or fluorescent gases, directional ambiguity, and/or large post-processing of data. After consideration of the merits of these techniques, the first two--with proper improvements--were deemed the most viable approaches for obtaining two-dimensional velocity information. Described herein are applications of these techniques in which a plane of laser light is used to obtain flow velocities in two dimensions simultaneously. These schemes employ photographic detection of Mie scattering from small (0.1 - 5  $\mu\text{m}$ ) particles or droplets seeded into cold flowing and combusting gases. The area within the flow field to be studied is determined by the size, shape, and orientation of the laser sheet. Local velocities are determined from individual particle images, while the group velocity of large-scale mixing structures can be determined by recording the evolution of the flow field.

The two-dimensional velocity techniques described include modulated particle-streak velocimetry, pulsed-laser velocimetry, and scanned-laser velocimetry. In each of these techniques, the laser-light sheet used for illumination is produced in a different manner. In modulated particle-streak velocimetry, a 5-W argon-ion laser is used to form a light sheet which is modulated by a Bragg cell so as to encode the streak produced by a particle as it travels within the light sheet. This encoding allows the time and directional ambiguities associated with streak velocimetry to be removed. The second technique is an offshoot of pulsed-particle imaging which has been successfully demonstrated.<sup>4,5</sup> The difference in the approach employed in the present investigation involves the use of a 6-kHz, 40-W copper-vapor laser to form the light sheet, which allows for recording of multiple pulses of the particle as it traverses the flow field; this is in contrast to the traditional double-pulse-ruby or -Nd:YAG laser approaches. The third technique is based upon an attempt to combine the encoding capability of the cw argon-ion laser with the high-energy density of pulsed-laser devices. This scanning-laser technique employs a rotating-mirror scanner to sweep a focused cw argon-ion beam at a high rate to form an effective light sheet.

Theory

The velocity-measurement schemes employed in these experiments utilized photographic film as the detection medium. Therefore, an understanding of the relationships between particle detectivity and experimental parameters such as f-number (f#), laser-energy density, and particle size is beneficial.

For particle imaging the exposure resulting from a particle in a laser-light sheet of energy  $W$  and area  $\Delta y \Delta z$  is given by<sup>5</sup>

$$\bar{e} = \frac{4}{\pi k^2 d_e^2} \frac{W}{\Delta y \Delta z} \int_0^{\Omega} \sigma^2 d\Omega \quad (1)$$

where  $k = 2\pi/\lambda$ ,  $\Omega$  is the collection angle of the lens system,  $\sigma$  the Mie-scattering cross

section of the particle, and  $d_e$  the nominal image diameter given by

$$d_e = (m^2 d_p^2 + d_s^2)^{1/2} \quad (2)$$

where

$$d_s = 2.44(m + 1)f\# \lambda \quad (3)$$

with  $m$  being the magnification of the image,  $f\#$  the ratio of the focal length to the lens diameter, and  $\lambda$  the wavelength of the laser source. The diffraction-limited burr image of the lens is given by  $d_s$ . For the small seed particles used during these experiments, the particle image recorded on film is actually the burr image and, thus, represents a lower limit to the image size--which will be important in determining the resolution of the velocity measurement.

Adrian, et al.,<sup>5</sup> calculated the Mie-scattering contribution to Eq. (1) and generated the family of curves for normalized exposure,  $f\#$ , and particle size shown in Fig. 1. Normalizing the exposure to the light-sheet energy density allows comparison to experimental conditions other than those reported in Ref. 5. The minimum exposure level of the film is given by the inverse of the ASA speed rating in ergs/cm<sup>2</sup>. For a 1000-ASA film, the minimum exposure corresponds to 1  $\mu$ J/m. In order to compare this value to the family of curves in Fig. 1, the exposure must be normalized to the energy density of the laser light sheet. In the case of the copper-vapor laser, the normalized value is  $3.125 \times 10^{-7}$  for an 8-mJ pulse in a 25-cm<sup>2</sup> sheet. A good-quality image is considered to be a density of one or a factor of ten times the gross fog level ( $3.125 \times 10^{-6}$ ). Plotting this value on the family of curves in Fig. 1 indicates the lower range of particle sizes which can be detected for a given camera  $f\#$ . The smallest particle for a density of one with an  $f\#$  of 5.6 is  $\sim 1 \mu$ m; for an  $f\#$  of 2.8, it is  $\sim 0.3 \mu$ m. If one, in fact, relaxes the detection criterion from ten to two, which will result in an adequate image in most cases, the lower limit for particle sizes becomes  $\sim 0.2$  ( $f\#$  2.8) and  $\sim 0.5 \mu$ m ( $f\#$  5.6).

For the streak-velocity case in which the argon-ion laser is used as the laser source, the minimum exposure level is considerably higher. The reason for this is two-fold: first, the energy density of the argon laser is much lower than that of the copper-vapor laser (6 W vs. 40 W average power); secondly, and more importantly, the particle typically is not motionless during the camera exposure but, in fact, moves which produces a streak. As a result the amount of scattered light imaged onto a given area of film will be small for a fast-moving particle. In the pulsed-laser case, the total energy is deposited during a 30-ns pulse and the particle does not have time to move during the laser pulse. This greatly increases the intensity of the scattered image for a given area of film. In the argon-ion case, a particle moving with a velocity of 1 m/s, exposed to a 6-W argon sheet of 25 cm<sup>2</sup>, will require 21  $\mu$ s to travel 21  $\mu$ m (three times the burr-image size), resulting in a minimum exposure requirement of  $1.98 \times 10^{-5}$ --approximately 666 times the fog exposure level required for the copper-vapor laser. Plotting this value along with the density-of-one value required for high-quality images indicates that only the smallest  $f\#$  lens will allow the detection of particles below 4  $\mu$ m. In the case of higher-velocity flows, the detectivity of the smaller particles will drop accordingly. Since the power of the argon-ion laser is already at a maximum, only a lower- $f\#$  lens and/or a faster, more-sensitive film will allow detection of the very small particles in the flow.

Because of the low energy in a cw laser sheet, the scanned-laser technique was conceived. In this approach the laser sheet is produced by scanning the laser beam with a high-speed rotating mirror. The effective increase in the energy density of the sheet formed in this manner corresponds to the ratio of the beam diameter to the height of the light sheet. In the non-scanning case the laser beam is expanded to a 5-cm height. In the scanning case the beam diameter is  $\sim 200 \mu$ m. The increase in energy density of the sheet is, thus, on the order of 250. This corresponds to a nondimensional mean exposure of  $\sim 8 \times 10^{-8}$ . This level is approximately four times lower than that of the copper-vapor laser, allowing submicron-size particles to be detected.

Determination of the precision of the streak or pulsed-velocity method requires determination of the smallest displacement which can accurately be measured by the film (resolving power of the film). In order to understand the resolving capability of the film, one must examine the modulated transfer function (MTF). The MTF is a measure of the ability of the film to resolve accurately line pairs separated by a given distance. The function is defined by

$$MTF = \frac{I_{\max} - I_{\min}}{I_{\max} + I_{\min}} \quad (4)$$

where  $I_{max}$  is the intensity maximum of adjacent line pairs (or particle images) and  $I_{min}$  is the minimum intensity between the line pairs. As the line pairs/mm of the input image increases, a point is reached where the lines are no longer distinct and overlapping (cross-talk) occurs. For example, the film used for some of these experiments, Royal X-Pan,<sup>6</sup> exhibits a lower MTF value of 30%, which corresponds to a resolution of 70 line pairs/mm. This corresponds to a minimum spatial-resolving capability of 14.3  $\mu\text{m}$  between particle images. Thus, with a temporal pulse separation of 167  $\mu\text{s}$  for the 6-kHz copper-vapor laser, a velocity-resolution limit of 0.09 m/s is reached. The ability to realize this limit in practice will depend upon the experimental conditions and post-processing procedures.

The resolution limit of the scanned-laser and the pulsed-laser techniques is determined in a similar manner in that the film records distinct images whose minimal spatial and temporal resolution determines the lower velocity resolution limit. The particle-image separation, however, can be controlled by changing the scan rate of the spinning-mirror, unlike the copper-vapor-laser case where the repetition rate is fixed. By decreasing the scanning rate, the time interval between particle images and, thus, the velocity resolution can be increased.

In particle-streak-velocity experiments, the length of the encode pattern in conjunction with the burr-image size determines the limiting velocity ranges. Here the attempt is to measure the length of the particle streak. The streak length is controlled by the velocity of the particle and the exposure time of the film which must be sufficiently long to identify at least one encode pattern. The resolution of the velocity measurement can thus be optimized for the velocity range expected in the flow to be studied. If one assumes, as in the case of the pulsed-laser velocity, that the limiting resolution of the film corresponds to an MTF of 30%, then the minimum length described by the encode unit period can be no shorter than 14  $\mu\text{m}$ . The minimum length for a complete encode is nine unit periods and, thus, 126  $\mu\text{m}$ . The maximum length of the encode can be no longer than the length of the film (120 mm). With the upper and lower limits in length defined, the maximum and minimum velocities can be computed as a function of the encode period. Thus, for an encode period of 2 ms, velocities ranging between 0.06 and 60 m/s may be captured on the same photograph. This dynamic range of 1000 in velocity-measurement capability is typical for a wide selection of encode periods.

### Experimental Results

#### Particle-Streak Velocimetry

To accomplish particle-streak velocimetry, the system depicted in Fig. 2 was assembled. The 5-W multimode output of a Spectra Physics Model 2020 argon-ion laser is formed into a sheet through the use of various combinations of cylindrical lenses. The sheet focuses to 1 mm in thickness through the sample volume, and its height is determined by the lens combination and spacing for the desired area/intensity of coverage. The entire sheet is switched on and off by means of an IntraAction Corporation Model AOM-355 Acousto-Optic Modulator. A seed particle traveling within the pulsating sheet appears as a series of streaks recorded by a camera which views normal to the sheet. The spatial and temporal length of the streak allows determination of the velocity of the particle and, subsequently, the velocity of the surrounding flow. Spatial distances are obtained by comparison to calibrated scales, and temporal characteristics are set by the modulator drive frequencies.

For this technique to be most useful in flow diagnostics, two problems must be overcome: 1) the uncertainty involving the residence time of a particle in the light sheet, and 2) the directional ambiguity of the streak. The former arises because the particle may have a velocity component which is perpendicular to the sheet and, therefore, could cross the sheet in less than one complete sheet "on" period. The latter arises because the absolute direction of the streak path cannot be determined from a regular pattern of streaks. Both of these problems can be corrected by implementing a sheet-encoding scheme similar to that reported by Marko and Rama<sup>7</sup> which modulates the light in a unique on/off pattern. As illustrated in Fig. 2, the encoding pattern chosen for these experiments consists of three successive light "on" periods in the ratio 1:2:4. The total length of time required to generate this encode pattern can be adjusted for the velocities of interest. Thus, if one complete encode pattern is recorded, the residence time of the particle in the sheet and the particle direction are precisely defined.

An example of the particle-streak velocimetry obtained with this system is shown in Fig. 3. The streaks of a 2-ms encoding period are recorded from alumina particles (1 - 5  $\mu\text{m}$  diam.) entrained in a propane diffusion flame produced from a 1-cm fuel tube having 0.5 SCFM propane flow. The streaks in this photograph demonstrate that flow velocities ranging from 3.3 to 3.8 m/s exist within the central portion of the flame.

## Pulsed-Laser Velocimetry

Pulsed-laser velocimetry involves the use of a high-repetition-rate pulsed laser which, rather than producing a streak on the film, records the particle position as a series of dots whose temporal spacing is well known. This technique was implemented with a Plasma Kinetics Model 451 Copper-Vapor Laser and sheet-forming cylindrical lenses. The laser produces 8-mJ pulses of  $\sim 30$ -ns duration and operates at a frequency of 6 kHz for a temporal resolution of 167  $\mu$ s. The problem of particle-direction ambiguity exists with this system also, and its solution requires an encoding scheme which rejects certain of the copper-vapor pulses. Although no problems are anticipated in implementing such an encoding scheme with this laser, no attempt was made to use this scheme for the present experiments.

One advantage of this technique is the increased energy per pulse which translates into a stronger scattering for more effective film recording. In addition, the high frequency of the copper-vapor-laser operation allows very high flow velocities to be observed. Figure 4 shows the tracks of alumina seed particles in a nonreacting air jet from a 1-cm nozzle. The particle velocities range from 8 to 45 m/s.

The high-velocity measurement capability of this technique allows the study of turbulent phenomena as well as transient one-of-a-kind events such as the ignition of a pyrotechnic material. Figures 5 and 6 show results obtained with two types of pyrotechnic materials which were illuminated during combustion with the copper-vapor-laser sheet. Successive frames are shown which were recorded by a 6000-frames/s cine camera synchronized to the laser firing. The ignition shown in Fig. 5 was characterized by a small visible flash. A ceramic cap which covered the material remained intact and can be tracked for many frames beyond its preignition position. The second type (Fig. 6) exhibited a very large flash during which the main combustion processes were taking place. The ignition causes the formation of very hot gases which flow away from the sample holder at  $\sim 300 - 500$  m/s. In the wake of the hot jet is a large vortex structure which evolves much more slowly and persists for several hundred milliseconds after ignition.

## Scanned-Laser Velocimetry

Experiments with the particle-streak and pulsed-laser velocity-measurement techniques made it clear that consideration should be given to features such as intensities, repetition rates, ease of encoding, and clarity and uniformity of the laser sheet produced. The system diagrammed in Fig. 7 was constructed so as to retain the most desirable features from both techniques, minimize their weaknesses, and combine the results into a single, simple optical system. As indicated in the figure, a Lincoln Laser Company Rotating Mirror Scanner (RMS) is employed to sweep the 5-W multimode output of a Spectra Physics Model 2020 Argon-Ion Laser across a large-diameter concave mirror (M). The reflected sweep pattern consists of parallel ray paths, with the focus of each ray being determined by the focal length and placement of a focusing lens (L).

Formation of a scanned sheet of laser light in the manner described above has several advantages for use in illumination of seed particles. The parallel light rays in the scanned pattern produce a well-defined sheet having uniform intensity distribution. A very thin sheet (200  $\mu$ m) is obtained due to the tight focusing which is made possible by the Gaussian intensity profile of the argon-ion laser beam in addition to the curved reflecting mirror. By concentrating the maximum output of the laser source into each scanning element of the sheet, the intensity of the laser energy available for scattering from seed particles is increased by several orders of magnitude over that of conventional light sheets formed by means of cylindrical lenses. The scanner mirror consists of ten individual facets which, when rotated by its synchronous drive motor, can provide scan rates from 300 to 5000 Hz and, thus, allow velocities between 0.1 and several hundred meters per second to be measured. The scanner can provide two functions if certain facets are partially masked. First, if the laser energy is reflected from the unmasked portion, the normal 10 scan lines per scanner revolution can be produced. Secondly, if reflection from the portion masked as shown in Fig. 7 is selected, a uniquely ordered scan pattern can be encoded. This encoded scan consists of a reflecting facet followed by a nonreflecting (masked) facet, two reflecting facets, a masked facet, three reflecting facets, and two masked facets. The resulting one-two-three encode pattern provides unambiguous determination of particle direction and residence time within the sheet for velocity determination.

Examples of the capabilities of this sheet-lighting system are shown in Figs. 8 - 11. In Fig. 8 dry air containing  $\text{TiCl}_4$  is flowing above a splitter plate in a Plexiglas channel of rectangular cross section. The air flow above the plate is 1.0 m/s and is acoustically driven at 73 Hz. Moist air is flowing below the splitter plate at 0.5 m/s. As the two flows interact,  $\text{TiO}_2$  particles are formed, and the dynamics of the resulting flow field are well defined by the exposure to a single scan of the laser light sheet. A useful extension of this visualization can be seen in Fig. 9 where the scan rate of the laser light through the

flow has been increased to allow two scans of the flow field at an interval of 11 ms. Such a multiple-scan technique can provide considerable information concerning the velocity, transport characteristics, and evolution of large-scale structures.

The capability of the encoded scan pattern in resolving flow direction is demonstrated in Fig. 10. The flow field in this figure is created by a bluff body (4.5-cm diam.) surrounded by a flowing annulus (20-cm diam.) of air. Phenolic microballoons (15 - 50  $\mu\text{m}$  diam.) were introduced into the annulus flow and their entrainment with the combusting propane fuel jet (4.7-mm diam) recorded over one-half of the bluff-body face. The flow of the counter-clockwise inward-spiraling particles on the right in the figure is easily distinguished from the clockwise flowing track visible in the lower left of the figure near the central fuel jet. These particle tracks also serve to demonstrate the capability of the particle-streak technique to determine two velocity components as well as facilitate two-dimensional velocity mapping.

In a more streamlined flow such as that of Fig. 11, where the direction of flow is known a priori, nonencoded scanning can be employed for velocity determination. This photograph shows traces of phenolic microballoons in air flowing through a 1-cm-diam. jet. A sheet scan rate of 400 Hz was used to illuminate the particles. The tracks represent flow velocities of 0.58 m/s near the exit of the nozzle which decrease to 0.47 m/s at a height of 3.4 cm in the jet.

The ability of the rotating-mirror scanner system to obtain accurate velocity information was validated by comparison to a more-standard technique--Laser Doppler Velocimetry (LDV). This comparison was performed in a 1.5-cm-diam. air jet which was seeded with mineral-oil droplets with a measured Sauter mean diameter of 4.4  $\mu\text{m}$ . A 5000-scan-lines/s encoded scan pattern is imposed upon the droplets shown in Fig. 12. An Aerometrics, Inc. two-component phase/Doppler particle analyzer<sup>5</sup> was employed to perform velocity and droplet-size profiles within the spray. At the several locations compared, the average velocity obtained from the two techniques was found to agree to within  $\sim 8\%$  over centerline values ranging from 6.7 m/s at 1 cm to 5.3 m/s at 12-cm heights.

#### Conclusion

The techniques investigated have proven to be very attractive for two-dimensional velocity measurements in complex flows. The particle-streak-velocimetry scheme employing an argon-ion laser sheet displays the highest degree of flexibility in measuring velocity, but the associated relatively low particle visibility is a drawback. Pulsed-laser velocimetry, to the contrary, greatly enhances particle visibility, allowing smaller particles to be tracked. However, schemes to encode the lighting sheet are more complex and less flexible with the copper-vapor laser. A simple but efficient method of incorporating the most desirable aspects of both of these techniques has been demonstrated in a rotating-mirror scanner system. It is estimated that flow velocities between 0.1 and 250 m/s can be measured conveniently with the proper application of these methods. The capability of these velocity-measurement schemes in obtaining quantitative data in the more difficult environment of very low flow or high temperature appears to be limited only by the ability to produce and maintain the proper seed densities in the regions of interest.

#### Acknowledgments

This work was supported under Contract F33615-85-C-2562 with the Air Force Wright Aeronautical Laboratories/Aero Propulsion Laboratory at Wright-Patterson Air Force Base, Ohio. The authors gratefully acknowledge the editorial and technical assistance of Mrs. Marian M. Whitaker in the preparation of this manuscript as well as the pyrotechnic materials and assistance provided by Dr. Larry Dosser of Monsanto Research Mound Facility in Miamisburg, OH.

#### References

1. Dimotakis, P. E., F. D. Debussy, and M. Kouchesfahani (1981). *PHYS. FLUIDS* 24 995.
2. Adrian, R. J., and C. S. Yao (1983). "Development of Pulsed Laser Velocimetry (PLV) for Measurements of Fluid Flow," in *Proceedings, Eighth Biennial Symposium on Turbulence* (G. Patterson and J. L. Zakin, Eds.) (Conference held at University of Missouri, Rolla, MO, 1983).
3. Barker, D. B., and M. E. Fourny (1977). *OPT. LETT.* 1 135.
4. McDaniel, J. C., B. Hiller, and R. K. Hanson (1983). *OPT. LETT.* 8 51.
5. Adrian, R. J., and C. S. Yao (1985). *APPL. OPT.* 24 44.

6. Petche, K. S. (1978). "Photosensitive Materials," in Handbook of Optics (W. C. Driscoll, Ed.) McGraw-Hill Book Co., New York.
7. Marko, K. A., and L. Ramai (1985). APPL. OPT. 24 3666.
8. Bachalo, W. D., and M. J. Houser (1984). "Development of the Phase/Doppler Spray Analyzer for Liquid Drop Size and Velocity Characterization," Paper AIAA-84-1199 Presented at the 20th Joint Propulsion Conference, June 11-13, 1984, Cincinnati, OH.

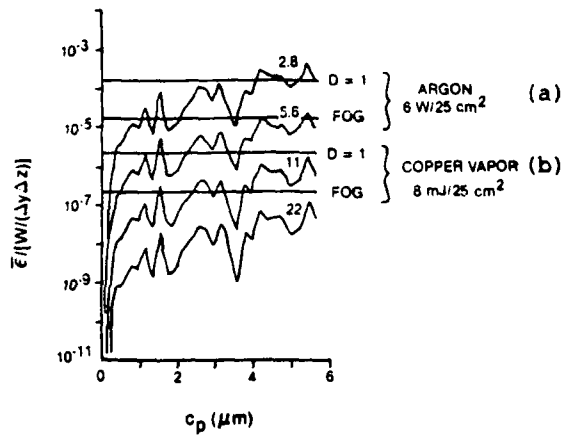


Figure 1. Nondimensional Mean Exposure as Function of Particle Size with Royal X-Pan Film for (a) Particle-Streak Case and (b) Pulsed-Laser Case.

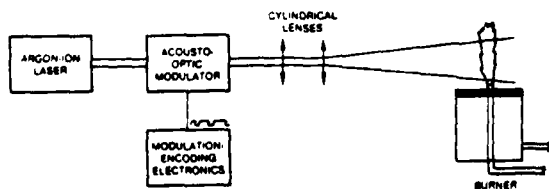


Figure 2. Particle-Streak-Velocimetry System with Encoding Scheme.

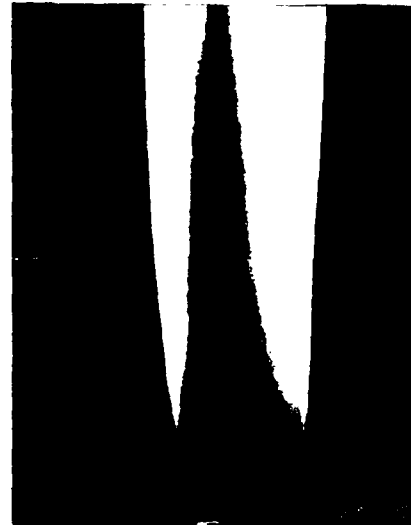


Figure 3. Encoded Particle-Streak Photograph of Seeded Propane Diffusion Flame.



Figure 4. Photograph of Seeded Nonreacting Air Jet Using Multiple-Pulsed Laser Velocimetry.

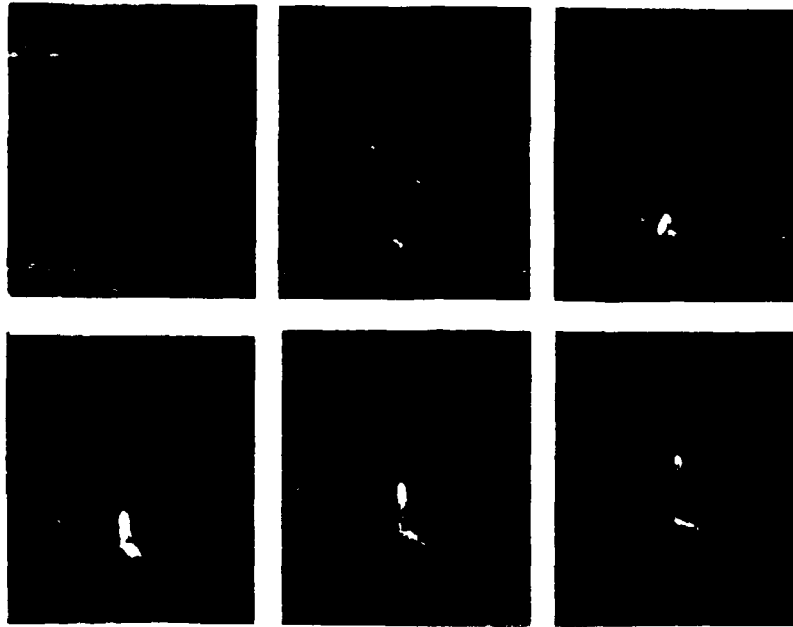


Figure 5. Evolution of Low-Flash-Pyrotechnic Ignition.  
Successive frames taken at 6000-Hz rate.

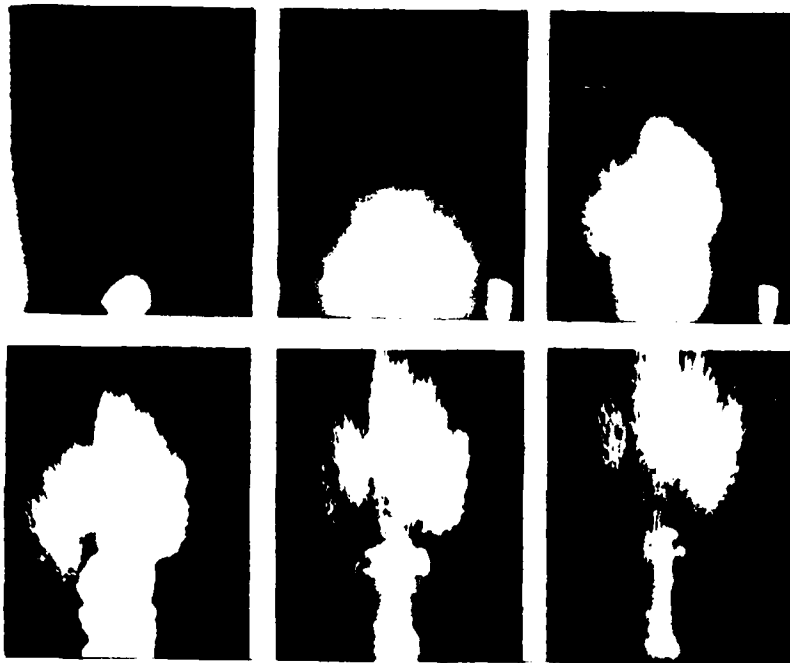


Figure 6. Evolution of High-Flash-Pyrotechnic Ignition.  
Successive frames taken at 6000-Hz rate.

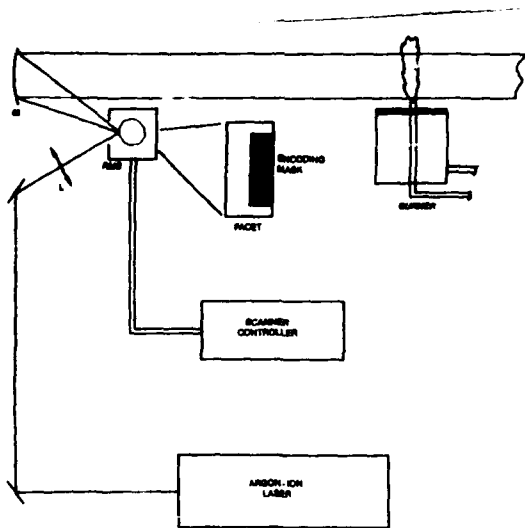


Figure 7. Rotating-Mirror Scanner System for Two-Dimensional Velocity Measurement and Flow Visualization.



Figure 11. Particle Track in Air Through 1-cm-diam. Jet.



Figure 8. Single Scan of Vortice Formation After Splitter Plate (air flow right to left).



Figure 9. Two Scans of Vortice Formation Separated by 11-ms Interval.



Figure 10. Encoded Scan Pattern in Recirculation Zone of Combusting Propane.



Figure 12. Encoded Track of Oil Droplets in Air Jet.

# Investigation of Velocity and Turbulence Intensity Measurement Limitations of the Phase Doppler Particle Analyzer

G.L. Switzer<sup>1</sup> and T.A. Jackson  
Air Force Wright Aeronautical Laboratories  
Aero Propulsion Laboratory  
Wright-Patterson AFB OH 45433

## ABSTRACT

The Phase Doppler Particle Analyzer (PDPA) offers the potential for simultaneous measurements of gas and droplet velocity and droplet diameter in two-phase, complex, recirculating flows. If this potential is to be realized, all aspects of the measurements must be evaluated for precision and reliability. Measurements have been made with the PDPA in both high-velocity (30m/s) and low-velocity (1m/s) flows. These same flows were analyzed with a TSI, Inc. two-color laser-Doppler velocimeter and a hot-wire anemometer, respectively. An evaluation of the results obtained with the three measurement techniques has identified certain configurations of the PDPA instrument which can produce significant errors in the determination of velocity and rms velocity. The error analyses conducted on the PDPA are presented herein along with identification of the sources of measurement error. Also, possible solutions to the problems are described.

## INTRODUCTION

Successful engineering of two-phase flow systems is critical to a variety of applications. In developing such systems it is desirable to have a thorough understanding of the interaction between the dispersed and carrier phases. To this end a great amount of research effort has been invested in both analytical and experimental studies. The study to be reported in this paper is experimental. The objective of the effort is to evaluate the limitations of an instrument, developed primarily to characterize the size and velocity of droplets, in measuring the velocity (mean, rms, and higher order moments) of the gas phase.

The Phase Doppler Particle Analyzer (PDPA) is an interferometric-based instrument designed to measure the size and velocity of spherical, translucent particles. Its theory of operation has been described in numerous publications (Bachalo, 1980; Bachalo and Houser, 1984). Further, its ability to size

1. Systems Research Laboratory, a Division of Arvin/Calspan  
2800 Indian Ripple Road, Dayton OH 45440-3696

liquid droplets has been evaluated by several investigators and found to be acceptable (e.g., Jackson and Samuelsen, 1987; Dodge et al, 1987).

Two features of the PDPA design make it potentially useful for simultaneously characterizing both phases of a two-phase flow. First, it has a broad sizing range (35:1 for a given optic and electronic configuration of the instrument). In one setup it has the potential to measure both gas and droplet velocities, using the particle sizing capability as a means of identifying the size of the scatterer and, thereby, discriminating between droplet and gas velocity. Second, a large number of realizations (of order 90K) can be taken for each data point. In a spray with a broad size distribution, this large amount of data should permit the acquisition of a sufficient amount of velocity information on very small scatterers to provide a statistically significant base with which to generate the gas phase velocity moments.

In utilizing the PDPA to characterize a high speed and a low speed air flow (30m/s and 1m/s) several measurement errors surfaced. Details of comparisons made between the PDPA and a standard laser Doppler anemometer (LDA) and a hot-wire anemometer can be found in other papers (Obringer et al, 1988; Aggarwal et al, 1988). In this paper the discussion will be confined to the phase Doppler instrument. While it is not suggested that all of the measurement discrepancies can be attributed to the PDPA, the investigation reported herein identifies several limitations to its operation as an LDA instrument in the current configuration.

### EXPERIMENT

A two-color PDPA was evaluated for its accuracy in making velocity and rms velocity measurements. Only one channel has been examined. For the purpose of this evaluation several features of the PDPA should be noted. First, it uses a circular, transmission-type, diffraction grating as both a beam splitter (using the two first-order beams) and as a frequency shifting device for each channel. The grating has three tracks with line pair widths at the center of each track of 6.08, 11.45, and 21.4 micrometers (Figure 1). On the order of 30% of the incident beam energy is retained in each of the two first order beams used to form the interference probe volume. For a given optical configuration, the three grating tracks offer a selection between three beam spacings in the transmitter (three fringe spacings at the probe volume) of the PDPA. The grating is rotated by a motor in order to shift the fringes. The motor speed is variable and its value is carefully checked by optical encoders. It provides for a range of frequency shifts (in combination with the appropriate tracks) between 0.2 and 8MHz.

Second, the signal processors of the PDPA operate with an 80MHz clock speed. This speed contributes to setting the

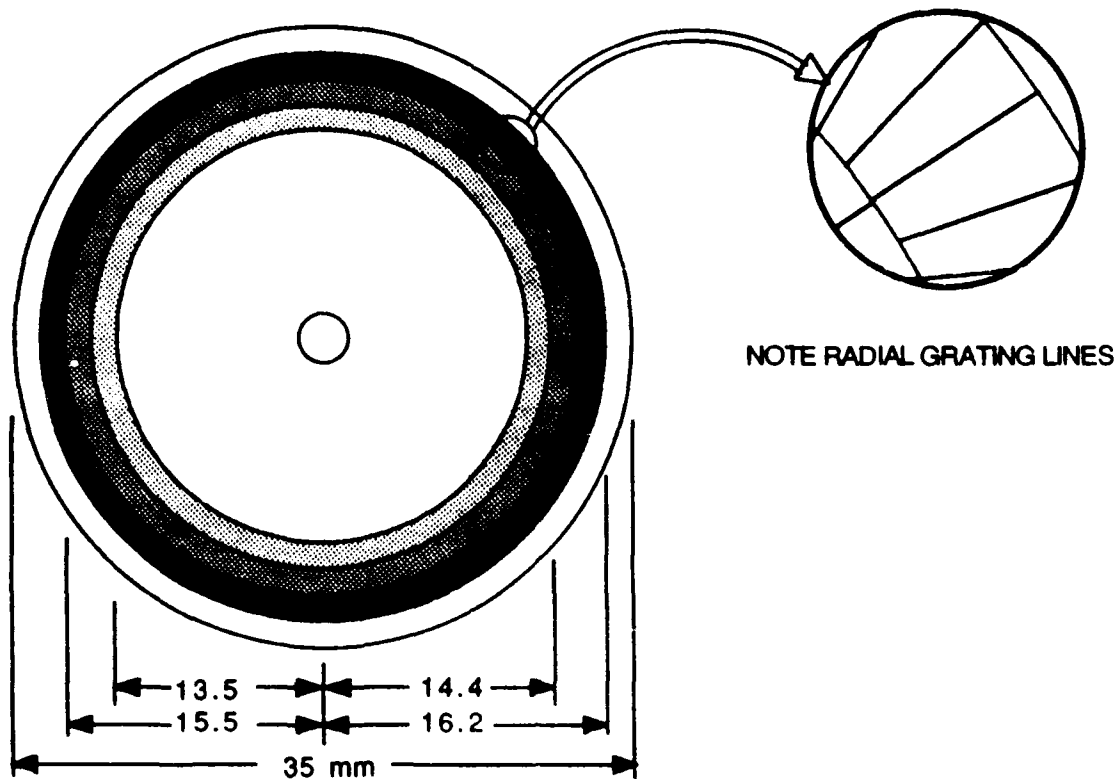


**FIGURE 1 Diffraction grating for beam splitting and frequency shift**

resolution of the instrument as it is the number of clock cycles per Doppler burst which define the burst.

Finally, the measurement range of the instrument, both size and velocity, is divided into fifty bins. Velocity and size information is stored as bin counts and the actual floating point value of velocity and size is lost after the measurement is assigned to the appropriate bin. In some cases this method of storage results in a loss of resolution, i.e., the bin width is larger than the instrument resolution.

A discrepancy was noted between the velocity measurements of the PDPA and other instruments. The following test was designed to evaluate the phase Doppler measurement accuracy. A variable speed, light beam chopper was employed as a source of stable and accurately known rotational frequencies. Infrared light emitting diodes and phototransistors sensing the chopper blade movement stabilized the rotational frequency to within  $\pm 0.3\%$  of the desired value. In addition to the digital frequency readout of the chopper system, an independent frequency determination was obtained with a frequency counter driven by the output of a PIN photodiode illuminated by a Helium Neon laser directed through an aperture in the chopper blade. A boron fiber approximately six micrometers in diameter was placed along a radii of the chopper blade and extended 1.5mm beyond the edge of the blade. The blade was then positioned so that the fiber swept through the probe volume of the PDPA, generating very clean Doppler bursts. The

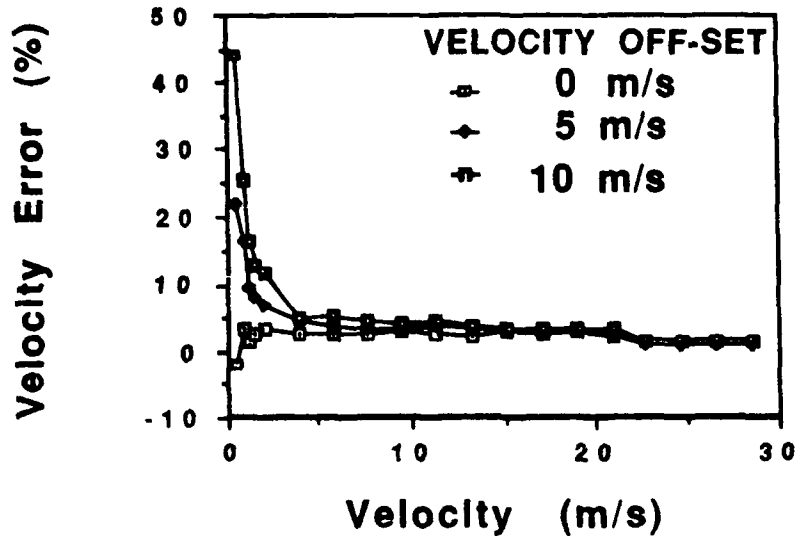


FIGURE 2a Velocity measurement error as a function of mean velocity

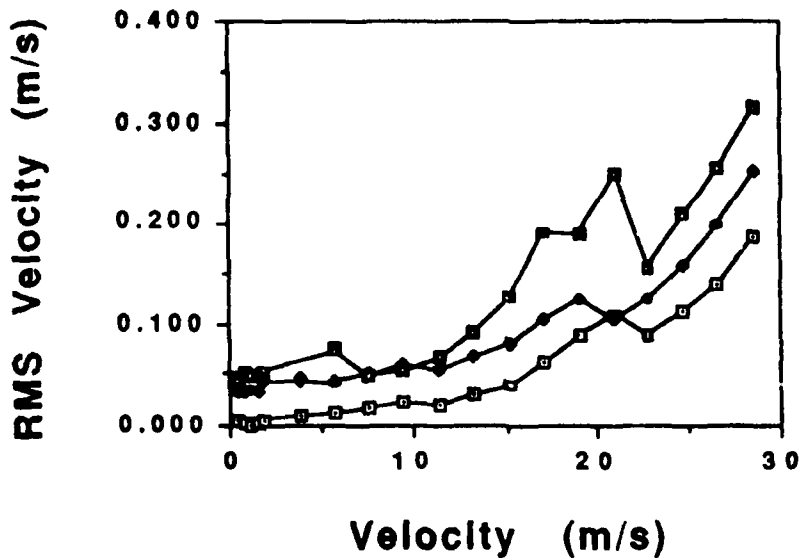


FIGURE 2b RMS velocity as a function of mean velocity

diameter of the circle swept out by the fiber was 120.90mm  $\pm$  0.03mm. This diameter along with the rotational frequency provided a precise determination of the linear speed of the scatterer through the probe volume.

### RESULTS

In Figure 2a the tangential velocity of the fiber moving on the wheel is indicated on the horizontal axis. The vertical axis

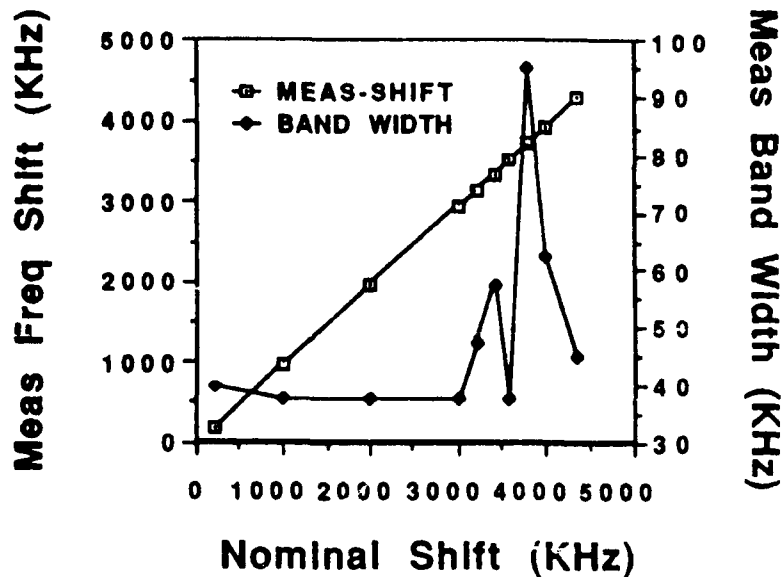


FIGURE 3. Spectrum analysis of the diffraction grating rotational frequencies

represents the difference between the mean velocity measurement of the PDPA and the known fiber velocity expressed in percent of the known velocity. The three plots are for three values of frequency shift or shift velocity (0, 5, and 10m/s). Above 20m/s the PDPA velocity measurement is good for all values of frequency shift. Between 2 and 20m/s the measurement is still good but there is a consistent error of approximately 3%. Below 2m/s the error in the measurement is very high when frequency shift is used.

Figure 2b indicates the companion rms velocity measurements. At the highest mean velocity the rms varies from 0.2 to 0.3m/s, less than a 1% error relative to the mean measurement. At the lowest measured mean velocity, however, the measured rms is 12% of the mean velocity for frequency shifted measurements. This is a substantial error in measuring low speed, low turbulence flows.

A direct measurement of the frequency shift generated by the rotating grating of the PDPA has been made in an attempt to isolate the error in the rms measurement. This is accomplished by imaging the PDPA probe volume through a microscope objective onto a measurement plane containing a PIN photodiode connected to spectrum analyzer. The signals produced by the diode are analyzed for various rates of frequency shifting as set by the velocity offset parameter of the PDPA. For each velocity offset, two frequency characteristics have been observed: the average frequency of fringe movement and the noise about this value. The data obtained from these measurements are shown in Figure 3. As can be seen by this data, the frequency shift set by the PDPA is very near that measured. However, there is a noise bandwidth of at least 35kHz present at all rotational speeds. At low values of

frequency shift this level of noise is a significant contribution to the measured rms.

The existence of the noise band about the nominal shift frequency implies that either the rate of rotation of the grating or the line pair spacings are not uniform. To isolate these possible effects, another method of determining the rotational rate and stability of the grating has been employed. An alignment laser is reflected from the surface of the grating disc at near zero grazing incidence. The reflected beam is observed to move in a circular orbit as the grating is rotated. A PIN photodiode is placed in this path and its output analyzed with a counter and spectrum analyzer. The results of this analysis indicate the rate of rotation is stable. The fact that the reflected beam moved in a circle casts immediate suspicion upon the uniformity of the line spacing on the grating as seen by the focused PDPA beam. If the center of the grating precesses around the center of rotation or if the surface of the grating is not flat, the point on the grating where the incident beam is focused will move radially as the grating is rotated. As can be seen in Figure 1, any radial movement results in a change in grating line pair spacing (between 5 and 10% depending on the track in use).

#### CONCLUSIONS

The Phase Doppler Particle Analyzer is a viable instrument for use in two-phase flows. In its current configuration and with judicious use of frequency shifting it accurately measures mean flow velocity. Currently it does not characterize low speed, low turbulence flows satisfactorily when any level of frequency shift is used. It performs acceptably in this regard when there is no imposed shift velocity. The error associated with shifting arises from an oscillation in the movement of the grating as it is rotated. This oscillation superimposes at least a 35kHz band onto the measurement. This can overwhelm the rms measurement in low turbulence flows.

With regard to high speed flows of modest to high turbulence levels, the results are not conclusive. Some of the apparent error may be associated with the rotational stability of the grating as described above. However, there is also some suspicion that the error may be linked to the resolution of the data after it has been stored as bin information. This issue is unresolved.

Currently, efforts to correct deficiencies and resolve open items are underway. A more stable grating motor is being identified, the flatness of existing grating wheels is being checked, the processor speed has been increased by a factor of five (to 400MHz), and an option has been written into the processing software to change the data storage to gain access to the full resolution of the instrument.

### ACKNOWLEDGEMENT

The cooperation of Dr. W.D. Bachalo and his staff at Aerometrics, Inc. in identifying possible sources of measurement error in the PDPA instrument as well as corrective action is gratefully acknowledged.

### REFERENCES

Aggarwal, S.K. et al (1988) "Vaporization behavior of multi-component fuel droplets in low temperature streams", Central States Section of the Combustion Inst., Spring Meeting, Indianapolis IN

Bachalo, W.D. (1980) "Method for measuring the size and velocity of spheres by dual-beam light-scatter interferometry", Applied Optics Vol 19, pp 363-370

Bachalo, W.D. and Houser, M.J. (1984) "Development of the phase/Doppler spray analyzer for liquid drop size and velocity characterization" 20th AIAA Joint Propulsion Conf, AIAA-84-1199

Dodge, L.G. et al (1987) "Comparison of drop size measurement techniques in fuel sprays: Malvern laser diffraction and Aerometrics phase Doppler" Applied Optics Vol 26, No 11

Jackson, T.A. and Samuelsen, G.S. (1987) "Droplet sizing interferometry: a comparison of the visibility and phase/Doppler techniques" Applied Optics Vol 26, No 11, pp 2137-2143

Obringer, C.A. et al (1988) "The influence of particle size on the measurement of turbulence characteristics in two-phase flows" to be published in the Proceedings of the 1988 ICLASS mtg, JAPAN

## The Development of a Water-Cooled Droplet-on-Demand Generator\*

Gary L. Switzer  
Systems Research Laboratories, Inc.  
A Division of Arvin/Calspan  
2800 Indian Ripple Road  
Dayton, OH 45440-3696

The technology for controlling production of liquid droplets has found many applications. While some of these techniques have commercial application, many more have been developed for use in a research environment for studies of droplet behavior and interactions. The development of many different methods for droplet generation has been necessitated by the requirements of particular applications--from controlling the flow of ink onto printer paper to the precise placement of pesticides. Although droplet-diameter ranges of from tens to hundreds of micrometers are common to many generation techniques, operating parameters such as frequency, velocity, size uniformity, liquid composition, and droplet number densities can vary considerably, depending upon the desired result. Design considerations and development of one technique for single-droplet (droplet-on-demand) generation are described herein. Although the generator described is being developed for a specific research application, its construction and operational characteristics are sufficiently versatile to permit its application to many studies requiring the production of isolated droplets.

A program in progress to study the rate of vaporization of various types and combinations of liquid fuels requires a generator which can inject droplets axially into a flow of air heated to 400 K without perturbing the velocity or temperature uniformity of the flow. Single monosized droplets are required having diameters in the range 50 - 90  $\mu\text{m}$ , each droplet having identical initial velocity and trajectory. An essential characteristic of the system involves long-term stability. That is, once a droplet of given diameter and velocity is produced, these two parameters must remain stable for a period of up to 0.5 hr. while relative diameter measurements are being performed. The experimental configuration containing the droplet generator is shown in Fig. 1. One problem presented by this configuration is that the droplet generator, located at the tip of the droplet-generator support, requires thermal isolation over its 60-cm length from the heated air flow to prevent pre-vaporization of the fuel. This isolation is provided by a water-cooled sheath which also serves as a support for the generator.

The configuration of the droplet-on-demand generator is diagrammed in Fig. 2. The generator operation is based on a piezoelectric (PZT) cylinder 0.7 mm ID x 1.3 mm OD x 19 mm in length. A voltage pulse applied between the inner and outer surfaces of the PZT causes the cylinder to contract radially. This contraction creates a pressure wave which forces liquid in the cylinder through a glass nozzle whose aperture diameter is equal to that of the desired droplet. The most critical aspect of this generator design is the shape and quality of the nozzle which is formed by melting and polishing glass capillary tubing. A properly formed nozzle produces clean, single droplets with PZT

\*Work supported by USAF Contract No. F33615-85-C-2562.

drive voltages as low as 10 V. One of the most useful features incorporated in the design shown in Fig. 2 is a nozzle-mounting configuration which allows convenient removal of the glass tip for cleaning or replacement.

Seven operational parameters have been identified which have a major influence upon successful generator performance, the most sensitive of these being PZT drive-voltage amplitude, pulse width, pulse-repetition frequency, and liquid pressure. The viscosity of the liquid, PZT temperature, and rise and fall times of the PZT pulse also impact generator performance but to a lesser extent. Proper generator operation, as shown in Fig. 3, requires a delicate balance among these seven parameters. When control of these parameters is exerted with sufficient sensitivity and stability, the generator performs very reliably.

Development efforts during this study resulted in a compact, versatile, reliable technique for production of single liquid droplets and introduction of these droplets into a hostile environment. The droplet-on-demand system as presently configured has produced droplets using water, hexane, and decane as the working fluids. Through precise control of the operational parameters, several discrete droplet diameters in the range 40 - 90  $\mu\text{m}$  can be stably generated from a single 65- $\mu\text{m}$  nozzle aperture. Droplet-generation frequencies range from one droplet up to a stream of droplets at 1 kHz, with adjustable exit velocities varying between 0.2 and 10 m/s. The generator has demonstrated capability in operating in any orientation and in temperature environments in excess of 500 K. A shortened version of this design could prove to be even more efficient, although the difficulties created by the extreme length required by the present application have been overcome.

## References

1. T. A. Jackson, G. L. Switzer, S. K. Aggarwal, and K. Nguyen, "Vaporization Behavior of Multicomponent Fuel Droplets in Low-Temperature Streams," Presented at the 1988 Spring Technical Meeting of the Central States Section of the Combustion Institute, Combustion Fundamentals and Applications Section, May 2-3, 1988, Indianapolis, IN.

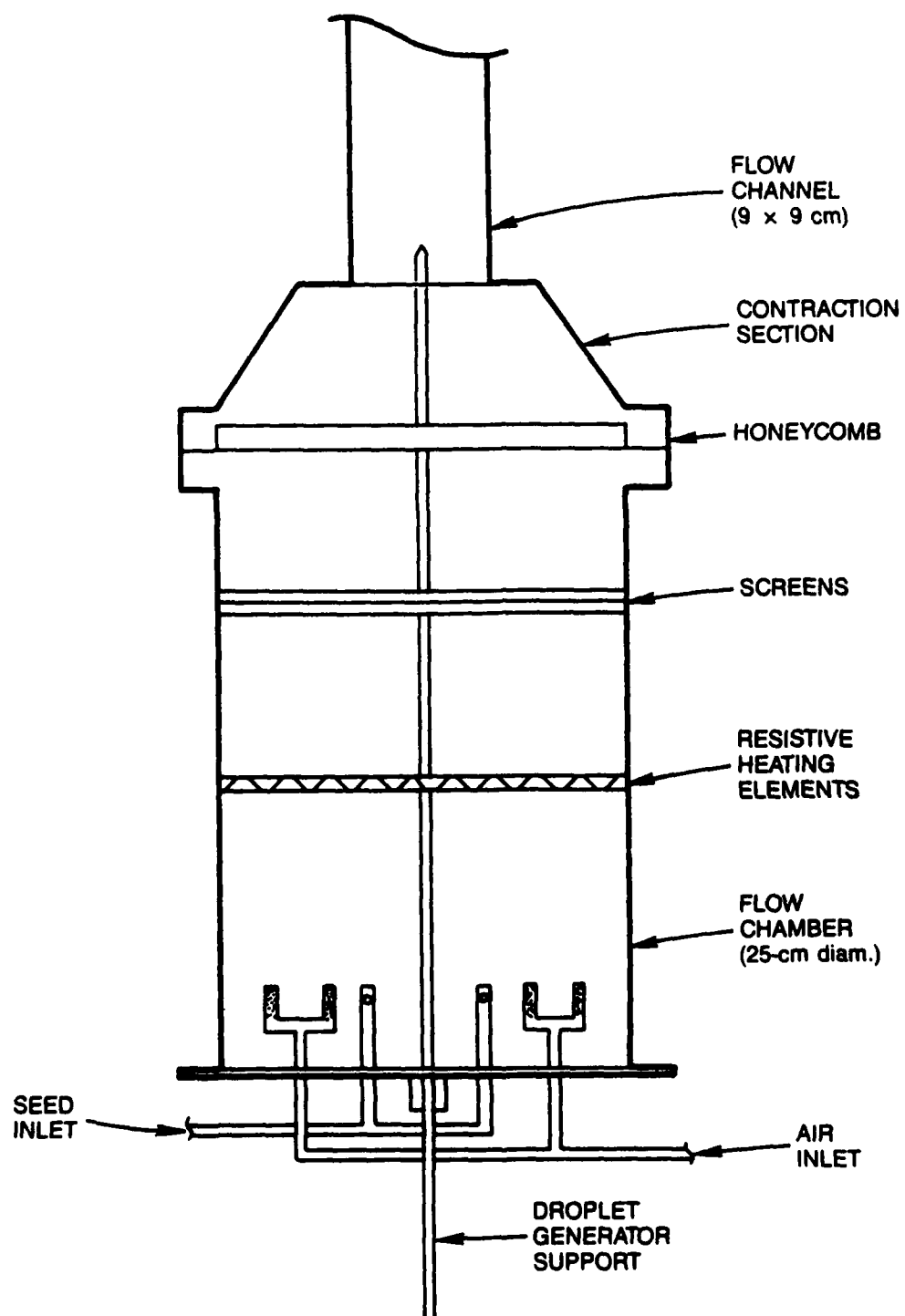


Figure I. Diagram of Flow Chamber Employed for Droplet-Vaporization Studies.

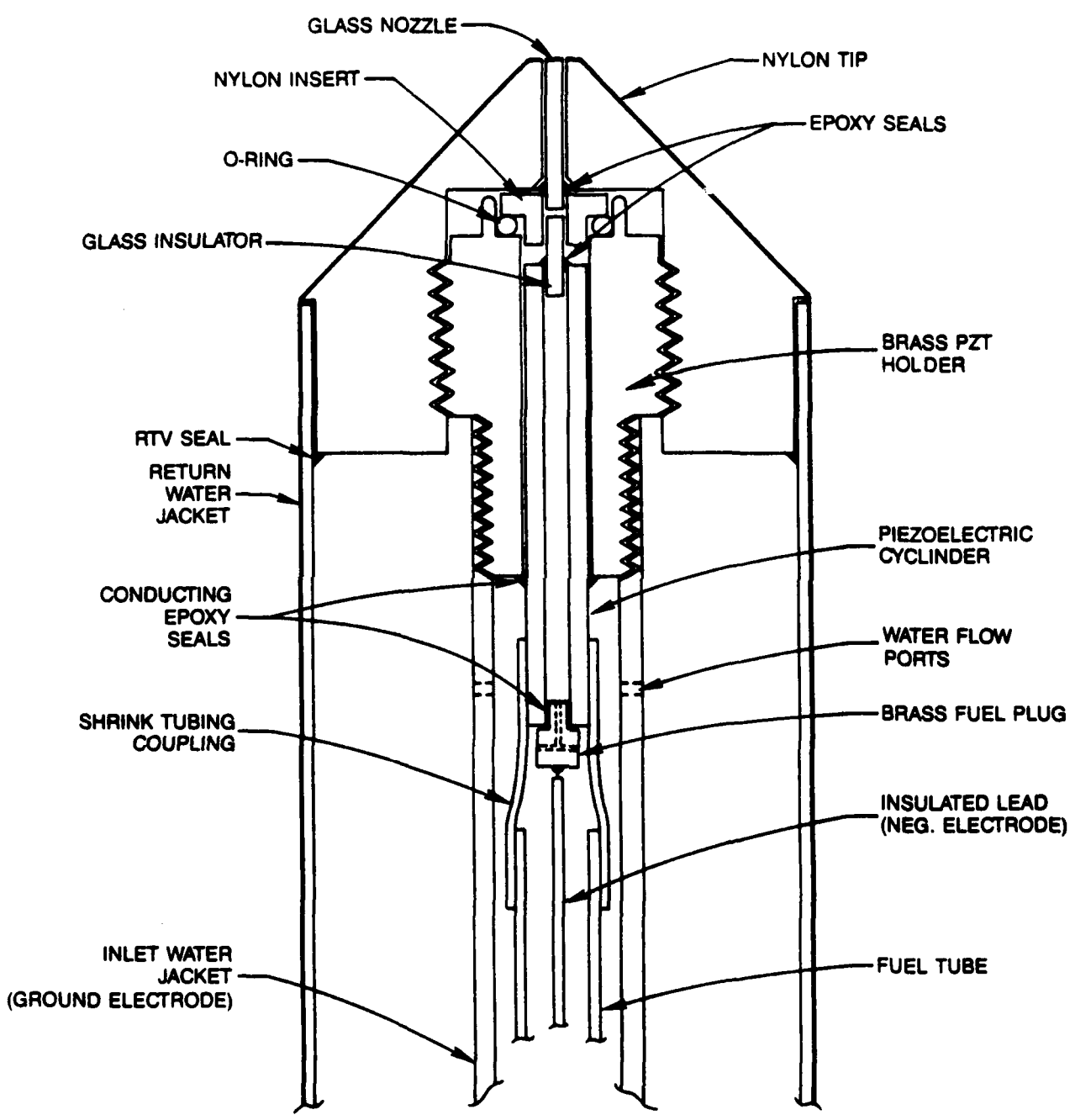


Figure 2. Schematic Diagram of Water-Cooled Droplet-on-Demand Generator.

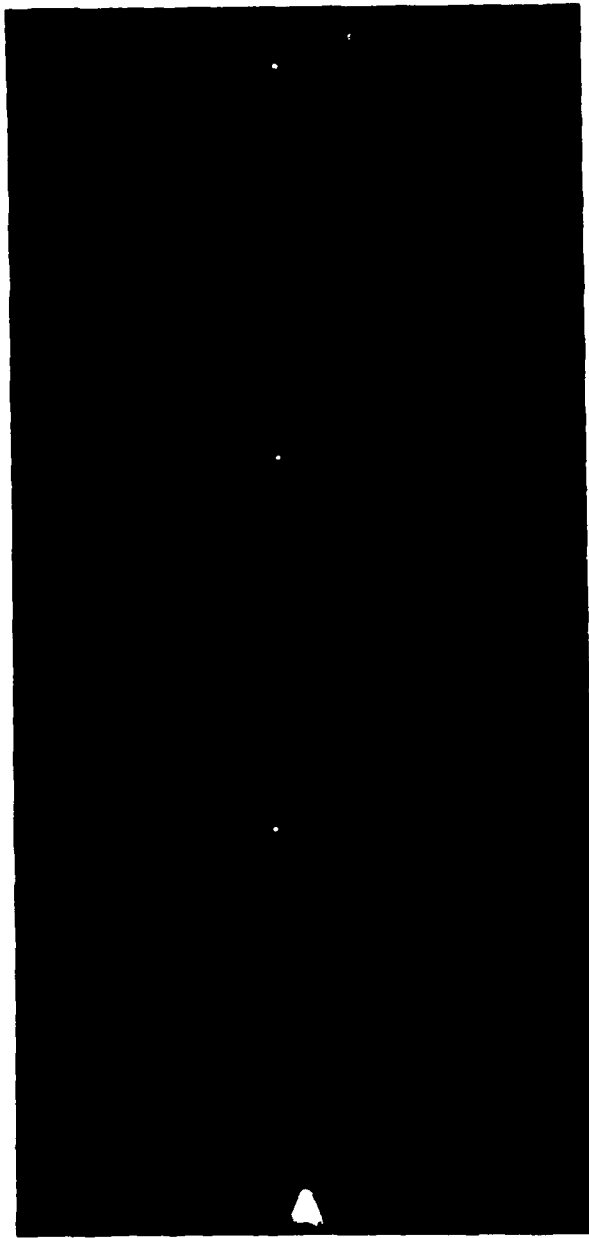


Figure 3. Generation of 55- $\mu$ m Droplets at 10-Hz Rate.

# AN INTEGRATED SPECTROSCOPIC - INTERFEROMETRIC INSTRUMENT FOR SPRAY COMBUSTION DIAGNOSTICS

by

G.L. Switzer\*, T.A. Jackson, C.A. Obringer, and J.S. Stutrud

Aero Propulsion and Power Laboratory

Air Force Wright Research and Development Center

Wright-Patterson AFB OH 45433

## ABSTRACT

An optical diagnostic instrument has been constructed, which integrates the capabilities of the Coherent Anti-Stokes Raman Spectroscopy (CARS) technique with those of the Phase Doppler Particle Analyzer (PDPA). The resulting CARS/PDPA system provides a non-intrusive capability with which to measure gas and droplet behavior in spray flames. Gas temperature and velocity and droplet size and velocity can be measured nearly simultaneously with excellent spatial resolution. The CARS system electronics supplies a 7 millisecond, gated window to the PDPA instrument in which it can acquire data. The CARS laser firing and its resulting measurement of gas temperature is centered within the window. Some of the capabilities of the combined instrument are demonstrated in an atmospheric, complex flow spray flame.

## INTRODUCTION

Liquid fueled combustion systems are common, integral elements of the power plants for many applications. Research focused on extending the performance limitations of these devices is widespread. Historically, instrumentation available for such studies has been limited to intrusive probes, photography, and external performance measurement devices such as thrust stands and exhaust gas emission analysis. Laser based diagnostic techniques have recently broadened the experimental capabilities of fuel spray research. Useful techniques include laser Doppler velocimetry (LDV), coherent anti-Stokes Raman spectroscopy (CARS), and phase Doppler particle analysis (PDPA). Each of these techniques, as well as other related diagnostic tools, have unique characteristics and capabilities. None provide a complete picture of the two-phase combustion process.

---

\* Systems Research Laboratories  
Division of ARVIN/CALSPAN  
Dayton OH 45440

The CARS and PDPA systems, when used together, provide an opportunity to evaluate many of the dominant features of a combusting fuel spray. In previous work on combustion systems fueled with gaseous propane (1) a CARS system was combined with a two-component LDV instrument in order to measure gas temperature and two components of gas velocity. Temperature and velocity measurements were collected within 4 microseconds of each other, facilitating examination of the relationship between time averaged thermal and flow fields. An additional dimension to the diagnostic problem is added when the fuel is introduced as a liquid. For this current investigation the CARS/PDPA combined system offers the opportunity to make droplet size and velocity measurements as well as obtain gas phase temperature and velocity information. This paper details the process by which the CARS and PDPA instruments are combined and reports our initial attempts to utilize the combined CARS/PDPA instrument in a complex reacting, two-phase flow.

## INSTRUMENTATION

### The Components

The CARS instrument is based on a pulsed Nd:YAG laser and is operated in a folded BOXCARS optical configuration. It samples the vibrational spectra of molecular nitrogen, measuring gas temperature with an accuracy ranging from  $\pm 20\text{K}$  at  $2000\text{K}$  to  $\pm 40\text{K}$  at  $300\text{K}$ . The optical probe volume is approximately 1 cubic millimeter, with a 150 micrometer diameter waist. Details of this configuration can be found elsewhere (2, 3). Its performance has been successfully demonstrated in the hostile environment of a large scale combustor (4).

The PDPA is based on a continuous wave Argon ion laser. It is a two-component system, measuring particle size and two orthogonal velocity components. Size discrimination is used to assign measured velocities to the gas phase or droplet phase statistics. Particle velocities up to  $\pm 100\text{m/s}$  and diameters between 0.7 and 400 micrometers are measurable with the instrument in its current configuration. The probe volume is of order  $10^{-3}$  cubic millimeters with a 100 micrometer diameter waist. This instrument has been predominantly used in non-reacting flows (5), although limited results have been reported for combusting sprays.

### Combining the Pieces

The optical configuration for the combined CARS/PDPA instrument is shown in Figure 1. The optical axes of the instrument lie in

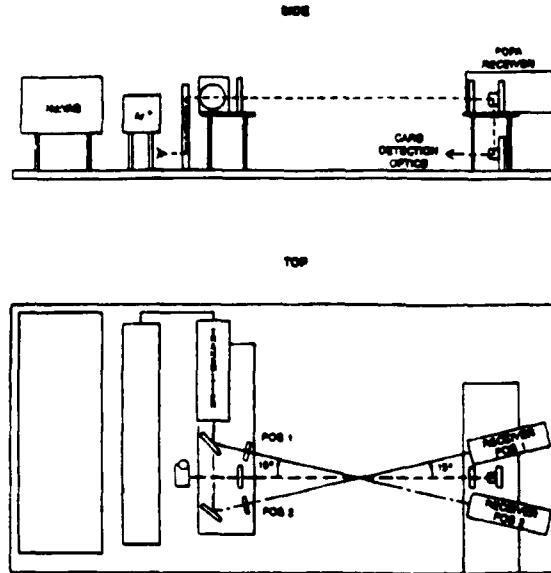


Figure 1. Optical Layout of the combined CARS/PDPA instrument

a horizontal plane, physically configured to measure a horizontally moving flow field. This design was chosen to best satisfy two operational constraints. First, combining these two optical systems require that a total of seven laser beams (three for CARS and four for PDPA) be directed to a common focal volume. A coaxial optical geometry would best resolve axial and radial velocity components. However, since the relative spacing of the beams of each diagnostic technique is nearly the same, the requirements for the physical placement of beam handling optics in a coaxial arrangement preclude its use. Second, while the CARS collects forward scattered energy, the optimum performance of the PDPA requires that it collect light at a  $30^\circ$  off-axis, forward position. To satisfy this requirement, while leaving space to physically position the transmission and receiving optics of both systems, the axes of both the PDPA transmitter and receiver are aligned  $15^\circ$  to the same side of the CARS axis. See the paths labeled "position 1" and "position 2" in Figure 1. Two positions of the PDPA equipment are required to maximize the measurement coverage of the instrument in light of the limited optical access of the test article. Insertion or removal of one reflecting optic and the corresponding positioning of the PDPA receiver module allows convenient switching between the two positions.

Data can be acquired with this system in one of two modes: continuous or gated. During continuous operation each measurement technique accumulates data independently. While CARS informa-

tion is generated in 10 nanosecond laser pulses at a repetition rate of 10 Hz, the PDPA continuously processes Doppler bursts produced by the passage of a particle through a set of interference fringes. In gated operation the CARS operation is unchanged. The PDPA system, however, is gated, acquiring data only during a 7 millisecond window which is centered about the CARS measurement event. The timing diagram for this mode of operation is shown in Figure 2.

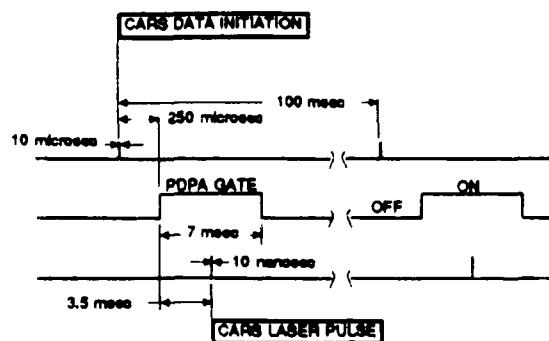


Figure 2. CARS/PDPA timing sequence

The purpose of a gated mode of operation is to synchronize the acquisition of data from the two instruments to allow near-simultaneous collection of velocity, temperature, and drop size information. To insure that each phase/Doppler measurement can be matched to the proper CARS data point several timing aids are included in the data recording procedure. At the beginning of data collection each successive CARS measurement is assigned a shot number. This number also becomes the gate number for the corresponding PDPA gate. Upon application of the first gate pulse to the PDPA, two 32-bit timers are initialized. One timer, the run time, runs continuously throughout the data accumulation and records the arrival time of each PDPA measurement. This timer acts a second check for insuring proper gate numbering since its values are grouped in increments of 100 milliseconds corresponding to the 10 Hz gated operation. The other clock, the gate time, is initialized at the start of each gate, thus maintaining a high precision record of the arrival time of each measurement within individual 7 millisecond gates. Since the CARS measurement event occurs at a fixed 3.5 milliseconds from the start of the PDPA gate pulse, the gate timer is used to define how "simultaneous" events within the gate occur.

#### EXPERIMENTAL

An atmospheric, liquid fueled combustor has been used to evaluate the CARS/PDPA. It is illustrated schematically in Figure 3. The research burner is axisymmetric with its inlet plane coincident with the face of a 14 cm diameter centerbody. The centerbody is concentrically mounted in a 25.4 cm diameter duct. Air flows through the annulus formed between the center-

body and the duct at a rate of 1 kg/sec. The mean air velocity in the annulus is 24.1 m/s. The standard Air Force aviation distillate fuel, JP-4, is injected from a Delevan pressure atomizer

(model 2.0/30) fitted flush into the face of

the centerbody. The fuel flow rate is 6.5 kg/hr, matching the energy flux used in operating this burner with propane fuel in the earlier, single-phase combustion study (See Reference 4).

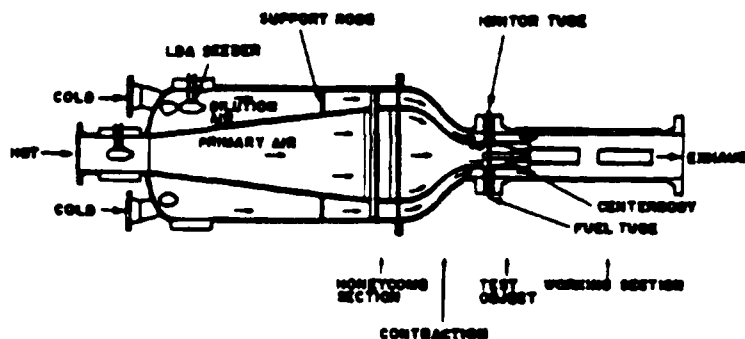


Figure 3. Atmospheric combustor layout

## RESULTS

Two aspects of the instrument performance have been evaluated. The first consideration is the quality of the spray analysis when the PDPA is operated in a gated mode; that is, with blocks of data recorded in 7 millisecond windows, opening with a frequency of 10 Hz. Essentially this mode of operation is analogous to an LDV post-processing technique, constant time interval sampling. This correction is often used to eliminate biasing effects of variable density flows. It is not clear that such a "correction" is needed to characterize the spray and the cost of this mode of operation is a substantially reduced effective data rate. The second consideration is the quality of the CARS temperature data in the presence of droplets. If a droplet is in the vicinity of the measurement volume during the CARS laser firing the droplet can create a background signal that distorts or completely obscures the nitrogen spectra. The effect of particle breakdown during the collection of the CARS signal has been evaluated and reported (6). The local number density limit was estimated for 80 micron droplets at  $10^3$  drops per cubic centimeter. Signal recovery was approximately 80% of the affected spectra.

### Gated PDPA Spray Measurements

The spray has been characterized one centimeter from the nozzle face with the PDPA operated in both the gated and continuous modes. Figures 4a and 4b illustrate the results. The solid curve in each figure represents cold spray measurements with water. They are included as a reference. Some differences are expected due to physical differences in the two fluids (primarily density and viscosity) and differences in the ambient gas environment (local gas velocity and temperature). It is expected

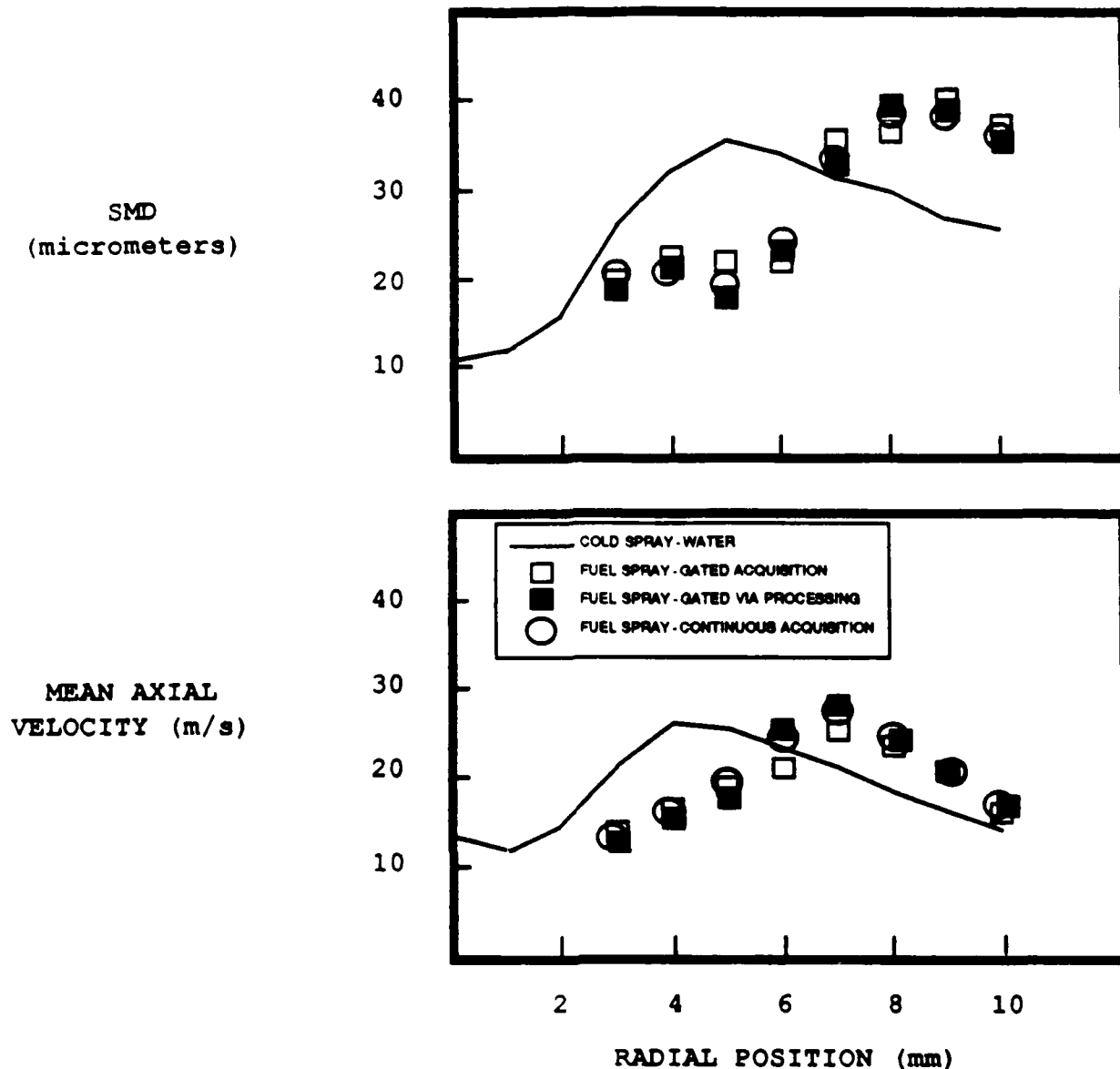


Figure 4. Radial profiles of droplet size and velocity within the fuel spray 1 cm from the nozzle face

that at this position, 1 cm from the nozzle, the measurement profiles should take on similar shapes. As evident in the figure the hot and cold measurements are similar. The hot measurements, however, are radially shifted by approximately 3 mm. The complex, recirculating flow pattern established by the large bluff body at the injection plane may be pulling the spray radially outward. This has yet to be established.

There are no significant differences between the continuous and gated spray measurements for either droplet size or velocity (open symbols). The continuous data was also post-processed in a way to simulate the gated operation. That is only data within 7 millisecond windows, spaced 100 milliseconds apart were processed (darkened symbols). Again these fall in line with the

other data. Thus, gating has no influence on the droplet measurements. The effect of gating is, however, expected to be important in interpreting gas phase measurements with this combined instrument and the issue will have to be revisited when the gas phase measurements are included.

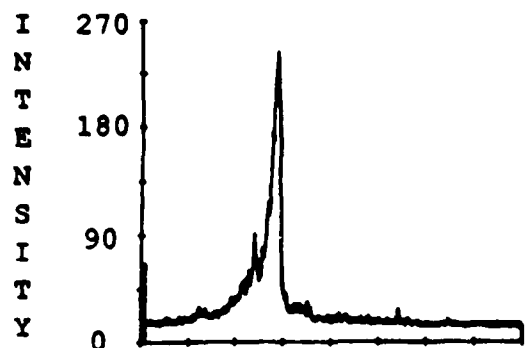
#### CARS Measurements within Spray Flames

The CARS behavior in the presence of the spray has been more predictable than that of the PDPA. Two types of signal interference were expected and observed. Figure 5 presents five illustrations of the types of spectra observed in this spray flame. The narrow sharp peak surrounded by a low baseline in Figure 5a shows a relatively clean CARS spectrum free from background contributions. The temperature of this spectrum is found in Figure 5b by a fit to a calculated spectral library. The "goodness" of fit of the experimental and library spectra is calculated to be  $\pm 14$  K. Figures 5c, e, and f represent more typical measurements in this spray flame environment. The CARS signal contains the peak broadening influence of a non-resonant interference from the CARS beam interaction with fuel vapor, 5c; or contains the broadband noise associated with droplet breakdown, 5f; or a combination of both influences as illustrated in Figure 5e. If not properly compensated, these contributions to the recorded spectra can result in significant errors in the gas temperature measurement.

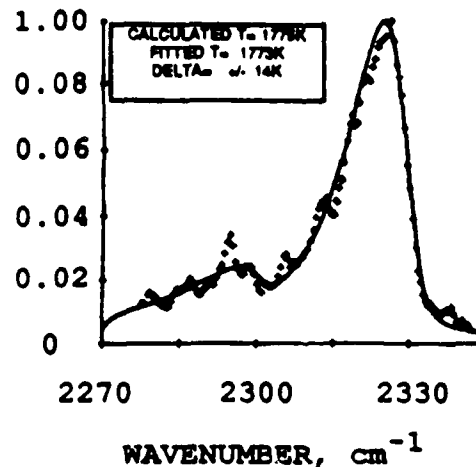
Figure 6 illustrates the radial gas phase temperature profiles made with the CARS in the fuel spray environment at 4 cm downstream of the injection plane. Droplets were present at two of the five radial measurement stations. The local droplet number density as measured by the PDPA are also included on the figure for reference. To illustrate the effects of background influences the temperature data was processed by four methods. In the first case temperature reduction was performed with no compensation for either type of background influence.

In the second case only the correction for the non-resonant contribution was made, eliminating the fuel vapor contribution to the CARS signals. Near the centerline and at the outer edges of the reaction zone the concentration of fuel vapor is expected to be low and fuel droplets are not present; CARS data should be well behaved. Near the spray at the 2 and 3 cm stations droplets are present but no correction is made for droplet breakdown. There is a peak in the gas temperature where one might expect a depression. That is, in the spray itself evaporation rates are high and oxygen is scarce resulting in low gas-phase temperatures.

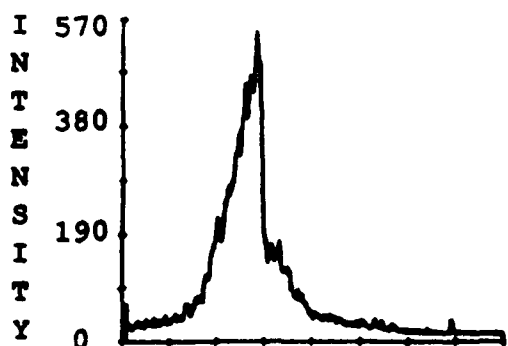
(a) "Clean" CARS Spectrum



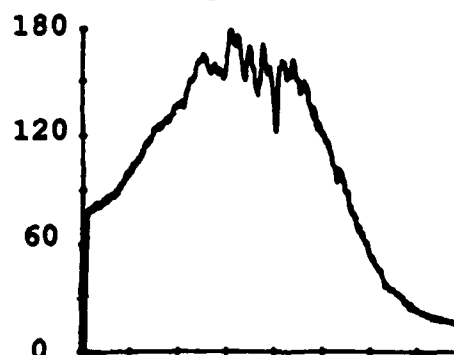
(b) "Clean" CARS Temperature Fit



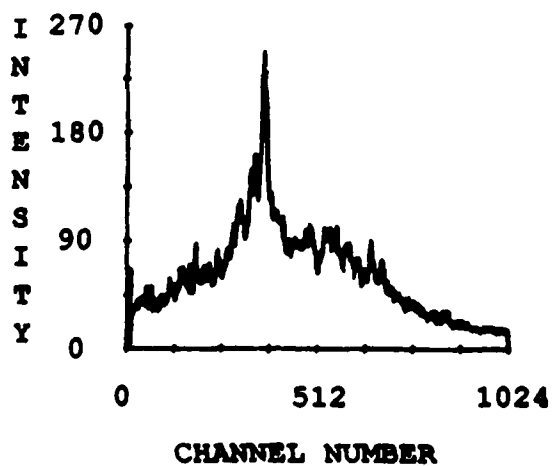
(c) CARS plus Non-resonant Interference



(d) Broadband Interference from Droplet Breakdown



(e) CARS plus Non-resonant and Broadband Interference



(f) CARS plus Broadband Interference

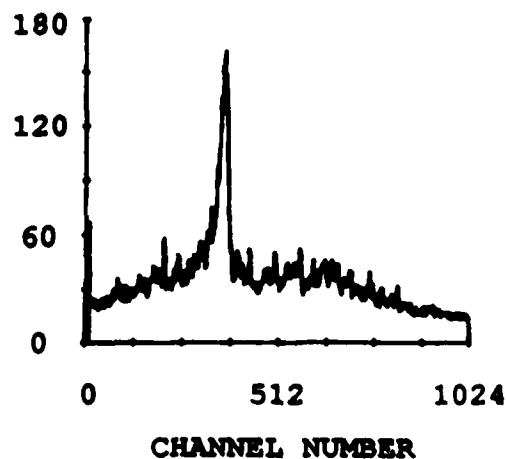


Figure 5. CARS spectra in a reacting spray flame

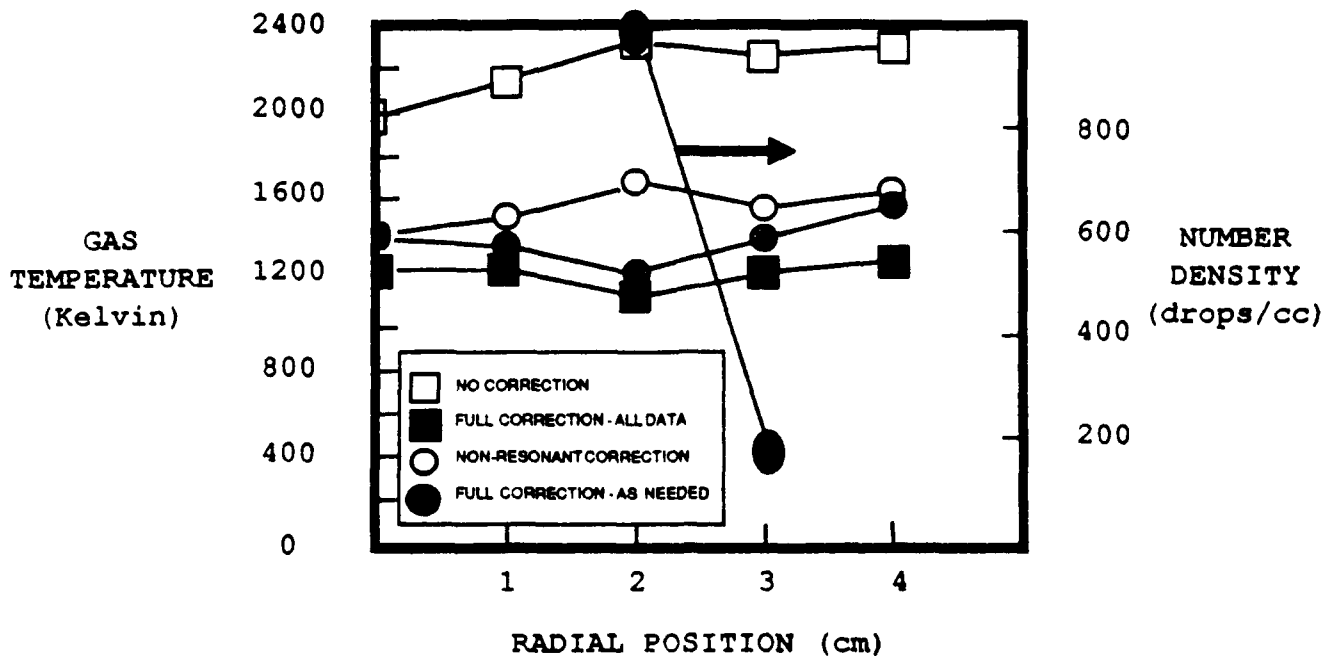


Figure 6. Gas temperature radial profile

In the third processing scheme corrections for the non-resonant contribution and droplet breakdown were both instituted on all the spectra (whether or not a correction is warranted). The profile labeled "full correction - all data" represents the results. Temperatures are suppressed hundreds of degrees. Note also that the centerline and outer edge measurements are substantially altered even though no droplets were found by the PDPA instrument in these regions.

The final processing approach represents a more rational correction methodology. The results are represented by the profile labeled "full correction - as needed." In this case the spectra were examined individually to determine if a correction for droplet breakdown was warranted. To make this determination we examined the measured intensity on channels far removed from the CARS spectrum. If there was a substantial increase in intensity on these channels, a background proportional to the pure breakdown spectra of Figure 5d was subtracted from the spectra before fitting it to the library spectra. The results are consistent with measurements one would expect. That is the centerline and outer edge temperatures are the same as those determined by applying only the non-resonant correction; and temperature decreases near the spray.

#### CONCLUSIONS

Combining the measurement capabilities of the CARS and PDPA provide a powerful tool for measurements in two-phase, reacting flows. Neither instrument is being operated in an optimal en-

vironment and the PDPA is restricted to operate at low collection frequencies. However, when near-simultaneous gas and droplet phase measurements are desirable, such measurements are possible.

Gated operation of the PDPA is analogous to applying an equal time interval correction scheme to the data. Such a correction is desirable in flows with significant density gradients. In flows where a correction is not needed, acquiring gated PDPA data has no adverse consequence except low effective data rates.

CARS data are clearly sensitive to the combustion environment. Large concentrations of evaporated fuel distort the measurement. This has been observed on other work (4) and the correction scheme developed in these previous efforts apply to the spray flame. However, an additional correction is required for signal distortion due to droplet breakdown. The major challenges here lie in automating the detection of breakdown and in continued refinement and rigorous evaluation of the correction.

#### REFERENCES

1. Goss, L.P., et al (1988). Combined CARS/LDA instrument for simultaneous temperature and velocity measurements," *Experiments in Fluids*, Vol 6, pp. 189-198.
2. Switzer, G.L., et al (1980). "Application of CARS to simulated practical combustion systems," *J of Energy*, Vol. 4, pp. 209-215.
3. Switzer, G.L. and Goss, L.P. (1982). "A hardened CARS system for temperature and species-concentration measurements in practical combustion devices," Temperature: Its Measurement and Control in Science and Industry, Vol 5, edited by J.F. Schooley, American Institute of Physics, NY, pp. 583-587.
4. Switzer, G.L., et al (1986). "CARS measurements in the near-wake region of an axisymmetric bluff-body combustor," *AIAA Journal*, Vol 24, No 7, pp 1155-1162
5. Jackson, T.A. (1988). "Droplet sizing interferometry," *Invited Review, 2nd Symposium on Liquid Particle Size Measurement Techniques*, American Society for Testing and Materials
6. Dunn-Rankin, D., et al (1988). "Effect of droplet induced breakdown on CARS temperature measurements," *Western States Section/The Combustion Inst.*, Paper WSS/CI 88-96, Irvine CA